UNIVERSITÀ
DEGLI STUDI
DI TRIESTE

UNIVERSITÀ DEGLI STUDI DI TRIESTE

XXXVII CICLO DEL DOTTORATO DI RICERCA IN

NANOTECNOLOGIE

CARBON NANODOTS: BUILDING BLOCKS FOR THE PRECISE SYNTHESIS OF NANO- AND MICROSTRUCTURES

Settore scientifico-disciplinare: **CHIM/06**

DOTTORANDA
MARIA SBACCHI

COORDINATORE
PROF. ALBERTO MORGANTE

SUPERVISORE DI TESI
PROF. MAURIZIO PRATO

CO-SUPERVISORE DI TESI
PROF. PIERANGELO GOBBO

ANNO ACCADEMICO 2023/2024

Table of Contents

Abbreviations

AEMA	Aminoethyl methacrylate
AFM	Atomic Force Microscopy
AIBN	2,2′-Azobis(2-methyl propionitrile)
ATR-FTIR	Attenuated Total Reflectance-Fourier Transformed Infrared
Boc	*Tert*-butyloxycarbonyl
CDs	Carbon Dots
CNDs	Carbon NanoDots
d	Doublet
δ	Chemical shift
Đ	Dispersity
DLS	Dynamic Light Scattering
DMF	*N,N*-Dimethyl Formamide
DOSY	Diffusion Ordered Spectroscopy
DP	Differential Pressure
EDA	Ethylene diamine
GOx	Glucose oxidase
GPC	Gel Permeation Chromatography
HPLC	High Performance Liquid Chromatography
HRP	Horseradish peroxidase
IP	Inlet Pressure
KT	Kaiser Test
LALS	Low Angle Light Scattering
LCST	Lower Critical Solution Temperature
m	Multiplet
NHS	*N*-hydroxysuccinimide
NIPAA	*N*-isopropyl acrylamide
NMR	Nuclear Magnetic Resonance
p	Para
PL	Photoluminescence
PNIPAA	Poly(*N*-isopropyl acrylamide)
PTFE	Poly(Tetrafluoroethylene)
QY	Quantum Yield

RAFT	Reversible Addition-Fragmentation chain Transfer
RALS	Right Angle Light Scattering
RDRP	Reversible Deactivation Radical Polymerization
RhB	Rhodamine B
RI	Refractive Index
RSD	Relative Standard Deviation
s	Singlet
SEC	Size Exclusion Chromatography
t	Triplet
TBAB	Tetrabutylammonium bromide
TEA	Triethyl amine
TEM	Transmission Electron Microscopy
TFA	Trifluoroacetic acid
THF	Tetrahydrofuran
UV	Ultraviolet
UV-Vis	Ultraviolet-Visible

Abstract

Engineering microcompartments to exhibit life-like behaviors is one of the major challenges for bottom-up synthetic biology and nanotechnology. These microcompartments are defined as protocells when mimicking key biological functions, such as compartmentalization, selective permeability, and catalytic activity. One emerging category of protocells is colloidosomes, micro-compartmentalized assemblies built from amphiphilic colloidal particles. Organic colloidosomes, typically composed of protein-based nanocomposites, have drawbacks such as low stability over time and high production costs. In contrast, Carbon NanoDots (CNDs) offer significant advantages due to their unique physicochemical properties, including excellent photostability, tunable fluorescence, low toxicity, and ease of functionalization. These properties position CNDs as promising platforms for fabricating more complex structures.

The objective of this Thesis is to exploit CNDs as building blocks for protocell synthesis while investigating the composition, superficial chemistry, and reactivity of these carbon nanomaterials with molecular and nanomaterial species.

The essential scientific concepts are described as a general introduction in the first chapter, focusing on the information useful for the following discussion.

In the second chapter, the characterization of CNDs using multi-detector Gel Permeation Chromatography is explored. Initially, the synthesis and purification of *L*-arginine and ethylenediamine-derived CNDs are evaluated through various characterization techniques. Then, GPC analyses are employed to determine the molecular weight moments and distribution of different CND batches, supported by ζ-potential and Dynamic Light Scattering measurements. The investigation extends to quantify and exploit CND surface functionalities for derivatization reactions, revealing insights into their interfacial reactivity.

The third chapter investigates the exploitation of interfacial reactivity of CNDs for their covalent assembly *via* Copper(I)-catalyzed azide-alkyne cycloaddition to form carbon-based suprastructures. Functionalized CNDs are used to construct these suprastructures and their optical and photophysical properties are examined, revealing energy transfer processes between different types of emitting CNDs.

The fourth chapter discusses the synthesis and characterization of the amphiphilic units for colloidosomes fabrication, namely CND/polymer nanoconjugates. The chapter initially focuses on the design and synthesis of an *N*-isopropyl acrylamide-based copolymer through Reversible Addition-Fragmentation Chain Transfer (RAFT) polymerization and the study of its thermoresponsive properties. The CND/polymer nanoconjugates retained the key characteristics

of both the CNDs and copolymers, and the study of their composition are carried out by multi-detector GPC.

The fifth chapter investigates the fabrication of CND-based colloidosomes *via* the Pickering emulsion technique. After engineering these microcapsules, they are characterized using microscopy techniques and evaluated for their enzyme-like activity, representing a significant advancement toward developing a new type of protocells.

The sixth and final chapter delineates the general conclusions, providing a critical assessment of the work carried out in this Thesis.

Chapter I – General Introduction

1.1 Carbon Dots

The manipulation of matter at the nanoscale – between 1 and 100 nm – has generated a wide range of nanomaterials, driving advancements in the applied science of nanotechnology.[1–4] An eclectic element such as carbon[5] is an example of how the tuning of physical and chemical properties (*e.g.*, size, shape, morphology, composition, chemistry) is pivotal for the development of nanomaterials and nano-based devices for specific and advanced applications.[6–12]

Carbon dot (CD) is an umbrella term for photoluminescent carbon-based nanomaterials. Over the past two decades, they have gained such significant interest that they are now recognized as a well-established class of nanoparticles. CDs have a size below 10 nm, a quasi-spherical shape, and are constituted of carbon, hydrogen, and oxygen atoms.[13]

These nanomaterials were serendipitously discovered in 2004 by Xu *et al.* during the purification of single-walled carbon nanotubes *via* electrophoresis, where they appeared as fluorescent carbon particles.[14] A few years later, CDs were synthesized through methods such as laser ablation of bulk carbon sources or electrochemical treatment of multi-walled carbon nanotubes.[15,16] In 2008, Bourlinos *et al.* reported the first synthesis of small, fluorescent carbogenic nanoparticles using organic molecular precursors through a one-step pyrolysis method.[17]

Classifying CDs is challenging, as current synthetic methods can produce a wide variety of carbon nanomaterials. Nevertheless, a common approach to their categorization is based either on their photoluminescence properties or their structural characteristics.

According to the first classification, CDs can be divided into graphene quantum dots (GQDs), carbon quantum dots (CQDs), carbon nanodots (CNDs), and carbonized polymer dots or polymer-like dots (CPDs).[18,19] GQDs are disc-shaped nanoparticles consisting of one or a few layers of graphene, formed during the exfoliation of graphitic materials, and exhibit quantum confinement behavior. CQDs are quasi-spherical nanoparticles characterized by a multi-layered crystalline graphitic core with delocalized band structures, which accounts for the term “quantum”. In contrast, CNDs also possess a quasi-spherical morphology but do not exhibit quantum confinement effects due to their carbonized amorphous structure. Lastly, CPDs are polymer and carbon-based hybrids, characterized by crosslinked structures that self-assemble into a quasi-spherical shape.[18,19] However, discriminating between these types of CDs can be difficult, as establishing a clear correlation between their structure and photoluminescence is not yet straightforward.

Alternatively, relying on their structural properties, CDs are typically described as core-shell structures. The core can be either amorphous or graphitic, with the latter usually forming at synthesis temperatures above 300 °C. Meanwhile, the shell is generally rich in functional groups.[20] To synthesize all these types of CDs, the approaches are divided into top-down and bottom-up (**Figure 1.1**).[21,22]

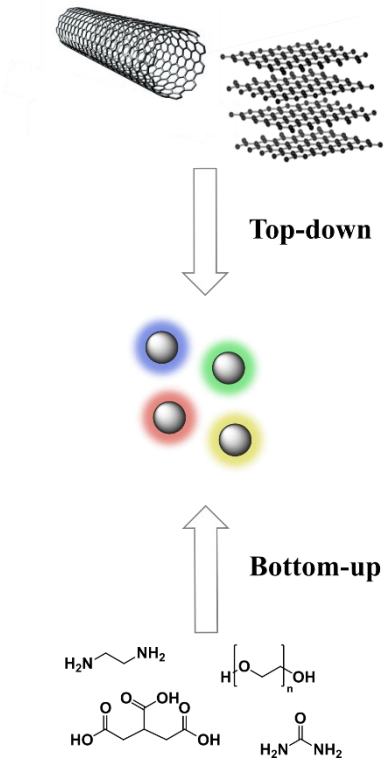

Figure 1.1. *Schematic representation of the synthetic routes yielding CDs.*

The top-down methods, such as arc discharge, laser ablation, and electrochemical oxidation, use bulk carbon-based materials (*e.g.*, graphite, carbon nanotubes, carbon black). These approaches are advantageous for scalability, as they typically produce large quantities of CDs. However, they often require harsh experimental conditions, including high pressures and temperatures, which can complicate the synthetic process. Moreover, top-down methods frequently introduce structural defects into the resulting materials, potentially affecting their photoluminescence and overall performances.[20,23]

In contrast, bottom-up routes focus on building CDs from organic molecular precursors through methods like pyrolysis, microwave-assisted synthesis, and solvothermal treatments. Starting from smaller building blocks, these methods offer greater control over CD size, shape, and surface chemistry, potentially leading to improved optical properties. This approach also allows for the synthesis of higher-quality CDs with fewer defects, while facilitating the incorporation of functional groups that can be tailored for specific applications. Each route offers distinct

advantages and challenges, influencing the selection of the method based on the desired characteristics and applications of the final product. Overall, bottom-up methods are preferable to exert a fine-tuning of CD properties.[19,24]

Another important parameter that significantly impacts the physicochemical properties of CDs, affecting aspects like particle size, graphitization, surface functional groups, and doping, is the pre-synthetic control, consisting of the choice of carbon precursors and synthetic procedures. Notably, certain structural features of the starting materials can be retained in the final nanoparticles, providing some predictability in their properties. For instance, dopants such as heteroatoms (*e.g.*, nitrogen, boron, sulfur, selenium) and metals (*e.g.*, lanthanides) can be efficiently incorporated during synthesis.[25,20]

In addition to pre-synthetic control, modifying the surface composition of CDs through post-synthetic strategies offers a promising route to further optimize and broaden their functional applications. While post-synthetic methods primarily affect surface functional groups, they generally leave the core properties and composition unchanged. Moreover, leveraging the surface chemistry of CDs has enabled the development of various functional CD-based materials.[26,27,18]

An overview of tunable core-shell parameters of CDs is reported in **Figure 1.2**.

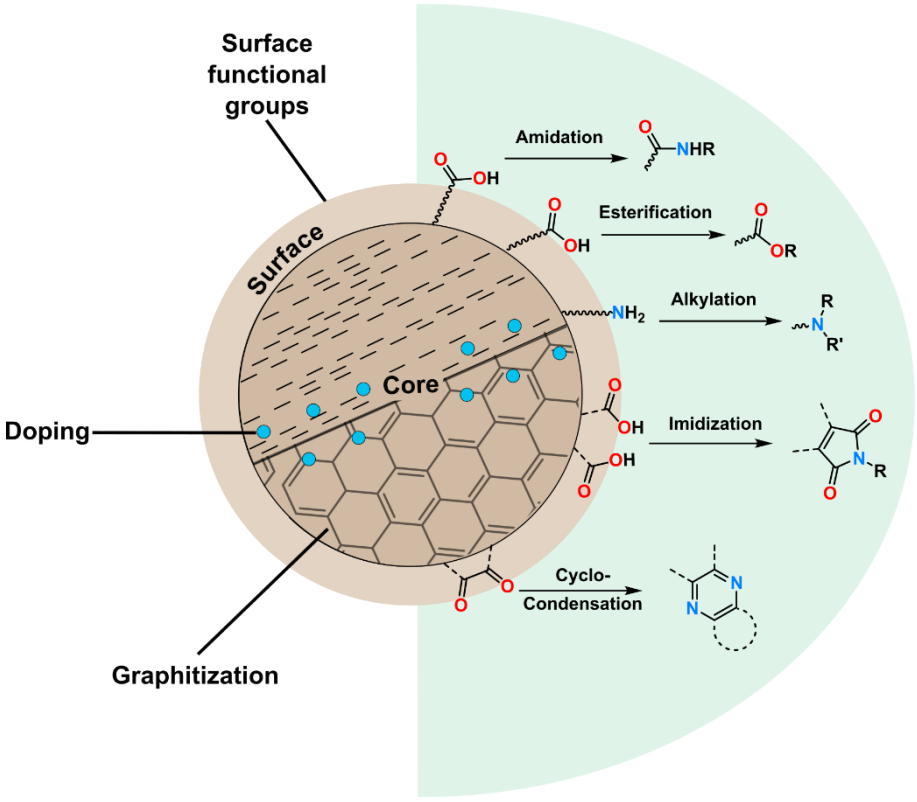

Figure 1.2. *Schematic representation of the tunable core-shell parameters of CDs.*

Despite the numerous synthetic approaches to produce CDs discussed previously, their formation mechanism is still not yet fully understood. This limits the precise tailoring of CD properties – particularly their fluorescence – based on the nature of the carbon precursors or the synthetic methodologies used. However, recent studies have introduced promising approaches to better elucidate and rationalize the formation process of these nanomaterials, primarily through the combination of various spectroscopic techniques and theoretical calculations.[28–30]

To fully understand the CD formation process and effectively utilize these nanomaterials, it is essential to rigorously purify them and perform a comprehensive characterization of the synthesized CDs to limit inconsistencies, ensure accurate separation from by-products, and assessment of nanomaterial properties.[31,32]

Although there is currently no standardized method for purifying CDs, purification techniques can be broadly categorized into two groups: removal (*e.g.*, centrifugation, filtration, dialysis, frequently employed for purifying water-soluble samples) and separation techniques (*e.g.*, chromatography and electrophoresis). Typically, the choice of the protocol depends on the dispersibility of the sample.[33,32]

Centrifugation is favored for its speed and ease of use, even though it may leave molecular impurities that can affect the structure and properties of CDs.[34,35] In the same way, filtration is also widely used due to its simplicity and efficiency in removing larger impurities, however, it is even less efficient in removing smaller contaminants as compared to centrifugation.[36,37] To overcome this issue, it is necessary to couple these methodologies with dialysis. Optimizing the dialysis process – particularly the molecular weight cut-off of the membrane, as well as the duration and frequency of water replacement – is essential for achieving optimal results.[38,39] For CDs that are soluble in organic solvents, methods such as liquid-liquid extraction or precipitation with suitable solvents can be exploited to remove residual molecules. However, these methods are ineffective for separating CDs based on their size or surface functional groups.[32] In those cases, electrophoresis, silica gel chromatography, and High Performance Liquid Chromatography (HPLC) can be useful, even though they might not be straightforward and require careful sample preparation, specialized equipment, and high costs.[40,41,31] As a general rule, to enhance purification quality, there is a common trend towards combining multiple techniques, leading to higher purity levels in CD samples.[33]

After the purification step, a comprehensive characterization of the synthesized nanomaterials is crucial, not only to confirm the successful formation of CDs but also to assess their purity and explore their physicochemical properties.

Nuclear magnetic resonance (NMR) spectroscopy can play a significant role in the analysis of CD purity. Unlike simple organic molecules, CDs exhibit more complex and heterogeneous structures, which result in broad, unresolved signals rather than sharp, well-defined peaks.[32] This is due to the varying environments experienced by protons in CDs, producing spectra similar to those observed for polydisperse polymers.[42] Furthermore, NMR spectra of macromolecules or nanoparticles tend to show broader linewidths due to slower molecular tumbling.[43] In contrast, small molecules usually produce sharp NMR signals, making it easier to detect their residual presence in CND samples. NMR can also provide insights into the size homogeneity of CND samples. Diffusion-ordered spectroscopy (DOSY) allows for the measurement of diffusion coefficients, which can distinguish between different species in the sample. This technique is widely used in polymer chemistry and provides key information about the macromolecular nature of the components based on their diffusion rates. Larger molecules, such as polymers or nanomaterials, diffuse more slowly than smaller ones like monomers or molecules, allowing a clear differentiation between them.[44,32] Other techniques such as transmission electron microscopy (TEM) and atomic force microscopy (AFM) are commonly used to analyze CD size, size distribution, and morphology, and to determine whether they possess a graphitic or amorphous crystalline structure.[45] The information about the core type can be further validated through X-ray diffraction (XRD) or Raman spectroscopy.[20] X-ray photoelectron spectroscopy (XPS) is also an essential technique that provides detailed insights into the elemental composition and bonding types in the sample. This method is particularly valuable for characterizing doped CDs, allowing for the quantification of the doping agent.[46]

In addition to structural information, understanding the surface functionalities of CDs is critical, as these can significantly influence their photocatalytic behavior and post-functionalization modifications that can be carried out. Functionalization can enhance charge carriers' separation, extend the excited-state lifetime, and promote interactions with target substrates.[47,48] For instance, the types and amounts of surface acid/base sites can be evaluated through standard pH titration, while the quantity of primary and secondary aliphatic and aromatic amines can be measured using $^{19}F\{^{1}H\}$-NMR spectroscopy with *p*-fluoro cinnamaldehyde, as demonstrated in our recent study.[49] The Kaiser test, a selective colorimetric assay, is another method for specifically quantifying primary amines.[50]

The optical and electrochemical properties of CDs are usually linked to (*i*) sp^2-conjugated core domains, (*ii*) surface functionalization, and (*iii*) heteroatom doping.[51] Heteroatom doping, in particular, can enhance charge carriers' separation and reduce their recombination, while also slowing redox reaction kinetics, trapping photogenerated electrons at surface sites.[47] Nitrogen-

doped CDs, for example, typically exhibit improved catalytic performance due to nitrogen being similar in size to carbon, allowing integration into the π-orbital system and raising the highest occupied molecular orbital (HOMO) level, thereby narrowing the bandgap.[52] Conversely, boron doping introduces an electron-deficient character by decreasing charge density through its empty π orbitals.[47,53] Multi-doped CDs, which often display higher photoluminescence quantum yield (QY) and superior performance, and metal-doped CDs have also been reported, commonly derived from organometallic complexes or metallic salts.[53–55] Additionally, some organic solvents, such as formamide, can act as dopants, since by-products derived from their decomposition may be integrated into the CD structure during the synthetic process.[56]

The optical properties of CDs are typically characterized by UV-Vis spectroscopy. Most CDs exhibit a primary absorption band below 300 nm, corresponding to π–π* transitions of C=C bonds, and a secondary tailing band between 300 and 400 nm, associated with n-π* transitions of C=O bonds.[53] The photoluminescence properties of CDs – fluorescence, phosphorescence, and upconverted photoluminescence – are of significant interest for various applications, with fluorescence being the most widely studied.[57,58] CDs typically display excitation-dependent emission spectra and large Stokes shifts, unusual phenomena among traditional molecular fluorophores and semiconductor nanoparticles, likely arising from the intrinsic heterogeneity of the sample.[51] Measuring the photoluminescence quantum yield (QY), which quantifies the ratio of emitted to absorbed photons, provides further insight into the emission properties.[59] Cadranel *et al.* have shown that CDs synthesized at lower temperatures tend to exhibit higher QYs, while higher temperatures increase graphitization, reduce surface functionalities, and lower QYs, due to longer excitation lifetimes leading to non-radiative relaxation pathways.[45]

The electrochemical properties are primarily assessed *via* cyclic voltammetry (CV), which is the most widely used method to provide information about the ground-state redox potentials, *i.e.*, the energy gap between the lowest unoccupied molecular orbital (LUMO) and the HOMO.[60,61] This gap is crucial, as it must be equal to or smaller than the energy of the photon source for CDs to effectively perform as photocatalysts.[62]

Additionally, leveraging CD moieties, it is possible to post-functionalize them, significantly changing their properties, thus broadening their applicability and allowing for further tailoring even after CD synthesis[18,63,64]

CDs found applications in the energy science field to improve solar cells performances,[65–67] prepare light-emitting diodes (LEDs),[68,69] and promote the conversion of solar energy into fuels.[70–72] However, owing to their low toxicity, hydrophilicity, biocompatibility, and stability, they find applications also in the biomedical field, being used for phototherapy, bioimaging, and drug

delivery.[73–78] At last, due to their ease of synthesis and functionalization, and their unique photo-redox properties, they are increasingly employed as (photo)organocatalysts to photodegrade pollutants, synthesize new valuable products, and mimic enzymatic behavior.[19,48,79–81]

Although CDs have numerous potential applications on their own, their combination with other (nano)materials – such as two-dimensional (2D) materials, metals, and polymers – creates hybrid composite materials that exhibit superior and advanced properties compared to their components.[82–84]

The most employed synthetic methods to prepare these CD-based composites include physical mixing, hydrothermal/solvothermal treatment, and chemical reduction. Physical mixing is an eco-friendly route but yields weaker interactions in the final hybrid, while hydrothermal treatment offers better control over composite size and shape but under harsher conditions. On the other hand, chemical reduction is a very interesting method, since it is based on the reduction of metal precursors into nanoparticles promoted by CDs that act as reducing agents.[85,86]

Falara *et al.* recently described how CD incorporation into 2D materials like graphene oxide, carbon nitrides, and transition metal dichalcogenides can expand their application.[85] Graphene-based materials have a high surface area and excellent mechano- and electrical properties, however, they tend to aggregate limiting their application.[87] The addition of CDs increases even more graphene-based materials' surface area and improves their conductivity and electron transfer abilities. These hybrids are applied as energy storage devices, heavy metal detectors in aqueous matrixes, and gas sensors.[88–90] Besides, graphitic carbon nitride (g-C_3N_4) is a semiconductor material with a similar molecular structure to graphene, which presents good physicochemical stability and low toxicity.[91] The synthesis of hybrids with CDs improves g-C_3N_4 photocatalytic properties by enhancing charge separation efficiency and broadening its absorption range, making these composites useful for environmental remediation and carbon dioxide reduction.[92–95] Lastly, transition metal dichalcogenides, such as molybdenum disulfide, have drawn significant interest due to their unique properties and easy availability.[96] However, they present some disadvantages like easy restacking and inefficient separation and transfer of photogenerated charge carriers.[97] Combining transition metal dichalcogenides with CDs delivers hybrids with improved photocatalytic performances applied for organic dye degradation and photodetection.[98,99]

Moreover, CD-metal composites represent a significant category of CD-based materials. Both noble and transition metals are widely used in fields like optoelectronics and biomedicine due to their distinct electrical and optical properties.[100] Consequently, integrating metals with CDs to enhance their photoelectric performance has gained considerable attention. The metal counterpart can be in three different forms – metal ions/atoms, metal nanoparticles, and metal oxides – and the

most employed elements are gold, cobalt, zinc, platinum, and manganese.[86] It can be either synthesized beforehand or formed *in situ* and combined with CDs. The designed composites will have improved optical properties, by modulation of their band structure by the presence of the metal, and biocompatible features, arising from CDs.[101–103] For this reason, hybrid materials find applications in bio-imaging and -sensing, and in drug delivery.[86]

Eventually, another family of CD-based materials is CD/polymer composites. In most cases, these composites are fabricated either by blending CDs into the polymer matrix or passivating the CD surface with a polymer.[104,105] Of particular interest is the possibility to graft polymeric structures onto CD surface, exploiting carbon nanomaterial superficial chemistry. As described previously, modifications of CD shells enhance their photo- and thermal stability and photoluminescence,[106] and give them new properties such as external stimuli responsiveness (*e.g.*, pH, temperature),[107–109] enabling them to be applied in bioimaging, tissue engineering, and optoelectronics.[110,111]

1.2 Reversible Addition-Fragmentation chain Transfer Polymerization

Given the significance of CD-polymer composites, it is essential to introduce fundamental concepts of polymer chemistry, including their synthesis methods. Polymerization processes are generally divided into two main categories: step-growth and chain-growth polymerizations.[112] The latter involves a sequence of three stages – initiation, propagation, and termination – where monomers are gradually consumed throughout the reaction.[113] Among chain-growth techniques, reversible addition-fragmentation chain transfer (RAFT) polymerization has gained significant attention over the past two decades.[114]

RAFT polymerization is a form of reversible deactivation radical polymerization (RDRP), often called living or controlled radical polymerization. It mimics many characteristics of living polymerization while preserving the versatility of radical-based methods. Essentially, living polymerizations are reactions in which chain termination or transfer is eliminated, allowing for continuous chain growth. In contrast, controlled polymerizations, like RAFT polymerization, suppress but do not eliminate termination, enabling greater control over polymer growth and molecular weight distribution.[115] Consequently, RDRP enables the production of polymers with predictable molecular weights, low dispersity (Đ), and the ability for continued chain growth.[114]

RDRP relies on a balance between active and dormant chains, which can be established through two mechanisms: *(i)* reversible deactivation, as seen in atom transfer radical polymerization (ATRP), for example, or *(ii)* degenerative transfer, as in RAFT polymerization. In a degenerative transfer mechanism, the total number of radicals remains constant during the activation-

deactivation process, so an external source of radicals, usually a radical initiator, is necessary.[114] **Figure 1.3** shows a scheme of the RAFT polymerization mechanism.

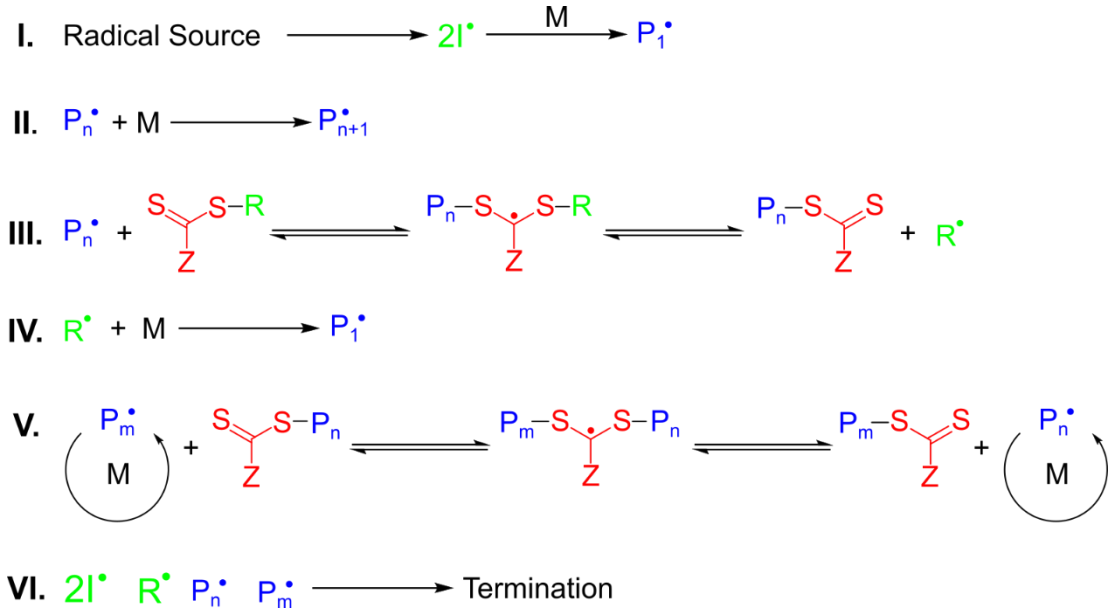

Figure 1.3. *Proposed mechanism of RAFT polymerization.*

Step I involves the activation of the initiator, which can occur through thermal, redox, or light-induced mechanisms.[116–118] Upon activation, the initiator decomposes into two radical fragments ($I^{\bullet}$), which react with a monomer molecule (M) to form a propagating polymeric radical ($P_1^{\bullet}$). In Step II, this propagating radical chain of length *n* ($P_n^{\bullet}$) adds to a monomer to form a longer chain propagating of radicals ($P_{n+1}^{\bullet}$). In Step III, a polymeric radical ($P_n^{\bullet}$) reacts with the RAFT agent – or chain-transfer agent (CTA), a thiocarbonylthio compound with selected R- and Z-groups – to form a RAFT adduct radical. This intermediate can undergo reversible fragmentation, either regenerating the original polymeric radical ($P_n^{\bullet}$) or producing a new radical ($R^{\bullet}$) and a polymeric RAFT agent (macroCTA). Then, the newly formed radical $R^{\bullet}$ reacts with another monomer (M) in Step IV, initiating the growth of a new active polymer chain. Step V represents the main RAFT polymerization equilibrium, where a rapid interchange occurs between the macroCTA (dormant chains) and the active propagating chains, allowing radicals to transfer back and forth passing through a RAFT adduct radical intermediate. This equilibrium ensures that all chains have equal opportunities for growth, leading to a narrow dispersity ($1.05 < Đ < 1.3$). To efficiently work, the rate of the addition/fragmentation equilibrium of the RAFT polymerization must be faster than the rate of monomer propagation, meaning less than one monomer is added per activation cycle, ensuring uniform chain growth. Finally, in Step VI, the remaining active chains undergo a bi-

radical termination process, where two radical chains react and terminate, forming chains that can no longer propagate.[119]

The RAFT process versatility comes from the careful selection of Z- and R-groups in the CTA. The Z-group controls the reactivity of the C-S bond toward radical addition, while the R-group affects chain fragmentation and propagation. For good control over the polymerization process, the R-group must balance radical stability and reactivity to ensure that polymer chains grow at the same rate, resulting in narrow molecular weight distributions. Typically, R-groups that mimic monomer radicals or initiators are particularly effective.[120]

Moreover, the RAFT polymerization technique stands out for its ability to handle a wide range of functional monomers. Vinyl monomers are categorized into more activated monomers (MAMs), where the double bond is conjugated to an aromatic ring (*e.g.*, styrene, acrylates), and less activated monomers (LAMs), where the double bond is adjacent to one or more oxygen, nitrogen, halogen or sulfur lone pairs (*e.g.*, vinyl acetate, vinyl chloride) based on their reactivity.[121] MAMs require CTAs that stabilize the intermediate radical, such as trithiocarbonates or dithiobenzoates, while LAMs, with less stable radicals, are better controlled using xanthates or dithiocarbamates, which promote radical propagation.[122] RAFT effectively controls the polymerization of most monomers, with some exceptions for those containing nucleophilic groups (*e.g.*, primary and secondary amines) that may react with the thiocarbonylthio group in the RAFT agent.[123]

Overall, RAFT polymerization offers a high control and tolerance over a wide range of monomers and reaction conditions, even though it requires a careful fine-tuning of reaction parameters such as the choice of CTA, monomer, and initiation method.[124]

1.3 Gel Permeation Chromatography

Another important aspect of polymer chemistry is the precise characterization of the polymeric structures. The bulk properties of synthetic and natural polymers are heavily influenced by their molecular characteristics, such as molecular weight and structure. These features have a direct impact on physical properties like strength and toughness.[125]

To accurately measure these molecular properties, Gel Permeation Chromatography (GPC), also known as Size Exclusion Chromatography (SEC) or Gel Filtration Chromatography (GFC), is the gold standard technique.[126–128] It is widely applied to characterize macromolecules such as synthetic and natural polymers, proteins, and nucleic acids such as RNA and DNA. For polymers, GPC is primarily used to determine molecular mass averages and distributions.[129]

GPC is a type of liquid chromatography which separates molecules based on their hydrodynamic size.[128] GPC requires the sample to be fully dissolved in a mobile phase, with individual molecules

dispersed and not interacting with each other. This liquid phase passes through column(s) packed with a gel matrix made up of highly porous spherical particles (stationary phase).[130] Common materials for these gels include cross-linked polymers such as polystyrene, acrylates, or silica.[131] An isocratic pump maintains a constant flow of eluent through the column, and the sample solution is introduced into this flow using an injection valve and loop. Ideally, there should be no interaction between the sample and the column packing material, meaning that separation is based solely on the diffusion of the analyte as the solution moves through the stationary phase.[132] If the analyte does not absorb onto the stationary phase, the separation process will be driven purely by entropy. The standard free energy change (ΔG^0) of a chromatographic process is typically described as reported in **Equation 1**:

$$\Delta G^{\circ} = \Delta H^{\circ} - T \times \Delta S^{\circ} \qquad \textbf{Equation 1}$$

where $\Delta H°$ is the change in standard enthalpy, $\Delta S°$ is the change in standard entropy, and T is the absolute temperature. However, ΔG^0 can also be written in terms of the partition function K, as reported in **Equation 2**:

$$\Delta G^{\circ} = R \times T \times ln\ K \qquad \textbf{Equation 2}$$

where R is the gas constant, T is the absolute temperature, and K is the partition function. Since GPC is free from enthalpic contributions,[133] **Equation 3** can be written by combining **Equation 1** and **2**:

$$-\Delta S^{\circ} = R \times ln\ K \qquad \textbf{Equation 3}$$

indicating that the separation process should not depend on the temperature. However, temperature can still have a minor influence on the outcome since it affects solvent viscosity and the diffusion rates of the sample.[134]

For a separation process driven purely by diffusion, it is essential to select a mobile and stationary phase combination that ensures no interaction between the two. In this scenario, analytes diffuse in and out of the pores of the stationary phase packing material as the mobile phase moves the sample through the column. Small molecules, being able to access more pores and penetrate deeper into the packing material, experience greater delay compared to larger molecules. Consequently, the separation occurs based on hydrodynamic size, with larger molecules eluting from the column first.[129] Knowing this, two extreme cases can be described: analytes bigger than the biggest pores of the stationary phase or smaller than the smallest pores. In the first case, analytes larger than the largest pores in the packing material will not experience any delay in their elution and thus will

not be separated. These molecules will elute together, having traveled only through the interstitial volumes of the column (void volume). Conversely, in the second case, molecules smaller than the smallest pores will diffuse into all the pores of the gel matrix, and they also will not be separated from each other and elute as the last fraction. In all the intermediate cases, analytes partially penetrate the packing material and can be separated. This defines the effective range for a GPC separation.[135]

To obtain the polymer compositional information, it is essential to couple the chromatographic separation to a set of detectors. These usually can be divided into two categories: concentration-sensitive detectors, which include UV-Vis absorption, differential refractometer (DRI) or refractive index (RI) detectors, infrared absorption, and density detectors, and molecular weight sensitive detectors, which include light scattering (LS) detectors, such as low angle light scattering (LALS) and multi-angle light scattering (MALS). Therefore, the resulting chromatogram is a curve of the weight distribution of the polymer as a function of retention volume.[135–137]

The GPC instrument set-up (OMNISEC, Malvern Panalytical) used for this Thesis project is the one illustrated in **Figure 1.4.a**. It consists of a column oven followed by four detectors connected in series, namely a differential refractometer, a diode-array-based UV-Vis spectrophotometer (both responding to sample concentration), a light scattering (responding to sample molecular weight), and a viscometer (responding to sample intrinsic viscosity). **Figure 1.4.b** shows how a tetra-detector chromatogram appears.

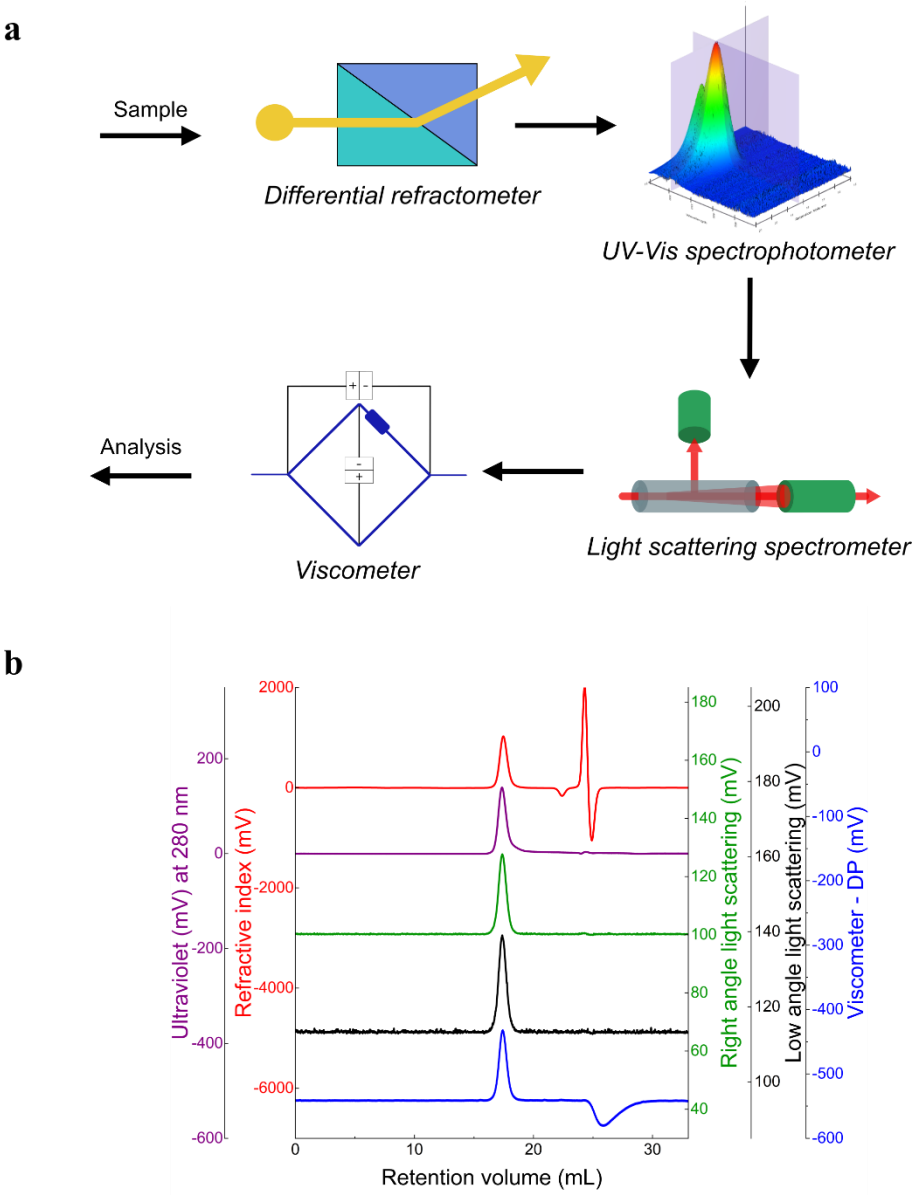

Figure 1.4. a) *Schematic representation of tetra-detector GPC set-up;* ***b)*** *Example of tetra-detector chromatograms.*

The RI of a solution changes linearly with the increment of sample concentration compared to the RI of the pure solvent, particularly at low sample concentrations. A schematic description of the basic components of an RI detector is as follows: a light source irradiates a flow cell, which consists of two compartments (**Figure 1.4.a**, in teal and blue), one holds the pure mobile phase (reference cell), and the other contains the eluent with the sample flowing through the detector (sample cell). If there is a difference in the refractive index between the two compartments, the light will be deflected.[135,138] This deflection, which is proportional to the analyte concentration in the flow cell, is then detected and corresponds to the refractive index increment dn/dC, which describes how the refractive index of the solution depends on concentration. The value of dn/dC

is influenced by the chemical composition of the sample and the eluent, and it is usually positive, although there are some exceptions (*e.g.*, silicone in toluene). Additionally, the refractive index of the eluent is affected by temperature and pressure, so maintaining a stable temperature within the detector is crucial.[139,140] Since most of the injected solutions contain solvent or salt molecules smaller than the gel matrix pores (*i.e.*, too small to be separated), a peak corresponding to these species will always appear on the RI detector chromatogram, commonly referred to as the solvent peak or permeation peak (**Figure 1.5**). This peak marks the end of the measurement (total permeation volume), and it is independent of the sample.[135]

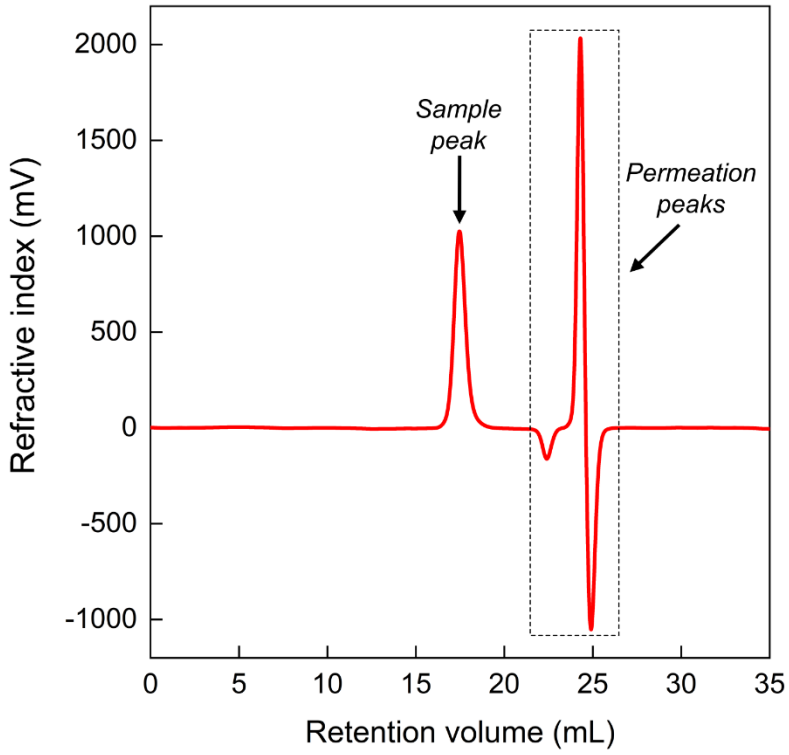

Figure 1.5. *Example of RI chromatogram of a polymer where is observable the sample peak and the permeation peaks assigned to the used eluent.*

Concerning the UV detector, if the analyte molecules absorb light within the UV light wavelength range, this absorption can be measured. According to the Beer-Lambert law, the analyte concentration can be calculated from the absorbance, if the attenuation coefficient of the analyte is known, as described in **Equation 4**.[141]

$$A = \varepsilon \times C \times l \qquad \textbf{Equation 4}$$

where A is the absorbance, ε is the molar absorption coefficient, C is the sample concentration, and l is the path length. The ε coefficient easily correlates to the calculated GPC value of dA/dC, the specific absorption coefficient, through **Equation 5**:

$$\frac{\varepsilon}{M_w} = \frac{d\ A}{d\ C} \qquad \textbf{Equation 5}$$

where M_w is the molecular weight of the analyzed species.

Therefore, the equations (**Equation 6** and **7**)[142] of the two concentrations detectors can be written as follows:

$$RI\ signal\ (mV) = K_{RI} \times \frac{d\ n}{d\ C} \times C \qquad \textbf{Equation 6}$$

$$UV\ signal\ (mV) = K_{UV} \times \frac{d\ A}{d\ C} \times C \qquad \textbf{Equation 7}$$

where K_{RI} and K_{UV} are the constants of the RI and UV detectors, respectively, determined during the instrument calibration, dn/dC is the sample refractive index increment, dA/dC is the sample specific absorption coefficient, and C is the concentration of the sample giving that output signal. The properties of the light scattered by molecules and particles vary depending on the sample nature, size, and molecular weight, as defined in the Rayleigh equation[143,144] (**Equation 8**):

$$\frac{K \times C}{R_\theta} = \left(\frac{1}{M_w} + 2 \times A_2 \times C\right) \times \frac{1}{P_\theta} \qquad \textbf{Equation 8}$$

where C is the sample concentration, θ is the measurement angle, R_θ is the Rayleigh ratio (*i.e.*, the ratio of scattered light intensity to incident light intensity) at the measurement angle θ, M_w is the weight average molecular weight, A_2 is the second virial coefficient. K and P_θ are more complex terms to define. K is a constant that depends on the system, solvent, and sample being measured (**Equation 9**):

$$K = \frac{4 \times \pi^2}{\lambda_0^4 \times N_A} \times \left(n_0 \times \frac{d\ n}{d\ C}\right)^2 \qquad \textbf{Equation 9}$$

where λ_0 is the laser wavelength in a vacuum, N_A is Avogadro's number, n_0 is the refractive index of the solvent, and dn/dC is the refractive index increment of the sample.[143,144] Since the dn/dC value is squared in **Equation 9**, it will have a substantial influence on the K value, meaning that it should be accurately determined. Instead, the $1/P_\theta$ value defines the angular dependence of the scattered light according to **Equation 10**:

$$\frac{1}{P_\theta} = 1 + \left(\frac{16 \times \pi^2 \times n_0^2 \times R_g^2}{3 \times \lambda_0^2}\right) \times \left(n_0 \times \frac{dn}{dC}\right)^2 \times sin^2\left(\frac{\theta}{2}\right)$$ **Equation 10**

where n_0 is the refractive index of the solvent, R_g is the radius of gyration of the sample, λ_0 is the laser wavelength in a vacuum, dn/dC is the refractive index increment of the sample, and θ is the measurement angle.[143,144] **Equation 10** shows that $1/P_\theta$ depends on various factors related to both the sample and the measurement. When the molecule is small relative to the laser wavelength, it behaves like a point scatterer, scattering light evenly in all directions. These are known as isotropic scatterers. However, as the molecule increases in size, its structure becomes significant, and different points within the molecule scatter photons interfering with each other – both constructively and destructively – rather than scattering independently. This results in anisotropic scattering, where the scattered light intensity varies based on the observation angle.[145] As a general rule, angular dependence becomes relevant when the molecule diameter exceeds 1/20th of the laser wavelength. Below this size, molecules scatter isotropically, while above this threshold, they scatter anisotropically. Most instruments use lasers with wavelengths between 633 and 670 nm, so the limit for isotropic scattering is between 15.8 and 16.8 nm in radius. This nominal threshold of around 15 nm radius marks the onset of measurable angular dependence and serves as the lower limit for accurately measuring molecular size, *i.e.*, R_g.[128,146]

In the case of anisotropic scatter, the measured light intensity would be lower than expected if the molecule was isotropic. Calculating molecular weight using this reduced intensity and the Rayleigh equation would result in an underestimation. To correct for this, the scattered light intensity should be measured at a 0° angle since, following **Equation 10**, $\sin^2(\theta/2)$ equals 0, making $1/P_\theta$ equal to 1. In this scenario, the scattered light intensity would accurately reflect the molecular weight, just as it does for smaller molecules when measured at 90°. Unfortunately, it is impractical to measure at 0° since the intensity of the illuminating laser at that angle is far greater than the scattered light, making it impossible to isolate only the scattered light.[147]

The OMNISEC instrument possesses two light scattering set-ups. A Right Angle Light Scattering (RALS) device is designed to measure the intensity of light scattered at a 90° angle from the incident beam. The molecular weight of the sample is calculated directly from the intensity measured and the sample concentration. RALS systems offer several advantages, such as an excellent signal-to-noise ratio and high sensitivity, as the light passes through the window at a 90° angle, minimizing noise caused by changes in the refractive index. On the other hand, a LALS detector measures the intensity of light scattered at a very small angle, as close to 0° as possible, in this case 7°. Recalling **Equation 10**, at 7°, $\sin^2(\theta/2)$ is just 0.0037, resulting in less than 1%

error in molecular weight calculation, even for very large molecules, allowing the calculated molecular weight to be very close to the actual value.

By combining **Equation 8** to **10**, it can be delivered **Equation 11**, governing the LS detectors[142]:

$$LS\ signal\ (mV) = K_{LS} \times M_w \times \left(\frac{dn}{dC}\right)^2 \times C \qquad \textbf{Equation 11}$$

where K_{LS} is the detector constant determined during the instrument calibration, M_w is the weight average molecular weight, dn/dC is the refractive index increment, and C is the sample concentration.

The primary aim of GPC analysis is to determine the molecular mass and mass distribution of the analyte. Polymers are inherently polydisperse, meaning they consist of molecules with varying chain lengths within a single sample. In contrast, proteins are usually monodispersed, where each molecule has the same amino acid sequence and mass, although they can form oligomers and aggregates in solution. As a result, molecular mass measurements in SEC/GPC are reported as average values. There are three different defined molecular weight moments (**Equation 12-14**):[148]

$$M_n = \frac{\sum n_i M_i}{\sum n_i} \qquad \textbf{Equation 12}$$

$$M_w = \frac{\sum n_i M_i^2}{\sum n_i M_i} \qquad \textbf{Equation 13}$$

$$M_z = \frac{\sum n_i M_i^3}{\sum n_i M_i^2} \qquad \textbf{Equation 14}$$

where M_n, M_w and M_z are the number-average, weight-average, and z-average molecular mass, respectively, M_i is the molecule mass, and n_i is the number of molecules being measured. The ratio M_w/M_n represents the width of the molecular mass distribution and corresponds to the dispersity Đ of the sample.

Finally, the last detector comprises a four-capillary differential viscometer and it is used to determine the sample intrinsic viscosity. Particularly, this is the solute contribution to the overall solution viscosity, and it is expressed as in **Equation 15**:[142,149,150]

$$IV = [\eta] = \left(\frac{\eta - \eta_0}{\eta_0}\right) \times \frac{1}{C} \qquad \textbf{Equation 15}$$

where η_0 is the viscosity of the solvent, η is the viscosity of the solution, and C is the sample concentration. The four-capillary bridge design of the viscometer is arranged in a balanced bridge configuration (**Figure 1.6.a**).

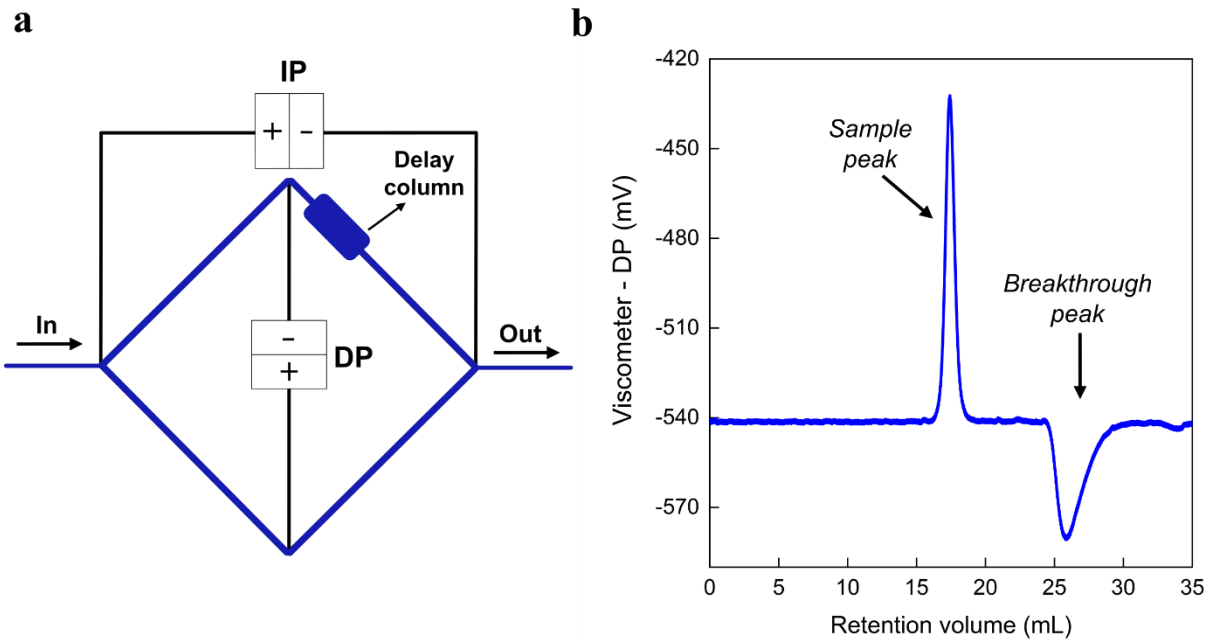

Figure 1.6. a) *Schematic representation of GPC viscometer, where IP is the inlet pressure and DP is the differential pressure between the capillaries;* ***b)*** *Example of viscometer chromatogram where is observable the sample peak and the breakthrough peak associated with the sample eluting from the delay column.*

Differential pressure transducers measure the pressure difference DP (differential pressure) across the midpoint of the bridge and the pressure difference IP (inlet pressure) from inlet to outlet. A delay volume is inserted in the circuit, to provide a reference flow during the sample elution. In a typical DP chromatogram (**Figure 1.6.b**), the first peak corresponds to the sample as it elutes into the viscometer capillaries, while solvent flows through the capillary with the delay column. The second, negative peak is the breakthrough in the delay volume since the sample is just in the delay column and the other capillaries contain solvent. The breakthrough peak is not required for the calculation and is simply an artifact of the measurement. The position of this artifact peak can be simply controlled by the size of the delay volume and the length of the analytical run so that it does not interfere with the analytical peak and is fully eluted before the next sample. **Equation 16** displays the correlation between the viscometer signal and its intrinsic viscosity.

$$V_{i\,ss\,d\,g}(mV) = K_{V_{i\,s}} \times I\,V \times C \qquad \textbf{Equation 16}$$

where $K_{Visc.}$ is the constant of the detector determined during the instrument calibration, IV is the intrinsic viscosity of the sample, and C is the sample concentration.

The intrinsic viscosity of a sample can yield information on its structure since correlates to its density. Specifically, Mark-Houwink parameters can deliver information on the branching of the structure.[151]

With a deep understanding of the equations governing the detectors, the only unknown parameters left are the specific constants for each detector, which are determined through the calibration. There are three possible calibration methods: conventional, universal, and multi-detector calibration.

Conventional calibration is the simplest GPC/SEC set-up consisting of a single-detector system, using either an RI or UV detector, which directly measures the sample concentration. This method requires running well-characterized standards to create a calibration curve, mapping molecular weight (specifically peak molecular weight, M_p) to retention volume. When an unknown sample is analyzed, the molecular weight of each data point is estimated based on this curve. However, the results are considered relative molecular weight values, since they depend on the standards used, which might not match the molecular structure of the sample. The main advantages are its cost-effectiveness with minimal components and straightforward calculations. However, the main drawback is that the results may not accurately reflect the true molecular weight if the sample structure or shape differs from the standards. This limitation may lead to misleading results.[135,152,153]

The universal calibration uses both a concentration detector, usually a differential refractometer and a viscometer detector to account for differences in molecular structure and shape, providing more accurate data. This method allows the calculation of molecular weight moments as well as intrinsic viscosity, hydrodynamic radius (R_h), and Mark-Houwink parameters. The viscometer detects changes based on the molecular structure in the solution, making it possible to correct for differences between the standards and the sample. This leads to more reliable results compared to conventional calibration. Although universal calibration is independent of the standards used, a calibration curve is still required, and its accuracy depends on several factors such as column type, mobile phase, flow rate, and temperature.[135,154,155]

Multi-detector calibration with light scattering, also known as triple detection, uses a light scattering detector combined with a concentration detector to determine the absolute molecular

weight of the sample, independent of a calibration curve. As explained before, the intensity of scattered light directly correlates to the molecular weight. Additional detectors like viscometers or UV-Vis are often exploited to provide a comprehensive analysis of molecular properties such as IV, R_h, R_g, and branching, along with molecular composition. Each detector in the system measures a different aspect of the sample, enabling precise calculations of various parameters without relying on a calibration curve. Light scattering detectors, in particular, offer the significant advantage of determining the molecular weight with high accuracy through a straightforward calibration process using just a single narrow standard.[152,155,156]

Overall, the GPC technique using a multi-detection calibration ensures the most reliable results, arising from the chemical and structural characteristics of each sample. This approach not only enhances the analysis of polymeric samples but also expands applicability to more complex species, including nanomaterials.

1.4 Protocells

Synthetic biology aims to design and fabricate artificial cellular systems, known as protocells, to understand the fundamental principles of life.[157] Protocells are self-assembled artificial systems of micrometric size, synthesized from non-living precursors and designed to perform one or more functions typical of biological cells, such as functional metabolism, intercellular communication through diffusive chemical signals, motility, cell growth, and division.[158,159]

Compared to biological cells, which are highly complex systems, protocells offer a simpler model to study fundamental aspects of cellular biology. Additionally, since they are often built from more robust artificial materials, protocells can be exposed to chemical and physical conditions that are incompatible with biological cells. This feature allows greater control over their properties and the ability to introduce new functionalities not found in natural cells.[160]

Artificial cells are highly designable and versatile, with control over their size, architecture, compartmentalization, and membrane composition during their fabrication.[161] Since they are not living systems, they do not necessarily require specific culture conditions or nutrients, nor do they respond to environmental or mechanical stress unless designed to do so. This makes protocells more stable and predictable in a variety of conditions, enabling more controlled and reproducible experiments.[160]

Protocells hold a vast potential for applications in fields such as biotechnology, medicine, and environmental science, with the ambitious long-term goal of advancing our understanding of the origin of life.[157] In biotechnology, they are used as bioreactors for applications such as biofuel

production, pharmaceuticals, tissue engineering, and wastewater treatment.[159,162,163] A particularly promising application is artificial photosynthesis within protocells, which enables light-induced carbon fixation and the production of oxygen and energy.[164–166] Protocells provide a stable, controlled compartment for housing the components needed for photosynthesis, such as catalysts, enzymes, and photosystems.[157] In medicine, protocells are used as drug delivery carriers, improving drug biocompatibility and enabling controlled, prolonged release of active ingredients.[167,168] They also play a crucial role in constructing biosensors, as they can be programmed to detect and measure specific target molecules.[169] Additionally, protocells are used to simulate and understand processes that may have led to the development of the first forms of life on Earth.[170,171]

To design and fabricate protocells, two different but complementary synthetic strategies can be adopted: the top-down and bottom-up approaches.[158,161] The top-down approach involves starting with a living organism (such as cells, bacteria, or viruses) and reducing its genetic material to the minimum required to maintain essential properties, or replacing its genome entirely with a synthetic one.[172,173] In contrast, the bottom-up approach utilizes the self-assembly of non-living components (such as simple molecules, polymers, and biomolecules) to create synthetic cellular structures that replicate the fundamental characteristics of biological cells.[173,174]

Protocells are classified into two main categories based on their composition, structure, and intended purpose: typical and non-typical.[161] Typical protocells are artificial structures designed with biomolecular components and lipid membranes, structurally similar to living cells, and aim to replicate the fundamental functions of biological cells.[161,175] In contrast, non-typical protocells are engineered materials that mimic at least one property of biological cells but may have different structures and compositions. These can include non-biological materials, such as polymers and nanoparticles, designed to create innovative structures with unique properties and applications.[161,176]

There are several types of protocells, each exhibiting distinct properties and characteristics. Specifically, protocells can be divided into three main categories: (*i*) vesicles, (*ii*) membrane-free compartments, and (*iii*) colloidosomes **Figure 1.7**.[177]

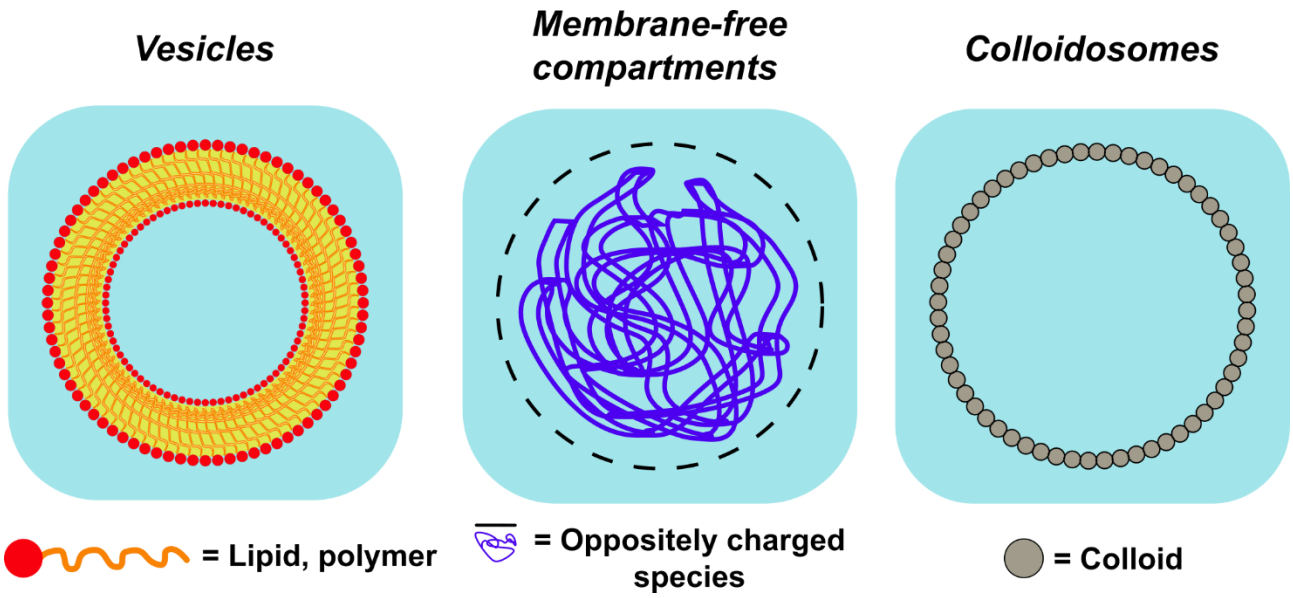

Figure 1.7. *Illustration of the three main categories of protocell models currently available: vesicles (*e.g.*, liposomes, polymersomes), membrane-free models (*e.g.*, microgels and coacervates, and colloidosomes.*

Vesicles consist of a bilayer membrane, similar to biological cells. This category includes liposomes and polymerosomes, which are characterized by a double-layered membrane.[178] Vesicles are self-assembled and typically exhibit low permeability and stability within a narrow range of chemical and physical conditions, making them valuable for applications like drug delivery.[179] Membrane-free compartments encompass coacervates and microgels. Coacervates are microdroplets composed of polyions held together by electrostatic forces and formed through liquid-liquid phase separation (LLPS).[180] Instead, microgels consist of polymer networks that can absorb and retain significant amounts of water or other solvents. Microgels possess a three-dimensional reticulated structure, contributing to their biocompatibility and ability to serve as model substrates for studying cellular processes.[181]

Colloidosomes are microcapsules composed of amphiphilic colloidal particles and are built using a bottom-up approach through the self-assembly of the colloids at the interface of a biphasic system (*e.g.*, an emulsion), followed by chemical crosslinking to create stable, semipermeable membranes.[182] Colloidosomes are typically fabricated through the Pickering emulsion technique, where colloidal particles stabilize the interface between two immiscible liquids, such as oil and water.[177] The type of emulsion – water-in-oil or oil-in-water – depends on the nature of the colloidal particles – hydrophilic or hydrophobic – and their interaction with the two phases.[177]

A monolayer of colloidal particles will form around the emulsion droplets, creating a semipermeable membrane. This membrane has an intrinsic porosity due to the imperfect packing

of the colloidal particles, influencing and allowing selective permeability.[177,183] This provides for the selective transport of molecules based on their size and charge, which is essential for applications of these protocells in drug delivery or enzyme-catalyzed reactions.[184,185]

To ensure stability and prevent the de-emulsification of colloidosomes, the colloidal particles are usually crosslinked. Common crosslinking methods include sintering and chemical crosslinking.[186–188] The latter is often preferred since it leads to the formation of a robust membrane without the need for high temperatures, which is an important aspect when working with temperature-sensitive biomolecules like enzymes. This methodology yields crosslinked structures using reactions such as disulfide formation, click chemistry, amide couplings, or other covalent bonds.[187,189,190] Controlling the crosslinking density also influences the final permeability of the colloidosome membrane.[177]

During the formation of the emulsion, cargo molecules such as drugs, enzymes, or other biologically relevant molecules can be encapsulated inside the colloidosome lumen. The permeability of the membrane allows these encapsulated materials to be released in a controlled manner in response to external stimuli (*e.g.*, pH, temperature).[191] After crosslinking, the colloidosomes are typically transferred into a continuous water phase by dialysis, to remove the oil phase and stabilize the colloidosomes in an aqueous environment for further applications.[177]

The colloidal particles forming the colloidosomes membrane can be based on either inorganic or organic materials, although inorganic colloidosomes are prevalently described in the literature.[182] Common materials to build inorganic colloidosomes are silica nanoparticles, gold and silver nanorods, magnetic iron oxide nanoparticles, and clay.[177]

Among these, silica nanoparticle-based colloidosomes are the most widely studied due to their ease of functionalization.[192] The hydrophobicity of silica can be easily adjusted by modifying surface silanol groups. These amphiphilic nanoparticles can be then used to form Pickering emulsions crosslinked with tetramethoxysilane (TMOS) or tetraethoxysilane (TEOS) to further stabilize the colloidosomes, enabling their transfer into a continuous phase.[193]

Gold and silver nanorod-based colloidosomes can be produced by creating Pickering emulsions with nanorods coated in amphiphilic polymers like poly(N-isopropylacrylamide) (PNIPAA) and poly(diallyldimethylammonium chloride) (PDDA), which can be stabilized through covalent crosslinking, van der Waals forces, and ionic interactions.[194]

Magnetic iron oxide (magnetite) nanoparticles are rendered hydrophobic with fatty acids and can also create water-in-oil magnetic Pickering emulsions.[195]

Finally, clay-based colloidosomes have been generated using Fe(III)-rich montmorillonite. These clay microparticles are made amphiphilic by coupling methyltriethoxysilane to their surface

hydroxyl groups, to form colloidosomes in water-in-oil Pickering emulsions, which can then be crosslinked with TMOS *via* silylation.[196]

On the other hand, colloidosomes made from organic materials are also known as proteinosomes. These are formed by conjugating proteins, such as bovine serum albumin (BSA) with amphiphilic polymers like PNIPAA, delivering protein/polymer nanoconjugates.[197] By incorporating PNIPAA, which exhibits thermoresponsive properties, the membrane permeability of proteinosomes can be controlled by temperature changes. Moreover, it was proved that these protein-based colloidosomes can encapsulate enzymes or other biomacromolecules, allowing them to function as bioreactors or catalysts for complex enzymatic reactions.[198] Also these organic colloidosomes can be chemically crosslinked to ensure their stability and develop more complex bio-mimetic systems.[199]

Considering all these aspects, colloidosomes offer significant advantages due to their robust and highly tunable membrane structures, making them an emerging and adaptable model in the field of synthetic biology and protocell research.

1.5 References

1. Whitesides, G. M. & Grzybowski, B. Self-Assembly at All Scales. *Science* **295**, 2418–2421 (2002).
2. Amadi, E. V., Venkataraman, A. & Papadopoulos, C. Nanoscale self-assembly: concepts, applications and challenges. *Nanotechnology* **33**, 132001 (2022).
3. Koh, S. Strategies for Controlled Placement of Nanoscale Building Blocks. *Nanoscale Res Lett* **2**, 519 (2007).
4. Chai, Z., Childress, A. & Busnaina, A. A. Directed Assembly of Nanomaterials for Making Nanoscale Devices and Structures: Mechanisms and Applications. *ACS Nano* **16**, 17641–17686 (2022).
5. Krüger, A. *Carbon Materials and Nanotechnology*. (John Wiley & Sons, 2010).
6. Albanese, A., Tang, P. S. & Chan, W. C. W. The Effect of Nanoparticle Size, Shape, and Surface Chemistry on Biological Systems. *Annual Review of Biomedical Engineering* **14**, 1–16 (2012).
7. Zhu, S., Tang, S., Zhang, J. & Yang, B. Control the size and surface chemistry of graphene for the rising fluorescent materials. *Chem. Commun.* **48**, 4527–4539 (2012).
8. Ekiz-Kanik, F., Sevenler, D. D., Ünlü, N. L., Chiari, M. & Ünlü, M. S. Surface chemistry and morphology in single particle optical imaging. *Nanophotonics* **6**, 713–730 (2017).
9. Litti, L., Reguera, J., Abajo, F. J. G. de, Meneghetti, M. & Liz-Marzán, L. M. Manipulating chemistry through nanoparticle morphology. *Nanoscale Horiz.* **5**, 102–108 (2019).
10. Pelaz, B. *et al.* Diverse Applications of Nanomedicine. *ACS Nano* **11**, 2313–2381 (2017).
11. Singh, T. *et al.* Application of Nanotechnology in Food Science: Perception and Overview. *Front. Microbiol.* **8**, (2017).
12. Khan, Y. *et al.* Classification, Synthetic, and Characterization Approaches to Nanoparticles, and Their Applications in Various Fields of Nanotechnology: A Review. *Catalysts* **12**, 1386 (2022).
13. Chauhan, D. S., Quraishi, M. A. & Verma, C. Carbon nanodots: recent advances in synthesis and applications. *Carbon Lett.* **32**, 1603–1629 (2022).
14. Xu, X. *et al.* Electrophoretic Analysis and Purification of Fluorescent Single-Walled Carbon Nanotube Fragments. *J. Am. Chem. Soc.* **126**, 12736–12737 (2004).
15. Sun, Y.-P. *et al.* Quantum-Sized Carbon Dots for Bright and Colorful Photoluminescence. *J. Am. Chem. Soc.* **128**, 7756–7757 (2006).
16. Zhou, J. *et al.* An Electrochemical Avenue to Blue Luminescent Nanocrystals from Multiwalled Carbon Nanotubes (MWCNTs). *J. Am. Chem. Soc.* **129**, 744–745 (2007).

17. Bourlinos, A. B. *et al.* Surface Functionalized Carbogenic Quantum Dots. *Small* **4**, 455–458 (2008).
18. Arcudi, F., Đorđević, L. & Prato, M. Design, Synthesis, and Functionalization Strategies of Tailored Carbon Nanodots. *Acc. Chem. Res.* **52**, 2070–2079 (2019).
19. Rosso, C., Filippini, G. & Prato, M. Carbon Dots as Nano-Organocatalysts for Synthetic Applications. *ACS Catal.* **10**, 8090–8105 (2020).
20. Đorđević, L., Arcudi, F., Cacioppo, M. & Prato, M. A multifunctional chemical toolbox to engineer carbon dots for biomedical and energy applications. *Nat. Nanotechnol.* **17**, 112–130 (2022).
21. Wang, R., Lu, K.-Q., Tang, Z.-R. & Xu, Y.-J. Recent progress in carbon quantum dots: synthesis, properties, and applications in photocatalysis. *J. Mater. Chem. A* **5**, 3717–3734 (2017).
22. Yao, Y. *et al.* Carbon dots based photocatalysis for environmental applications. *Journal of Environmental Chemical Engineering* **10**, 107336 (2022).
23. Sendão, R. M. S., Esteves da Silva, J. C. G. & Pinto da Silva, L. Applications of Fluorescent Carbon Dots as Photocatalysts: A Review. *Catalysts* **13**, 179 (2023).
24. Corti, V. *et al.* Amine-Rich Carbon Dots as Novel Nano-Aminocatalytic Platforms in Organic Synthesis. *European Journal of Organic Chemistry* **2022**, e202200879 (2022).
25. Cheng, R. *et al.* Structure and Interface Modification of Carbon Dots for Electrochemical Energy Application. *Small* **17**, 2102091 (2021).
26. Yan, F. *et al.* Surface modification and chemical functionalization of carbon dots: a review. *Microchim Acta* **185**, 424 (2018).
27. Choi, J., Kim, N., Oh, J.-W. & Kim, F. S. Bandgap engineering of nanosized carbon dots through electron-accepting functionalization. *Journal of Industrial and Engineering Chemistry* **65**, 104–111 (2018).
28. Rigodanza, F. *et al.* Snapshots into carbon dots formation through a combined spectroscopic approach. *Nat Commun* **12**, 2640 (2021).
29. Bhuyan, R., Kommula, B., Bishwal, L., Mandal, S. & Bhattacharyya, S. From Small Molecules to Zero-Dimensional Carbon Nanodots: Chasing the Stepwise Transformations During Carbonization. *J. Phys. Chem. C* **126**, 16377–16386 (2022).
30. Xue, S. *et al.* The Formation Process and Mechanism of Carbon Dots Prepared from Aromatic Compounds as Precursors: A Review. *Small* **19**, 2206180 (2023).
31. Đorđević, L., Arcudi, F. & Prato, M. Preparation, functionalization and characterization of engineered carbon nanodots. *Nat Protoc* **14**, 2931–2953 (2019).

32. Bartolomei, B. & Prato, M. The Importance of the Purification Step and the Characterization of the Products in the Synthesis of Carbon Nanodots. *Small* **19**, 2206714 (2023).
33. Hu, Y., Seivert, O., Tang, Y., Karahan, H. E. & Bianco, A. Carbon Dot Synthesis and Purification: Trends, Challenges and Recommendations. *Angew Chem Int Ed* e202412341 (2024) doi:10.1002/anie.202412341.
34. Sendão, R. M. S. *et al.* Insight into the hybrid luminescence showed by carbon dots and molecular fluorophores in solution. *Phys. Chem. Chem. Phys.* **21**, 20919–20926 (2019).
35. Soni, N. *et al.* Absorption and emission of light in red emissive carbon nanodots. *Chem. Sci.* **12**, 3615–3626 (2021).
36. Ru, Y. *et al.* Rational Design of Multicolor-Emitting Chiral Carbonized Polymer Dots for Full-Color and White Circularly Polarized Luminescence. *Angewandte Chemie International Edition* **60**, 14091–14099 (2021).
37. La Ferla, B. & Vercelli, B. Red-Emitting Carbon Quantum Dots for Biomedical Applications: Synthesis and Purification Issues of the Hydrothermal Approach. *Nanomaterials* **13**, 1635 (2023).
38. Chen, C.-Y., Tsai, Y.-H. & Chang, C.-W. Evaluation of the dialysis time required for carbon dots by HPLC and the properties of carbon dots after HPLC fractionation. *New J. Chem.* **43**, 6153–6159 (2019).
39. Otten, M., Hildebrandt, M., Kühnemuth, R. & Karg, M. Pyrolysis and Solvothermal Synthesis for Carbon Dots: Role of Purification and Molecular Fluorophores. *Langmuir* **38**, 6148–6157 (2022).
40. Song, Y. *et al.* Investigation from chemical structure to photoluminescent mechanism: a type of carbon dots from the pyrolysis of citric acid and an amine. *J. Mater. Chem. C* **3**, 5976–5984 (2015).
41. Kokorina, A. A. *et al.* Gel electrophoresis separation and origins of light emission in fluorophores prepared from citric acid and ethylenediamine. *Sci Rep* **9**, 14665 (2019).
42. Kitayama, T. & Hatada, K. *NMR Spectroscopy of Polymers*. (Springer Science & Business Media, 2013).
43. Foster, M. P., McElroy, C. A. & Amero, C. D. Solution NMR of Large Molecules and Assemblies. *Biochemistry* **46**, 331–340 (2007).
44. Groves, P. Diffusion ordered spectroscopy (DOSY) as applied to polymers. *Polym. Chem.* **8**, 6700–6708 (2017).
45. Cadranel, A., Margraf, J. T., Strauss, V., Clark, T. & Guldi, D. M. Carbon Nanodots for Charge-Transfer Processes. *Acc. Chem. Res.* **52**, 955–963 (2019).

46. Zhang, Z. *et al.* Tuning photoluminescence and surface properties of carbon nanodots for chemical sensing. *Nanoscale* **8**, 500–507 (2015).
47. Sakdaronnarong, C., Sangjan, A., Boonsith, S., Kim, D. C. & Shin, H. S. Recent Developments in Synthesis and Photocatalytic Applications of Carbon Dots. *Catalysts* **10**, 320 (2020).
48. Sbacchi, M. *et al.* Shining Light on Carbon Dots: New Opportunities in Photocatalysis. *ChemCatChem* **15**, e202300667 (2023).
49. Filippini, G. *et al.* Mapping the Surface Groups of Amine-Rich Carbon Dots Enables Covalent Catalysis in Aqueous Media. *Chem* **6**, 3022–3037 (2020).
50. Gentile, G. *et al.* Tailoring the Chemical Structure of Nitrogen-Doped Carbon Dots for Nano-Aminocatalysis in Aqueous Media. *ChemSusChem* **16**, e202202399 (2023).
51. Ragazzon, G. *et al.* Optical processes in carbon nanocolloids. *Chem* **7**, 606–628 (2021).
52. Hu, C., Li, M., Qiu, J. & Sun, Y.-P. Design and fabrication of carbon dots for energy conversion and storage. *Chem. Soc. Rev.* **48**, 2315–2337 (2019).
53. Yu, Y. *et al.* Carbon Dots Based Photoinduced Reactions: Advances and Perspective. *Advanced Science* **10**, 2207621 (2023).
54. Saini, D. *et al.* Visible-Light-Promoted Photocatalytic Applications of Carbon Dots: A Review. *ACS Appl. Nano Mater.* **5**, 3087–3109 (2022).
55. Cardo, L. *et al.* Luminescent Carbon Nanodots Doped with Gadolinium (III): Purification Criteria, Chemical and Biological Characterization of a New Dual Fluorescence/MR Imaging Agent. *Small* **19**, 2206442 (2023).
56. Yao, X., Lewis, R. E. & Haynes, C. L. Synthesis Processes, Photoluminescence Mechanism, and the Toxicity of Amorphous or Polymeric Carbon Dots. *Acc. Chem. Res.* **55**, 3312–3321 (2022).
57. Cui, L., Ren, X., Sun, M., Liu, H. & Xia, L. Carbon Dots: Synthesis, Properties and Applications. *Nanomaterials* **11**, 3419 (2021).
58. Zhang, Q., Wang, R., Feng, B., Zhong, X. & Ostrikov, K. (Ken). Photoluminescence mechanism of carbon dots: triggering high-color-purity red fluorescence emission through edge amino protonation. *Nat Commun* **12**, 6856 (2021).
59. Zhu, S. *et al.* The photoluminescence mechanism in carbon dots (graphene quantum dots, carbon nanodots, and polymer dots): current state and future perspective. *Nano Res.* **8**, 355–381 (2015).
60. Elgrishi, N. *et al.* A Practical Beginner's Guide to Cyclic Voltammetry. *J. Chem. Educ.* **95**, 197–206 (2018).

61. Espinoza, E. M. *et al.* Practical Aspects of Cyclic Voltammetry: How to Estimate Reduction Potentials When Irreversibility Prevails. *J. Electrochem. Soc.* **166**, H3175 (2019).
62. Mandigma, M. J. P., Kaur, J. & Barham, J. P. Organophotocatalytic Mechanisms: Simplicity or Naïvety? Diverting Reactive Pathways by Modifications of Catalyst Structure, Redox States and Substrate Preassemblies. *ChemCatChem* **15**, e202201542 (2023).
63. Wang, Y. *et al.* Multicenter-Emitting Carbon Dots: Color Tunable Fluorescence and Dynamics Monitoring Oxidative Stress In Vivo. *Chem. Mater.* **32**, 8146–8157 (2020).
64. Arcudi, F. *et al.* Lighting up the Electrochemiluminescence of Carbon Dots through Pre- and Post-Synthetic Design. *Advanced Science* **8**, 2100125 (2021).
65. Chen, X. *et al.* Incorporating Graphitic Carbon Nitride (g-C3N4) Quantum Dots into Bulk-Heterojunction Polymer Solar Cells Leads to Efficiency Enhancement. *Advanced Functional Materials* **26**, 1719–1728 (2016).
66. Guo, X. *et al.* p-Type Carbon Dots for Effective Surface Optimization for Near-Record-Efficiency CsPbI2Br Solar Cells. *Small* **17**, 2102272 (2021).
67. Li, X. *et al.* Carbon Dots in Perovskite Solar Cells: Properties, Applications, and Perspectives. *Energy Fuels* **37**, 876–901 (2023).
68. Ji, C. *et al.* Light of carbon: Recent advancements of carbon dots for LEDs. *Nano Energy* **114**, 108623 (2023).
69. Shi, Y. *et al.* Carbon Dots for Electroluminescent Light-Emitting Diodes: Recent Progress and Future Prospects. *Advanced Materials* **35**, 2210699 (2023).
70. Luo, H., Guo, Q., Szilágyi, P. Á., Jorge, A. B. & Titirici, M.-M. Carbon Dots in Solar-to-Hydrogen Conversion. *Trends in Chemistry* **2**, 623–637 (2020).
71. Zhou, Y. *et al.* Colloidal carbon dots based highly stable luminescent solar concentrators. *Nano Energy* **44**, 378–387 (2018).
72. Achilleos, D. S. *et al.* Solar Reforming of Biomass with Homogeneous Carbon Dots. *Angewandte Chemie International Edition* **59**, 18184–18188 (2020).
73. Li, B. *et al.* Recent advances and prospects of carbon dots in phototherapy. *Chemical Engineering Journal* **408**, 127245 (2021).
74. Zhao, C. *et al.* Programmed Stimuli-Responsive Carbon Dot-Nanogel Hybrids for Imaging-Guided Enhanced Tumor Phototherapy. *ACS Appl. Mater. Interfaces* **14**, 10142–10153 (2022).
75. Du, J., Xu, N., Fan, J., Sun, W. & Peng, X. Carbon Dots for In Vivo Bioimaging and Theranostics. *Small* **15**, 1805087 (2019).
76. Wang, B. *et al.* Carbon Dots in Bioimaging, Biosensing and Therapeutics: A Comprehensive Review. *Small Science* **2**, 2200012 (2022).

77. Yang, T. *et al.* β-Cyclodextrin-Decorated Carbon Dots Serve as Nanocarriers for Targeted Drug Delivery and Controlled Release. *ChemNanoMat* **5**, 479–487 (2019).
78. Wang, Z.-X., Wang, Z. & Wu, F.-G. Carbon Dots as Drug Delivery Vehicles for Antimicrobial Applications: A Minireview. *ChemMedChem* **17**, e202200003 (2022).
79. Akbar, K., Moretti, E. & Vomiero, A. Carbon Dots for Photocatalytic Degradation of Aqueous Pollutants: Recent Advancements. *Advanced Optical Materials* **9**, 2100532 (2021).
80. Yu, Y. *et al.* Carbon Dots Based Photoinduced Reactions: Advances and Perspective. *Advanced Science* **10**, 2207621 (2023).
81. Lopez-Cantu, D. O. *et al.* Enzyme-mimicking capacities of carbon-dots nanozymes: Properties, catalytic mechanism, and applications – A review. *International Journal of Biological Macromolecules* **194**, 676–687 (2022).
82. Bettini, S. *et al.* Carbon nanodot-based heterostructures for improving the charge separation and the photocurrent generation. *Nanoscale* **11**, 7414–7423 (2019).
83. Mattinzoli, D. *et al.* Carbon dots conjugated to SN38 for improved colorectal anticancer therapy. *Materials Today Bio* **16**, 100286 (2022).
84. Yu, Z., Li, F. & Xiang, Q. Carbon dots-based nanocomposites for heterogeneous photocatalysis. *Journal of Materials Science & Technology* **175**, 244–257 (2024).
85. Falara, P. P., Zourou, A. & Kordatos, K. V. Recent advances in Carbon Dots/2-D hybrid materials. *Carbon* **195**, 219–245 (2022).
86. Wu, J. *et al.* Carbon dot composites for bioapplications: a review. *J. Mater. Chem. B* **10**, 843–869 (2022).
87. Yu, W., Sisi, L., Haiyan, Y. & Jie, L. Progress in the functional modification of graphene/graphene oxide: a review. *RSC Adv.* **10**, 15328–15345 (2020).
88. Zhang, X. *et al.* Design and preparation of a ternary composite of graphene oxide/carbon dots/polypyrrole for supercapacitor application: Importance and unique role of carbon dots. *Carbon* **115**, 134–146 (2017).
89. Li, L., Liu, D., Shi, A. & You, T. Simultaneous stripping determination of cadmium and lead ions based on the N-doped carbon quantum dots-graphene oxide hybrid. *Sensors and Actuators B: Chemical* **255**, 1762–1770 (2018).
90. Hu, J. *et al.* Enhanced NO_2 sensing performance of reduced graphene oxide by in situ anchoring carbon dots. *J. Mater. Chem. C* **5**, 6862–6871 (2017).
91. Ai, L. *et al.* Efficient Combination of $_g$-C_3N_4 and CDs for Enhanced Photocatalytic Performance: A Review of Synthesis, Strategies, and Applications. *Small* **17**, 2007523 (2021).

92. Tai, J. Y. *et al.* Facile green synthesis of fingernails derived carbon quantum dots for Cu^{2+} sensing and photodegradation of 2,4-dichlorophenol. *Journal of Environmental Chemical Engineering* **9**, 104622 (2021).
93. Seng, R. X., Tan, L.-L., Lee, W. P. C., Ong, W.-J. & Chai, S.-P. Nitrogen-doped carbon quantum dots-decorated 2D graphitic carbon nitride as a promising photocatalyst for environmental remediation: A study on the importance of hybridization approach. *Journal of Environmental Management* **255**, 109936 (2020).
94. Ong, W.-J. *et al.* Unravelling charge carrier dynamics in protonated g-C3N4 interfaced with carbon nanodots as co-catalysts toward enhanced photocatalytic CO2 reduction: A combined experimental and first-principles DFT study. *Nano Res.* **10**, 1673–1696 (2017).
95. Li, Q. *et al.* Enhanced CH_4 selectivity in CO_2 photocatalytic reduction over carbon quantum dots decorated and oxygen doping g-C3N4. *Nano Res.* **12**, 2749–2759 (2019).
96. Ren, Z. *et al.* Carbon quantum dots decorated MoSe2 photocatalyst for Cr(VI) reduction in the UV–vis-NIR photon energy range. *Journal of Colloid and Interface Science* **488**, 190–195 (2017).
97. Haque, F., Daeneke, T., Kalantar-zadeh, K. & Ou, J. Z. Two-Dimensional Transition Metal Oxide and Chalcogenide-Based Photocatalysts. *Nano-Micro Lett.* **10**, 23 (2017).
98. Li, N. *et al.* Facile Synthesis of Carbon Dots@2D MoS_2 Heterostructure with Enhanced Photocatalytic Properties. *Inorg. Chem.* **58**, 5746–5752 (2019).
99. Nguyen, D. A. *et al.* Highly Enhanced Photoresponsivity of a Monolayer WSe2 Photodetector with Nitrogen-Doped Graphene Quantum Dots. *ACS Appl. Mater. Interfaces* **10**, 10322–10329 (2018).
100. Kannan, K., Radhika, D., Sadasivuni, K. K., Reddy, K. R. & Raghu, A. V. Nanostructured metal oxides and its hybrids for photocatalytic and biomedical applications. *Advances in Colloid and Interface Science* **281**, 102178 (2020).
101. Zhu, P., Cheng, Z., Du, L., Chen, Q. & Tan, K. Synthesis of the Cu-Doped Dual-Emission Fluorescent Carbon Dots and Its Analytical Application. *Langmuir* **34**, 9982–9989 (2018).
102. Liu, W. *et al.* Triggered peroxidase-like activity of Au decorated carbon dots for colorimetric monitoring of Hg2+ enrichment in Chlorella vulgaris. *Analyst* **145**, 5500–5507 (2020).
103. Das, B., Girigoswami, A., Pal, P. & Dhara, S. Manganese oxide-carbon quantum dots nano-composites for fluorescence/magnetic resonance (T1) dual mode bioimaging, long term cell tracking, and ROS scavenging. *Materials Science and Engineering: C* **102**, 427–436 (2019).
104. Ganguly, S., Das, P., Banerjee, S. & Das, N. C. Advancement in science and technology of carbon dot-polymer hybrid composites: a review. *Funct. Compos. Struct.* **1**, 022001 (2019).

105. Kar, D. K., V, P., Si, S., Panigrahi, H. & Mishra, S. Carbon Dots and Their Polymeric Nanocomposites: Insight into Their Synthesis, Photoluminescence Mechanisms, and Recent Trends in Sensing Applications. *ACS Omega* **9**, 11050–11080 (2024).
106. Zulfajri, M. *et al.* Carbon Dot/Polymer Composites with Various Precursors and Their Sensing Applications: A Review. *Coatings* **11**, 1100 (2021).
107. Wu, S. *et al.* Facile fabrication of a CD/PVA composite polymer to access light-responsive shape-memory effects. *J. Mater. Chem. C* **8**, 8935–8941 (2020).
108. Forte, G., Consiglio, G., Satriano, C., Maugeri, L. & Petralia, S. A nanosized photothermal responsive core-shell carbonized polymer dots based on poly(N-isopropylacrylamide) for light-triggered drug release. *Colloids and Surfaces B: Biointerfaces* **217**, 112628 (2022).
109. Kariminia, S., Shamsipur, M. & Barati, A. Fluorescent folic acid-chitosan/carbon dot for pH-responsive drug delivery and bioimaging. *International Journal of Biological Macromolecules* **254**, 127728 (2024).
110. Feng, Z. *et al.* Carbon dot/polymer nanocomposites: From green synthesis to energy, environmental and biomedical applications. *Sustainable Materials and Technologies* **29**, e00304 (2021).
111. Adam, G. O., Sharker, S. M. & Ryu, J. H. Emerging Biomedical Applications of Carbon Dot and Polymer Composite Materials. *Applied Sciences* **12**, 10565 (2022).
112. Mandal, B. M. *Fundamentals Of Polymerization*. (World Scientific, 2012).
113. Aplan, M. P. & Gomez, E. D. Recent Developments in Chain-Growth Polymerizations of Conjugated Polymers. *Ind. Eng. Chem. Res.* **56**, 7888–7901 (2017).
114. Perrier, S. 50th Anniversary Perspective: RAFT Polymerization—A User Guide. *Macromolecules* **50**, 7433–7447 (2017).
115. Jenkins, A. D., Jones, R. G. & Moad, G. Terminology for reversible-deactivation radical polymerization previously called ‘controlled’ radical or ‘living’ radical polymerization (IUPAC Recommendations 2010). *Pure and Applied Chemistry* **82**, 483–491 (2009).
116. Gody, G., Maschmeyer, T., Zetterlund, P. B. & Perrier, S. Exploitation of the Degenerative Transfer Mechanism in RAFT Polymerization for Synthesis of Polymer of High Livingness at Full Monomer Conversion. *Macromolecules* **47**, 639–649 (2014).
117. Martin, L., Gody, G. & Perrier, S. Preparation of complex multiblock copolymers via aqueous RAFT polymerization at room temperature. *Polym. Chem.* **6**, 4875–4886 (2015).
118. Chen, M., Zhong, M. & Johnson, J. A. Light-Controlled Radical Polymerization: Mechanisms, Methods, and Applications. *Chem. Rev.* **116**, 10167–10211 (2016).
119. Barner-Kowollik, C. *Handbook of RAFT Polymerization*. (John Wiley & Sons, 2008).

120. Moad, G., Rizzardo, E. & Thang, S. H. Fundamentals of RAFT Polymerization. in *Fundamentals of Controlled/Living Radical Polymerization* (eds. Tsarevsky, N. V. & Sumerlin, B. S.) 205–249 (The Royal Society of Chemistry, 2013).

121. Moad, G. RAFT polymerization to form stimuli-responsive polymers. *Polym. Chem.* **8**, 177–219 (2016).

122. Rizzardo, E. *et al.* RAFT Polymerization: Adding to the Picture. *Macromolecular Symposia* **248**, 104–116 (2007).

123. Yildirim, T. *et al.* RAFT made methacrylate copolymers for reversible pH-responsive nanoparticles. *Journal of Polymer Science Part A: Polymer Chemistry* **53**, 2711–2721 (2015).

124. Hill, M. R., Carmean, R. N. & Sumerlin, B. S. Expanding the Scope of RAFT Polymerization: Recent Advances and New Horizons. *Macromolecules* **48**, 5459–5469 (2015).

125. Fetters, L. J., Lohse, D. J., Richter, D., Witten, T. A. & Zirkel, A. Connection between Polymer Molecular Weight, Density, Chain Dimensions, and Melt Viscoelastic Properties. *Macromolecules* **27**, 4639–4647 (1994).

126. Johnson, J. F. & Porter, R. S. Gel permeation chromatography. *Progress in Polymer Science* **2**, 201–256 (1970).

127. Trathnigg, B. Size-Exclusion Chromatography of Polymers. in *Encyclopedia of Analytical Chemistry* (ed. Meyers, R. A.) (Wiley, 2000).

128. Striegel, A., Yau, W. W., Kirkland, J. J. & Bly, D. D. *Modern Size-Exclusion Liquid Chromatography: Practice of Gel Permeation and Gel Filtration Chromatography*. (John Wiley & Sons, 2009).

129. Maley, L. E. Application of gel permeation chromatography to high and low molecular weight polymers. *Journal of Polymer Science Part C: Polymer Symposia* **8**, 253–268 (1965).

130. Viovy, J. L. & Lessec, J. Separation of macromolecules in gels: Permeation chromatography and electrophoresis. in *Polymer Analysis and Characterization* 1–41 (Springer, Berlin, Heidelberg, 1994).

131. Brewer, A. K. GPC Column Materials. in *Encyclopedia of Polymeric Nanomaterials* (eds. Kobayashi, S. & Müllen, K.) 1–13 (Springer, Berlin, Heidelberg, 2021).

132. Ardö, Y. & Kristiansen, K. R. ANALYSIS | Chromatographic Methods. in *Encyclopedia of Dairy Sciences* (ed. Roginski, H.) 55–62 (Elsevier, Oxford, 2002).

133. Held, D. & Kilz, P. Size-exclusion chromatography as a useful tool for the assessment of polymer quality and determination of macromolecular properties. *Chemistry Teacher International* **3**, 77–103 (2021).

134. Kowalczyk, J. S. & Herbut, G. Influence of temperature on separation processes in adsorption liquid chromatographic systems. *Journal of Chromatography A* **196**, 11–20 (1980).

135. Wu, C.-S. *Handbook Of Size Exclusion Chromatography And Related Techniques: Revised And Expanded*. (CRC Press, 2003).

136. Laguna, M. T. R., Medrano, R., Plana, M. P. & Tarazona, M. P. Polymer characterization by size-exclusion chromatography with multiple detection. *Journal of Chromatography A* **919**, 13–19 (2001).

137. Ortín, A., López, E., del Hierro, P., Sancho-Tello, J. & Yau, W. W. Simplified Robust Triple Detection Methods for High Temperature GPC Analysis of Polyolefins. *Macromolecular Symposia* **377**, 1700044 (2018).

138. Brun, Y., Gorenstein, M. V. & Hay, N. New Approach to Model Fitting in Multi-Detector Gpc. *Journal of Liquid Chromatography & Related Technologies* **23**, 2615–2639 (2000).

139. Coto, B., Escola, J. M., Suárez, I. & Caballero, M. J. Determination of d*n*/d*c* values for ethylene–propylene copolymers. *Polymer Testing* **26**, 568–575 (2007).

140. Ono, Y., Ishida, T., Soeta, H., Saito, T. & Isogai, A. Reliable dn/dc Values of Cellulose, Chitin, and Cellulose Triacetate Dissolved in LiCl/N,N-Dimethylacetamide for Molecular Mass Analysis. *Biomacromolecules* **17**, 192–199 (2016).

141. Mäntele, W. & Deniz, E. UV–VIS absorption spectroscopy: Lambert-Beer reloaded. *Spectrochimica Acta Part A: Molecular and Biomolecular Spectroscopy* **173**, 965–968 (2017).

142. Mansuroğlu, B. & Mustafaeva, Z. Characterization of water-soluble conjugates of polyacrylic acid and antigenic peptide of FMDV by size exclusion chromatography with quadruple detection. *Materials Science and Engineering: C* **32**, 112–118 (2012).

143. Hjertberg, T., Kulin, L.-I. & Sörvik, E. Laser light scattering as GPC detector. *Polymer Testing* **3**, 267–289 (1983).

144. Podzimek, S. The use of GPC coupled with a multiangle laser light scattering photometer for the characterization of polymers. On the determination of molecular weight, size and branching. *J of Applied Polymer Sci* **54**, 91–103 (1994).

145. Burchard, W. Static and dynamic light scattering from branched polymers and biopolymers. in *Light Scattering from Polymers* 1–124 (Springer, Berlin, Heidelberg, 1983).

146. Kratochvíl, P. *Classical Light Scattering from Polymer Solutions*. (Elsevier, 1987).

147. Malvern Panalytical. Static Light Scattering technologies for GPC - SEC explained. Available online: https://www.malvernpanalytical.com/en/learn/knowledge-center/whitepapers/wp130627slstechnologiesgpcsecexplained.

148. Koltzenburg, S., Maskos, M. & Nuyken, O. *Polymer Chemistry*. (Springer Nature, 2023).

149. Held, D. & Kilz, P. GPC/SEC as a Key Tool for Assessment of Polymer Quality and Determination of Macromolecular Properties. in *Monitoring Polymerization Reactions* 171–199 (John Wiley & Sons, Ltd, 2013).
150. Miercke, L. J. W., Robbins, R. A. & Stroud, R. M. Tetra Detector Analysis of Membrane Proteins. *Current Protocols in Protein Science* **77**, 29.10.1-29.10.30 (2014).
151. Masuelli, M. A. Mark-Houwink Parameters for Aqueous-Soluble Polymers and Biopolymers at Various Temperatures. *Journal of Polymer and Biopolymer Physics Chemistry* **2**, 37–43 (2014).
152. Zammit, M. D. & Davis, T. P. A comparison of calibration procedures for the analysis of broad molecular weight distributions using size exclusion chromatography with multiple detection. *Polymer* **38**, 4455–4468 (1997).
153. Vander Heyden, Y., Popovici, S. T. & Schoenmakers, P. J. Evaluation of size-exclusion chromatography and size-exclusion electrochromatography calibration curves. *Journal of Chromatography A* **957**, 127–137 (2002).
154. le Maire, M., Viel, A. & Møller, J. V. Size exclusion chromatography and universal calibration of gel columns. *Analytical Biochemistry* **177**, 50–56 (1989).
155. Podzimek, S. Molar mass distribution by size exclusion chromatography: Comparison of multi-angle light scattering and universal calibration. *Journal of Applied Polymer Science* **136**, 47561 (2019).
156. Laguna, M. T. R., Medrano, R., Plana, M. P. & Tarazona, M. P. Polymer characterization by size-exclusion chromatography with multiple detection. *Journal of Chromatography A* **919**, 13–19 (2001).
157. Gözen, I. *et al.* Protocells: Milestones and Recent Advances. *Small* **18**, 2106624 (2022).
158. Buddingh', B. C. & van Hest, J. C. M. Artificial Cells: Synthetic Compartments with Life-like Functionality and Adaptivity. *Acc. Chem. Res.* **50**, 769–777 (2017).
159. Ghosh, B. Artificial cell design: reconstructing biology for life science applications. *Emerging Topics in Life Sciences* **6**, 619–627 (2022).
160. Salehi-Reyhani, A., Ces, O. & Elani, Y. Artificial cell mimics as simplified models for the study of cell biology. *Exp Biol Med (Maywood)* **242**, 1309–1317 (2017).
161. Xu, C., Hu, S. & Chen, X. Artificial cells: from basic science to applications. *Materials Today* **19**, 516–532 (2016).
162. Gruhl, F. J., Rapp, B. E. & Länge, K. Biosensors for Diagnostic Applications. in *Molecular Diagnostics* (eds. Seitz, H. & Schumacher, S.) 115–148 (Springer, Berlin, Heidelberg, 2013).

163. Marrot, B., Barrios-Martinez, A., Moulin, P. & Roche, N. Industrial wastewater treatment in a membrane bioreactor: A review. *Environmental Progress* **23**, 59–68 (2004).

164. Lee, K. Y. *et al.* Photosynthetic artificial organelles sustain and control ATP-dependent reactions in a protocellular system. *Nat Biotechnol* **36**, 530–535 (2018).

165. Gobbo, P. *et al.* Catalytic processing in ruthenium-based polyoxometalate coacervate protocells. *Nat Commun* **11**, 41 (2020).

166. Altamura, E. *et al.* Single Compartment Approach for Assembling Photosynthetic Protocells. in *Advances in Bionanomaterials II* (eds. Piotto, S., Concilio, S., Sessa, L. & Rossi, F.) 223–232 (Springer International Publishing, Cham, 2020).

167. Zhao, F. *et al.* Nanoengineering of Stimuli-Responsive Protein-Based Biomimetic Protocells as Versatile Drug Delivery Tools. *Chemistry – A European Journal* **20**, 6880–6887 (2014).

168. Balasubramanian, V., Herranz-Blanco, B., Almeida, P. V., Hirvonen, J. & Santos, H. A. Multifaceted polymersome platforms: Spanning from self-assembly to drug delivery and protocells. *Progress in Polymer Science* **60**, 51–85 (2016).

169. Boyd, M. A. & Kamat, N. P. Designing Artificial Cells towards a New Generation of Biosensors. *Trends in Biotechnology* **39**, 927–939 (2021).

170. Mansy, S. S. & Szostak, J. W. Reconstructing the Emergence of Cellular Life through the Synthesis of Model Protocells. *Cold Spring Harb Symp Quant Biol* **74**, 47–54 (2009).

171. Dzieciol, A. J. & Mann, S. Designs for life: protocell models in the laboratory. *Chem. Soc. Rev.* **41**, 79–85 (2011).

172. Blain, J. C. & Szostak, J. W. Progress Toward Synthetic Cells. *Annual Review of Biochemistry* **83**, 615–640 (2014).

173. Mann, S. Systems of Creation: The Emergence of Life from Nonliving Matter. *Acc. Chem. Res.* **45**, 2131–2141 (2012).

174. Rasmussen, S., Chen, L., Nilsson, M. & Abe, S. Bridging Nonliving and Living Matter. *Artificial Life* **9**, 269–316 (2003).

175. Saraniti, M. Designing biomimetic nanomachines. *Nature Nanotech* **3**, 647–648 (2008).

176. Yoo, J.-W., Irvine, D. J., Discher, D. E. & Mitragotri, S. Bio-inspired, bioengineered and biomimetic drug delivery carriers. *Nat Rev Drug Discov* **10**, 521–535 (2011).

177. Park, J. H. *et al.* Colloidosomes as a Protocell Model: Engineering Life-Like Behaviour through Organic Chemistry. *European Journal of Organic Chemistry* **2022**, e202200968 (2022).

178. Zhu, Y., Cao, S., Huo, M., Hest, J. C. M. van & Che, H. Recent advances in permeable polymersomes: fabrication, responsiveness, and applications. *Chem. Sci.* **14**, 7411–7437 (2023).

179. Rideau, E., Dimova, R., Schwille, P., Wurm, F. R. & Landfester, K. Liposomes and polymersomes: a comparative review towards cell mimicking. *Chem. Soc. Rev.* **47**, 8572–8610 (2018).

180. Donau, C. *et al.* Active coacervate droplets as a model for membraneless organelles and protocells. *Nat Commun* **11**, 5167 (2020).

181. Ahmed, E. M. Hydrogel: Preparation, characterization, and applications: A review. *Journal of Advanced Research* **6**, 105–121 (2015).

182. Wei, M., Lin, Y. & Qiao, Y. Engineered colloidosomes as biomimetic cellular models. *Giant* **13**, 100143 (2023).

183. Hunter, S. J. & György, C. Sub-micron colloidosomes with tuneable cargo release prepared using epoxy-functional diblock copolymer nanoparticles. *Journal of Colloid and Interface Science* **675**, 999–1010 (2024).

184. Huang, X., Li, M. & Mann, S. Membrane-mediated cascade reactions by enzyme–polymer proteinosomes. *Chem. Commun.* **50**, 6278–6280 (2014).

185. Guo, T. *et al.* Dynamic Hybrid Colloidosomes via Electrostatic Interactions for pH-Balanced Low Premature Leakage and Ultrafast Cargo Release. *Nano Lett.* **19**, 6065–6071 (2019).

186. Hsu, M. F. *et al.* Self-assembled Shells Composed of Colloidal Particles: Fabrication and Characterization. *Langmuir* **21**, 2963–2970 (2005).

187. Gobbo, P. *et al.* Programmed assembly of synthetic protocells into thermoresponsive prototissues. *Nature Mater* **17**, 1145–1153 (2018).

188. Myrgorodska, I., Jenkinson-Finch, M., Moreno-Tortolero, R. O., Mann, S. & Gobbo, P. A Novel Acid-Degradable PEG Crosslinker for the Fabrication of pH-Responsive Soft Materials. *Macromolecular Rapid Communications* **42**, 2100102 (2021).

189. Huang, X., Patil, A. J., Li, M. & Mann, S. Design and Construction of Higher-Order Structure and Function in Proteinosome-Based Protocells. *J. Am. Chem. Soc.* **136**, 9225–9234 (2014).

190. Zhou, P. *et al.* Programmable Modulation of Membrane Permeability of Proteinosome upon Multiple Stimuli Responses. *ACS Macro Lett.* **5**, 961–966 (2016).

191. Sun, Q., Chen, J.-F. & Routh, A. F. Coated colloidosomes as novel drug delivery carriers. *Expert Opinion on Drug Delivery* **16**, 903–906 (2019).

192. Tang, F., Li, L. & Chen, D. Mesoporous Silica Nanoparticles: Synthesis, Biocompatibility and Drug Delivery. *Advanced Materials* **24**, 1504–1534 (2012).

193. Li, M., Green, D. C., Anderson, J. L. R., Binks, B. P. & Mann, S. In vitro gene expression and enzyme catalysis in bio-inorganic protocells. *Chem. Sci.* **2**, 1739–1745 (2011).

194. Chen, Z. *et al.* Light-Gated Synthetic Protocells for Plasmon-Enhanced Chemiosmotic Gradient Generation and ATP Synthesis. *Angewandte Chemie International Edition* **58**, 4896–4900 (2019).

195. Rodríguez-Arco, L., Li, M. & Mann, S. Phagocytosis-inspired behaviour in synthetic protocell communities of compartmentalized colloidal objects. *Nature Mater* **16**, 857–863 (2017).

196. Sun, S. *et al.* Chemical Signaling and Functional Activation in Colloidosome-Based Protocells. *Small* **12**, 1920–1927 (2016).

197. Huang, X. *et al.* Interfacial assembly of protein–polymer nano-conjugates into stimulus-responsive biomimetic protocells. *Nat Commun* **4**, 2239 (2013).

198. Gobbo, P. *et al.* Programmed assembly of synthetic protocells into thermoresponsive prototissues. *Nature Mater* **17**, 1145–1153 (2018).

199. Galanti, A. *et al.* A Floating Mold Technique for the Programmed Assembly of Protocells into Protocellular Materials Capable of Non-Equilibrium Biochemical Sensing. *Advanced Materials* **33**, 2100340 (2021).

Chapter II – Multi-detector Gel Permeation Chromatography Characterization of Carbon NanoDots

Abstract

In this Chapter, the characterization of Carbon NanoDots (CNDs) by multi-detector Gel Permeation Chromatography (GPC) technique and the evaluation of the interfacial moiety reactivity of CNDs are deeply discussed.

Initially, we examined the successful synthesis and purification of *L*-arginine and ethylenediamine-derived CNDs, through different characterization methods.[1] This part of the project was carried out within the Prato group, under the supervision of Prof. Pierangelo Gobbo and Prof. Maurizio Prato.

Thereafter, multi-detector GPC analyses are performed on different batches of CNDs developing a robust calculation procedure to deliver CND molecular weight and molecular weight distribution. At this stage, ζ-potential and Dynamic Light Scattering (DLS) measurements are performed to corroborate the obtained GPC results, since they are related to the hydrodynamic size and superficial charge of the analyzed nanomaterials. This part of the project was carried out during a three-month internship at Malvern Panalytical Ltd (UK), under the supervision of Dr. Serena Agostini and Prof. Pierangelo Gobbo.

Eventually, we investigate how CND superficial moieties can be quantified and exploited for derivatization reactions with probe molecules, changing the perspective for describing the interfacial reactivity of CNDs. This part of the project was carried out within Prato and Gobbo groups, under the supervision of Prof. Pierangelo Gobbo and Prof. Maurizio Prato.

2.1 Introduction

Although studies on Carbon Dots (CDs) are becoming more and more abundant every year,[2] there is still not a clear-cut, widely accepted methodology for their accurate physicochemical characterization.[3] Thus, there are still unaddressed issues concerning the mechanisms of the CDs synthesis and the understanding of their structure-property relationship.[4–6]

Usually, several purification methods for CDs are reported in the literature, such as centrifugation, filtration, dialysis, electrophoresis, chromatography, or a combination of these techniques.[7] Specifically, chromatography is a purification method widely used to separate and identify components of a mixture.[8] Silica gel chromatography is one of the most exploited methods and several examples are described, highlighting especially the possibility of separating CDs from undesired molecular by-products.[9,10] Additionally, Size Exclusion Chromatography (SEC) and High-Performance Liquid Chromatography (HPLC) can be employed to reach the high-level purity of the sample.[11–14]

Nevertheless, using chromatography as a characterization technique rather than only a purification method could advance the development of a unified approach for the assessment of CD purity and synthesis reproducibility. The development of an effective characterization strategy would reveal the structure and composition of CNDs and improve their application consistency by preventing small molecules from being the source of their intrinsic fluorescence.[15] Moreover, by knowing the number of interfacial moieties per CND, it might be possible to unlock new insights to expand their application in (photo)catalysis and (bio)conjugation chemistry.[16–19]

Given that CNDs are considered the missing link between molecular and nanomaterials science due to their nanometric dimensions and functional group-rich surface, as well as the fact that they are sometimes associated with polymer-like materials,[20,21] determining their molecular weight and molecular weight distribution would be essential for disclosing the CND structure. Moreover, since CNDs are frequently employed to synthesize composites by taking advantage of their surface chemistry,[22,23] knowing their molecular weight could provide information on the precise number of moieties on the CND surface as well as on the resulting hybrid structures. Finally, CNDs are widely used in catalysis,[24,25] including the relatively new topic of nanozymes.[26] To identify these carbon nanomaterials as catalysts, it is important to understand the reaction mechanism and use them in catalytic amounts,[27] which requires again determining their molecular weight.

Multi-detector Gel Permeation Chromatography (GPC), as previously described in Chapter I, is a powerful characterization technique that provides sample absolute molecular weight and molecular weight distribution without relying on standard calibration curves.[28] Even though it is a

long-time well-established characterization methodology for polymer chemistry,[29,30] it has also already been applied to the characterization of complex bio-systems.[31]

In this chapter, using *L*-arginine-derived CNDs as the case study, it will be demonstrated how multi-detector GPC can determine features of CNDs that are not commonly investigated and provide information regarding the purity of these nanomaterials. Furthermore, GPC data will be paired with those obtained from ^{1}H-Nuclear Magnetic Resonance (NMR), Diffusion Ordered Spectroscopy (DOSY), Dynamic Light Scattering (DLS), and Atomic Force Microscopy (AFM) to offer new insights into the fundamental properties of CNDs. To the best of our knowledge, this is the first time that absolute molecular weight obtained by multi-detection analysis has been reported for CNDs, as few earlier reports used standard calibration methods.[32]

2.2 Results and Discussion

2.2.1 Synthesis and Purification of CNDs

CNDs were synthesized from *L*-arginine and ethylenediamine (EDA) in water *via* a well-established and fast microwave-assisted procedure. Afterwards, vacuum filtration, dialysis against MilliQ water, and freeze-drying delivered the final purified carbon nanomaterials (**Figure 2.1**).[1] The dialysis performed after the synthesis is crucial because it allows for the removal of small molecules, some of which are fluorescent and often responsible for the observed properties of CNDs samples reported in literature.[3]

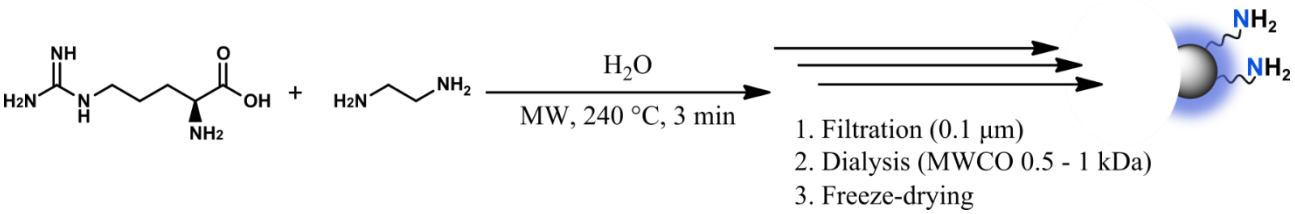

Figure 2.1. *Reaction and purification scheme yielding CNDs.*

To verify their successful synthesis and purification, CNDs were characterized by ^{1}H and DOSY NMR spectroscopy, UV-Vis and fluorescence spectroscopy, Attenuated Total Reflectance - Fourier Transformed Infrared (ATR-FTIR) spectroscopy, AFM, and DLS.

In detail, ^{1}H NMR and DOSY (**Figure 2.2**) spectra showed the absence of impurities (*i.e.*, no sharp peaks with detectable multiplicity) and provided the diffusion coefficient (D_0) of CNDs. In **Figure 2.2.b**, it is recognizable a homogeneous signal pattern arising from the nanomaterials and not from molecules, which would have signals comparable to the solvent residual peak. The found D_0 value of $(2.75 \pm 0.24)\times10^{-10}$ m^2 s^{-1} is consistent with literature data on other types of CNDs.[33]

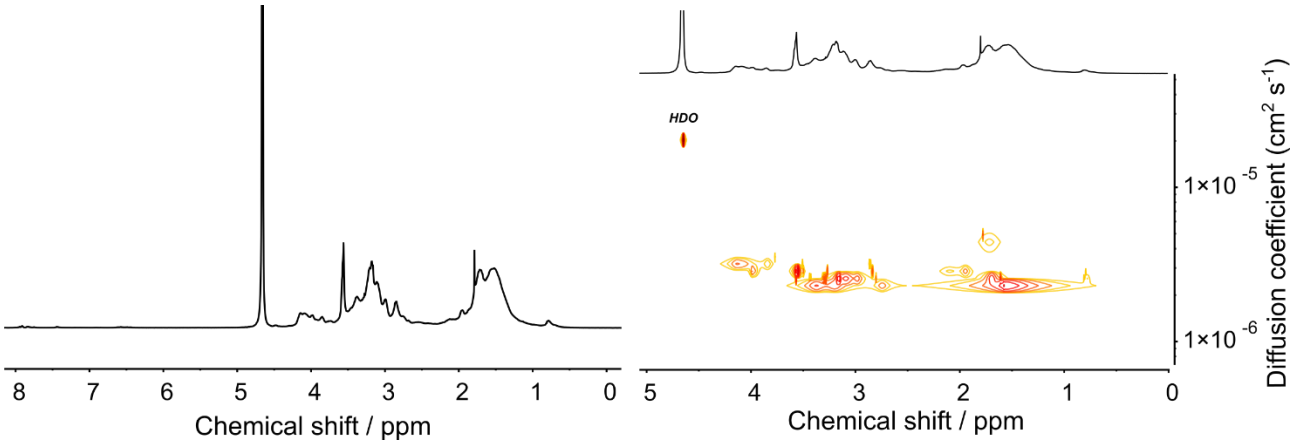

Figure 2.2. a) *^{1}H-NMR fingerprint spectrum of CNDs in deuterium oxide referenced against solvent residual peak (δH: 4.79 ppm);* ***b)*** *DOSY trace of CNDs in deuterium oxide, solvent residual peak at 4.79 ppm.*

AFM analysis (**Figure S2.1**) confirmed the spherical shape of these nanomaterials with an average size of 3.96 ± 1.41 nm, and ATR-FTIR spectroscopy (**Figure S2.2**) validated the presence of expected functional groups (*e.g.*, hydroxy, amine, carbonyl groups) according to molecular precursors used for CNDs synthesis.

Furthermore, UV-Vis and fluorescence spectroscopy (**Figure S2.3**) were employed to characterize the optical properties of these CNDs, proving their inherent blue fluorescence and wavelength-dependent emitting behavior.

Through this initial set of characterizations, we were able to verify that the used work-up procedure delivered well-purified nanomaterials and that these arginine-derived CNDs were obtained as previously reported in the literature.[1]

2.2.2 Multi-detector Gel Permeation Chromatography Characterization

Once it was proven that we had a pure nanomaterial, CND molecular weight was determined using a tetra-detector GPC system. For an accurate GPC analysis, the chromatographic elution of the sample of interest has to be as effective as possible, meaning that there must be no interactions between the sample and the column stationary phase. Therefore, it is necessary to tune several elution conditions (*e.g.*, eluent choice, type of columns, column oven temperature, flow rate) to prevent this potential issue and to allow for an interaction-free separation.

In our case, after some screening tests to find the best GPC set-up, we eluted CNDs on the cationic stationary phase using 0.1 M sodium nitrate with 0.5 V/V% acetic acid (pH 2.6) solution as the mobile phase (**Table 2.1** for complete chromatographic conditions. See Experimental Section,

Materials and methods for more details on columns). The eluent was selected considering the chemical nature of specific CND superficial groups, namely primary amines, which would be positively charged at low pH values. Since the stationary phase is composed of polymethacrylate beads with cationic groups on their surface, the interaction between the nanomaterials and the column packing will be minimized (*i.e.*, repulsive electrostatic interactions).
To verify this assumption, we carried out ζ-potential measurements of CNDs in the chosen eluent. We obtained a positive value of 12.13 ± 2.81 mV (see Experimental Section, Materials and methods for more details), validating our choice for the chromatographic set-up.

Table 2.1. *GPC set-up for CND analysis.*

Stationary phase	Cationic columns
Mobile phase	0.1 M $NaNO_3$ pH 2.6/CH_3COOH
Concentration (mg mL^{-1})	5
Injection Volume (µL)	70
Flow rate (mL min^{-1})	0.5
Autosampler Temperature (°C)	4
Column Oven Temperature (°C)	20
Detector Oven Temperature (°C)	20

Multi-detector GPC chromatograms of CNDs are reported in **Figure 2.3.a**, showing a positive response (*i.e.*, peak at higher mV values with respect to the baseline) of each detector to the sample flowing through. Specifically, the Refractive Index and UV detectors gave a response proportional to sample concentration, while light-scattering and viscometer detectors are sensible to sample molecular weight and viscosity, respectively (see Chapter I, 1.3 Gel Permeation Chromatography). The principal quality parameters that we look for in a chromatogram are peak symmetry and tailing. Particularly, in an ideal chromatogram the peak symmetry should be as high as possible, whereas the tailing should be minimized. **Figure 2.3.a** displayed a unimodal distribution indicating presence of one species. The shown chromatograms were of high quality since the peaks are symmetric, except for a slight tailing in the Right Angle Light Scattering (RALS) curve linked to a minor interaction with the column.

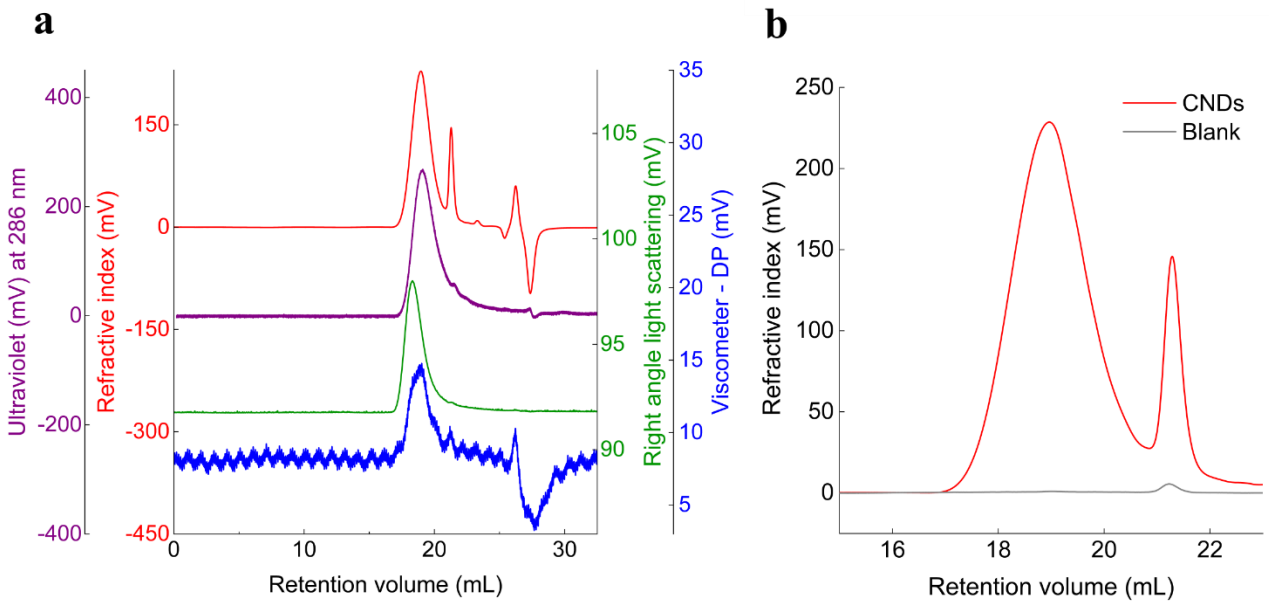

Figure 2.3. a) *Chromatograms of CNDs (0.1 M $NaNO_3$ + 0.5 V/V% acetic acid (pH 2.6) on cationic columns), from top to bottom, refractive index curve (red), UV curve (purple), light scattering curve (green), and viscometer curve (blue), respectively;* ***b)*** *Refractive index overlay of CNDs (red) and blank (grey) curves.*

Moreover, we observed an excellent repeatability of multiple injections for each detector response (Experimental Section, **Figure S2.4**).

To determine the molecular weight moments (M_n and M_w) and distribution of CNDs, it is essential to define the refractive index increment (dn/dC), the difference in refractive index between the sample and the solvent. This is a parameter retrievable from the integration of the Refractive Index (RI) chromatogram area, and it is used in combination with light scattering detector data to yield desired outcomes (See **Equation 1 – 3**). The value of dn/dC is fundamental to calculate the absolute molecular weight, thus it must be calculated with high precision and accuracy to avoid misleading results.

In **Figure 2.3.b**, a positive peak at a retention volume of 21.5 mL can be noted in the blank curve (grey). This is part of the permeation peaks (or system peaks) related to the chosen eluent/column system and associated with air bubbles or little impurities of inorganic salts used to prepare the eluent solution. Following the CNDs RI trace (red), it is observable a partial CND contribution to the permeation peaks, because otherwise CND and blank curves would overlay at 21.5 mL elution volume. Since the RI is one of the two GPC detectors reacting to the sample concentration and considering that the permeation peaks are excluded from the integration area considered for molecular weight distribution calculation, we might underestimate the dn/dC, and consequently

overestimate CND molecular weight moments, not knowing the precise sample concentration underlying the RI chromatogram.

To address this issue, we developed a procedure to precisely obtain the concentration of the sample of the integrating area of the RI chromatogram. To fully understand it, we need to recall the simplified equations governing three of the four GPC detectors (**Equation 1 – 3**):

$$RIsignal(mV) = K_{RI} \times \frac{dn}{dC} \times C \qquad \textbf{Equation 1}$$

$$UVsignal(mV) = K_{UV} \times \frac{dA}{dC} \times C \qquad \textbf{Equation 2}$$

$$LSsignal(mV) = K_{LS} \times M_w \times \left(\frac{dn}{dC}\right)^2 \times C \qquad \textbf{Equation 3}$$

where for **Equation 1** K_{RI} is the constant of the RI detector determined during the instrument calibration, dn/dC is the sample refractive index increment, and C is the concentration of the sample giving that output signal. For **Equation 2**, K_{UV} is the constant of the UV detector determined during the instrument calibration, dA/dC is the specific absorption coefficient, and C is the concentration of the sample giving that output signal. Lastly, for **Equation 3**, K_{LS} is the constant of the LS detector determined during the instrument calibration, M_w is the molecular weight of the sample, dn/dC is the sample refractive index increment, and C is the concentration of the sample giving that output signal.

Therefore, we exploited the second detector responding to the sample concentration – the UV detector – since it does not show any permeation peaks. We integrated the whole UV peak and used **Equation 2** to determine the dA/dC of CNDs, using the input concentration (*i.e.*, the known concentration at which the sample was prepared). After that, we solved **Equation 2** for the concentration and used the calculated dA/dC to integer the UV peak area corresponding to the RI peak, not considering the permeation peaks. This allowed us to quantify the actual concentration (*i.e.*, corrected concentration) beneath that RI peak area. Knowing the correct concentration, we could use **Equation 1** to calculate the dn/dC of CNDs and hence, exploiting **Equation 3**, molecular weight moments and dispersity (Đ) (for complete tables of parameters used for these calculations see Experimental Section, 2.4.3 Multi-detector Gel Permeation Chromatography Analysis of CNDs).

Table 2.2 reported the results before and after the sample concentration correction, and we could confirm that the initial sample dn/dC was underestimated. Moreover, we found out that the sample recovery was quantitative, and the analysis was performed on 80% of the sample, on average. This

suggested that the portion eluting with the permeation peak is small hydrodynamic size species which are intrinsically present in CND samples.

Table 2.2. *Comparison between multi-detector GPC results with input sample concentration and corrected sample concentration.*

	dn/dC (mL g^{-1})	**M_n (g mol^{-1})**	**M_w (g mol^{-1})**
From input concentration	0.158	4800	6500
From corrected concentration	0.194	3900	5300

According to the obtained results, arginine and EDA-derived CNDs had a number average molecular weight (M_n) and a weight average molecular weight (M_w) of 3927 ± 8 g mol^{-1} and 5272 ± 12 g mol^{-1}, respectively, and the nanomaterials were nearly monodispersed (Đ = 1.34).

To check that our initial hypothesis was correct (*i.e.*, determine the dA/dC from sample UV signal and its input concentration) and test whether could be an influence caused by an interaction with the stationary phase, we performed GPC runs of CNDs without columns. These experiments are called tubing tests. They consisted of replacing columns with a long PTFE tube and running the sample in the same elution conditions used before. In this way, even though there was not an actual chromatographic separation, the sample chromatograms were still registered, analyzed, and then compared to the previously acquired ones.

It should be mentioned that data obtained from a tubing test experiment will always deliver higher values, in terms of dA/dC and dn/dC, compared to a normal chromatographic run. This is because all impurities or small molecules from the sample or the eluent are not separated and therefore contribute to the recorded signals. Injecting well-purified materials helps minimize this overestimation.

By doing so, we could confirm that our CND dA/dC estimation was accurate, validating the molecular weight distribution results obtained (see Experimental Section, 2.4.3 Gel Permeation Chromatography for a detailed table on all obtained results).

During GPC analyses of different CND batches, few differences in RI traces arose. In **Figure 2.4.a** are shown RI chromatograms of three different CND batches, injected at the same concentration. In two of them (red and green profiles) was visible a bimodal peak and an increased contribution to the permeation peaks. Since smaller species eluted at the permeation peaks, we correlated the GPC chromatograms to the corresponding ^{1}H-NMR spectra. In **Figure 2.4.b** was evident that the second and the third spectrum (from the top, red and green profiles, respectively) are the ones that

showed signals associable to molecular species, with a distinguishable multiplicity, in the region between 4.5 and 2.5 ppm (**Figure 2.4.b** inset).

This might have happened because the purification procedure was not rigorously followed. For instance, the dialysis step can be influenced by a change in the schedule of water replacement, thus leading to different outcomes in retained by-products. Specifically, as was further investigated and demonstrated in a recent report,[34] the number of times of changing dialysis water and the amount of water against which the sample is dialyzing are pivotal to deliver purified and reproducible CNDs. As a general rule, an accurate purification avoids the wrong association of molecular features (*e.g.*, fluorescence, in most cases) to CND properties.[15,35]

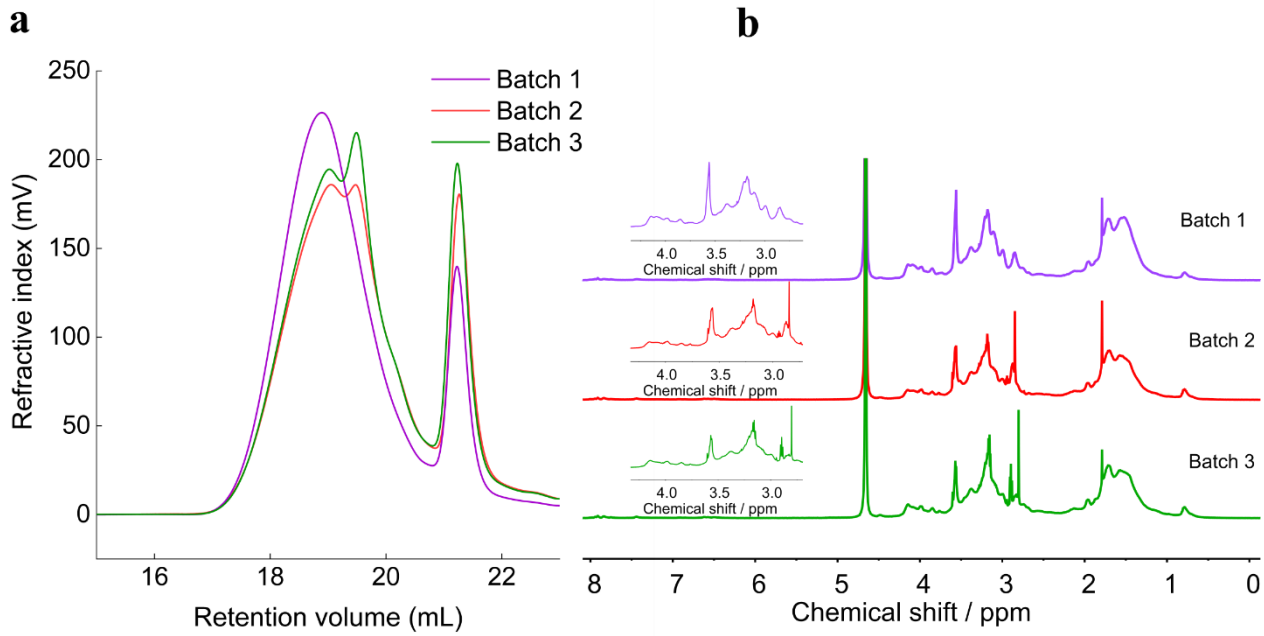

Figure 2.4. a) *RI chromatograms of different CND batches at the same concentration (5 mg mL^{-1}, 0.1 M $NaNO_3$ + 0.5 V/V% acetic acid pH 2.6 on cationic columns);* ***b)*** *^{1}H NMR spectra of the same three batches (1 to 3, from the top to the bottom, respectively) referenced against solvent residual peak (δH: 4.79 ppm), with corresponding insets in the region of interest (4.5 – 2.5 ppm) showing sharp signals in spectra 2 and 3.*

Nevertheless, these results led us to conclude that the RI detector was extremely sensitive to synthesis variability. Moreover, by applying the same calculation procedure previously explained, we obtained consistent results even considering the batch variability (see Experimental Section, 1.4.3 Gel Permeation Chromatography for a detailed table on all obtained results).

Surprisingly, the dn/dC of CNDs was always found to be *ca.* 0.2 mL g^{-1}, independently from the presence of a bimodal peak. This confirmed the robustness of the synthetic protocol used and

should draw attention to always being careful during the purification step of these complex nanomaterials.

Finally, another parameter retrievable from a GPC analysis is the hydrodynamic size of the sample. In detail, the hydrodynamic radius, calculated by combining the data of the viscometer and light scattering detectors, is the radius of an equivalent theoretical sphere that increases the fluid (eluent) viscosity by the same amount as the sample of interest. Therefore, by definition, it is different from the hydrodynamic radius obtained by a DLS experiment, since it is the radius of a hypothetical hard sphere that diffuses at the same rate as the particle being measured. This sphere comprises the core particle plus anything that is bound to its surface (solvated particle).

We performed DLS measurements in the same conditions of a chromatographic run (concentration of 5 mg mL^{-1}, solubilized in 0.1 M $NaNO_3$ with 0.5 V/V% acetic acid pH 2.6, 4 °C) and the results are shown in **Figure 2.5**.

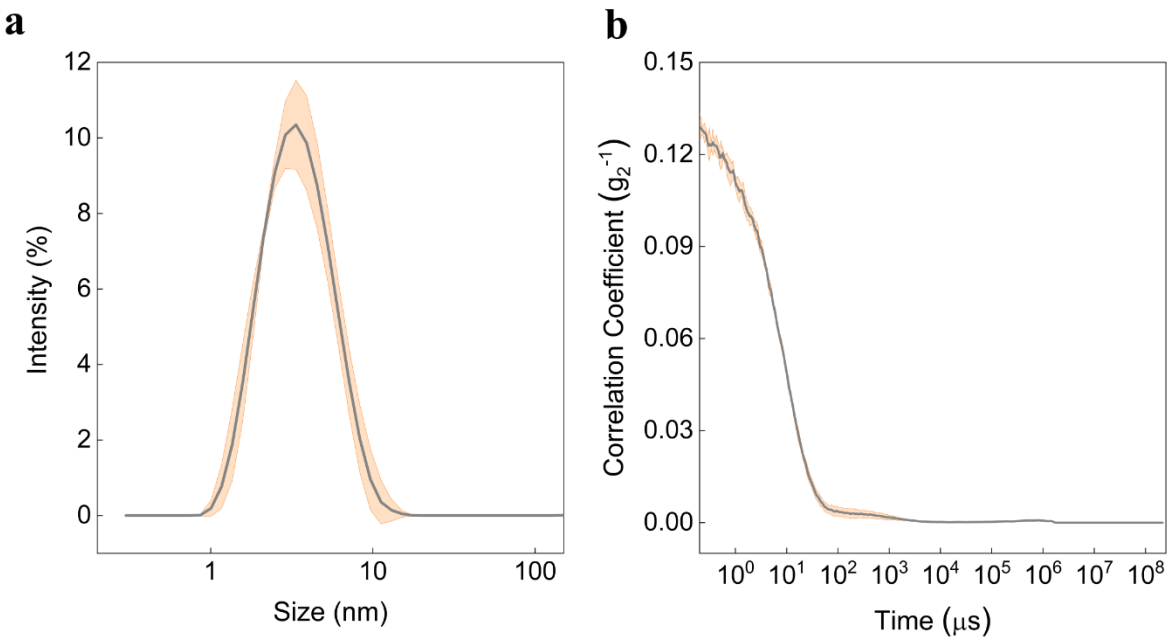

Figure 2.5. a) *Size distribution by intensity of CNDs (5 mg mL^{-1}, 0.1 M $NaNO_3$ + 0.5 V/V% acetic acid (pH 2.6), 4 °C);* ***b)*** *Correlogram of CNDs (5 mg mL^{-1}, 0.1M $NaNO_3$ + 0.5 V/V% acetic acid (pH 2.6), 4 °C).*

CND average hydrodynamic size was found to be 3.8 ± 0.2 nm (**Figure 2.5.a**), and their polydispersity index (PDI) was 0.27 ± 0.03. This latter describes the intensity of light scattered by diverse fractions of particles of different size, and CND could be considered moderately polydisperse since their PDI was in a range of values between 0.1 – 0.4.[36]

In **Figure 2.5.b** is shown the corresponding correlogram, from which we could retrieve additional information. Its intercept was not as high as expected – an ideal value is around 0.8-0.9 g_2^{-1}. This was due to the CND small size and intrinsic fluorescence, two factors that usually lead to a reduction of the correlation coefficient. The correlation held time (*i.e.*, time at which the correlation curve starts to decay) was quite short and the curve slope decayed fast, both hints of a small sized nanomaterial.[37] Lastly, the profile baseline was a bit elevated at longer time values, linked to the presence of few bigger aggregates that are visible also in the intensity distribution profile as a broad low-intensity band at around 1000 nm (**Figure S1.5**). This could also contribute to CND PDI value being higher than 0.1 (highly monodisperse).[36]

By comparing these findings with those obtained through GPC and AFM analyses, we confirmed that they were comparable considering the experimental error, and they agreed in term of CND size (**Table 2.3**) and dispersity of the sample. In particular, Đ values from GPC characterization (Đ = 1.34) and PDI from DLS analysis (PDI = 0.27) both led us deduce that arginine-derived CNDs were moderately monodispersed nanomaterials, considering that we did not have any control over their dimensions during the synthetic steps.

Table 2.3. *Comparison between CNDs hydrodynamic size obtained from different characterization techniques.*

Characterization technique	Hydrodynamic size (nm)	Solvent
GPC	2.8 ± 0.2	0.1 M $NaNO_3$ pH 2.6/CH_3COOH
DLS	3.8 ± 0.2	0.1 M $NaNO_3$ pH 2.6/CH_3COOH
AFM	3.9 ± 1.4	Methanol
AFM*	2.5 ± 0.8	MilliQ water

*Previously published data on these CNDs.[1]

All these findings suggested that the multi-detector GPC technique could be implemented as a powerful characterization tool to improve CNDs quality in terms of batch reproducibility and, just with a single run, to deliver information on nanomaterial molecular weight distribution, dispersity and hydrodynamic size as well.

2.2.3 Quantification of Interfacial Reactive Groups on CNDs

Knowing CND molecular weight moments and distribution paves the way to the quantification of reactive groups on their surface. This is relevant for the (bio)conjugation of these nanomaterials with molecules, enzymes, and (nano)materials, using their superficial chemistry.

The predominantly exploited functional groups of arginine and EDA-derived CNDs are primary amines. Therefore, to give new insights into CND superficial composition, we used their molecular weight to obtain the accurate number of available moieties.

To achieve this, Kaiser test (KT) was performed (see Experimental Section, 2.4.4 Quantification of CND Primary Aliphatic Amines by Kaiser Test). KT is a colorimetric test in which ninhydrin, upon reaction with amines, is converted in deep blue/purple derivatives, called Ruhemann's purple. These complexes have an absorption maximum at 570 nm and the intensity of this peak is directly proportional – by the Beer-Lambert law – to the quantity of primary aliphatic amines in the sample. Considering the M_n of CNDs, we could reformulate the KT results – usually reported in μmol of amines per g of sample – pointing out the number of primary aliphatic amines per CND.

In **Figure 2.6** are shown the absorption spectra obtained for KT of CNDs at 120 °C and at room temperature (r.T). The former temperature was chosen because it is the standard for carrying out the KT, whilst the latter was chosen because CND post-functionalization reactions are often performed at room temperature. At 120 °C the number of primary aliphatic amines on CND surface was higher (7 ± 1) than at room temperature (2 ± 1). This evidence is linked to the accessibility of functional groups that are more prone to react with increasing temperature.

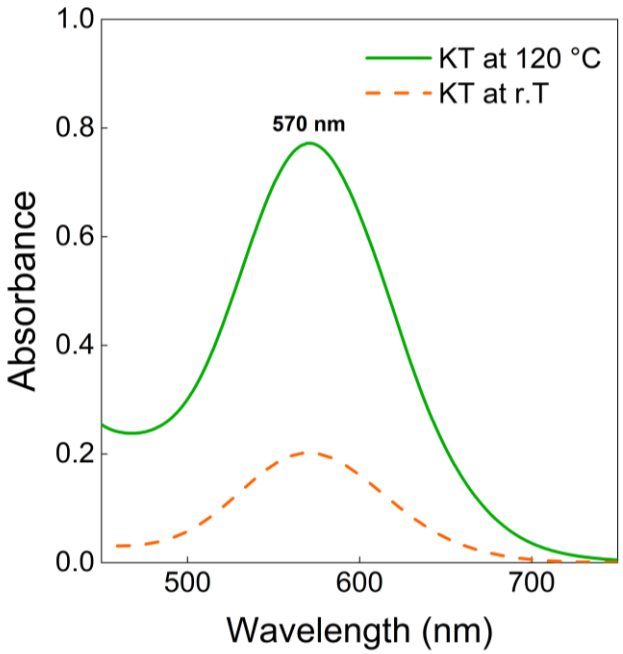

Figure 2.6. *Absorbance maxima (570 nm) of Ruhemann's purple complex formed after KT of CNDs performed at 120 °C (green line) and at room temperature (orange dashed line).*

Additionally, it was interesting to reformulate the amount of other functional groups already quantified in previously published scientific papers on *L*-arginine-derived CNDs.[38] In **Table 2.4** is reported an overview of superficial moieties of CNDs.

Table 2.4. Average numbers of different interfacial reactive groups per CND.

Superficial groups	Technique	Average number	Source
Primary aliphatic amines	KT at 120 °C	7 ± 1	This work
Primary aliphatic amines	KT at r.T	2 ± 1	This work
Total amines	^{19}F NMR	16	Filippini *et al.*[38]
Total acid/base sites	pH titration	42	Filippini *et al.*[38]

Among all listed data, the availability of two primary amines per CND at room temperature confirmed the possibility of assembling nanometric structures at that temperature, supporting the synthesis of arginine-derived CND-based hybrid materials reported in the literature.[39,40]

2.2.4 Proof of Concept of Interfacial Reactivity of CNDs

Finally, we decided to probe the interfacial reactivity of CNDs as a proof-of-concept application, by carrying out the conjugation reaction of CNDs to *p*-fluorobenzaldehyde *via* imine formation.[41] We chose to monitor the reaction by ^{19}F NMR spectroscopy (**Figure 2.7**, see Experimental Section, 2.4.5 Proof-of-concept amine reactivity of CNDs by ^{19}F-NMR spectroscopy).

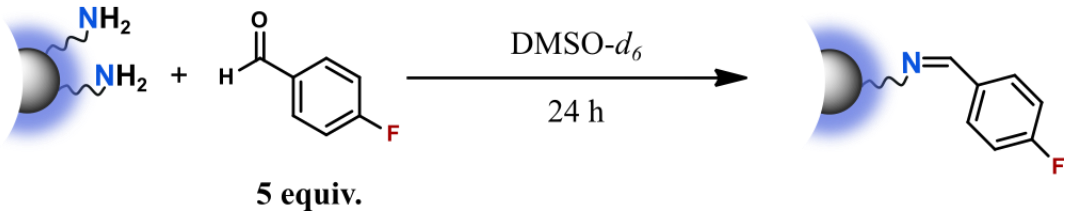

Figure 2.7. *Reaction scheme of imine formation on CND surface.*

We mixed our CNDs with an excess of reactive aldehyde in deuterated DMSO (DMSO-d_6) at room temperature and then added a fluorinated internal standard (IS, trifluoro toluene) to quantify the number of fluorinated formed imines. A typical ^{19}F NMR spectrum is shown in **Figure 2.8.a**, in which imines produced on the CND surface were visible as multiplets centered at -110 ppm (**Figure 2.8.a** inset). This evidence was in accordance with the chemical shift value obtained for the imines derived from fluorinated model molecular imine (benzylamine, see Experimental Section, 2.4.5 Proof-of-concept amine reactivity of CNDs by ^{19}F-NMR spectroscopy, **Figure 2.10**) and with previously published results on similar systems.[41]

Initially, a kinetic study was performed (**Figure 2.8.b**). To be sure that all reactive moieties underwent a complete conjugation, the maximum reaction time of 24 hours was set up. From these experiments, we determined that the number of primary amines available per CND was 6 ± 1, confirming the results obtained with KT.

Then, we ran the same reaction at 120 °C to assess whether there was a difference, as found for the KT. This experiment yielded the same results, meaning that ^{19}F-NMR tests directly delivered the total number of these moieties available. This outcome was probably due to the higher reactivity of *p*-fluorobenzaldehyde than ninhydrin used in KT.

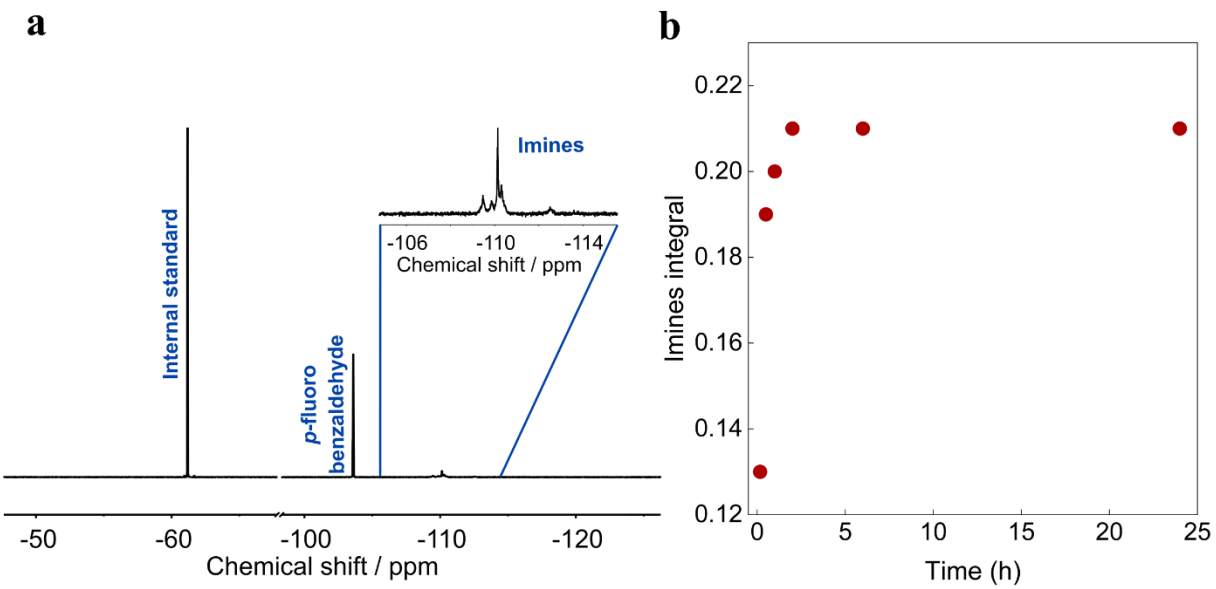

Figure 2.8. a) *^{19}F-NMR spectrum in DMSO-*d_6 *(400 MHz, r.T) showing imine derivatives of CNDs (-61.18 ppm internal standard (trifluoro toluene), -103.59 ppm* p-*fluoro benzaldehyde*, -109 – -111 *ppm imines);* ***b)*** *Kinetic curve of imine formation over 24 h at room temperature.*

With these proof-of-concept experiments, we confirmed that functional group derivatization reactions – in this case using primary amines – can be performed directly on the CND surface. This may pave the way for the fabrication of more complex (nano)structures.

2.3 Conclusions

In summary, this chapter begins by confirming the successful synthesis and purification of CNDs derived from *L*-arginine and ethylenediamine, verified through different characterization techniques, including NMR, AFM, UV-Vis, and fluorescence spectroscopy. Then, we carried out a detailed analysis of these carbon nanomaterials using multi-detector GPC. By optimizing chromatographic conditions, we achieved the effective CND elution and developed a robust calculation method to precisely determine their molecular weight moments and distribution. This allowed us to determine that *L*-arginine and EDA-derived CNDs had an average M_n of 3927 g mol^{-1}, an average M_w of 5300 g mol^{-1}, and an Đ of 1.34.

Additionally, we demonstrated the high sensitivity of the refractive index detector to synthesis variability, yielding insights comparable to those from ^{1}H NMR spectroscopy. The hydrodynamic size values obtained for CNDs through GPC were also consistent with measurements from DLS and AFM, confirming the GPC method reliability. This multi-detector GPC analysis allowed us to uncover novel details about the CND surface composition, specifically revealing the number of reactive moieties per nanomaterial. Through KT analyses and proof-of-concept experiments, involving the reaction of CND functional groups with a fluorinated probe, we determined that each CND had on its surface, on average, two primary aliphatic amines available for room-temperature reactions.

As future studies, this methodological approach can be adapted to investigate other types of CNDs, potentially broadening its applicability. From a general perspective, this work has significant implications to expand the basic knowledge on CNDs, paving the way for their precise and tunable application in different fields, such as (photo)catalysis, and assembling these nanomaterials in more complex hybrid systems. Specifically, knowing CND molecular weight unlocks the possibility to precisely design and synthesize CND-based structures and (re)formulate outcomes in catalysis to evaluate whether CNDs promote organic transformations in a catalytic loading.

2.4 Experimental Section

2.4.1 Materials and Methods

L-Arginine (≥ 98%), ethylenediamine (≥ 99.5%), methanol (≥ 99.9%), citric acid monohydrate (99%), sodium citrate tribasic dihydrate (BioUltra), sodium nitrate ($NaNO_3$, EMSURE® ACS), and acetic acid were purchased from Sigma-Aldrich and used without further purification. MilliQ water was obtained from a Millipore Milli-Q Plus 185 apparatus and presented a resistivity of 18.2 MΩ cm. Dialysis tubes (SpectraPor® Float-A-Lyzer®) with molecular weight cut-off of 0.5 – 1 kDa were bought from Repligen.

Microwave-assisted synthesis was performed on a CEM Discover-SP and using a 10 mL glass microwave vial sealed with a modified PTFE (TFM) cap.

^{1}H-NMR spectra and DOSY experiments were recorded on a Varian Inova spectrometer (^{1}H: 500 MHz) equipped with Performa II-Z gradient coils with Absolute Value – gradient compensated stimulated Echo gHMBC. Chemical shifts were reported in ppm using the solvent residual signal as an internal reference (D_2O: δH = 4.79 ppm). All spectra were recorded at 25 °C and were analyzed with MestReNova v12.0.1-20560.

AFM images were obtained with a Nanoscope IIIa (VEECO Instruments) using tapping mode with a HQ:NSC19/ALBS probe (80 kHz; 0.6 N/m) (MikroMasch). Samples were prepared by drop-casting methanol solutions (concentration around 1 ng mL^{-1}) on an exfoliated mica substrate. The obtained micrographs were analyzed with Gwyddion 2.63.

Attenuated Total Reflectance (ATR) Fourier-Transform Infrared spectroscopy was performed on a Shimadzu IRAffinity1S equipped with a QATR-10 with diamond crystal. Samples were analyzed as powders by placing them on the crystal and pressing them to record the spectrum.

Absorption spectra were collected with an Agilent Cary 5000 UV-Vis spectrophotometer. Spectra were acquired at a concentration of 1 mg mL^{-1} in MilliQ water at room temperature, using 10 mm path-length quartz cuvettes.

Fluorescence spectra were recorded on an Edinburgh instruments FS5 spectrofluorometer using a 150 W CW Ozone-free xenon arc lamp as the source and a Photomultiplier R928P (spectral coverage: 200 nm – 900 nm) as detector. All spectra were registered with an absorbance equal to 0.1 in MilliQ water at room temperature using 10 mm path-length quartz cuvettes.

GPC measurements were performed on an OMNISEC RESOLVE/OMNISEC REVEAL system from Malvern Panalytical Ltd. The OMNISEC RESOLVE system comprises an isocratic pump with continuous back seal washing that can operate between 0.005 - 10 mL/min of flowrate and with an accuracy of ±1%, a degasser with > 90% degassing capacity, a thermostated autosampler

(4 – 60 °C) with a 250 µL glass syringe and a 300 µL injection loop, a column oven containing two Tosoh Bioscience TSKgel GMPW$_{XL}$-CP (G6000 + G3000PWXL-CP) cationic size exclusion chromatography (SEC) columns connected in series. The OMNISEC REVEAL comprises four detectors: *(1)* Refractive index deflection detector operating at 640 nm and with a 12 µL reference cell; *(2)* Diode-array-based UV-Vis spectrophotometer working between 190 – 900 nm (accuracy < 1 nm) and equipped with 7.5 µL cell with a 10 mm path length; *(3)* Light scattering detector comprising a Right Angle Light Scattering detector (RALS) positioned at 90° to the sample flow, and a Low Angle Light Scattering detector (LALS) positioned at 7° to the sample flow, the light source is a 640 nm laser (50 mW), the cell volume is 18 µL; *(4)* 4-capillary Wheatstone bridge viscometer with self-balancing mechanism, user-exchangeable capillaries and one delay column. Column and detector ovens were kept at 20 °C, whereas the autosampler was kept at 4 °C. A typical run was performed using 0.1 M $NaNO_3$ + 0.5 V/V% acetic acid – to reach pH 2.6 – as mobile phase, which was pre-filtered through a bottle vacuum filter funnel with a 0.22 µm PES membrane (Steritop®, Merck). CND samples were prepared at a concentration of *ca.* 5 mg mL^{-1}, dissolved in the eluent, and filtered through 0.45 µm regenerated cellulose syringe filters.

ζ-Potential and DLS measurements were performed on a Zetasizer Ultra Red (Malvern Panalytical Ltd) using a ζ-Potential cuvette (Malvern Panalytical Ltd, model DTS1070) and a low-volume quartz batch cuvette (Malvern Panalytical Ltd, model ZEN2112), respectively. CND samples were prepared at a concentration of *ca.* 5 mg mL^{-1} in a pre-filtered sodium nitrate solution (0.1 M $NaNO_3$ + 0.5 V/V% acetic acid pH 2.6). Before measurement, sample solutions were also filtered through a 0.45 µm regenerated cellulose syringe filter.

^{19}F-NMR spectra were recorded on Varian 400 MHz spectrometer (^{19}F: 376 MHz). All spectra were recorded at 25 °C.

2.4.2 Synthesis of CNDs

The synthesis of CNDs was carried out according to a previously published procedure.[1] Briefly, L-Arginine (87.0 mg, 0.5 mmol), ethylenediamine (33.0 µL, 0.5 mmol), and MilliQ water (100 µL) were added in a 10 mL glass microwave vial. The reactor was heated at 240 °C using 200 W power for 3 minutes. The obtained crude was diluted with MilliQ water and filtered through a 0.1 µm PTFE membrane filter. The filtrate was dialyzed (MWCO: 0.5–1 kDa) against MilliQ water for 48 h (water bath was changed four times) and the resulting solution was freeze-dried to obtain a yellowish powder.

2.4.3 Multi-detector Gel Permeation Chromatography Analysis of CNDs

All CND analyses were performed by injecting – at the same concentration – 70 μL of sample and at a flow rate of 0.5 mL min^{-1}. In **Table S2.1** are reported the main parameters retrievable from a multi-detector GPC run yielded by inserting the input concentration or the corrected concentration. **Table S2.2** reported the dA/dC (*i.e.*, the molar absorption coefficient of the sample divided by its molecular weight) of CNDs obtained from a normal chromatographic run and a tubing test.

Table S2.1. *Comparison table between multi-detector GPC average results, namely refractive index increment, number average molecular weight, weigth average molecular weight, and hydrodynamic radius of different batches of CNDs obtained with input sample concentration and corrected sample concentration.*

Batch	Input concentration (mg mL^{-1})	dn/dC (mL g^{-1})	Mn (g mol^{-1})	Mw (g mol^{-1})	R_H (nm)	Corrected concentration (mg mL^{-1})	dn/dC (mL g^{-1})	Mn (g mol^{-1})	Mw (g mol^{-1})	R_H (nm)
1	5.47	0.158	4800	6500	1.42	4.49	0.194	3900	5300	1.41
2	5.34	0.153	6400	9300	1.50	4.05	0.201	4800	7000	1.52
3	5.26	0.162	6000	8800	1.45	4.02	0.213	4500	6700	1.45

Table S2.2. *Comparison table between multi-detector GPC average results, namely dA/dC at 286 nm, of different batches of CNDs obtained from a chromatographic run and a tubing test.*

Batch	dA/dC (mL g^{-1} cm^{-1})	dA/dC tubing (mL g^{-1} cm^{-1})
1	2.002	1.880
2	2.284	2.489
3	2.796	2.490

2.4.4 Quantification of CND Primary Aliphatic Amines by Kaiser Test

KT, whose mechanism is shown in **Figure 2.9**,[42] was carried out by using a commercially available kit (Sigma Aldrich) and according to a modified procedure.[43] Briefly, 1 mg of purified CNDs was weighed in a 4 mL glass vial. Then, 75 µL of a phenolic solution in ethanol (80%), 100 µL of a KCN solution in pyridine/water and 75 µL of a ninhydrin solution in ethanol (6%) were added in this specific order. The solution was left reacting either at room temperature or at 120 °C for 10 minutes. The resulting solution was diluted with 60 V/V% ethanolic aqueous solution, and its absorption spectrum was recorded. A solution without CNDs was used as a reference blank. Aliphatic primary amines on the CNDs surface were quantified from the absorbance value at 570 nm, using a molar absorption coefficient of 15000 M^{-1} cm^{-1} for Ruhemann's purple complex. Experiments were repeated in triplicate for each reaction condition.

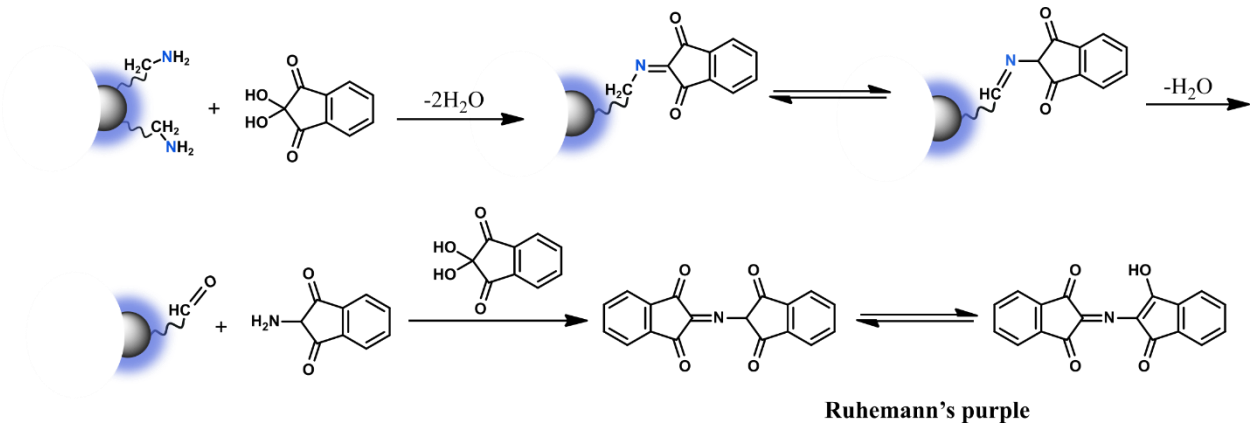

Figure 2.9. *Proposed mechanism for KT reactions on CNDs.*[42]

2.4.5 Proof-of-concept Amine Reactivity of CNDs by ^{19}F-NMR Spectroscopy

All the ^{19}F-NMR quantification experiments were performed by dissolving 10 mg of CNDs in 750 µL of deuterated DMSO and by adding 5 equivalents of *p*-fluorobenzaldehyde. The solution was left to react for 24 hours either at room temperature or at 120 °C. Experiments were repeated in triplicate at each temperature. All the spectra were registered at 25 °C and using trifluoro benzene as the internal standard.

Figure 2.10 showed the ^{19}F NMR spectra of fluorinated imines formed from the reaction of *p*-fluoro benzaldehyde with benzylamine and CNDs, respectively.

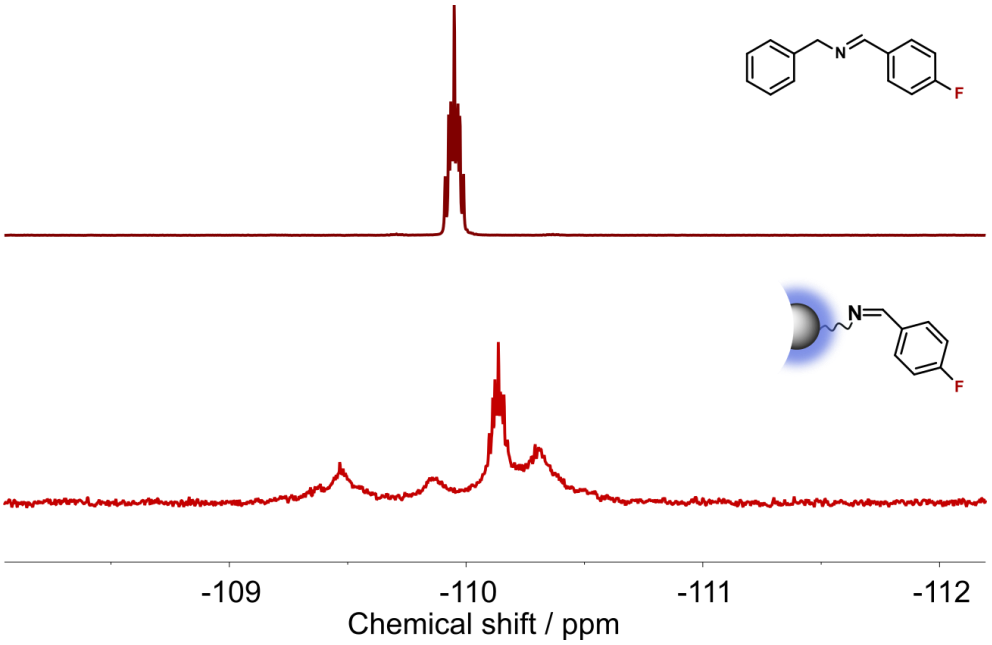

Figure 2.10. *^{19}F-NMR spectrum in DMSO-*d_6 *(400 MHz, r.T) showing imine derivatives of benzylamine (top dark red spectrum, -109.9 ppm) and CNDs (bottom red spectrum,* -109 – -110.5 *ppm).*

2.4.6 Supplementary Figures

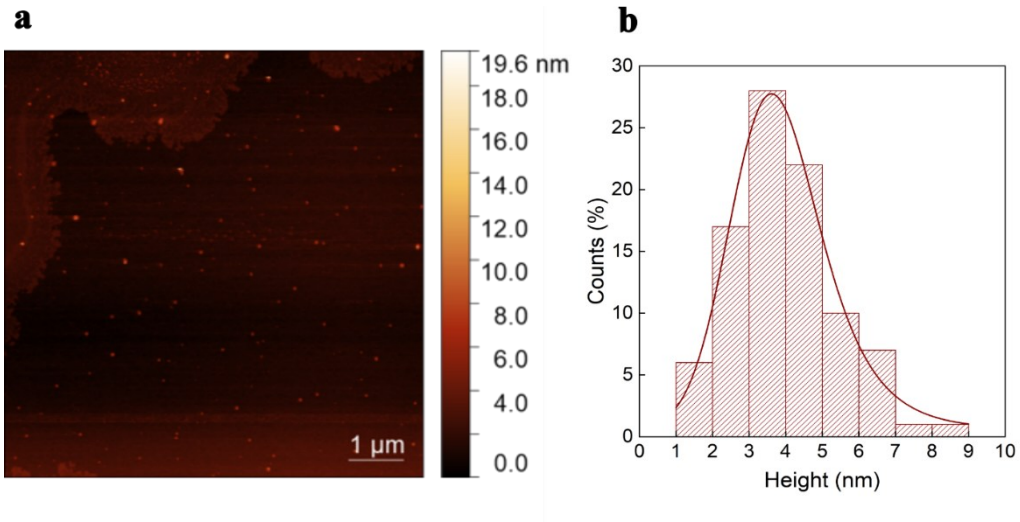

Figure S2.1. *AFM of purified CNDs:* ***a)*** *Micrograph of purified CNDs, color brightness indicates the relative height, from lowest (dark) to highest (bright);* ***b)*** *Size distribution of purified CNDs. The average size is 3.9 ± 1.4 nm.*

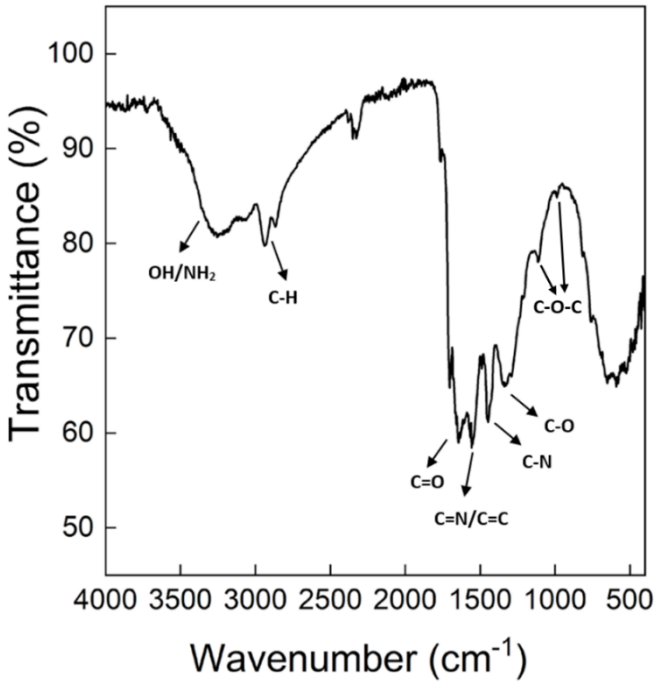

Figure S2.2. *ATR-FTIR spectrum of purified CNDs. According to literature, peak assignation is described as follows: C-O-C bonds (1194, 1111 cm^{-1}), C-O bonds (1350, 1318 cm^{-1}), C=O bonds (1655, 1704, 1767 cm^{-1}), C=N (1557 cm^{-1}), C-N (1492, 1437 cm^{-1}), C-H bonds (2932, 2862 cm^{-1}), O-H/N-H bonds (3300 cm^{-1}).*[1]

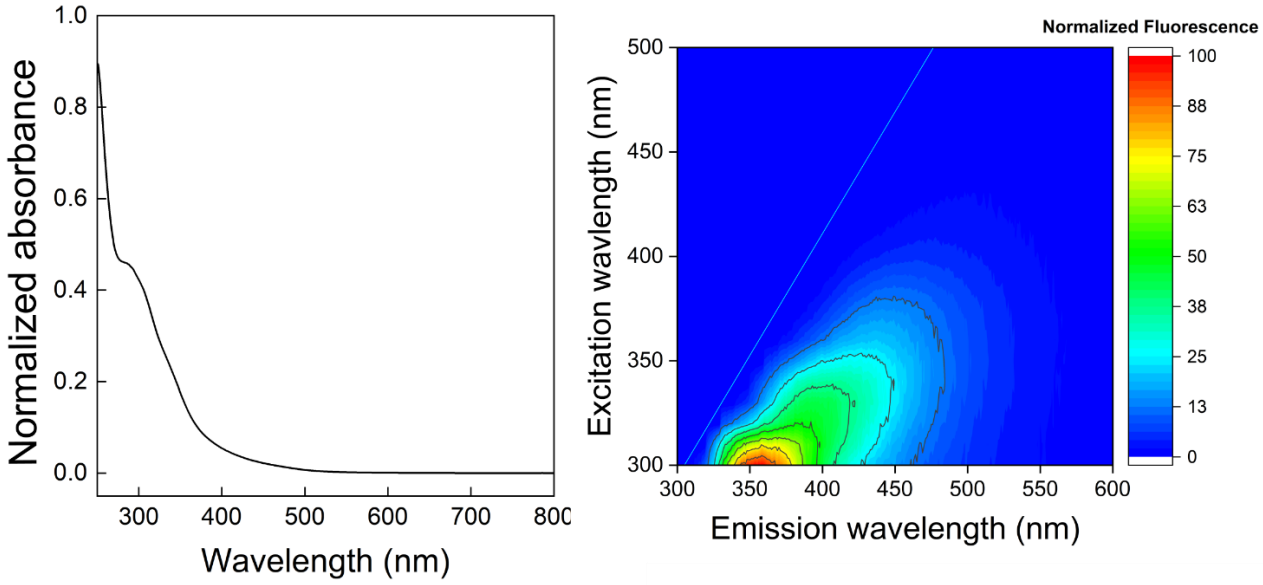

Figure S2.3. *Absorption and emission properties of purified CNDs:* ***a)*** *Normalized UV-Vis spectrum of purified CNDs (1 mg mL^{-1} in MilliQ water);* ***b)*** *Normalized fluorescence emission map of purified CNDs in MilliQ water (sample absorbance at 286 nm (maximum) = 0.1). The shown light blue line limits the region of real values acquired during the experiments.*

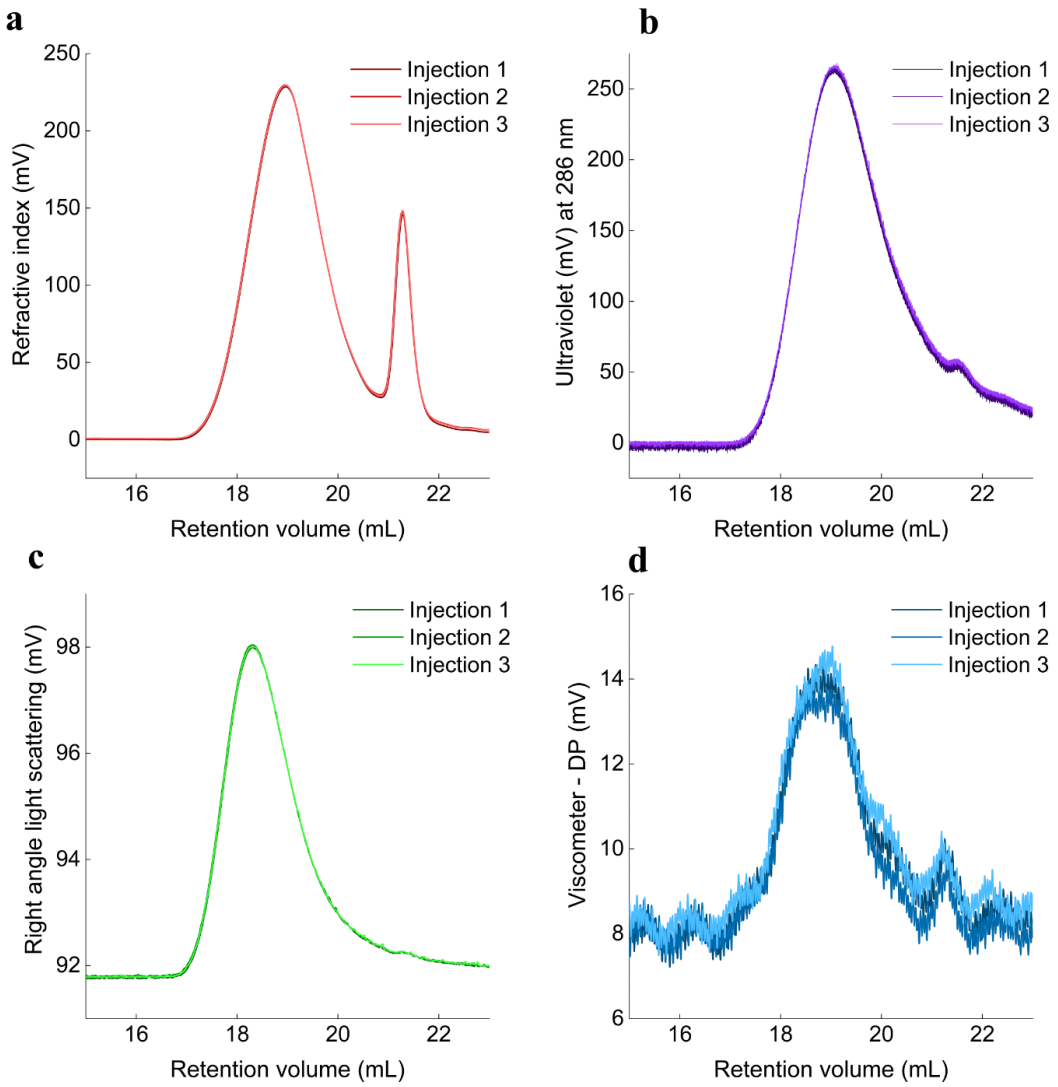

Figure S2.4. *GPC chromatogram overlays of CND for three different injections (0.1M $NaNO_3$ + 0.5 V/V% acetic acid (pH 2.6) on cationic columns):* ***a)*** *refractive index curves (red),* ***b)*** *UV curves (purple),* ***c)*** *right angle light scattering curves (green),* ***d)*** *viscometer (DP) curves (blue).*

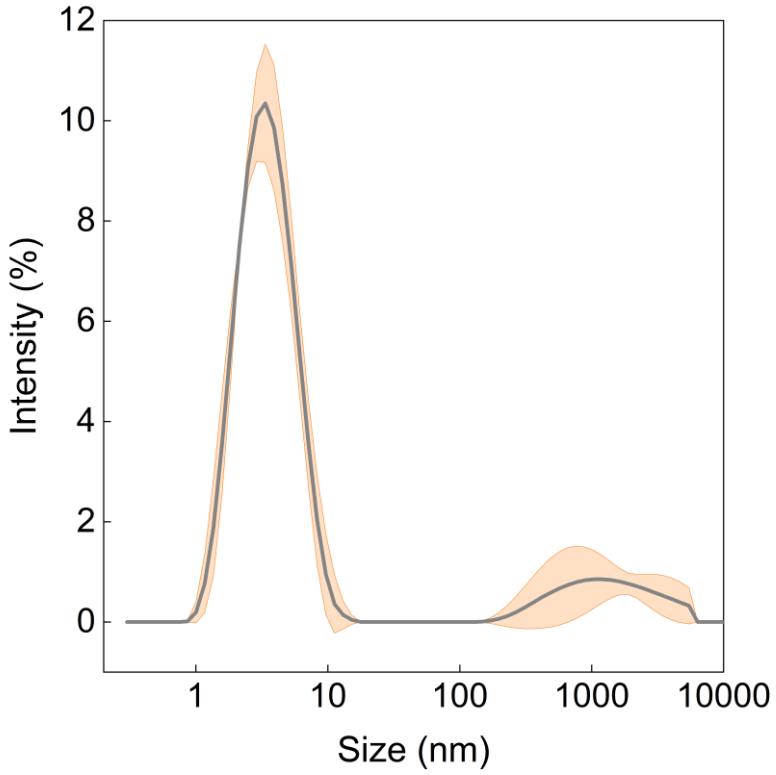

Figure S2.5. *Size distribution by intensity of CNDs (5 mg mL^{-1}, 0.1M $NaNO_3$ + 0.5 V/V% acetic acid (pH 2.6), 4 °C). Some aggregates are visible as a low-intensity band centered at around 1 µm.*

2.5 References

1. Arcudi, F., Đorđević, L. & Prato, M. Synthesis, Separation, and Characterization of Small and Highly Fluorescent Nitrogen-Doped Carbon NanoDots. *Angew. Chem. Int. Ed.* **55**, 2107–2112 (2016).
2. Li, J., Zhao, X. & Gong, X. The Emerging Star of Carbon Luminescent Materials: Exploring the Mysteries of the Nanolight of Carbon Dots for Optoelectronic Applications. *Small* **20**, 2400107 (2024).
3. Bartolomei, B. & Prato, M. The Importance of the Purification Step and the Characterization of the Products in the Synthesis of Carbon Nanodots. *Small* **19**, 2206714 (2023).
4. Qu, D. & Sun, Z. The formation mechanism and fluorophores of carbon dots synthesized via a bottom-up route. *Mater. Chem. Front.* **4**, 400–420 (2020).
5. Rigodanza, F. *et al.* Snapshots into carbon dots formation through a combined spectroscopic approach. *Nat. Commun.* **12**, 2640 (2021).
6. Yu, J., Yong, X., Tang, Z., Yang, B. & Lu, S. Theoretical Understanding of Structure–Property Relationships in Luminescence of Carbon Dots. *J. Phys. Chem. Lett.* **12**, 7671–7687 (2021).
7. Hu, Y., Seivert, O., Tang, Y., Karahan, H. E. & Bianco, A. Carbon Dot Synthesis and Purification: Trends, Challenges and Recommendations. *Angew. Chem. Int. Ed.* e202412341 (2024).
8. Robards, K. & Ryan, D. *Principles and Practice of Modern Chromatographic Methods*. (Academic Press, 2021).
9. Hinterberger, V., Damm, C., Haines, P., Guldi, D. M. & Peukert, W. Purification and structural elucidation of carbon dots by column chromatography. *Nanoscale* **11**, 8464–8474 (2019).
10. Guo, H. *et al.* A universal strategy to separate hydrophilic hybrid-light carbon quantum dots using pure water as eluent. *Appl. Mater. Today* **18**, 100528 (2020).
11. Zhou, Y. *et al.* Size-dependent photocatalytic activity of carbon dots with surface-state determined photoluminescence. *Appl. Catal. B Environ.* **248**, 157–166 (2019).
12. Trubetskaya, O. E. *et al.* High-performance size exclusion chromatography with online fluorescence and multi-wavelength absorbance detection for isolation of high-purity carbon dots fractions, free of non-fluorescent material. *J. Chromatogr. A* **1650**, 462251 (2021).
13. Michaud, V. *et al.* Well-separated water-soluble carbon dots via gradient chromatography. *Nanoscale* **13**, 13116–13128 (2021).
14. Wysocka, A., Waluda, Ł., Konefał, R. & Kasprzyk, W. Liquid chromatography methods as a solution to inaccuracies associated with purity assessment of citric acid-based carbon dots. *Microchem. J.* **205**, 111240 (2024).

15. Essner, J. B., Kist, J. A., Polo-Parada, L. & Baker, G. A. Artifacts and Errors Associated with the Ubiquitous Presence of Fluorescent Impurities in Carbon Nanodots. *Chem. Mater.* **30**, 1878–1887 (2018).
16. Bartolomei, B., Corti, V. & Prato, M. Chiral Carbon Nanodots Can Act as Molecular Catalysts in Chemical and Photochemical Reactions. *Angew. Chem. Int. Ed.* **62**, e202305460 (2023).
17. Carioscia, A. *et al.* Nitrogen-Rich Carbon Dots as Effective Catalysts in the 1,4-Reduction of α,β-Unsaturated Aldehydes via Ion Pair Asymmetric Nano-Organocatalysis. *ACS Catal.* **14**, 13429–13438 (2024).
18. Zhou, Y. *et al.* Direct conjugation of distinct carbon dots as Lego-like building blocks for the assembly of versatile drug nanocarriers. *J. Colloid Interface Sci.* **576**, 412–425 (2020).
19. Đorđević, L., Arcudi, F., Cacioppo, M. & Prato, M. A multifunctional chemical toolbox to engineer carbon dots for biomedical and energy applications. *Nat. Nanotechnol.* **17**, 112–130 (2022).
20. Mintz, K. J. *et al.* A deep investigation into the structure of carbon dots. *Carbon* **173**, 433–447 (2021).
21. Đorđević, L., Arcudi, F., Cacioppo, M. & Prato, M. A multifunctional chemical toolbox to engineer carbon dots for biomedical and energy applications. *Nat. Nanotechnol.* **17**, 112–130 (2022).
22. Chen, B. B., Liu, M. L. & Huang, C. Z. Carbon dot-based composites for catalytic applications. *Green Chem.* **22**, 4034–4054 (2020).
23. Xu, Q. *et al.* Carbon dot/inorganic nanomaterial composites. *J. Mater. Chem. A* **10**, 14709–14731 (2022).
24. Corti, V. *et al.* Amine-Rich Carbon Dots as Novel Nano-Aminocatalytic Platforms in Organic Synthesis. *Eur. J. Org. Chem.* **2022**, e202200879 (2022).
25. Sbacchi, M. *et al.* Shining Light on Carbon Dots: New Opportunities in Photocatalysis. *ChemCatChem* **15**, e202300667 (2023).
26. Lopez-Cantu, D. O. *et al.* Enzyme-mimicking capacities of carbon-dots nanozymes: Properties, catalytic mechanism, and applications – A review. *Int. J. Biol. Macromol.* **194**, 676–687 (2022).
27. Robert, A. & Meunier, B. How to Define a Nanozyme. *ACS Nano* **16**, 6956–6959 (2022).
28. Held, D. & Kilz, P. Size-exclusion chromatography as a useful tool for the assessment of polymer quality and determination of macromolecular properties. *Chem. Teach. Int.* **3**, 77–103 (2021).

29. Runyon, J. R., Barnes, D. E., Rudd, J. F. & Tung, L. H. Multiple detectors for molecular weight and composition analysis of copolymers by gel permeation chromatography. *J. Appl. Polym. Sci.* **13**, 2359–2369 (1969).
30. Monaco, A., Drain, B. & Becer, C. R. Detailed GPC analysis of poly(*N* -isopropylacrylamide) with core cross-linked star architecture. *Polym. Chem.* **12**, 5229–5238 (2021).
31. Markova, N. *et al.* Biophysical Characterization of Viral and Lipid-Based Vectors for Vaccines and Therapeutics with Light Scattering and Calorimetric Techniques. *Vaccines* **10**, 49 (2021).
32. Campalani, C., Causin, V., Selva, M. & Perosa, A. Fish-Waste-Derived Gelatin and Carbon Dots for Biobased UV-Blocking Films. *ACS Appl. Mater. Interfaces* **14**, 35148–35156 (2022).
33. Cardo, L. *et al.* Luminescent Carbon Nanodots Doped with Gadolinium (III): Purification Criteria, Chemical and Biological Characterization of a New Dual Fluorescence/MR Imaging Agent. *Small* **19**, 2206442 (2023).
34. Chen, C.-Y., Tsai, Y.-H. & Chang, C.-W. Evaluation of the dialysis time required for carbon dots by HPLC and the properties of carbon dots after HPLC fractionation. *New J. Chem.* **43**, 6153–6159 (2019).
35. Xiong, Y., Schneider, J., Ushakova, E. V. & Rogach, A. L. Influence of molecular fluorophores on the research field of chemically synthesized carbon dots. *Nano Today* **23**, 124–139 (2018).
36. Bhattacharjee, S. DLS and zeta potential – What they are and what they are not? *J. Controlled Release* **235**, 337–351 (2016).
37. Babick, F. Dynamic light scattering (DLS). in *Characterization of Nanoparticles* 137–172 (Elsevier, 2020).
38. Filippini, G. *et al.* Mapping the Surface Groups of Amine-Rich Carbon Dots Enables Covalent Catalysis in Aqueous Media. *Chem* **6**, 3022–3037 (2020).
39. Bartolomei, B. *et al.* Synthetic Strategies for the Selective Functionalization of Carbon Nanodots Allow Optically Communicating Suprastructures. *Angew. Chem. Int. Ed.* **63**, e202316915 (2024).
40. Cacioppo, M. *et al.* Symmetry-Breaking Charge-Transfer Chromophore Interactions Supported by Carbon Nanodots. *Angew. Chem. Int. Ed.* **59**, 12779–12784 (2020).
41. Gentile, G. *et al.* Tailoring the Chemical Structure of Nitrogen-Doped Carbon Dots for Nano-Aminocatalysis in Aqueous Media. *ChemSusChem* **16**, e202202399 (2023).
42. Jarre, G., Heyer, S., Memmel, E., Meinhardt, T. & Krueger, A. Synthesis of nanodiamond derivatives carrying amino functions and quantification by a modified Kaiser test. *Beilstein J. Org. Chem.* **10**, 2729–2737 (2014).

43. Iannazzo, D. *et al.* Functionalization of multi-walled carbon nanotubes with coumarin derivatives and their biological evaluation. *Org Biomol Chem* **10**, 1025–1031 (2012).

Chapter III – Design and Synthesis of Carbon NanoDot-based Suprastructures

Abstract

This Chapter explores the covalent assembly of Carbon NanoDots (CNDs) to form carbon-based suprastructures, employing click chemistry in particular the Copper(I)-catalyzed azide-alkyne cycloaddition (CuCAAC).

Firstly, we have chosen as a case study blue-emitting CNDs, previously reported in our group.[1] These are post-functionalized with different acyl chlorides, bearing either azide or alkyne moieties, to obtain CNDs soluble in organic solvents – essential to perform the CuAAC reaction. We use different equivalents of acyl chloride with respect to the Kaiser Test (KT) of CNDs to map and quantify their surface functionalities. The final products are characterized by NMR and IR spectroscopy, as well as UV-Vis and fluorescence spectroscopy.

Afterward, we perform the CuCAAC reactions between CNDs and model fluorinated molecules to assess whether the reaction occurred. The successful formation of the click products is confirmed by ^{1}H- and ^{19}F-NMR spectroscopy, and we also quantify the number of fluorinated moieties installed on the material surface.

Leveraging on the obtained surface quantification, we prepare the first building blocks functionalizing blue-emitting CNDs with alkyne moiety. For the second building block, we use green-emitting CNDs, recently reported from our group,[2] functionalizing with an azide moiety. After performing the click reaction, the final product is characterized by ^{1}H-NMR spectroscopy and fluorescence spectroscopy, Atomic Force Microscopy (AFM), and Transmission Electron Microscopy (TEM) to prove the formation of desired suprastructures.

Finally, the photophysical properties of the connected CNDs are investigated, discovering the optical communication between the different nanoparticles.

This project was carried out within the Prato group alongside Dr. Beatrice Bartolomei and Dr. Cristian Rosso, who both conceived the idea and under the supervision of Prof. Maurizio Prato. I have taken care of the molecules and nanomaterials preparation, from the synthesis of acyl chlorides to the synthesis of post-functionalized CNDs, and part of their characterization. TEM characterization was performed by Dr. Kralj (Materials Synthesis Department, Jožef Stefan Institute, Ljubljana), while the group of Prof. Guldi (Friedrich-Alexander Universität Erlangen-Nürnberg, Germany) carried out the photophysical characterizations. A significant part of this work has been published in 2024.[3]

3.1 Introduction

The controlled assembly of molecules and nanoparticles into desired nanoarchitectures is one of the major challenges of nanotechnology.[4] A key aspect of the bottom-up assembly of nanoarchitectures is the control of the surface composition of the building blocks. Therefore, precise control of the functional groups of nanoparticles enables their selective reaction toward the synthesis of complex structures.[5]

This is widely achieved with metallic and inorganic nanoparticles,[6] whereas, according to the state of the art, only limited examples concerning CDs are reported even though they could represent promising and smart starting units. Indeed, CDs are typically defined as having a carbon-based core surrounded by a shell with surface functionalities.[7] In 2006, Sun *et al.* describes the first example of CD post-functionalization reaction attaching simple organic species to CD surface, such as diamine-terminated oligomeric poly(ethylene glycol), highlighting that nanoparticle photoluminescence increases after their passivation.[8]

In the case of CND, their surface reactivity has been widely explored in establishing non-covalent bonds, such as electrostatic interactions, coordinative bonds, and hydrogen bonds with various other molecules and materials.[9,10] On the other hand, covalent derivatization has been used to modify carbon nanoparticle surface by anchoring the desired species.[11] The so-fabricated hybrids might have valuable emerging traits from their constituents, which have repercussions in advancing their applications in scientific fields, such as energy and medicinal science.[12–14] To accomplish this, performing selective functionalization of CNDs is of practical importance, although it is still challenging.

In recent years, our group has developed various nanohybrids by combining nitrogen-rich CNDs, synthesized from *L*-arginine and ethylenediamine, with photo- and electro-active molecules, such as ruthenium(II) tris(2,2′-bipyridyl), porphyrins, and phthalocyanines.[15–19] In all these cases, nitrogen-rich CND-based hybrids have been synthesized by leveraging the amino groups on the CND surface. This strategy is broadly supported by the extensive use of amino functionalities in the design and creation of innovative and smart nanomaterials. Amino groups enable precise tuning of nanomaterial properties, playing a pivotal role in expanding the applicability of CNDs to advanced fields such as optoelectronics, photovoltaics, and medicinal chemistry.[20]

These functional materials aim to create valuable nanohybrids where the integration of unique properties of the combined components opens new possibilities for advanced applications.

An interesting strategy to overcome this limitation is click chemistry. The click methodology has many advantages, such as one-pot reactions, no by-products, and high reaction selectivity.[21] For these reasons, click chemistry has been applied to a myriad of systems, spanning from material

science to biology.[22–26] Specifically, the Cu(I)-catalyzed alkyne-azide cycloaddition (CuAAC) is one of the most studied click transformations, in which an azide reacts with an alkyne to form a 5-membered heteroatom ring (triazole) at room temperature.[27]

In this Chapter, we examine the use of CuAAC reactions on CNDs to selectively bind these materials with probe molecules. Initially, we use a fluorinated tag to quantify the number of anchoring points on the CND surface. Based on these data, we install acyl chlorides bearing either alkyne or azide moieties on the nanomaterials. Thereafter, this general methodology has been extended to connect CNDs of different natures, thus forming unprecedented covalent suprastructures with remarkable molecular control. In particular, we choose two types of CNDs previously developed in our group. CNDs-1 are synthesized starting from *L*-arginine and ethylenediamine, while CNDs-2 are prepared from citric acid and (*S*)-2-(aminomethyl)-1-Boc-pyrrolidine.[1,2] These particles present emission in different regions of the visible spectrum, while they both possess amines and other polar functionalities on the surface, allowing for their post-functionalization. As a result, we were able to build optical communicating suprastructures that might form a basis for the design of advanced interacting architectures.

3.2 Results and Discussion

3.2.1 Post-functionalization of CNDs

CNDs-1 and CNDs-2 had a surface rich in functional groups such as amines, alcohols, and carboxylic acids (**Figure 3.1**, see Experimental Section 3.4.3 Synthesis of CNDs). Based on this, a general post-functionalization reaction might be a coupling with acyl chlorides. Moreover, it was important to identify a tool to probe the number of installed moieties on the material surface after the functionalization. To achieve this, we implemented a fluorine-labeling strategy combined with ^{19}F NMR spectroscopy. Indeed, this sensitive method offered the possibility to study the chemistry of the CND shell without interference from the other NMR signals.[28,29]

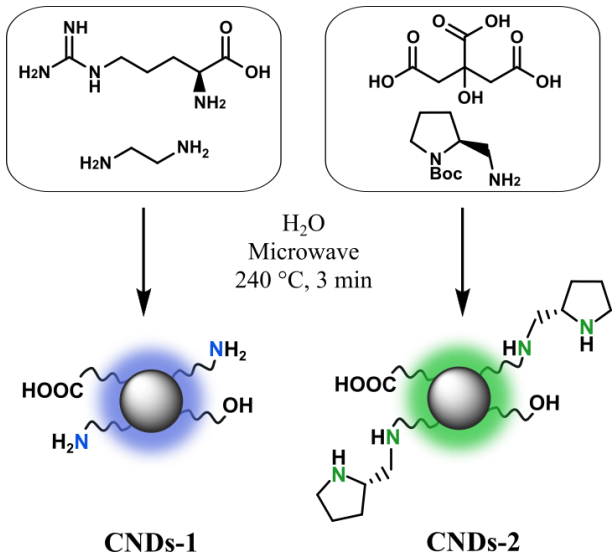

Figure 3.1. *General scheme for the synthesis of CNDs-1 and CNDs-2.*[2,3]

Firstly, we chose to perform this post-functionalization study just on CNDs-1, choosing them as case study. In this regard, the fluorinated molecular probe 12,12,12-trifluorodo-dec-10-ynoic acid (1) has been synthesized (see Experimental section, 3.4.2 Synthesis of acyl chlorides) and subsequently converted into the corresponding acyl chloride (2). The coupling reaction between CNDs-1 and 2, *via* amide bond formation, was carried out in *N,N*-dimethylformamide (DMF) in the presence of triethyl-amine (TEA) as a base, at room temperature (**Figure 3.2a**). The functionalized CNDs-3 resulted to be soluble in organic solvents, such as chloroform. This was an essential and desired feature, to then perform the CuAAC reaction in a biphasic system and facilitate the isolation of the desired product.

Leveraging on their new solubility, the purification of these materials was performed with a chloroform/water extraction, to remove the coupling by-products, followed by a precipitation with

diethyl ether to get rid of the unreacted 2. CNDs-3 were characterized through ^{1}H NMR spectroscopy. The spectrum showed the diagnostic signals associated with the protons close to the carboxyl group at around 2–2.5 ppm, which are more shielded with respect to those corresponding of 2, in agreement with the presence of a less electron-withdrawing group (**Figure 3.2.b** and **c**). Moreover, the peaks associated with the alkyl protons at around 1–1.5 ppm experienced a broadening due to the proximity to the CND surface, as expected.[30]

Finally, ^{19}F NMR spectroscopy was performed to further confirm the functionalization of CNDs-1. **Figure 3.2.b** and c insets displayed that both the CNDs-3 sample and the starting material 2 exhibited a signal at -49 ppm. This specific NMR peak can indicate the quantity of fluorinated sites installed on CNDs-3, by using an internal standard (trifluoro toluene). Consequently, the obtained value of 1450 µmol g^{-1} is consistent with previous findings.[1,29]

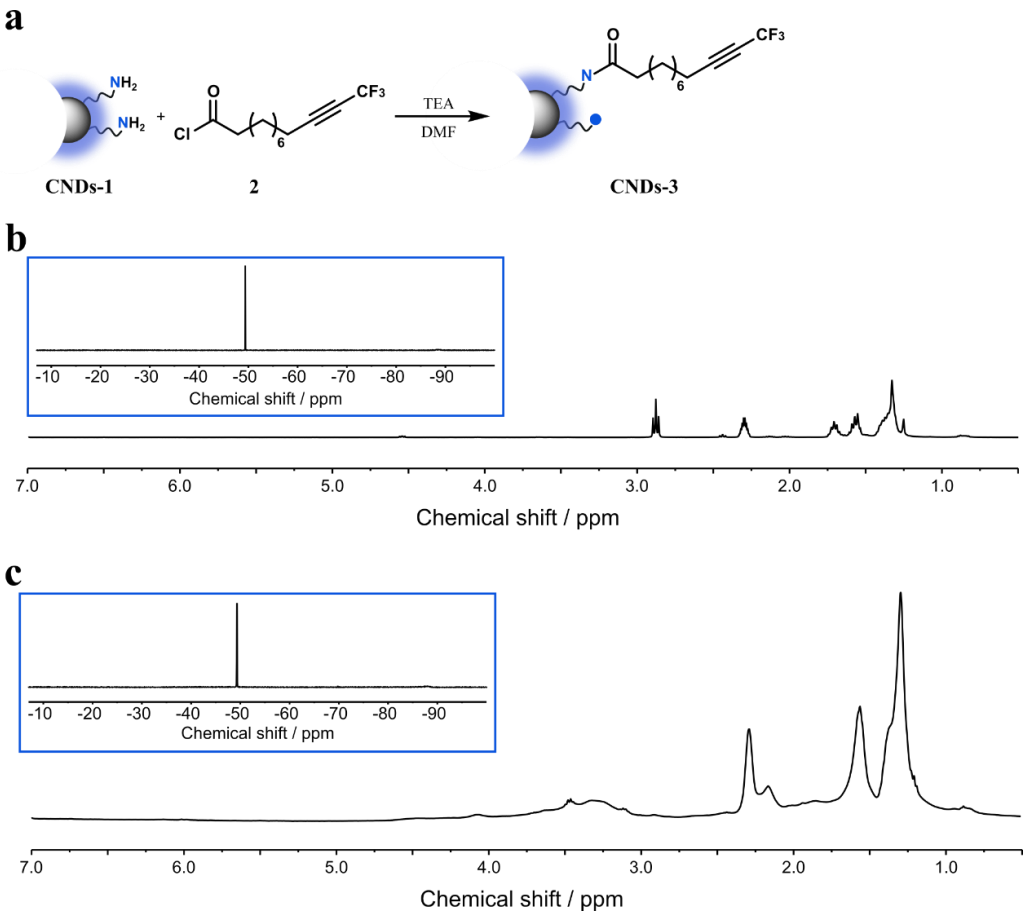

Figure 3.2. a) *General scheme for the coupling between CNDs-1 and acyl chloride 2. The colored labels correspond to the depicted functionalities. Conditions: CNDs-1 (25 mg), 2 (0.34 mmol), TEA (0.34 mmol), DMF (4 mL);* ***b)*** *^{1}H NMR of 2 in deuterated chloroform referenced against solvent residual peak (δH: 7.26 ppm) (400 MHz, r.T), inset ^{19}F NMR ($CDCl_3$, 376 MHz, r.T);* ***c)*** *^{1}H NMR of CNDs-3 in deuterated chloroform referenced against solvent residual peak (δH: 7.26 ppm) (400 MHz, r.T), inset ^{19}F NMR ($CDCl_3$, 376 MHz, r.T).*

To prove the generality of our approach, the same protocol was applied to CNDs-2. This yielded the functionalized nanomaterials CNDs-4 (see Experimental Section, 3.44 Post-functionalization of CNDs with acyl chlorides), with 320 µmol g^{-1} of fluorinated superficial moieties, corresponding to the quantification of available superficial amines previously reported (**Figure 3.3**).[2]

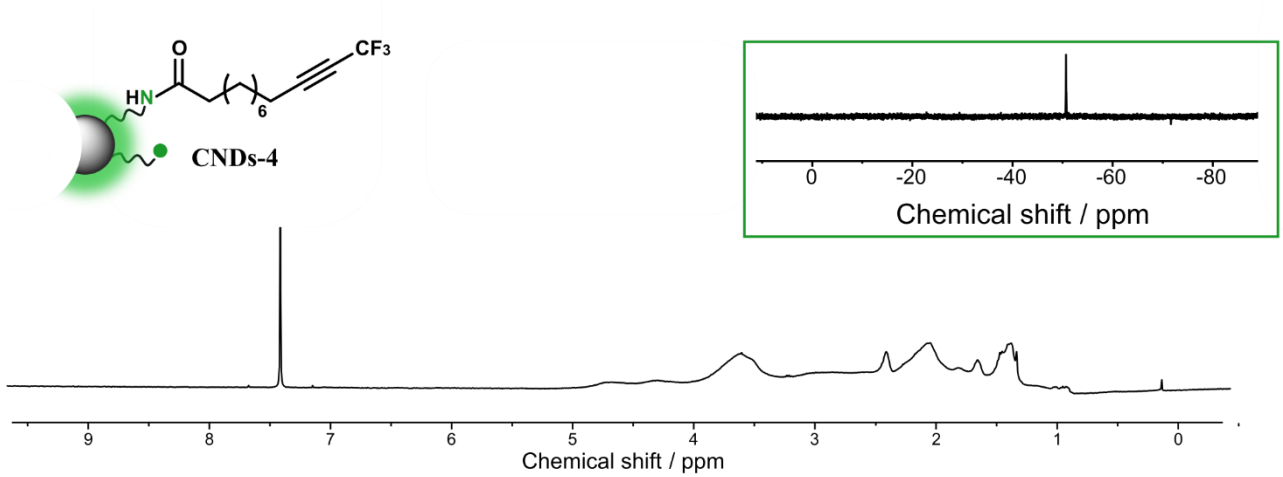

Figure 3.3. *^{1}H NMR of CNDs-4 in deuterated chloroform referenced against solvent residual peak (δH: 7.26 ppm) (400 MHz, r.T), inset ^{19}F NMR ($CDCl_3$, 376 MHz, r.T).*

Afterwards, we demonstrated that the quantity of fluorinated moieties functionalizing the CND surface could be controlled. Hence, we repeated the reaction on CNDs-1 employing lower amounts of 2 and saturating the remaining functionalities with octanoyl chloride to ensure the solubility in organic solvents (see Experimental Section, 3.4.4 Post-functionalization of CNDs with Acyl Chlorides).

The quantification by ^{19}F NMR spectroscopy of the corresponding products provided the trend reported in **Figure 3.4**. This outcome demonstrated the CND surface coverage could be finely tuned by simply changing the stoichiometry of the used reactant.

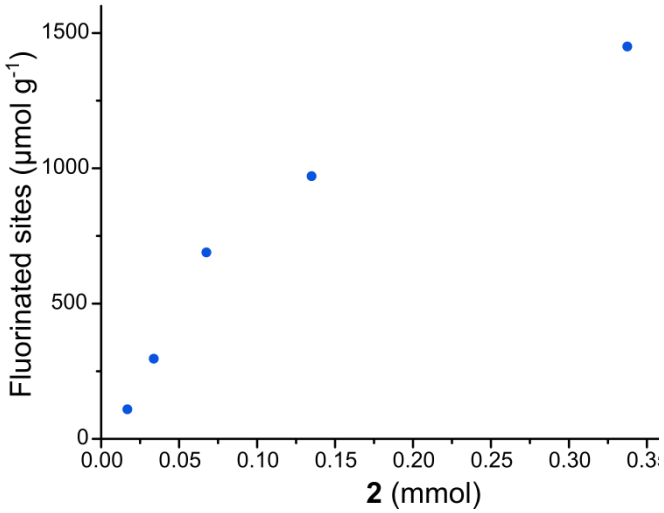

Figure 3.4. *Number of fluorinated sites installed on CNDs-1 after reaction with increasing amounts of 2 (0.02 – 0.14 mmol) followed by saturation with octanoyl chloride (0.34 mmol) and TEA (0.34 mmol).*

3.2.2 Mapping of CND Surface Functionalities

Knowing that we could precisely functionalize the CND surface and probe the quantity of installed moieties as well, we moved to a specific CND derivatization to perform click reactions between carbon-based nanoparticles.

Initially, we functionalized CNDs-1 with an acyl chloride bearing a terminal alkyne, namely 11-(prop-2-yn-1-yloxy) undecanoyl chloride (3), (see Experimental Section, 3.4.2 Synthesis of acyl chlorides), by employing the previously described conditions (0.34 mmol of 3, corresponding to the last point of trend showed in **Figure 3.4**) to saturate CNDs-1 surface.

The so-synthetized CNDs-5 (see Experimental Section, 3.4.4 Post-functionalization of CNDs with acyl chlorides) was left to react with a model fluorinated azide, 1-(azidomethyl)-3,5-bis(trifluoromethyl)benzene (4), to deliver CNDs-6 (**Figure 3.5.a**). This click reaction was carried out in a biphasic system (chloroform/MilliQ water, 1:1 V/V) using $CuSO_4$ as catalyst and sodium ascorbate (NaAsc) as reducing agent (see Experimental Section, 3.4.5 Click reactions between CNDs and fluorinated molecules).[31]

As can be seen in **Figure 3.5.b**, CNDs-5 (see Experimental Section, 3.4.4 Post-functionalization of CNDs with acyl chlorides) displayed the ^{1}H NMR diagnostic alkyne signal at around 2.4 ppm, along with the α-oxo protons at 4.1 and 3.5 ppm. By observing the ^{1}H NMR spectrum of product CNDs-6 instead, it was notable that the presence of the triazole signal at 7.6 ppm and the absence of the signal related to the terminal alkyne of CNDs-5 (**Figure 3.5.d**). Furthermore, the deshielding

of the protons adjacent to the heterocyclic system was evident, by comparing the CNDs-6 ^{1}H NMR spectrum with the one of the fluorinated azide molecule (**Figure 3.5.c**). In the same fashion, an intense ^{19}F NMR peak at around -63 ppm confirmed the success of the reaction (**Figure 3.5.c** and **d** insets).

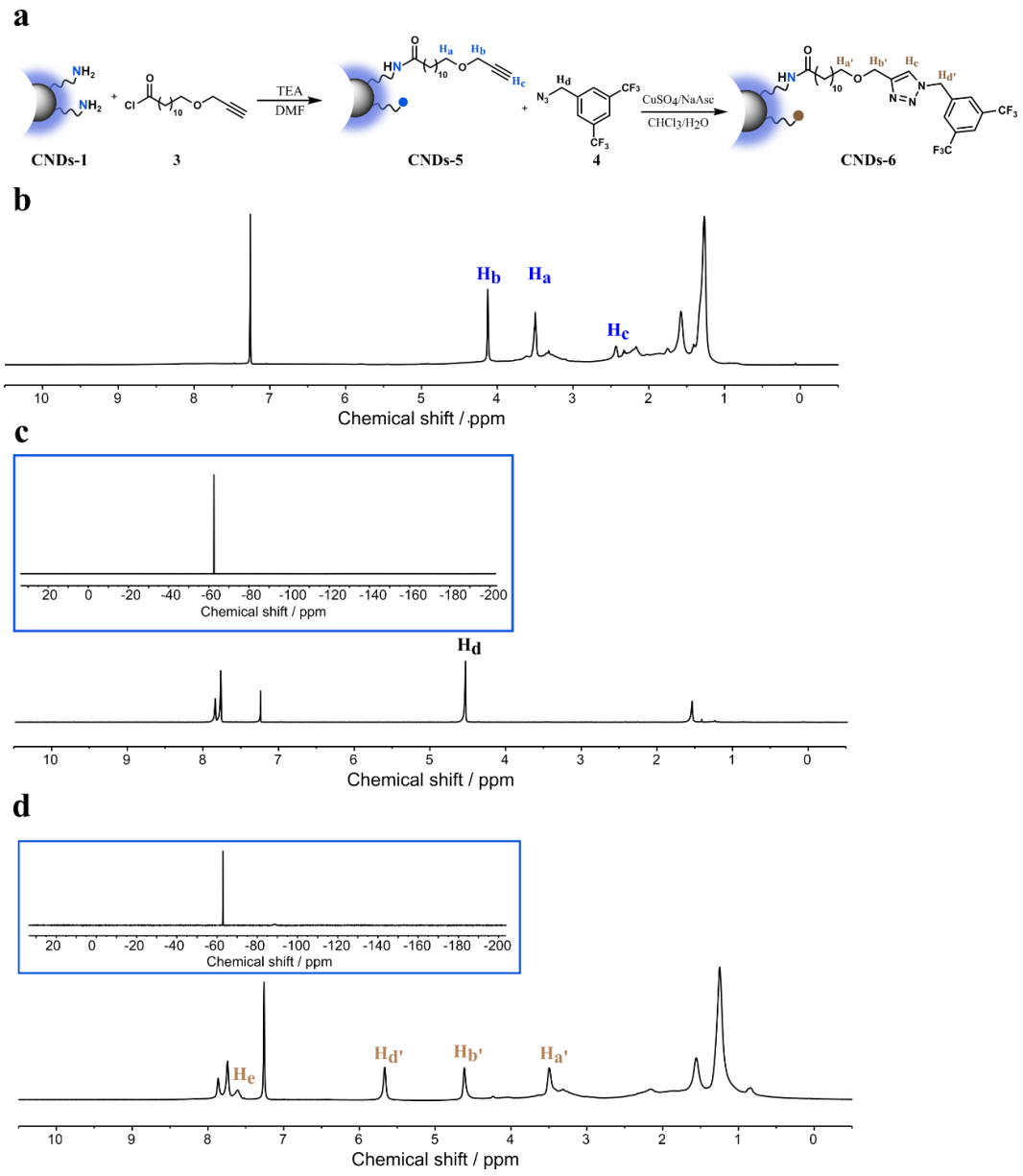

Figure 3.5. a) *General scheme for the click reaction between CNDs-1 with 3 and following click reaction between formed CNDs-5 and fluorinated azide 4. The colored labels correspond to the depicted functionalities. Conditions: CNDs-1 (25 mg), 2 (0.34 mmol), TEA (0.34 mmol), DMF (4 mL); CNDs-5 (15 mg), 4 (0.2 mmol), $CuSO_4 \cdot 5H_2O$ (0.02 mmol), NaAsc (0.04 mmol), $CHCl_3$ (1 mL), H_2O (1 mL), 24 h;* ***b)*** *^{1}H NMR of CNDs-5 in deuterated chloroform referenced against solvent residual peak (δH: 7.26 ppm) (400 MHz, r.T);* ***c)*** *^{1}H NMR of 4 in deuterated chloroform referenced against solvent residual peak (δH: 7.26 ppm) (400 MHz, r.T), inset ^{19}F NMR ($CDCl_3$, 376 MHz,*

r.T); ***d)*** *^{1}H NMR of CNDs-6 in deuterated chloroform referenced against solvent residual peak (δH: 7.26 ppm) (400 MHz, r.T), inset ^{19}F NMR ($CDCl_3$, 376 MHz, r.T).*

At the same time, we functionalized CNDs-2 with an azide moiety using 11-azidoundecanoyl chloride (5), hence obtaining CNDs-7 (**Figure 3.6.a**). These presented the key ^{1}H NMR signal at around 3.2 ppm related to the protons in alpha to the azide since it perfectly corresponded to the signal of the analogous molecule (**Figure 3.6.b** and **c**). Additionally, the presence of azide functionality was further assessed by FT-IR spectroscopy, which showed the typical N=N=N stretching peak at about 2100 cm^{-1}, absent in CNDs-2 (**Figure 3.7**).

In the case of CNDs-7, the CuCAAC reaction with a model molecular alkyne, 1-((prop-2-yn-1-yloxy)methyl)-3,5-bis(trifluoromethyl)benzene (6), provided the corresponding adduct (**Figure 3.7.a**). NMR spectroscopy proved the successful formation of the click reaction product CNDs-8. In particular, we could observe the triazole protons in its ^{1}H spectrum and the fluorine signal at -63 ppm in its ^{19}F NMR spectrum (**Figure 3.7.d** and **inset**).

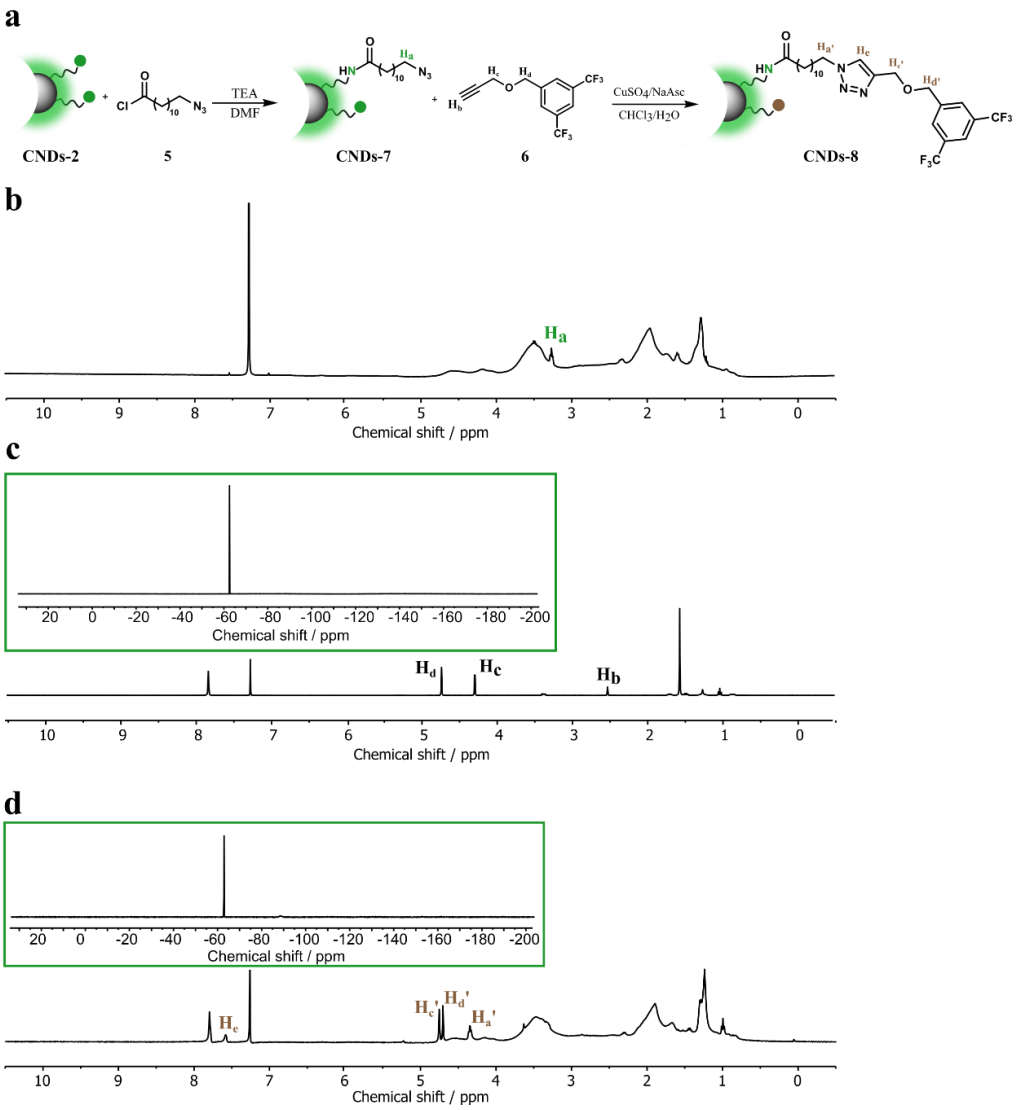

Figure 3.6. a) *General scheme for the click reaction between CNDs-2 with 5 and following click reaction between formed CNDs-7 and fluorinated alkyne 6. The colored labels correspond to the depicted functionalities. Conditions: CNDs-2 (25 mg), 5 (0.08 mmol), TEA (0.08 mmol), DMF (4 mL); CNDs-7 (15 mg), 6 (0.05 mmol), $CuSO_4 \cdot 5H_2O$ (0.05 mmol), NaAsc (0.01 mmol), $CHCl_3$ (1 mL), H_2O (1 mL), 24 h;* ***b)*** *^1H NMR of CNDs-7 in deuterated chloroform referenced against solvent residual peak (δH: 7.26 ppm) (400 MHz, r.T);* ***c)*** *^1H NMR of 6 in deuterated chloroform referenced against solvent residual peak (δH: 7.26 ppm) (400 MHz, r.T), inset ^{19}F NMR ($CDCl_3$, 376 MHz, r.T);* ***d)*** *^1H NMR of CNDs-8 in deuterated chloroform referenced against solvent residual peak (δH: 7.26 ppm) (400 MHz, r.T), inset ^{19}F NMR ($CDCl_3$, 376 MHz, r.T).*

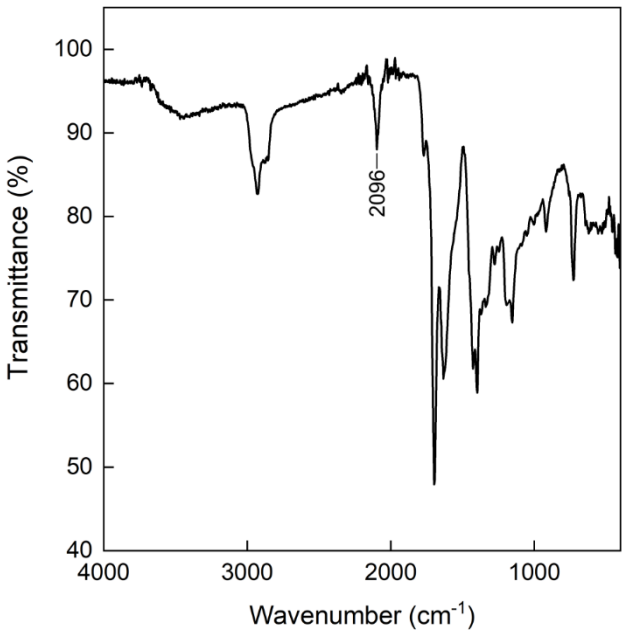

Figure 3.7. *ATR-FTIR spectrum of CNDs-7. Azide (N=N=N) stretching band is visible at 2096 cm^{-1}.*

These results confirmed once more the development of a general methodology to functionalize CNDs by click chemistry, leading the way to couple these particles with desired species through high selectivity and control.

3.2.3 Assembly of Covalently Linked Suprastructures *via* Click Chemistry

After having performed a click reaction between CNDs and molecular species, we passed to build CND suprastructures by performing a click reaction between the two complementary CNDs, namely CNDs-5 and CNDs-7.

The previously performed quantifications allowed us to have remarkable control over the reaction stoichiometry. In particular, the alkyne-bearing CNDs (CNDs-5) were employed in slight excess with respect to the azide counterpart (1.5 equiv.) to ensure a complete formation of the desired product. The final nanomaterial CNDs-9 was isolated after size exclusion chromatography (SEC, **Figure 3.8.a**, see Experimental Section, 3.4.6 Click reactions between CNDs).

^{1}H NMR spectroscopy clearly showed the successful interconnection of the two different CNDs through the typical triazole signal at around 7.5 ppm along with the signals of the methylene groups next to the triazole, at 4.6 and 4.3 ppm, respectively (**Figure 3.8.b**).

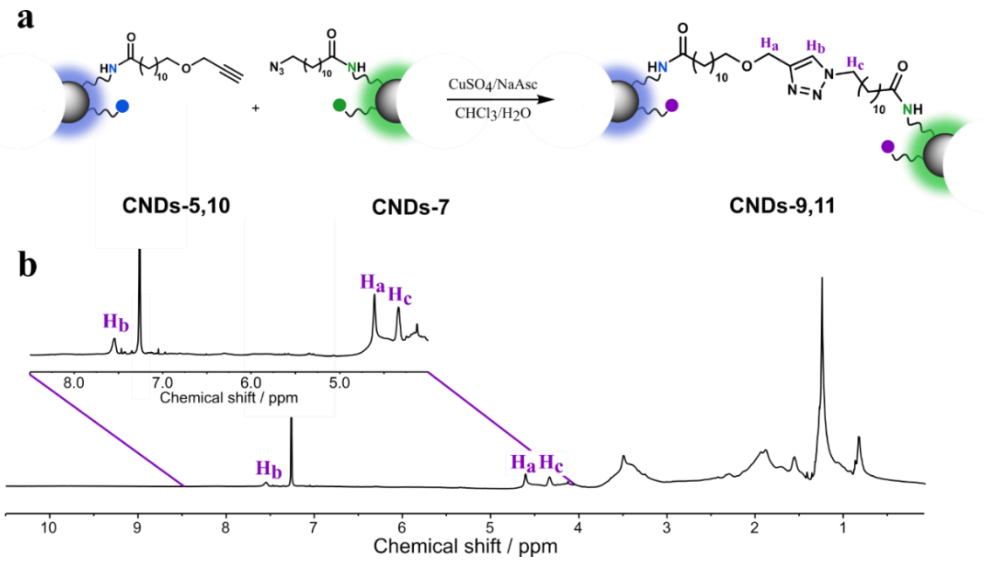

Figure 3.8. a) *General scheme for the click reaction between CNDs-5 and CNDs-7. The colored labels correspond to the depicted functionalities. Conditions: CNDs-5 (5 mg), CNDs-7 (15 mg), $CuSO_4 \cdot 5H_2O$ (0.005 mmol), NaAsc (0.01 mmol), $CHCl_3$ (1 mL), H_2O (1 mL), 24 h.* ***b)*** *^1H NMR of CNDs-9 in deuterated chloroform referenced against solvent residual peak (δH: 7.26 ppm) (400 MHz, r.T, inset of the 8.5 – 4 ppm region).*

Transmission electron microscopy (TEM) of CNDs-9 (**Figure 3.9.a** and **b**) shows the presence of larger structures compared to the dimensions of both CNDs-5 and CNDs-7 (**Figure 3.9.c-f**). Moreover, we could observe the presence of single dots inside the suprastructure in **Figure 3.9.b**.

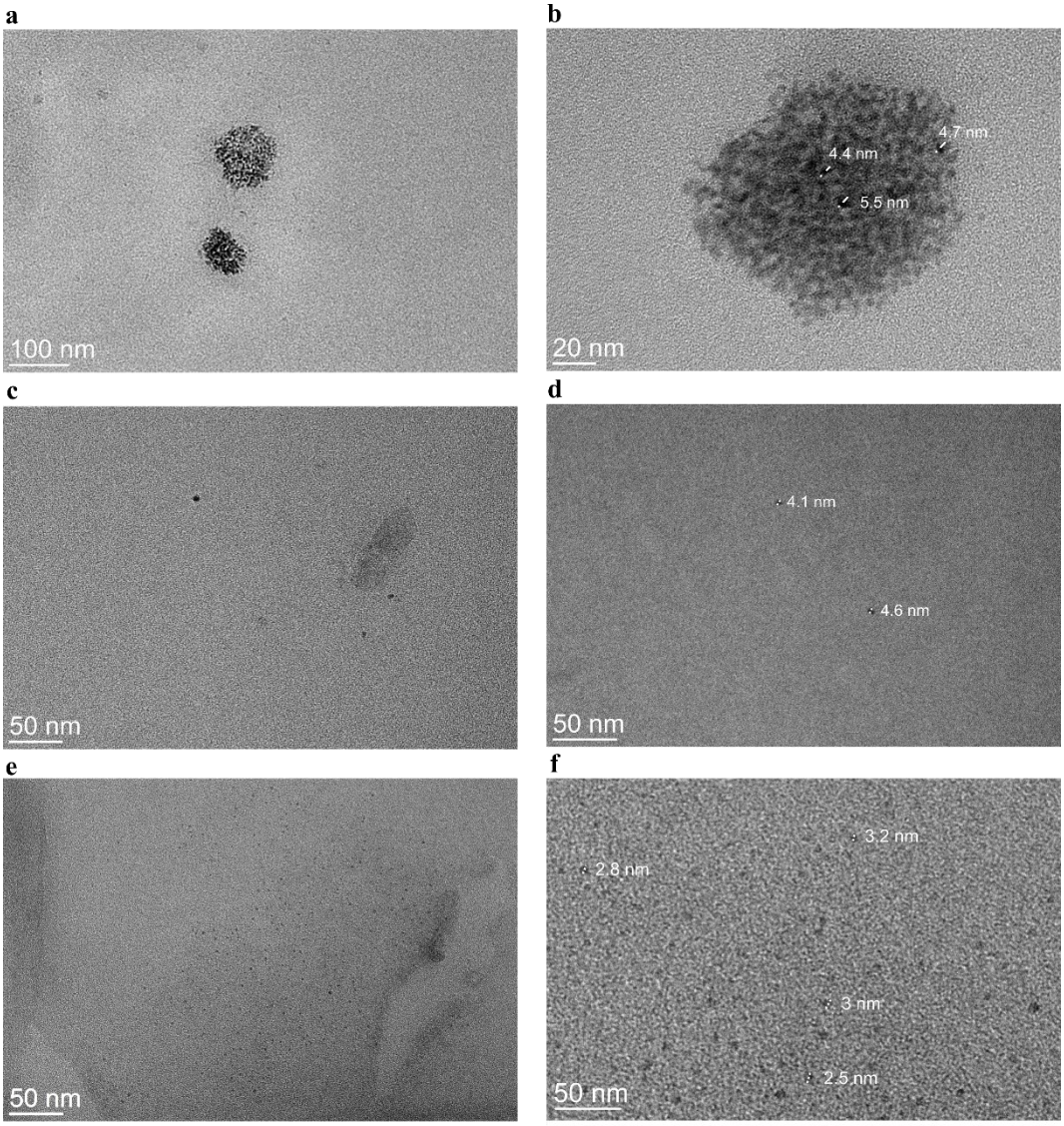

Figure 3.9. *TEM images of* ***a,b)*** *CNDs-9,* ***c,d)*** *CNDs-5, and* ***e,f)*** *CNDs-7.*

Leveraging on CND surface functionalities quantification that we previously carried out, we decided to fine-tune the morphology of the final structure by decreasing the quantity of installed alkyne moieties on CNDs-1. Based on this, we prepared CNDs-10 starting from CNDs-1 and a lower amount of 3 (0.07 mmol, corresponding to the third point of trend reported in **Figure 3.3**, see Experimental Section, 3.4.6 Click reactions between CNDs). By letting CNDs-10 and CNDs-7 undergo click reaction, we obtained CNDs-11 suprastructure (**Figure 3.8.a**). Compared to the previous case, TEM images (**Figure 3.10**) revealed smaller and less crowded structures, in agreement with a reduced number of reactive functionalities present on CNDs-10 compared to CNDs-5.

This finding demonstrated the potential to vary the final suprastructure arrangement by tuning the quantity of reactive functionalities bonded to the nanoparticles.

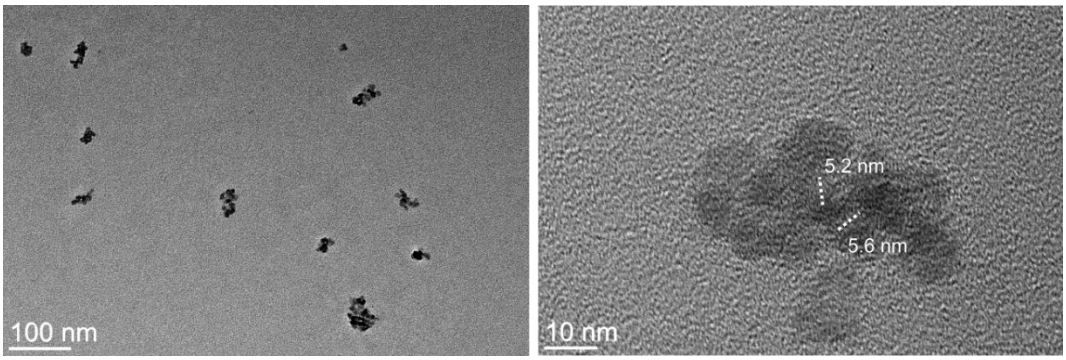

Figure 3.10. *TEM images of CNDs-11.*

3.2.4 Photophysical Studies on Covalent Suprastructures

The distinct photophysical properties of the connected CNDs offer an opportunity to explore their excited state behavior and interactions. Specifically, the ground-state electronic properties of the CNDs-11 and its individual fragments, CNDs-10 and CNDs-7, were analyzed using absorption spectroscopy. CNDs-10 in DMF exhibits absorption features in the UV region without defined maxima, with a tail extending into the visible region up to about 500 nm. CNDs-7 similarly shows broad absorptions, along with a distinct peak at 335 nm (**Figure 3.11**), commonly attributed to n-π* transitions from nitrogen-rich surface or fluorophore states.[11] In CNDs-11, this 335 nm peak broadens, indicating the presence of the CNDs-7 fragment and suggesting ground-state electronic interactions between CNDs-10 and CNDs-7 following the click reaction.

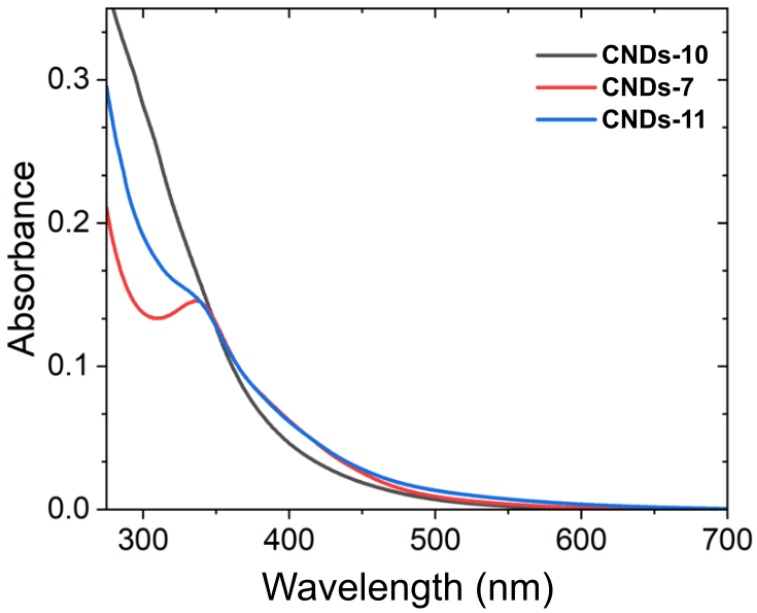

Figure 3.11. *Absorption spectra comparison of CNDs-10, CNDs-7, and CNDs-11, at the same concentration, in DMF.*

Photoluminescence (PL) excitation-emission mapping was used to investigate the excited-state electronic interactions in CNDs-11 (**Figure 3.12.a-c**). PL emission from CNDs-10, CNDs-7, and CNDs-11 was found to be excitation-dependent, which usually either points to the intrinsic variability of CNDs within the ensemble or indicates the existence of several emissive states.[1,2,11,32–34]

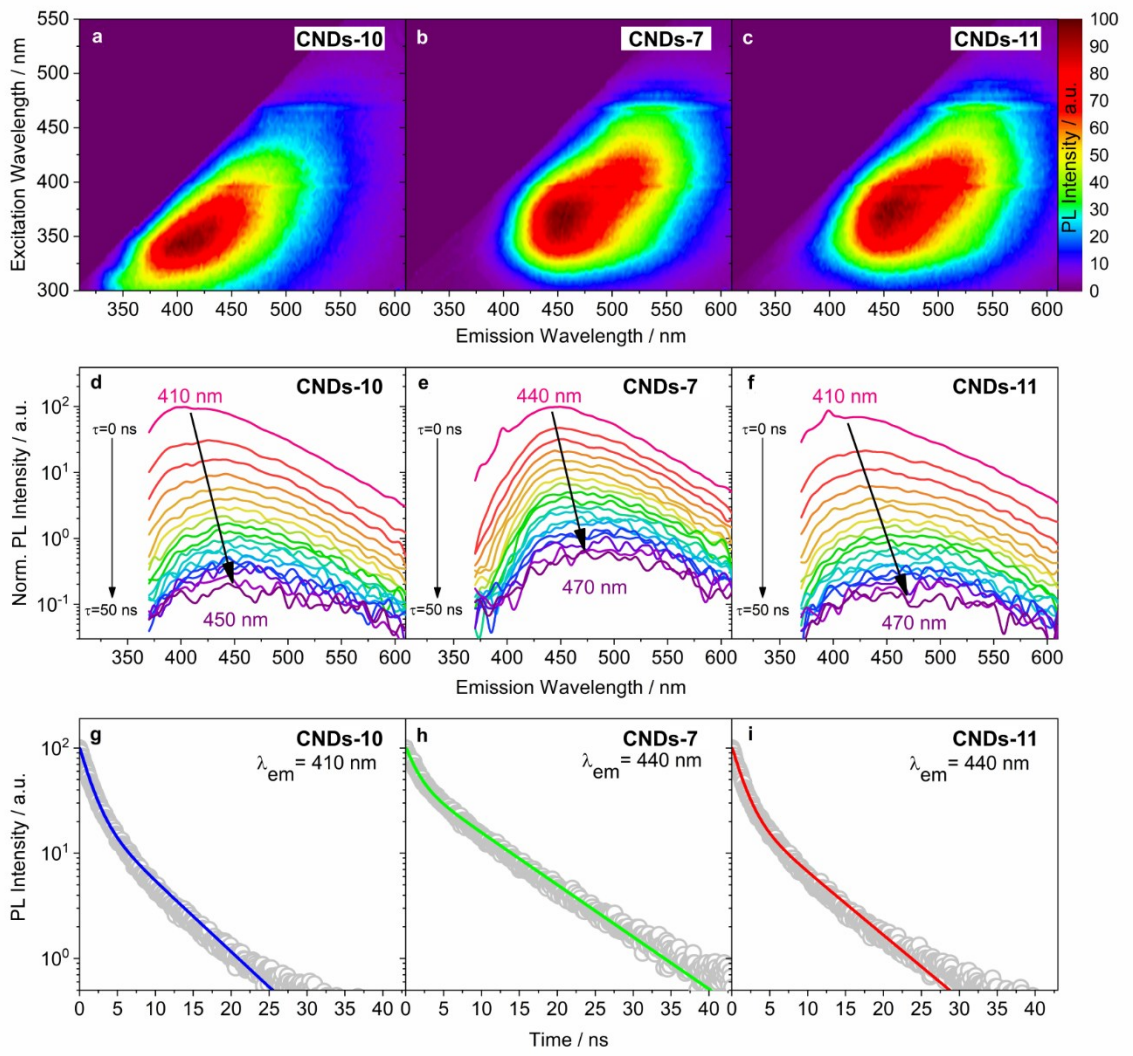

Figure 3.12. *Steady-state and time-resolved PL of CNDs-10, CNDs-7, and CNDs-11 in DMF.* ***a–c)*** *Excitation-emission color maps of CNDs-10, CNDs-7, and CNDs-11,* ***d-f)*** *Time-resolved emission spectra of CNDs-10, CNDs-7, and CNDs-11 measured under the same conditions as in the steady-state experiments under 355 nm excitation,* ***g-i)*** *Biexponential fitting of TRES data at different wavelengths resulting from global analysis.*

CNDs-10 in DMF exhibited a PL emission maximum at 410 nm when excited at 340 nm (**Figure 3.12.a**), while CNDs-7 showed a red-shifted emission with maxima at 365 nm for excitation and

450 nm for emission (**Figure 3.12.b**). Moreover, PL behavior of CNDs-11 closely resembled that of CNDs-7 (**Figure 3.12.c**). As a result, all of them expressed their absorption features in the same energy range, however, CNDs-7 had lower-energy PL active states compared to CNDs-10. In CNDs-11, CNDs-7-like low-energy PL emission dominates, suggesting an energy transfer from CNDs-10 to CNDs-7. The PL quantum yields (QY) were measured using the absolute method using an integrating sphere following photo-excitation at 350 nm, and the results were 5.0%, 10.3%, and 4.9% for CNDs-10, CNDs-7, and CNDs-11, respectively.

Then, time-resolved emission spectroscopy (TRES) was employed to study the PL emission dynamics of CNDs-10, CNDs-7, and CNDs-11 on the nanosecond timescale (**Figure 3.12.d-f**). Upon 355 nm excitation, CNDs-10 and CNDs-7 both exhibited time-dependent spectral shifts, from 410 to 450 nm for CNDs-10 and from 440 to 470 nm for CNDs-7 (**Figure 3.12.d** and **e**). CNDs-11 showed the most pronounced spectral transition from 410 to 470 nm, further supporting the hypothesis of energy transfer from high-energy-emitting CNDs-10 to low-energy-emitting CNDs-7 (**Figure 3.12.f**). Due to the complex nature of the CND photoluminescence, as indicated by excitation-dependent emission, a biexponential fitting was required. **Figure 3.12.g-i** showed the biexponential fitting of the data yielding lifetimes of 2.0 and 8.0 ns for CNDs-10, 2.4 and 9.9 ns for CNDs-7, and 1.4 and 7.1 ns for CNDs-11, suggesting additional decay pathways and significant excited-state interactions in CNDs-11. The rate constant for the 2.0 ns component of CNDs-10 increased from 5.0×10^{8} s^{-1} to 6.9×10^{8} s^{-1} in CNDs-11, corresponding to an energy transfer rate of 1.9×10^{8} s^{-1}.

Picosecond excited-state dynamics were studied using femtosecond transient absorption spectroscopy (fsTAS) with 390 nm excitation. CNDs-10, CNDs-7, and CNDs-11 yielded similar differential spectra, that is, excited state absorption (ESA) across the entire visible range next to ground state bleaching (GSB) and stimulated emission (SE) around 400 nm. Global analysis of the data was performed based on three exponential functions in each case (**Figure S3.1-3**). Two of them correspond to those nanosecond processes seen in the TRES measurements. Therefore, their lifetimes were fixed during the global analysis. The remaining lifetime was 60, 49, and 23 ps for CNDs-10, CNDs-7, and CNDs-11, respectively. The differential spectra associated with these picosecond lifetimes are similar for CNDs-10 and CNDs-11, with ESAs above 410 nm. CNDs-7 shows ESAs that maximize at 440 and 575 nm. This indicates that the initially populated excited state in the CNDs-11 suprastructure is centered on the CNDs-10 fragment. The underlying decay rate constant in the CNDs-11 is 4.4×10^{10} s^{-1}, higher than the $1.7\text{x}10^{10}$ s^{-1} seen in CNDs-10. This indicates an additional reactive channel, *i.e.*, an energy transfer from high-energy CNDs-10

centered excited states to low-energy CNDs-7 centered excited states, with a rate constant of $2.7x10^{10}$ s^{-1}.

The Jablonski diagram of the excited state processes in CNDs-10 and CNDs-7, as well as in CNDs-11, is summarized in **Figure 3.13**.

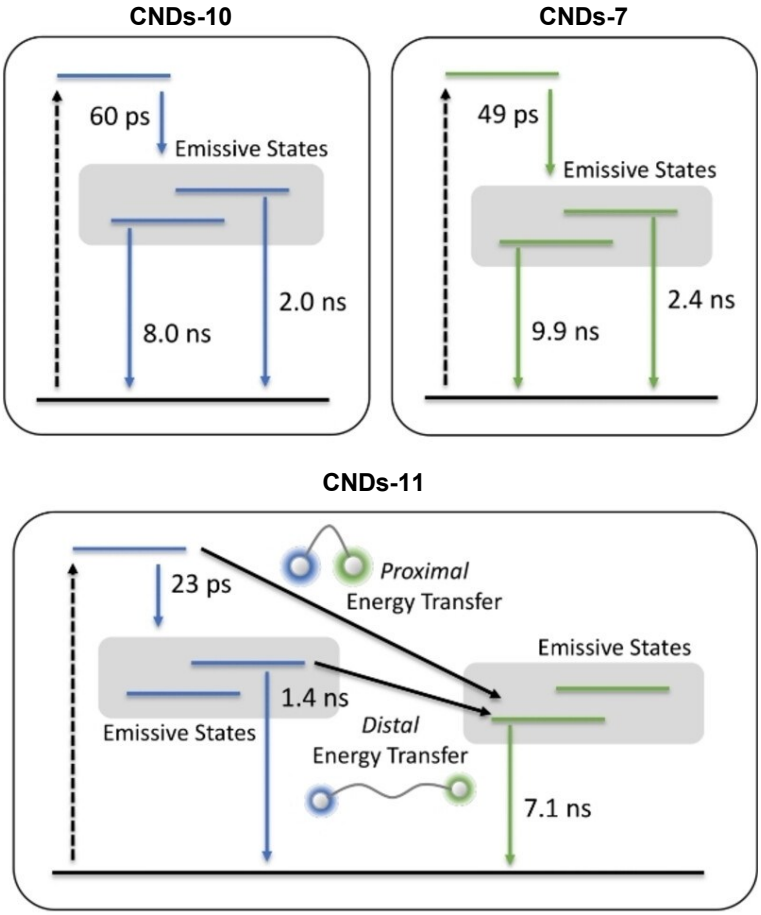

Figure 3.13. *Jablonski diagrams for CNDs-10, CNDs-7, and CNDs-11 showing energy transfers in proximal and distal conformations.*

Energy transfer on different timescales in the CNDs-11 suprastructures have two different energy transfer active configurations, arising from the flexible nature of the linker. First, a proximal configuration between the energy-donating CNDs-10 and the energy-accepting CNDs-7 results in an energy transfer in the picosecond regime, like that seen in electron donor-acceptor systems featuring short linkers.[35,36] On the other hand, a distal separation slows down the energy transfer into the nanosecond regime. This is a common feature in the long-range or bimolecular electron donor-acceptor reactivity.[37–39] It is not possible to rule out the population of additional emissive or non-emissive excited states in CNDs-10, CNDs-7, and CNDs-11, however, our model captures the

essential characteristics of their photophysics. In fact, TRES and TAS fittings improve only marginally upon consideration of more sophisticated models including additional decay channels.

3.3 Conclusions

To summarize, we investigated CNDs as versatile building blocks due to their unique characteristics that bridge the molecular and nanoscale domains. To begin, we quantified the reactive surface functionalities using a fluorine-labeling method combined with ^{19}F NMR spectroscopy. We then employed click chemistry to selectively couple CNDs to target probe molecules, extending this strategy to connect different types of CNDs and produce novel covalent suprastructures with precise molecular control.

The distinct photophysical properties of these interconnected CNDs provided a basis for studying their excited-state behavior and interactions. Specifically, investigations of alkyne- and azide-functionalized CNDs revealed unique UV-Vis absorption and excitation-dependent emissions. Within these covalently linked suprastructures, we observed optical communication between different particle types: high-energy, alkyne-functionalized particles facilitated energy transfer toward low-energy, azide-functionalized particle acceptors through two reaction channels, each with unique timescales influenced by bridge conformation.

As future outlooks, precise molecular weight information for the different CND types could enable even more refined designs of the suprastructures. Additionally, introducing rigid moieties onto CND surfaces may provide greater control over assembly directionality, paving the way for constructing advanced architectures.

This work aims to establish a new direction in the CND field by promoting the development of novel covalent assemblies based on carbon nanoparticles. For instance, by controlling the concentration of reactive functionalities on CNDs, we unlocked the potential to design nanoscale architectures with specialized shapes and properties.

3.4 Experimental Section

3.4.1 Materials and Methods

Commercial reagents, solvents, Sephadex LH20 were purchased from Sigma-Aldrich, Fluorochem, or VWR and used without further purification, unless otherwise stated. Dialysis tubes with molecular weight cut-off of 0.5-1 kDa were bought from Spectrum Labs. MilliQ water was obtained from a Millipore Milli-Q Plus 185 apparatus and presented a resistivity of 18.2 MΩ cm. MilliQ water was always used unless otherwise specified. Chromatographic purification of products was performed using flash chromatography on silica gel (SiO_2, 0.04-0.063 mm, 60 Å) purchased from Machery-Nagel, with the indicated solvent system according to the standard techniques or using a Biotage Isolera automated flash chromatography system with cartridges packed with silica (SiO_2, 0.04-0.063 mm, 60 Å). Thin-layer chromatography (TLC) analysis was performed on precoated Merck TLC plates (silica gel 60 GF254, 0.25 mm). Visualization of the developed chromatography was performed by checking UV absorbance (254 nm) as well as with potassium permanganate stain solution. Organic solutions were concentrated under reduced pressure on a Büchi rotary evaporator.

Microwave-assisted syntheses were performed on a CEM Discover-SP, using 10 mL glass microwave vials.

^{1}H and ^{13}C NMR spectra were obtained on Varian Inova spectrometer (^{1}H: 500 MHz, ^{13}C: 126 MHz) or Varian 400 MHz spectrometer (^{1}H: 400 MHz, ^{19}F: 376 MHz, ^{13}C: 101 MHz). Chemical shifts were reported in ppm using the solvent residual signal as an internal reference ($CDCl_3$: δH = 7.26 ppm, δC = 77.16 ppm). Coupling constants (J) were given in Hz and were averaged. Resonance multiplicity was described as s (singlet), d (doublet), t (triplet), m (multiplet), br (broad signal), dd (doublet of doublets), and dt (doublet of triplets). Carbon spectra were acquired with a complete decoupling for the proton unless specified. All spectra were recorded at 25 °C unless specified.

High resolution mass spectra (HRMS) were obtained on Bruker micrOTOF-Q (ESI-TOF).

ATR-Fourier-transform infrared spectroscopy was performed on a Shimadzu IRAffinity1S equipped with a QATR-10 with diamond crystal.

TEM images were acquired on Jeol, JEM 2100, Japan, at 200 kV. The TEM is equipped with Gatan camera and DigitalMicrographs software. Samples were drop-cast from a methanol or chloroform diluted solution (concentration in the order of μg mL^{-1}) on top of a copper grid (copper-grid-supported carbon film), purchased from Ted Pella, Inc.

Absorption spectra were collected with a Shimadzu UV-1900i spectrometer. Steady-state emission spectroscopy was performed using an Edinburgh FS5 spectrofluorimeter. Emission lifetimes and time resolved emission spectroscopy (TRES) were measured using a Fluorolog 3 time-correlated photon counting instrument from Horiba Jovin Yvon, a SuperK Fianium FIU6PP supercontinuum laser from NKT Photonics as the excitation source, and a R3809U-50 MCP photomultiplier from Hammamatsu, or with an Edinburgh FS5 spectrofluorimeter equipped with a VisUV picosecond laser system from PicoQuant (pulse duration < 85 ps). Ultrafast transient absorption experiments were conducted using an Astrella-F-1K amplified Ti:sapphire femtosecond laser system from Coherent, operating at a repetition rate 1kHz, 5.5 W power (5 mJ pulse energy), pulse duration of 80 fs, with TA pump / probe Helios detection system from Ultrafast Systems. White light was generated focusing a fraction of the fundamental 800 nm output onto a 2 mm CaF2 mounted on a translating crystal holder. A 1.2 mJ fraction of the fundamental is used for pump beam generation by a TOPAS Prime from Light Conversion with standard NirUVis extension. A depolarizer was placed in the pump beam to avoid rotational dynamics. Bandpass filters with ± 5 or ± 10 nm were used to ensure low spectral width and to exclude 800 nm photons. All measurements were conducted in a 2 mm quartz cuvette under argon atmosphere, using solutions with absorbances of 0.5-0.7. To analyze transient absorption data, we used a suggested procedure.[40] We start with SVD and global analysis, using an all-sequential decay model that provides evolution associated spectra of potentially intervening species, to determine the number of decaying species that participate in the decay cascade. However, this does not necessarily yield differential spectra with genuine physicochemical meaning. Afterwards, a target analysis is applied, using specific target models that result in species associated spectra 4 with true physicochemical meaning. Obtained data were treated by SVD, global and target analyses using the R- package TIMP and GloTarAn.[40–42]

3.4.2 Synthesis of Acyl Chlorides

Synthesis of 12,12,12-trifluorododec-10-ynoyl chloride (2)

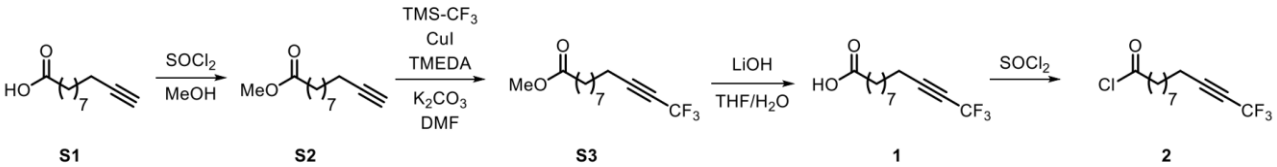

STEP 1. According to a modified literature procedure.[43] Undec-10-ynoic acid S1 (1.82 g, 10 mmol, 1 equiv.) was dissolved in dry methanol (40 mL, 0.25 M), then thionyl chloride (3.65 mL, 50 mmol, 5 equiv.) was added at 0°C and the resulting solution was stirred at room temperature for 4

hours. The reaction was quenched by the addition of a saturated solution of $NaHCO_3$ at 0°C and the mixture was extracted with ethyl acetate. The organic phase was dried over sodium sulfate and the solvent was removed under reduced pressure. The corresponding methyl 10-undecynoate (S2) was used without any further purification (1.83 g, 93% yield). The characterization data matched with the reported one.[43]

^{1}H NMR (400 MHz, $CDCl_3$) δ 3.66 (s, 3H), 2.30 (t, J = 7.5 Hz, 2H), 2.18 (td, J = 7.1, 2.6 Hz, 2H), 1.93 (t, J = 2.7 Hz, 1H), 1.61 (tt, J = 8.7, 4.2 Hz, 2H), 1.57 – 1.47 (m, 2H), 1.43 – 1.34 (m, 2H), 1.34 – 1.26 (m, 6H).

STEP 2. According to a modified literature procedure.[44] A mixture of CuI (1.4 g, 7.5 mmol, 1.5 equiv.), K_2CO_3 (2.1 g, 15 mmol, 3 equiv.), *N,N,N′,N′*-tetramethyl ethylenediamine (1.2 mL, 7.5 mmol, 1.5 equiv.) in *N,N*-dimethylformamide (DMF, 25 mL, 0.2 M) was stirred at room temperature for 15 minutes. Then, a first portion of trimethyl(trifluoromethyl)silane (1.5 mL, 10 mmol, 2 equiv.) was added at 0°C and the resulting mixture was stirred at room temperature for 5 minutes before cooling it down to 0°C. At this point, a solution of methyl 10-undecynoate (S2) (981 mg, 5 mmol, 1 equiv.) and trimethyl(trifluoromethyl)silane (1.5 mL, 10 mmol, 2 equiv.) in DMF (25 mL, 0.2 M) was added at 0°C and the overall mixture was stirred at room temperature overnight under air atmosphere. The reaction was quenched by the addition of a solution of ethylenediaminetetraacetic acid disodium salt (Na_2EDTA, 0.1 M, 50 mL) and the mixture was extracted with diethyl ether. The organic phase was dried over sodium sulfate and the solvent was removed under reduced pressure. The corresponding methyl 12,12,12-trifluorododec-10-ynoate (S3) was used without any further purification (1.22 g, 92% yield).

^{1}H-NMR (400 MHz, $CDCl_3$) δ 3.67 (s, 3H), 2.33 – 2.27 (m, 4H), 1.66 – 1.51 (m, 4H), 1.39 (m, 2H), 1.35 – 1.24 (m, 6H); 19F-NMR (376 MHz, CDCl3) δ -49.38 (t, J = 3.8 Hz); ^{13}C-NMR (101 MHz, $CDCl_3$) δ 174.28, 114.24 (q, J = 255.9 Hz), 89.38 (q, J = 6.3 Hz), 68.43 (q, J = 52.0 Hz), 51.46 (s), 34.10 (s), 29.09 (s), 29.08 (s), 28.82 (s), 28.68 (s), 27.26 (d, J = 1.3 Hz), 24.96 (s), 18.15 (d, J = 1.5 Hz); HRMS (ESI, positive mode) calculated for $C_{13}H_{19}F_3O_2$ $[M+H]^+$: 265.1410, found: 265.1416.

STEP 3. According to a modified literature procedure.[45] A mixture of S3 (793 mg, 3 mmol, 1 equiv.) and LiOH (144 mg, 6 mmol, 2 equiv.) in tetrahydrofuran/water (18 mL THF + 6 6 mL H2O, 3:1 v/v, 0.125 M tot) was vigorously stirred at room temperature for 6 hours. The reaction was quenched by the addition of an aqueous solution of hydrochloric acid (2 M, 10 mL) and the mixture was extracted with ethyl acetate. The organic phase was dried over sodium sulfate and the solvent was removed under reduced pressure. The corresponding 12,12,12-trifluorododec-10-ynoic acid (1) was used without any further purification (721 mg, 96% yield).

^{1}H-NMR (400 MHz, $CDCl_3$) δ 2.39 – 2.26 (m, 4H), 1.68 – 1.53 (m, 4H), 1.44 – 1.27 (br s, 8H). ^{19}F-NMR (376 MHz, $CDCl_3$) δ -49.39 (s); $_{13}$C-NMR (101 MHz, $CDCl_3$) δ 180.04 (s), 113.90 (q, J = 257.6 Hz), 89.40 (q, J = 6.9 Hz), 68.53 (q, J = 51.9 Hz), 34.12 (s), 29.12 (s), 29.06 (s), 28.87 (s), 28.74 (s), 27.31 (d, J = 1.5 Hz), 24.73 (s), 18.23 (d, J = 1.6 Hz); HRMS (ESI, positive mode) calculated for $C_{12}H_{17}F_3O_2$ $[M+Na]^+$: 273.1073, found: 273.1079.

STEP 4. According to a modified literature procedure.[46] A solution of 1 (200 mg, 0.8 mmol, 1 equiv.) in thionyl chloride (2.5 mL, 0.32 M) was refluxed for 2 hours. The volatiles were removed under reduced pressure and the corresponding 12,12,12-trifluorododec-10-ynoyl chloride 2 was immediately used without any further purification (199 mg, 93% yield).

^{1}H-NMR (400 MHz, $CDCl_3$) δ 2.88 (t, J = 7.3 Hz, 2H), 2.30 (tq, J = 7.4, 3.8 Hz, 2H), 1.71 (p, J = 7.2 Hz, 2H), 1.58 (p, J = 7.0 Hz, 2H), 1.41 – 1.27 (br m, 8H); ^{19}F-NMR (376 MHz, $CDCl_3$) δ -49.39 (t, J = 4.0 Hz). It was not possible to measure the ^{13}C-NMR and the HRMS (ESI) spectra because of the poor stability of compound 1.

Synthesis of 11-(prop-2-yn-1-yloxy)undecanoyl chloride (3)

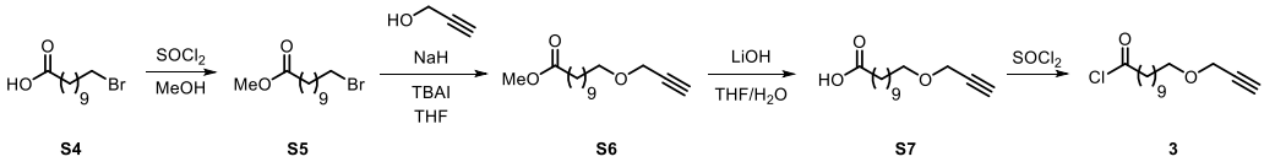

STEP 1. According to a modified literature procedure.[47] 11-bromoundecanoic acid S4 (2.65 g, 10 mmol, 1 equiv.) was dissolved in dry methanol (40 mL, 0.25 M), then thionyl chloride (3.65 mL, 50 mmol, 5 equiv.) was added at 0°C and the resulting solution was stirred at room temperature for 4 hours. The reaction was quenched by the addition of a saturated solution of $NaHCO_3$ at 0°C and the mixture was extracted with ethyl acetate. The organic phase was dried over sodium sulfate and the solvent was removed under reduced pressure. The corresponding methyl 11-bromoundecanoate (S5) was used without any further purification (2.51 g, 90% yield). The characterization data matched with the reported one.[47]

^{1}H-NMR (400 MHz, $CDCl_3$) δ 3.67 (s, 3H), 3.64 (s, 2H), 3.40 (t, J = 6.9 Hz, 2H), 2.30 (t, J = 7.5 Hz, 2H), 1.91 – 1.79 (m, 2H), 1.62 (t, J = 7.3 Hz, 2H), 1.42 (t, J = 7.4 Hz, 2H), 1.29 (s, 8H).

STEP 2. According to a modified literature procedure.[48] To a solution of propargyl alcohol (320 µL, 5.5 mmol, 1.2 equiv.) in dry THF (20 mL, 0.25 M) sodium hydride (60% wt, 202 mg, 5.1 mmol, 1.1 equiv.) was added portionwise at 0°C and the resulting mixture was stirred at 0°C for 1 hour. Then, S5 (1.3 g, 4.6 mmol, 1 equiv.) and tetrabutylammonium iodide (170 mg, 0.46 mmol, 0.1 equiv.) were added and the mixture was stirred at room temperature overnight. The reaction

was quenched by the addition of a saturated solution of NH_4Cl (20 mL) at 0°C and the mixture was extracted with ethyl acetate. The organic phase was dried over sodium sulfate and the solvent was removed under reduced pressure. The crude product was purified by flash column chromatography (cyclohexane/ethyl acetate 9:1), affording the desired methyl 11-(prop-2-yn-1-yloxy)undecanoate (S6) (822 mg, 71% yield).

^{1}H-NMR (400 MHz, $CDCl_3$) δ 4.13 (d, J = 2.4 Hz, 2H), 3.66 (s, 3H), 3.50 (t, J = 6.6 Hz, 2H), 2.41 (t, J = 2.4 Hz, 1H), 2.30 (t, J = 7.5 Hz, 2H), 1.67 – 1.50 (m, 4H), 1.25 – 1.35 (m, 12H); ^{13}C-NMR (101 MHz, $CDCl_3$) δ 174.45 (s), 80.18 (s), 74.15 (s), 70.40 (s), 58.12 (s), 51.55 (s), 34.22 (s), 29.61 (s), 29.58 (s), 29.49 (s), 29.46 (s), 29.33 (s), 29.24 (s), 26.18 (s), 25.06 (s); HRMS (ESI, positive mode) calculated for $C_{15}H_{26}O_3$ $[M+Na]^+$: 277.1774, found: 277.1775.

STEP 3. According to a modified literature procedure.[45] A mixture of S6 (763 mg, 3 mmol, 1 equiv.) and LiOH (144 mg, 6 mmol, 2 equiv.) in tetrahydrofuran/water (18 mL THF + 6 mL H_2O, 3:1 v/v, 0.125 M tot) was vigorously stirred at room temperature for 6 hours. The reaction was quenched by the addition of an aqueous solution of hydrochloric acid (2 M, 10 mL) and the mixture was extracted with ethyl acetate. The organic phase was dried over sodium sulfate and the solvent was removed under reduced pressure. The corresponding 11-(prop-2-yn-1-yloxy)undecanoic acid (S7) was used without any further purification (613 mg, 85% yield).

^{1}H-NMR (400 MHz, $CDCl_3$) δ 4.13 (d, J = 2.3 Hz, 2H), 3.51 (t, J = 6.7 Hz, 2H), 2.41 (t, J = 2.4 Hz, 1H), 2.34 (t, J = 7.5 Hz, 2H), 1.72 – 1.51 (m, 4H), 1.43 – 1.21 (m, 12H); ^{13}C-NMR (101 MHz, $CDCl_3$) δ 179.38 (s), 80.20 (s), 74.18 (s), 70.44 (s), 58.15 (s), 34.05 (s), 29.62 (s), 29.60 (s), 29.51 (s), 29.47 (s), 29.33 (s), 29.18 (s), 26.20 (s), 24.82 (s); HRMS (ESI, positive mode) calculated for $C_{14}H_{24}O_3$ $[M+Na]^+$: 263.1618, found: 263.1618.

STEP 4. According to a modified literature procedure.[46] A solution of S7 (192 mg, 0.8 mmol, 1 equiv.) in thionyl chloride (2.5 mL, 0.32 M) was refluxed for 2 hours. The volatiles were removed under reduced pressure and the corresponding 11-(prop-2-yn-1-yloxy)undecanoyl chloride (3) was immediately used without any further purification (180 mg, 87% yield). ^{1}H-NMR (400 MHz, $CDCl_3$) δ 4.13 (d, J = 2.5 Hz, 2H), 3.51 (t, J = 6.5 Hz, 2H), 2.88 (t, J = 7.2 Hz, 2H), 2.41 (t, J = 2.4 Hz, 1H), 1.71 (p, J = 7.2 Hz, 2H), 1.58 (br q, J = 7.4 Hz, 4H), 1.40 – 1.23 (br m, 10H). It was not possible to measure the ^{13}C-NMR and the HRMS (ESI) spectra because of the poor stability of compound 3.

Synthesis of 11-azidoundecanoyl chloride (S9)

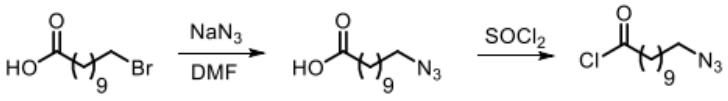

S4 S8 S9

STEP 1. According to a modified literature procedure.[49] 11-bromoundecanoic acid (S4) (2.65 g, 10 mmol, 1 equiv.) was dissolved in dry DMF (40 mL, 0.25 M), then sodium azide (1.30 g, 20 mmol, 2 equiv.) was added at room temperature and the resulting mixture was stirred at 60°C overnight. The reaction was quenched by the addition of water (50 mL) and the mixture was extracted with ethyl acetate. The organic phase was washed with a solution of LiCl (5% w/v, 50 mL), then dried over sodium sulfate and the solvent was removed under reduced pressure. The corresponding 11-azidoundecanoic acid (S8) was used without any further purification (2.15 g, 94% yield). The characterization data matched with the reported one.[49]

^{1}H-NMR (400 MHz, $CDCl_3$) δ 3.24 (t, J = 7.0 Hz, 2H), 2.33 (t, J = 7.5 Hz, 2H), 1.60 (dp, J = 14.4, 7.3 Hz, 4H), 1.41 – 1.25 (m, 12H).

STEP 2. According to a modified literature procedure.[46] A solution of S8 (182 mg, 0.8 mmol, 1 equiv.) in thionyl chloride (2.5 mL, 0.32 M) was refluxed for 2 hours. The volatiles were removed under reduced pressure and the corresponding 11-azidoundecanoyl chloride S9 was immediately used without any further purification (219 mg, 89% yield).

^{1}H-NMR (400 MHz, $CDCl_3$) δ 3.26 (t, J = 6.9 Hz, 2H), 2.88 (t, J = 7.3 Hz, 2H), 1.71 (p, J = 7.3 Hz, 2H), 1.59 (br q, J = 7.5 Hz, 4H), 1.51 – 1.13 (br m, 10H). It was not possible to measure the ^{13}C-NMR and the HRMS (ESI) spectra because of the poor stability of compound S9.

3.4.3 Synthesis of CNDs

CNDs-1 synthesis is described in Chapter II, Experimental Section, 2.4.2 Synthesis of CNDs.

CNDs-2 were synthesized according to a literature procedure.[2] (*S*)-2-(Aminomethyl)-1-Boc-pyrrolidine (100 mg) and citric acid (192 mg) were dissolved in Milli-Q water (100 µL) and then heated at 240 °C, and 150 W for 180 seconds. In the process of microwave heating, the solution changes color from pale yellow to brown as a result of formation of CNDs-2. The solution was diluted with chloroform ($CHCl_3$) and washed with water (3 times). The organic phase was dried over Na_2SO_4 and concentrated under reduced pressure. The solid was suspended in the minimum amount of chloroform and then precipitated with diethyl ether (10 mL) to induce the CNDs-2 precipitation. The precipitate was collected though centrifugation (6000 rpm, 10 min). The

precipitation process was repeated twice. After drying, the final material is obtained as a brownish powder (60 mg).

3.4.4 Post-functionalization of CNDs with Acyl Chlorides

General procedure

CNDs-1-2 (25 mg) were dissolved in anhydrous DMF (4 mL), then triethylamine (TEA), and the corresponding acyl chloride 2, 3, S9 were added at room temperature. The obtained mixture was stirred under Ar atmosphere for 3 days at room temperature. For CNDs-1, when a reduced amount of acyl chlorides was employed, the remaining functionalities of the particles were reacted with octanoyl chloride (0.34 mmol) and triethylamine (0.34 mmol) for additional 3 days. The reaction was then quenched with water and extracted with chloroform. The organic phase was dried over Na_2SO_4, and the solvent was removed under reduced pressure. The crude solid was dissolved in the minimum amount of chloroform (about 0.5 mL) and then precipitated by adding diethyl ether (10 mL) as anti-solvent. The precipitate was collected though centrifugation (6000 rpm, 10 min). The precipitation process was repeated twice. After drying under vacuum, the final product was obtained as a yellow-brown powder.

CNDs-1-2 functionalized with 2

CNDs-3

From CNDs-1 (25 mg), 2 (0.34 mmol), and TEA (0.34 mmol) after stirring for 3 days. Obtained mass = 31 mg.

CNDs-S1

CNDs-1 (25 mg), 2 (0.02 mmol), and TEA (0.02 mmol) were stirred for 3 days, then octanoyl chloride (0.34 mmol) and TEA (0.34 mmol) were added, and the mixture was stirred for additional 3 days. Obtained mass = 16 mg.

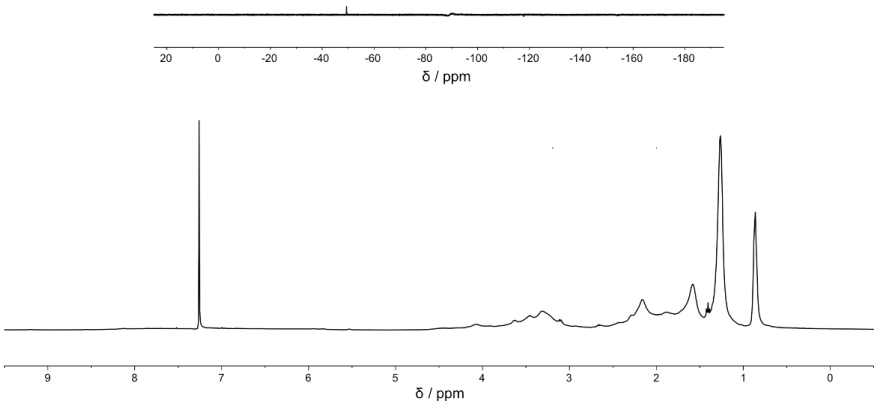

Figure 3.14. *CNDs-S1, ^{19}F NMR ($CDCl_3$, 376 MHz, r.T) (top) and ^{1}H NMR ($CDCl_3$, 400 MHz, r.T) (bottom).*

CNDs-S2

CNDs-1 (25 mg), 2 (0.034 mmol), and TEA (0.034 mmol) were stirred for 3 days, then octanoyl chloride (0.34 mmol) and TEA (0.34 mmol) were added, and the mixture was stirred for additional 3 days. Obtained mass = 25 mg.

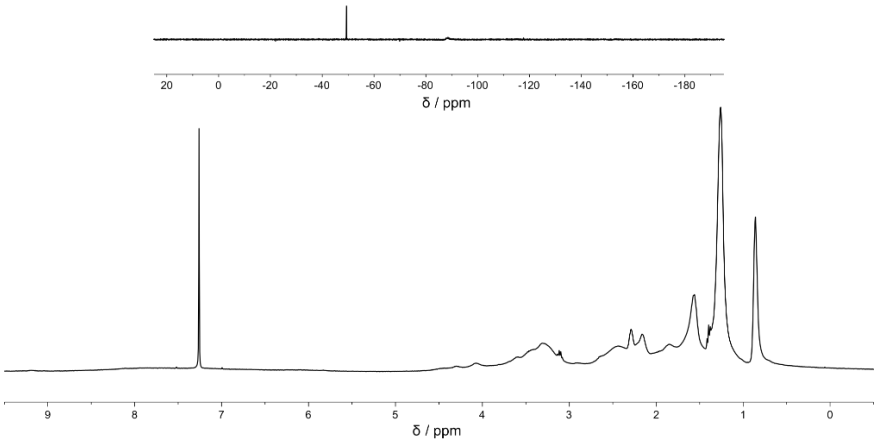

Figure 3.15. *CNDs-S2, ^{19}F NMR ($CDCl_3$, 376 MHz, r.T) (top) and ^{1}H NMR ($CDCl_3$, 400 MHz, r.T) (bottom).*

CNDs-S3

CNDs-1 (25 mg), 2 (0.07 mmol), and TEA (0.07 mmol) were stirred for 3 days, then octanoyl chloride (0.34 mmol) and TEA (0.34 mmol) were added, and the mixture was stirred for additional 3 days. Obtained mass = 23 mg.

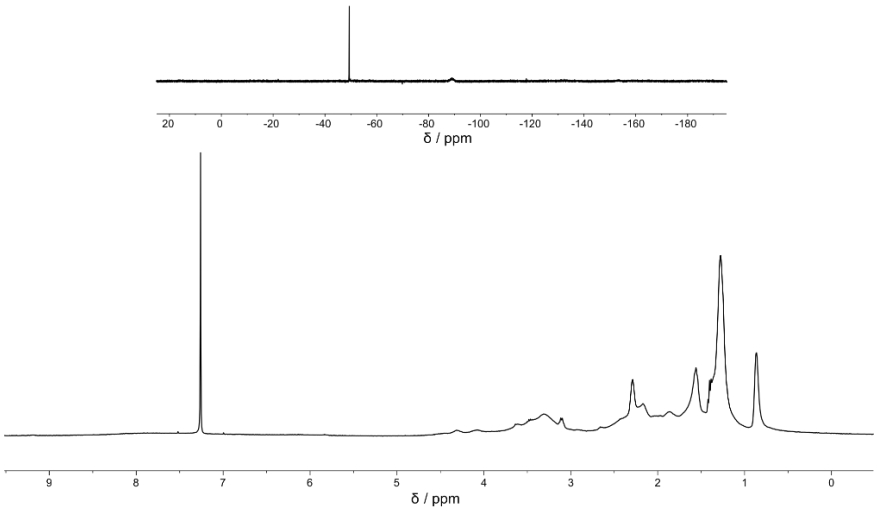

Figure 3.16. *CNDs-S3, ^{19}F NMR ($CDCl_3$, 376 MHz, r.T) (top) and ^{1}H NMR ($CDCl_3$, 400 MHz, r.T) (bottom).*

CNDs-S4

CNDs-1 (25 mg), 2 (0.14 mmol), and TEA (0.14 mmol) were stirred for 3 days, then octanoyl chloride (0.34 mmol) and TEA (0.34 mmol) were added, and the mixture was stirred for additional 3 days. Obtained mass = 24 mg.

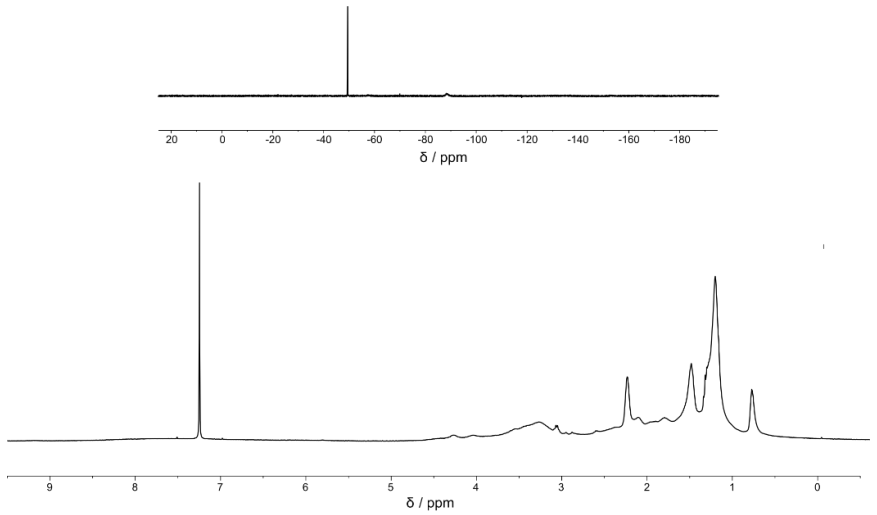

Figure 3.17. *CNDs-S4, ^{19}F NMR ($CDCl_3$, 376 MHz, r.T) (top) and ^{1}H NMR ($CDCl_3$, 400 MHz, r.T) (bottom).*

CNDs-1 functionalized with 3

CNDs-5

From CNDs-1 (25 mg), 3 (0.34 mmol), and TEA (0.34 mmol) after stirring for 3 days. Obtained mass = 34 mg.

CNDs-10

CNDs-1 (25 mg), 3 (0.07 mmol), and TEA (0.07 mmol) were stirred for 3 days, then octanoyl chloride (0.34 mmol) and TEA (0.34 mmol) were added, and the mixture was stirred for additional 3 days. Obtained mass = 14 mg.

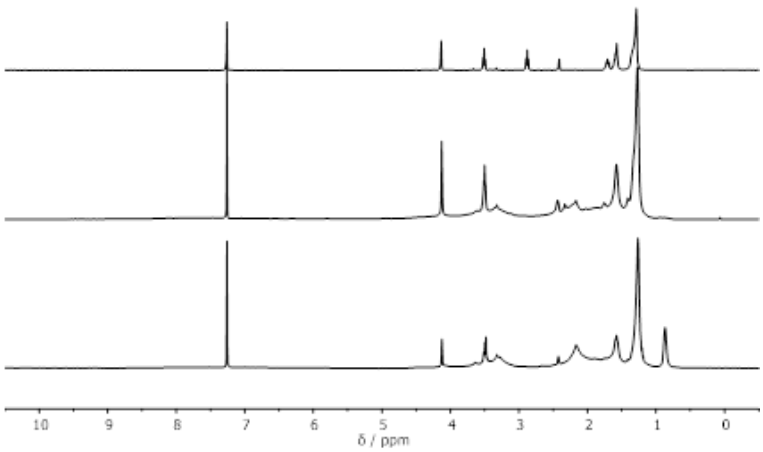

Figure 3.18. *^{1}H NMR of 3, CNDs-5, CNDs-10 ($CDCl_3$, 400 MHz, r.T).*

CNDs-2 functionalized with 5

CNDs-7

From CNDs-2 (25 mg), S9 (0.08 mmol), and TEA (0.08 mmol) after stirring for 3 days. Obtained mass = 18 mg.

3.4.5 Click Reactions between CNDs and Fluorinated Molecules

Synthesis of 1-(azidomethyl)-3,5-bis(trifluoromethyl)benzene (4)

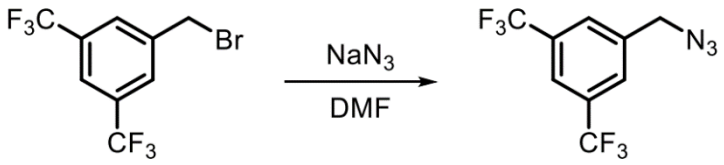

S10 **4**

Prepared according to a modified literature procedure.[50] 1-(bromomethyl)-3,5-bis(trifluoromethyl)benzene (S10) (307 mg, 1 mmol, 1 equiv.) was dissolved in dry DMF (4 mL, 0.25 M), then sodium azide (130 mg, 2 mmol, 2 equiv.) was added at room temperture and the resulting mixture was stirred at 60°C overnight. The reaction was quenched by the addition of water (5 mL) and the mixture was extracted with ethyl acetate. The organic phase was washed with a solution of LiCl (5% w/v, 5 mL), then dried over sodium sulfate and the solvent was removed under reduced pressure. The corresponding 1-(azidomethyl)-3,5-bis(trifluoromethyl)benzene (4) was used without any further purification (154 mg, 60% yield). The characterization data matched with the reported one.[50]

^{1}H-NMR (400 MHz, $CDCl_3$) δ 7.86 (s, 1H), 7.78 (s, 2H), 4.55 (s, 2H); ^{19}F-NMR (376 MHz, CDCl3) δ -62.97 (s); ^{13}C-NMR (101 MHz, $CDCl_3$) δ 138.36 (s), 132.38 (q, J = 33.5 Hz), 128.07 – 127.93 (m), 123.22 (d, J = 272.8 Hz), 122.46 – 122.15 (m), 53.70. It was not possible to measure the HRMS (ESI-MS) of compound 4 due to its poor tendency to ionize.

Synthesis of 1-((prop-2-yn-1-yloxy)methyl)-3,5-bis(trifluoromethyl)benzene (S11)

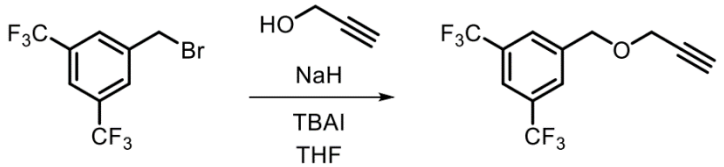

S10 **S11**

According to a modified literature procedure.[48] To a solution of propargyl alcohol (70 µL, 1.2 mmol, 1.2 equiv.) in dry THF (4 mL, 0.25 M) sodium hydride (60 wt%, 44 mg, 1.1 mmol, 1.1 equiv.) was added portionwise at 0°C and the resulting mixture was stirred at 0°C for 1 hour. Then, S10 (307 mg, 1 mmol, 1 equiv.) and tetrabutylammonium iodide (37 mg, 0.1 mmol, 0.1 equiv.) were added and the mixture was stirred at room temperature overnight. The reaction was quenched

by the addition of a saturated solution of NH_4Cl (10 mL) at 0°C and the mixture was extracted with ethyl acetate. The organic phase was dried over sodium sulfate and the solvent was removed under reduced pressure to give the desired 1-((prop-2-yn-1-yloxy)methyl)-3,5-bis(trifluoromethyl)benzene S11 (243 mg, 86% yield) without any further purification.
^{1}H-NMR (400 MHz, $CDCl_3$) δ 7.82 (s, 3H), 4.72 (s, 2H), 4.28 (d, J = 2.3 Hz, 2H), 2.52 (t, J = 2.4 Hz, 1H); ^{19}F-NMR (376 MHz, $CDCl_3$) δ -62.91 (s); ^{13}C-NMR (101 MHz, $CDCl_3$) δ 140.38 (s), 131.89 (q, J = 33.4 Hz), 127.72 (d, J = 3.8 Hz), 123.42 (q, J = 272.6 Hz), 121.84 (p, J = 3.8 Hz), 78.93 (s), 75.66 (s), 70.14 (s), 58.18 (s). It was not possible to measure the HRMS (ESI-MS) of compound 4 due to its poor tendency to ionize.

General procedure for the click reactions between CNDs and model molecules

CNDs-5 or CNDs-7 were dissolved in chloroform (1 mL) and the corresponding clickable reagent 4 or 6 was added. Then, a solution of $CuSO_4$•$5H_2O$ in water (0.5 mL) was poured into the reaction vessel, followed by a solution of sodium ascorbate (NaAsc) in water (0.5 mL). The resulting biphasic mixture was vigorously stirred for 24 hours at room temperature. The reaction mixture was then extracted with chloroform and washed with an aqueous solution of Na_2EDTA (0.1 M, 5 mL). The organic phase was dried over Na_2SO_4, and the solvent was removed under reduced pressure. The crude solid was dissolved in the minimum amount of chloroform (about 0.5 mL) and then precipitated by adding *n*-hexane (10 mL) as anti-solvent. The precipitate was collected though centrifugation (6000 rpm, 10 min). The precipitation process was repeated twice. After drying under vacuum, the final clicked dots CNDs-6 and CNDs-8 were obtained respectively as a yellow-brown powder.

CNDs-6

Obtained from CNDs-4 (15 mg), 4 (0.2 mmol), $CuSO_4$•$5H_2O$ (0.02 mmol), NaAsc (0.04 mmol). Obtained mass = 16.5 mg.

CNDs-8

Obtained from CNDs-6 (15 mg), S11 (0.05 mmol), $CuSO_4$•$5H_2O$ (0.005 mmol), NaAsc (0.01 mmol). Obtained mass = 20 mg.

3.4.6 Click Reactions between CNDs

General procedure for the click reactions between CNDs

CNDs-5,10 and CNDs-7 were dissolved in chloroform (1 mL) Then, a solution of $CuSO_4 \cdot 5H_2O$ in water (0.5 mL) was poured into the reaction vessel, followed by a solution of sodium ascorbate (NaAsc) in water (0.5 mL). The resulting biphasic mixture was vigorously stirred for 24 hours at room temperature. The reaction mixture was then extracted with chloroform and washed with an aqueous solution of Na_2-EDTA (0.1 M, 5 mL). The organic phase was dried over Na_2SO_4, and the solvent was removed under reduced pressure. The crude solid was purified by size exclusion chromatography (Sephadex LH-20) by using chloroform as mobile phase (2 mL min^{-1} operating at a pressure of 150 psi). Just the first fractions in which both the contribution of CNDs-4/8 and CNDs-6 can be clearly observed were collected. After drying under vacuum, the final interconnected dots CNDs-7,9 were obtained respectively as a yellow-brown powder.

CNDs-7

Obtained from CNDs-4 (5 mg), CNDs-6 (15 mg), $CuSO_4 \cdot 5H_2O$ (0.005 mmol), NaAsc (0.01 mmol). Obtained mass = 5 mg.

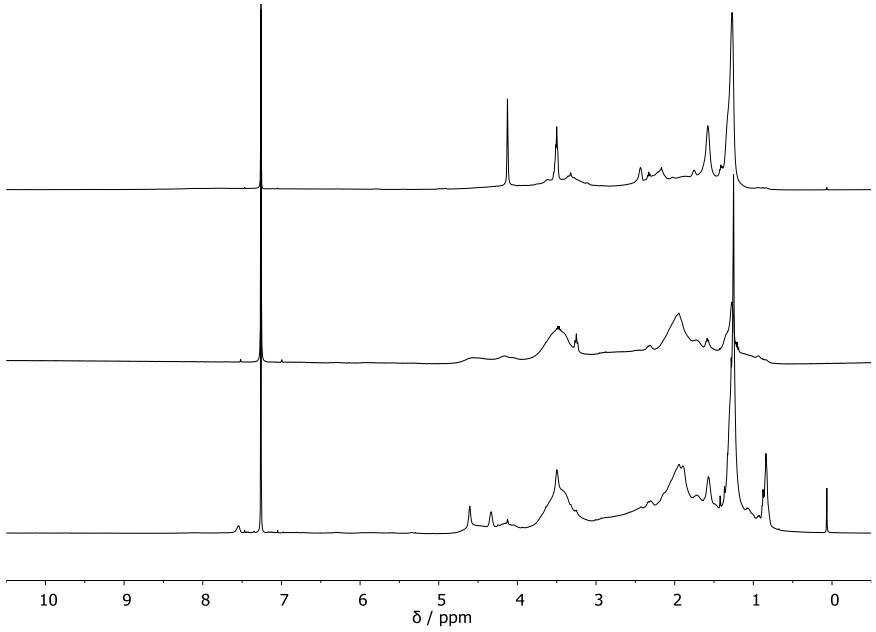

Figure 3.19. *CNDs-5, CNDs-7, CNDs-9, ^1H NMR ($CDCl_3$, 400 MHz, rt).*

CNDs-9

Obtained from CNDs-8 (10 mg), CNDs-6 (14 mg), $CuSO_4 \cdot 5H_2O$ (0.004 mmol), NaAsc (0.008 mmol). Obtained mass = 6.5 mg.

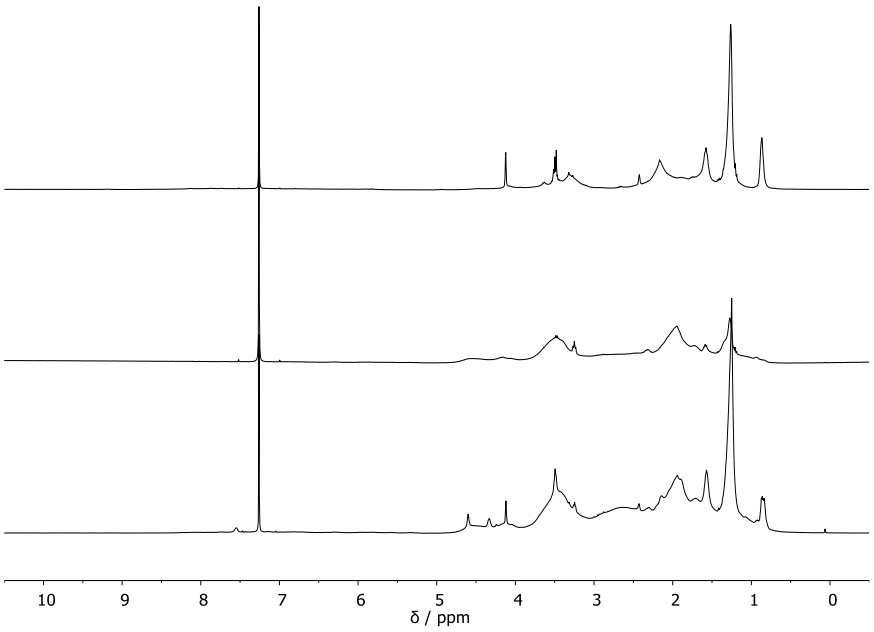

Figure 3.20. *CNDs-10, CNDs-7, CNDs-11, ^1H NMR ($CDCl_3$, 400 MHz, rt).*

3.4.7 Supplementary Figures

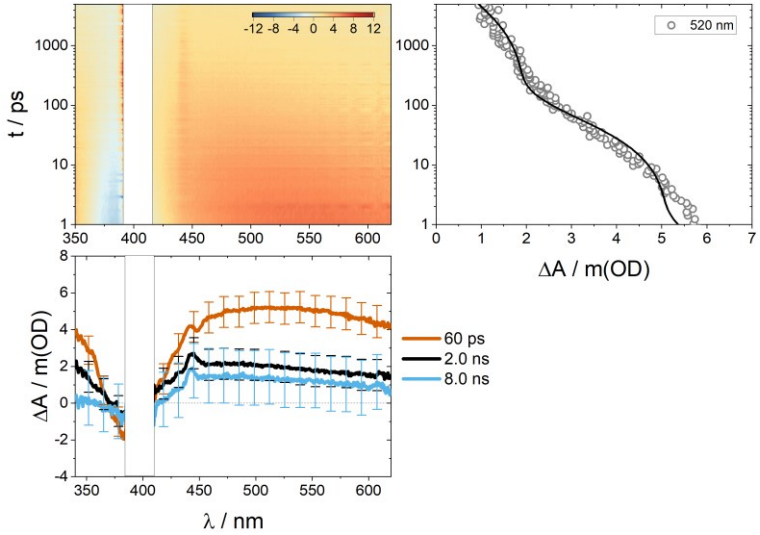

Figure S3.1. *Femtosecond transient absorption spectroscopy CNDs-10 in DMF. Top left: Color map of the evolution of differential absorption spectra. Top right: Experimental kinetic trace at 520 nm (dots) and fitting (line). Bottom left: Species-associated differential absorption spectra corresponding to lifetimes of 60 ps (red), 2.0 ns (black), and 8.0 ns (cyan).*

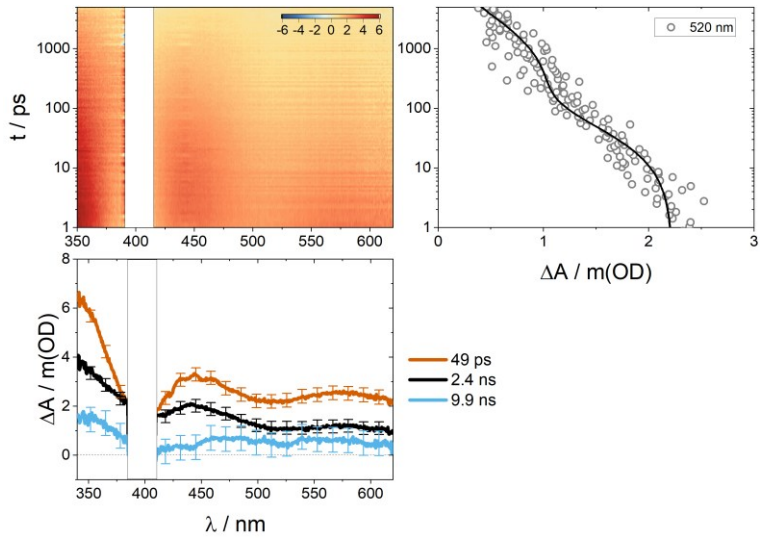

Figure S3.2. *Femtosecond transient absorption spectroscopy CNDs-7 in DMF. Top left: Color map of the evolution of differential absorption spectra. Top right: Experimental kinetic trace at 520 nm (dots) and fitting (line). Bottom left: Differential absorption spectra associated to lifetimes of 49 ps (red), 2.4 ns (black), and 9.9 ns (cyan).*

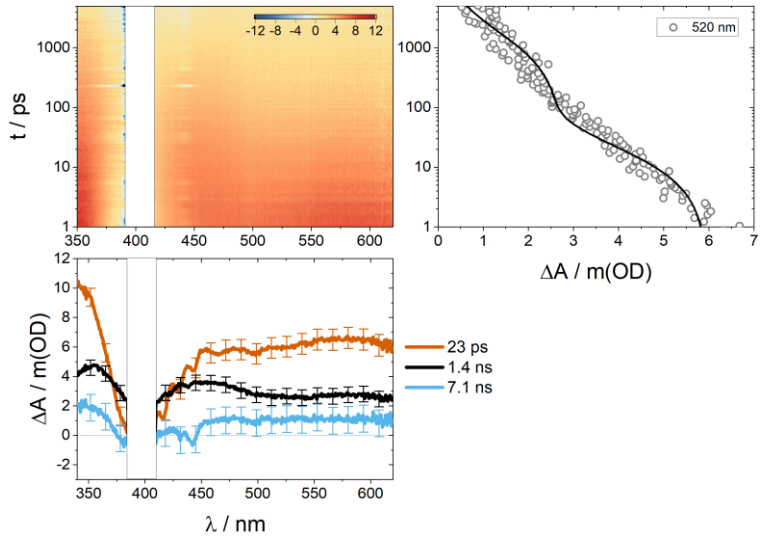

Figure S3.3. *Femtosecond transient absorption spectroscopy CNDs-11 in DMF. Top left: Color map of the evolution of differential absorption spectra. Top right: Experimental kinetic trace at 520 nm (dots) and fitting (line). Bottom left: Differential absorption spectra associated to lifetimes of 23 ps (red), 1.4 ns (black), and 7.1 ns (cyan).*

3.5 References

1. Arcudi, F., Đorđević, L. & Prato, M. Synthesis, Separation, and Characterization of Small and Highly Fluorescent Nitrogen-Doped Carbon NanoDots. *Angew. Chem. Int. Ed.* **55**, 2107–2112 (2016).

2. Bartolomei, B., Corti, V. & Prato, M. Chiral Carbon Nanodots Can Act as Molecular Catalysts in Chemical and Photochemical Reactions. *Angew. Chem.* **135**, e202305460 (2023).

3. Bartolomei, B. *et al.* Synthetic Strategies for the Selective Functionalization of Carbon Nanodots Allow Optically Communicating Suprastructures. *Angew. Chem.* **136**, e202316915 (2024).

4. Liu, M. *et al.* From Nanoscopic to Macroscopic Materials by Stimuli-Responsive Nanoparticle Aggregation. *Adv. Mater.* **35**, 2208995 (2023).

5. Huo, Q. & Worden, J. G. Monofunctional gold nanoparticles: synthesis and applications. *J. Nanoparticle Res.* **9**, 1013–1025 (2007).

6. Marro, N., Suo, R., Naden, A. B. & Kay, E. R. Constitutionally Selective Dynamic Covalent Nanoparticle Assembly. *J. Am. Chem. Soc.* **144**, 14310–14321 (2022).

7. de Boëver, R., Town, J. R., Li, X. & Claverie, J. P. Carbon Dots for Carbon Dummies: The Quantum and The Molecular Questions Among Some Others. *Chem. – Eur. J.* **28**, e202200748 (2022).

8. Sun, Y.-P. *et al.* Quantum-Sized Carbon Dots for Bright and Colorful Photoluminescence. *J. Am. Chem. Soc.* **128**, 7756–7757 (2006).

9. Cadranel, A. *et al.* Screening Supramolecular Interactions between Carbon Nanodots and Porphyrins. *J. Am. Chem. Soc.* **140**, 904–907 (2018).

10. Arcudi, F. & Đorđević, L. Supramolecular Chemistry of Carbon-Based Dots Offers Widespread Opportunities. *Small* **19**, 2300906 (2023).

11. Li, D. *et al.* Supra-(carbon dots) with versatile morphologies and promising optical properties. *Chem. Eng. J.* **454**, 140069 (2023).

12. Gomez, I. J., Arnaiz, B., Cacioppo, M., Arcudi, F. & Prato, M. Nitrogen-doped carbon nanodots for bioimaging and delivery of paclitaxel. *J. Mater. Chem. B* **6**, 5540–5548 (2018).

13. Ferrer-Ruiz, A. *et al.* Assessing the Photoinduced Electron-Donating Behavior of Carbon Nanodots in Nanoconjugates. *J. Am. Chem. Soc.* **142**, 20324–20328 (2020).

14. Bu, X. *et al.* Covalent Assembly of Clickable Carbon Nanodots in Water-in-Oil Emulsion for Enhanced Antibacterial Photothermal Therapy. *ACS Appl. Nano Mater.* **5**, 11447–11457 (2022).

15. Carrara, S., Arcudi, F., Prato, M. & De Cola, L. Amine-Rich Nitrogen-Doped Carbon Nanodots as a Platform for Self-Enhancing Electrochemiluminescence. *Angew. Chem. Int. Ed.* **56**, 4757–4761 (2017).

16. Arcudi, F. *et al.* Porphyrin Antennas on Carbon Nanodots: Excited State Energy and Electron Transduction. *Angew. Chem.* **129**, 12265–12269 (2017).

17. Gomez, I. J., Arnaiz, B., Cacioppo, M., Arcudi, F. & Prato, M. Nitrogen-doped carbon nanodots for bioimaging and delivery of paclitaxel. *J. Mater. Chem. B* **6**, 5540–5548 (2018).

18. Đorđević, L. *et al.* Synthesis and excited state processes of arrays containing amine-rich carbon dots and unsymmetrical rylene diimides. *Mater. Chem. Front.* **4**, 3640–3648 (2020).

19. Cacioppo, M. *et al.* Symmetry-Breaking Charge-Transfer Chromophore Interactions Supported by Carbon Nanodots. *Angew. Chem. Int. Ed.* **59**, 12779–12784 (2020).

20. Filippini, G. *et al.* Engineering Functional Nanomaterials Through the Amino Group. in *Methodologies in Amine Synthesis* 285–340 (John Wiley & Sons, Ltd, 2021).

21. Kolb, H. C., Finn, M. G. & Sharpless, K. B. Click Chemistry: Diverse Chemical Function from a Few Good Reactions. *Angew. Chem. Int. Ed.* **40**, 2004–2021 (2001).

22. Akitsu, T. *Current Topics in Chirality: From Chemistry to Biology*. (BoD – Books on Demand, 2021).

23. Taiariol, L., Chaix, C., Farre, C. & Moreau, E. Click and Bioorthogonal Chemistry: The Future of Active Targeting of Nanoparticles for Nanomedicines? *Chem. Rev.* **122**, 340–384 (2022).

24. Yoon, H. Y., Lee, D., Lim, D.-K., Koo, H. & Kim, K. Copper-Free Click Chemistry: Applications in Drug Delivery, Cell Tracking, and Tissue Engineering. *Adv. Mater.* **34**, 2107192 (2022).

25. Suazo, K. F., Park, K.-Y. & Distefano, M. D. A Not-So-Ancient Grease History: Click Chemistry and Protein Lipid Modifications. *Chem. Rev.* **121**, 7178–7248 (2021).

26. Agrahari, A. K. *et al.* Cu(I)-Catalyzed Click Chemistry in Glycoscience and Their Diverse Applications. *Chem. Rev.* **121**, 7638–7956 (2021).

27. Meldal, M. & Diness, F. Recent Fascinating Aspects of the CuAAC Click Reaction. *Trends Chem.* **2**, 569–584 (2020).

28. Marsh, E. N. G. & Suzuki, Y. Using 19F NMR to Probe Biological Interactions of Proteins and Peptides. *ACS Chem. Biol.* **9**, 1242–1250 (2014).

29. Filippini, G. *et al.* Mapping the Surface Groups of Amine-Rich Carbon Dots Enables Covalent Catalysis in Aqueous Media. *Chem* **6**, 3022–3037 (2020).

30. Bartolomei, B., Bogo, A., Amato, F., Ragazzon, G. & Prato, M. Nuclear Magnetic Resonance Reveals Molecular Species in Carbon Nanodot Samples Disclosing Flaws. *Angew. Chem. Int. Ed.* **61**, e202200038 (2022).

31. Himo, F. *et al.* Copper(I)-Catalyzed Synthesis of Azoles. DFT Study Predicts Unprecedented Reactivity and Intermediates. *J. Am. Chem. Soc.* **127**, 210–216 (2005).

32. Khan, S., Gupta, A., Verma, N. C. & Nandi, C. K. Time-Resolved Emission Reveals Ensemble of Emissive States as the Origin of Multicolor Fluorescence in Carbon Dots. *Nano Lett.* **15**, 8300–8305 (2015).

33. Sharma, A. *et al.* Origin of Excitation Dependent Fluorescence in Carbon Nanodots. *J. Phys. Chem. Lett.* **7**, 3695–3702 (2016).

34. Zhang, B. *et al.* Assignment of Core and Surface States in Multicolor-Emissive Carbon Dots. *Small* **19**, 2204158 (2023).

35. Cadranel, A. *et al.* Electronic Energy Transduction from {Ru(py)4} Chromophores to Cr(III) Luminophores. *Inorg. Chem.* **57**, 3042–3053 (2018).

36. Wang, D. *et al.* Elucidating interprotein energy transfer dynamics within the antenna network from purple bacteria. *Proc. Natl. Acad. Sci.* **120**, e2220477120 (2023).

37. Scholes, G. D. Long-Range Resonance Energy Transfer in Molecular Systems. *Annu. Rev. Phys. Chem.* **54**, 57–87 (2003).

38. Haedler, A. T. *et al.* Long-range energy transport in single supramolecular nanofibres at room temperature. *Nature* **523**, 196–199 (2015).

39. Liu, Y. *et al.* Weaving of organic threads into a crystalline covalent organic framework. *Science* **351**, 365–369 (2016).

40. van Stokkum, I. H. M., Larsen, D. S. & van Grondelle, R. Global and target analysis of time-resolved spectra. *Biochim. Biophys. Acta BBA - Bioenerg.* **1657**, 82–104 (2004).

41. Mullen, K. M. & Stokkum, I. H. M. van. TIMP: An R Package for Modeling Multi-way Spectroscopic Measurements. *J. Stat. Softw.* **18**, 1–46 (2007).

42. Snellenburg, J. J., Laptenok, S., Seger, R., Mullen, K. M. & Stokkum, I. H. M. van. Glotaran: A Java-Based Graphical User Interface for the R Package TIMP. *J. Stat. Softw.* **49**, 1–22 (2012).

43. Quesada, E., Acuña, A. U. & Amat-Guerri, F. New Transmembrane Polyene Bolaamphiphiles as Fluorescent Probes in Lipid Bilayers. *Angew. Chem. Int. Ed.* **40**, 2095–2097 (2001).

44. Tresse, C. *et al.* Practical Methods for the Synthesis of Trifluoromethylated Alkynes: Oxidative Trifluoromethylation of Copper Acetylides and Alkynes. *Adv. Synth. Catal.* **356**, 2051–2060 (2014).

45. Wang, Y., Qin, C., Jia, X., Leng, X. & Huang, Z. An Agostic Iridium Pincer Complex as a Highly Efficient and Selective Catalyst for Monoisomerization of 1-Alkenes to trans-2-Alkenes. *Angew. Chem. Int. Ed.* **56**, 1614–1618 (2017).

46. Abe, T., Tamura, M. & Sekiya, A. Electrochemical fluorination of several esters derived from oxolane-2-yl-carboxylic acid, oxolane-2-yl-methanol and oxane-2-yl-methanol. *J. Fluor. Chem.* (2005).

47. Minazzi, P., Lattuada, L., Menegotto, I. G. & Giovenzana, G. B. An enzymatic approach to bifunctional chelating agents. *Org. Biomol. Chem.* **12**, 6915–6921 (2014).

48. Chatterjee, S., Makai, S. & Morandi, B. Hydroxylamine-Derived Reagent as a Dual Oxidant and Amino Group Donor for the Iron-Catalyzed Preparation of Unprotected Sulfinamides from Thiols. *Angew. Chem. Int. Ed.* **60**, 758–765 (2021).

49. Anderson, C. A., Taylor, P. G., Zeller, M. A. & Zimmerman, S. C. Room Temperature, Copper-Catalyzed Amination of Bromonaphthyridines with Aqueous Ammonia. *J. Org. Chem.* **75**, 4848–4851 (2010).

50. Shin, K., Baek, Y. & Chang, S. Direct C-H Amination of Arenes with Alkyl Azides under Rhodium Catalysis. *Angew. Chem. Int. Ed.* **52**, 8031–8036 (2013).

Chapter IV – Synthesis and Characterization of CND/polymer Nanoconjugates

Abstract

This Chapter includes the synthesis and characterization of new Carbon NanoDots (CND)-based composites, namely CND/polymer nanoconjugates, with a particular focus on the study of their molecular weight distribution and composition *via* multi-detector Gel Permeation Chromatography (GPC).

In the first part of the chapter, we describe how a polymeric structure could be designed and fine-tuned, by employing Reversible Addition-Fragmentation chain Transfer (RAFT) polymerization. After polymer synthesis, we provide an in-depth characterization of the synthesized *N*-isopropyl acrylamide (NIPAA)-based copolymer, evaluating its thermoresponsive properties and determining its molecular weight moments and distribution by multi-detector GPC in both organic and aqueous conditions.

Subsequently, we move on to the two-step synthesis of CND/polymer nanoconjugates, assessing the effective achievement of the desired product by NMR spectroscopy. We thoroughly characterized these new composites, confirming the retention of key characteristics of both their starting materials (*i.e.*, intrinsic blue fluorescence of CNDs and thermoresponsive behavior of the NIPAA-based polymer).

The remainder of the chapter focuses on the compositional and multi-detector GPC characterization of CND/polymer nanoconjugates, providing deeper insights on their structure. These analyses corroborate the polymer-to-CND ratio predicted from the GPC studies on pristine CNDs (Chapter II), which was already confirmed for CND-based covalent assembly (Chapter III).

The synthesis and characterization of the polymer and of the CND/polymer nanoconjugates were carried out within the Gobbo group, under the supervision of Prof. Pierangelo Gobbo and Prof. Maurizio Prato, while GPC characterization was performed during a three-month internship at Malvern Panalytical Ltd (UK), under the supervision of Dr. Serena Agostini and Prof. Pierangelo Gobbo.

4.1 Introduction

The possibility of exploiting the interfacial chemistry of Carbon Dots (CDs) – specifically Carbon NanoDots (CNDs) in this Thesis, as described in Chapter II and III – paves the way to build new composite structures which might express different features from their starting materials, for example in terms of emissive properties or solubility.

Among the varieties of CD-based nanohybrids, CD/polymer nanocomposites are particularly interesting due to the CD capacity to enhance or modify mechanical or conductive properties of polymers that are already being used for specific applications in energy and environmental chemistry and biomedicine.[1]

Thermoresponsive polymers are a class of materials that can alter their physicochemical properties in response to temperature changes.[2] If increasing the temperature of a polymer solution leads to two immiscible liquid phases with different polymer concentrations, the mixture has a lower critical solution temperature (LCST). Conversely, if cooling the mixture creates two liquid phases, it exhibits an upper critical solution temperature (UCST).[3] This behavior is often reversible and modulates polymer hydrophilicity, which is widely utilized in biomedical applications, particularly for LCST-type polymers.[2]

Of particular significance, poly(*N*-isopropylacrylamide) (PNIPAA) has an amphiphilic nature and exhibits an LCST close to physiological temperature.[2,4] Structurally, PNIPAA has a hydrophobic backbone with a hydrophilic amide group and hydrophobic isopropyl moiety. Below the LCST, hydrogen bonding with water molecules keeps PNIPAA in a hydrated, coiled conformation; above the LCST, hydrogen bonds weaken, leading to dehydration and polymer aggregation (coil-to-globule transition). This phase shift is entropy-driven, triggered by dehydration at the critical temperature.[5]

Numerous examples of multifunctional PNIPAA-based system are designed based on either PNIPAA copolymerized with functional comonomers or PNIPAA combined with nanomaterials.[6] Several reports are available in the literature in which CDs and PNIPAA features are combined to fabricate, in most cases, hydrogels.[7–10] On the contrary, only a limited number of CD/PNIPAA nanocomposites synthesized exploiting CD surface covalent chemistry is available. These nanocomposites have found applications as drug-releasing agents, fluorescent tracers, and colloidal stabilizers.[11–13] Even though it is widely reported for other type of polymeric system and nanomaterials,[14–16] to the best of our knowledge, no examples are published on CD/PNIPAA nanosystems which exploit the polymer amphiphilicity in order to expand CD applicability.

Herein, our final aim is to fabricate CD-based microcapsules by exploiting the Pickering emulsion technique.[17] Therefore, the first step is to convert CDs into Pickering emulsifiers by making them amphiphilic, since CDs are hydrophilic in their pristine form.[18]

In order to achieve so, we grafted a NIPAA-based polymer onto CD surface, in the same fashion of precedent reports on protein/polymer nanoconjugates.[19]

In this Chapter we initially describe the synthesis of a NIPAA-based copolymer, carried out *via* RAFT polymerization, and its detailed characterization. RAFT polymerization technique is chosen due to its versatility in polymerizing a wide range of functional monomers, predictable polymer molecular weights, and narrow molecular weight distribution.[20] These desirable features allowed us to design a PNIPAA-based copolymer with the following features: amphiphilic structure, reactivity towards activated carbonyl moieties, and fluorescence tagging.

Subsequently, the synthesis and characterization of *L*-arginine and ethylenediamine-derived CND/polymer nanoconjugates is shown, with particular attention on their compositional GPC analysis.

4.2 Results and Discussion

4.2.1 Design of the Polymer Structure

As previously explained in Chapter I and in the Introduction of this Chapter, due to its amphiphilicity, a NIPAA-based polymer is essential to synthesize CND/polymer nanoconjugates. This is due to the intrinsic hydrophilicity of CNDs, which would not be efficient in stabilizing the Pickering emulsions for microcapsule assembly by themselves.[18]

Firstly, we synthesized a chain transfer agent, or RAFT agent in this case, bearing an activated carbonyl group (*i.e.*, mercaptothiazoline), which will be exploited for the coupling reaction with the CNDs. The RAFT agent (1) was synthesized following a procedure reported in literature and slightly modified by the Gobbo group (see Experimental Section, 4.4.2 Synthesis of RAFT agent).[19]

Alongside with the amphiphilicity, key features of our polymer design are the presence of primary amine sidechains and of a fluorescent label on the main polymer chain. In order to impart these properties to the CND/polymer nanoconjugates, NIPAA was copolymerized randomly with two acrylate-based comonomers, being 2-aminoethyl methacrylate (AEMA) and methacryloxyethyl thiocarbamoyl rhodamine B (RhB).

The first comonomer, AEMA, was chosen to exploit the primary amine moiety for the covalent crosslinking of CND-based microcapsules. In detail, the crosslinking of CND-based microcapsules is performed by reacting the primary amines with active groups of a crosslinking agent (see Chapter V for a detailed description) in order to form covalent bonds preventing microcapsule disassembly upon transferring the emulsion to a continuous phase. To prevent this moiety to undergo unwanted reaction during the synthesis of CND/polymer nanoconjugates, we protected the amine of the AEMA monomer with *tert*-butyloxycarbonyl (Boc) protecting group, synthesizing the Boc protected AEMA (AEMA*Boc) before polymerization.

The second chosen comonomer was a fluorescent methacrylate, particularly methacryloxyethyl thiocarbamoyl rhodamine B (RhB). This comonomer was selected to add a fluorescent label to the polymer, considering that the main characterization technique for CND-based microcapsules is fluorescence microscopy. Since CNDs are intrinsically fluorescent, the presence of a fluorescent label on the polymer chains allows us to image the polymer part of the CND/polymer nanoconjugates as well and prove their co-localization at the membrane of the microcapsules. Moreover, RhB was picked because its strong emission band – in the range of 580-680 nm depending on the fluorophore concentration[21,22] – does not overlap with CND emission band. Thus,

we could minimize the crosstalk between the fluorophores excitation and emission wavelengths, obtaining the best imaging conditions.

Eventually, the final desired polymer structure is poly(*N*-isopropylacrylamide-*co*-aminoethyl methacrylate*Boc protected-*co*-methacryloxyethyl thiocarbamoyl Rhodamine B) (PNIPAA-*co*-AEMA*Boc-*co*-RhB, 3).

4.2.2 Synthesis and Characterization of PNIPAA-*co*-AEMA*Boc-*co*-RhB

Firstly, the protection of AEMA with Boc protecting group was carried out and ^{1}H-NMR spectroscopy confirmed the synthesis of the desired product 2 (see Experimental Section, 4.4.3 Synthesis of AEMA*Boc).

Then, we moved to the RAFT polymerization of the PNIPAA-*co*-AEMA*Boc-*co*-RhB copolymer 3 (**Figure 4.1.a**, see Experimental Section, 4.4.4 RAFT polymerization of PNIPAA-*co*-AEMA*Boc-*co*-RhB). Briefly, NIPAA (χ = 99.48), AEMA*Boc (2, χ = 0.5), RhB (χ = 0.02), RAFT agent (1) and initiator 2,2′-Azobis(2-methylpropionitrile) (AIBN, molar ratio AIBN:RAFT agent 1:5) were solubilized in acetonitrile (CH_3CN) and transferred in a Schlenk tube. After degassing the mixture by three freeze-pump-thaw cycles, the solution was left reacting at 65°C for 13.5 hours.

After precipitation of the reaction crude in a mixture hexane/diethyl ether, we isolated a pink powder that was analyzed by ^{1}H-NMR spectroscopy which confirmed the successful polymerization (**Figure 4.1.b**). In the spectrum broad signals associated with a polymer were visible, as well as the signal associated to tert-butyl group of the Boc protecting group (1.44 ppm) and the methylene protons of the activated head group of the RAFT agent (**Figure 4.1.b** inset). By using an internal standard (DMF) method, it was possible to determine the conversion degree of the reaction (81%) and to estimate the M_n of copolymer 3 from the NMR spectrum of the isolated polymer, which was around 12,000 g mol^{-1}.

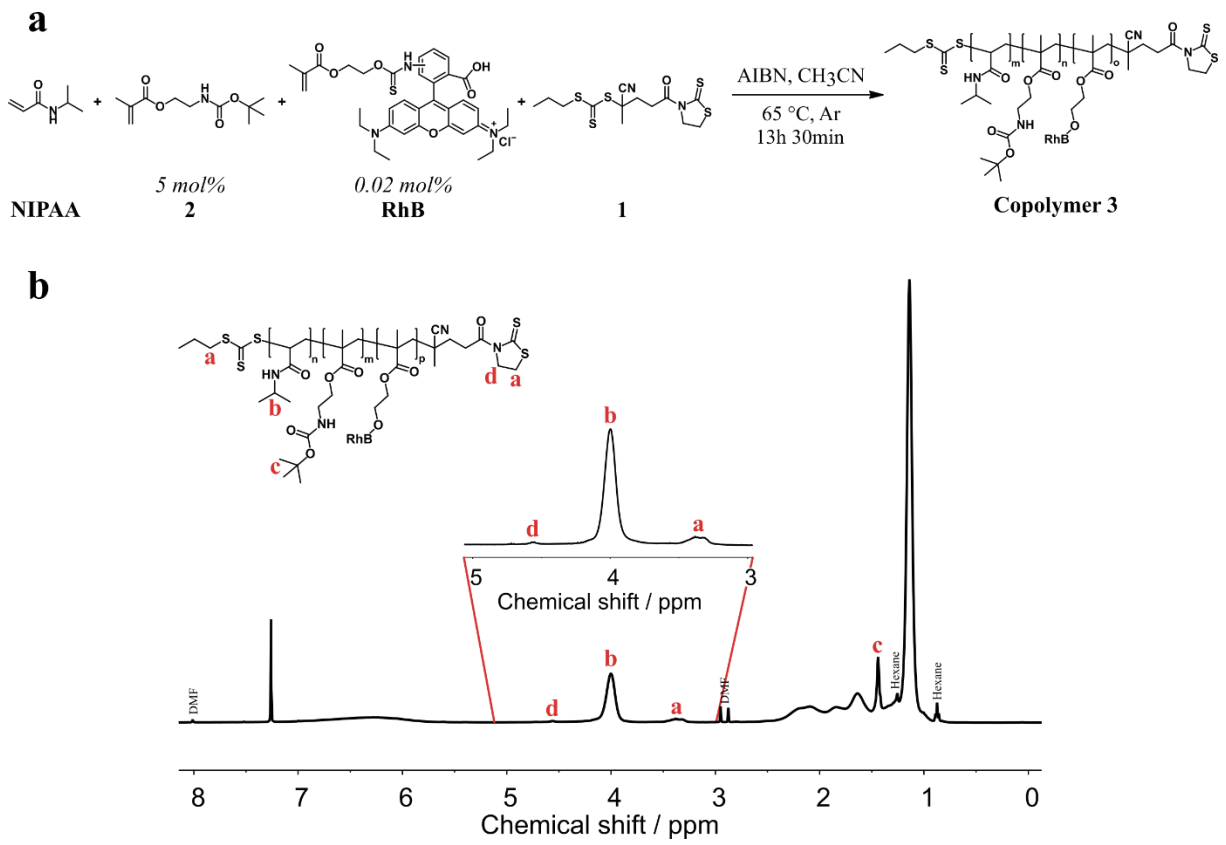

Figure 4.1. a) *RAFT polymerization scheme of copolymer **3**;* ***b)*** *^{1}H-NMR spectrum of copolymer **3** in deuterated chloroform, referenced against solvent residual peak (δH: 7.26 ppm, 400 MHz, r.T). Some residual solvent is detected in the spectrum: DMF (internal standard) 2.78 ppm (s), 2.94 ppm (s), 7.96 ppm (s); hexane (work-up) 0.88 ppm (t), 1.26 ppm (m).*

Then, ATR-FTIR spectroscopy (**Figure S4.1**) confirmed the presence of the expected functional groups (*i.e.*, amine, amide groups) according to the chosen monomer. Particularly, we detected the N-H stretching band at 3282 cm^{-1}, the C-H stretching bands at 2968 and 2920 cm^{-1}, and the stretching peak of carbonyl group of the amides at 1632 cm^{-1}.

Moreover, we also investigated the thermoresponsive properties of PNIPAA-*co*-AEMA*Boc-*co*-RhB, by determining its Lower Critical Solution Temperature (LCST) by turbidimetry.

Copolymer 3 showed a thermoresponsive reversible behavior, as shown in **Figure 4.2**. Considering the obtained hysteresis curves, the temperature-dependent trend is in accordance with literature results reported for pristine PNIPAA,[23] and the LCST of copolymer 3 resulted to be 24 ± 2 °C.

The lowering of this copolymer LCST compared to that of pristine PNIPAA (32 °C)[24] is due to the inclusion of the monomer 1 in the structure, since it has a strongly hydrophobic nature. This finding was in agreement with previous reports on LCST of PNIPAA influenced by the hydrophobicity of chosen comonomers or substituents.[25,26]

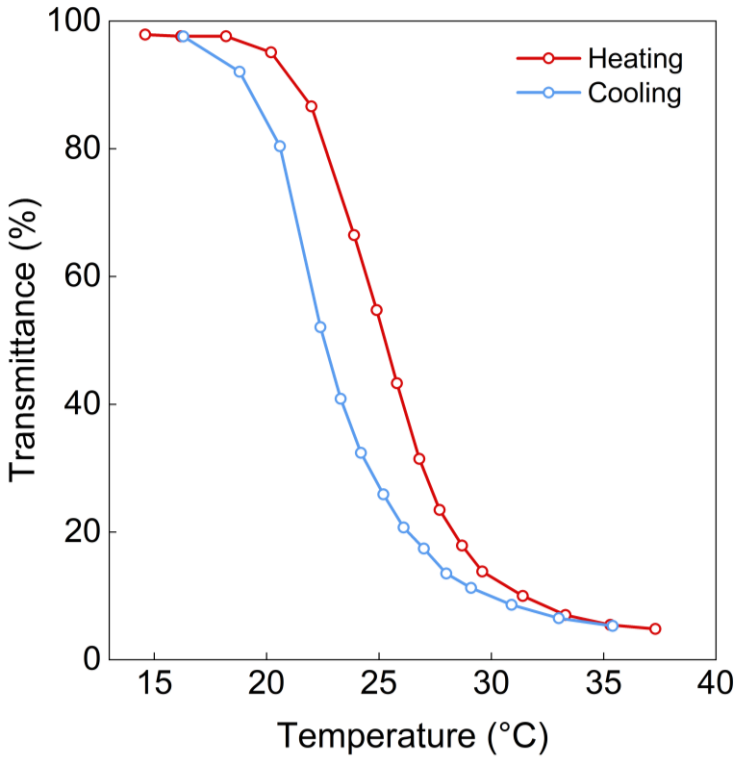

Figure 4.2. *Turbidimetric measurements of the LCST of copolymer 3 (PNIPAA*-co-*AEMA*Boc*-co-*RhB) (0.5 mg mL*$^{-1}$ *solution in MilliQ water). Red curve is registered increasing the temperature, while blue curve is registered decreasing the temperature. LCST was determined by measuring the temperature at which transmitted light (400 nm) corresponds to 50%.*

4.2.2.1 Multi-detector GPC Characterization of PNIPAA-*co*-AEMA*Boc-*co*-RhB

To determine PNIPAA-*co*-AEMA*Boc-*co*-RhB molecular weight, the polymer was firstly analyzed in organic conditions, reported in **Table 4.1**. Particularly, styrene-divinyl benzene-based columns (see Experimental Section, 4.4.1 Materials and Methods) were employed in combination with 1 w/V% tetrabutylammonium bromide (TBAB) in THF.

Table 4.1. *GPC organic set-up for copolymer 3 analysis.*

Stationary phase	T6000M + T2500
Mobile phase	1 w/V% TBAB in THF
Concentration (mg mL^{-1})	1
Injection Volume (µL)	100
Flow rate (mL min^{-1})	1
Autosampler Temperature (°C)	20
Column Oven Temperature (°C)	35
Detector Oven Temperature (°C)	35

With this set-up, the polymer delivered high quality chromatograms, both in term of peak symmetry and tailing, (**Figure 4.3.a**) with a monomodal distribution and a good reproducibility (see Experimental Section, 4.4.5 Multi-detector GPC analysis of PNIPAA-*co*-AEMA*Boc-*co*-RhB, **Figure S4.3**). **Figure 4.3.b** showed the chart of derived data, namely molecular weight, intrinsic viscosity and hydrodynamic radius, which decreased going from smaller (*i.e.*, high hydrodynamic size) to larger retention volume (*i.e.*, small hydrodynamic size), as expected.

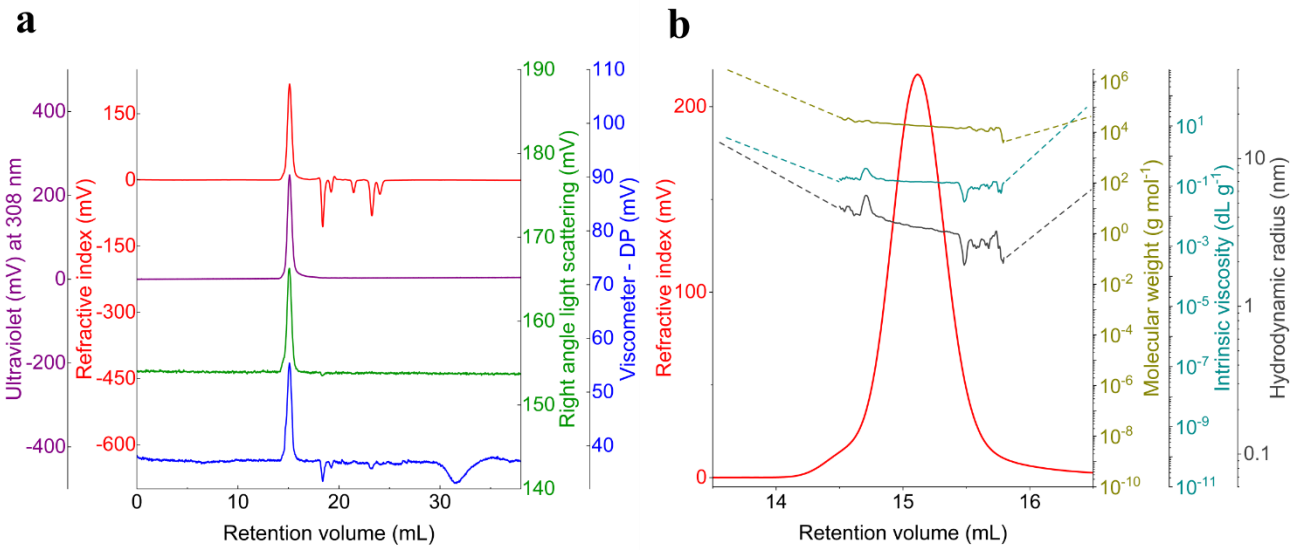

Figure 4.3. a) *GPC chromatograms of PNIPAA-co-AEMA*Boc-co-RhB (1 w/V% TBAB in THF) on T6000M + T2500 columns, from top to bottom, refractive index (RI) curve (red), ultraviolet (UV) curve (purple), right angle light scattering (RALS) curve (green), and viscometer curve (blue), respectively;* ***b)*** *Derived data of a PNIPAA-co-AEMA*Boc-co-RhB run, showing trends of molecular weight (dark yellow line), intrinsic viscosity (teal line), and hydrodynamic size (dark gray line) with respect to the polymer RI peak. The dashed lines reported for each trend are predicted values.*

To make sure our results were accurate, we followed the same calculation procedure employed for CNDs (see Chapter II). Therefore, we determined the concentration underlying the refractive index (RI) chromatographic peak exploiting the UV detector response. Specifically, we used the sample input concentration – the known concentration at which the sample was prepared – and the copolymer specific absorption coefficient, dA/dC, at 308 nm (*i.e.*, its absorption maximum). To validate this methodology, we carried out a tubing test to confirm that the dA/dC was correct (Experimental Section, 4.4.5 Multi-detector GPC analysis of PNIPAA-*co*-AEMA*Boc-*co*-RhB). The obtained results yielded a refractive index increment (dn/dC) of 0.158, were M_n of 18,383 ± 39 g mol^{-1}, M_w of 19,264 ± 94 g mol^{-1}, and a very low dispersity ($Đ$ = 1.05) as expected from a polymer synthesized *via* RAFT polymerization. These values were slightly higher if compared to the molecular weight calculated by ^{1}H NMR spectroscopy. According to the literature, NMR and GPC techniques show overall agreement at low molecular weights, while some discrepancies arise for high molecular weight samples. While ^{1}H NMR spectroscopy identifies the proton signals associated with specific bonds and delivers sample molecular weight by simple calculations – sometimes considering only the most abundant monomer in the polymer structure – it does not

reveal its distribution. On the other hand, GPC determines the sample molecular weight from its dn/dC and takes into account the molecular weight distribution of the whole polymer sample.[27,28] Consequently, GPC can be considered a more reliable characterization technique for polymer molecular weights moment and distribution.

Having characterized the copolymer 3 in organic conditions, where the polymer does not display thermoresponsive properties, we moved to multi-detector GPC analysis of this NIPAA-based copolymer into aqueous conditions. This GPC characterization was carried out to then study the structure of the composite material of CNDs with copolymer 3. In order to do so, we need the complete GPC characterization of the constituting materials of the CND/polymer nanoconjugates in the same elution conditions (*i.e.*, aqueous conditions for this system, since CNDs are not soluble into organic solvents) (see 4.2.3.1 Multi-detector and Compositional GPC Characterization of CND/polymer Nanoconjugates).

In order to develop the most suitable chromatographic conditions to analyze the polymer in an aqueous set-up, we first investigated whether there was a correlation between its thermoresponsive behavior and the salt type and concentration in solution. This was because the copolymer 3 exhibited a LCST near room temperature.

This type of correlation was found in the Hofmeister series (**Figure 4.4**), which ranks the relative influence of ions on the physical behavior of a wide variety of aqueous processes. This behavior is more pronounced for anions than cations and is quite general.[29]

Anions: $HCO_2^- > CH_3CO_2^- > F^- > Cl^- > Br^- > NO_3^- > I^- > ClO_4^- > SCN^-$

Cations: $Li^+ > Cs^+ > Rb^+ > Na^+ > NH_4^+ > (CH_3)_4N^+ > (C_2H_5)_4N^+$

Figure 4.4. *Hofmeister series of anions and cations arranged from the most kosmotropic to the most chatropic (from left to right).*

Ions on the left are called kosmotropes, which tend to induce the precipitation of PNIPAA from solution and prevent its unfolding, whereas ions on the right are chaotropes, which increase polymer solubility. Chloride is usually considered the dividing line between these two types of behavior.[30]

In **Figure 4.5** are reported plot of the lower critical solution temperature values for PNIPAA as a function of salt concentration for a series of 11 different salts.[31]

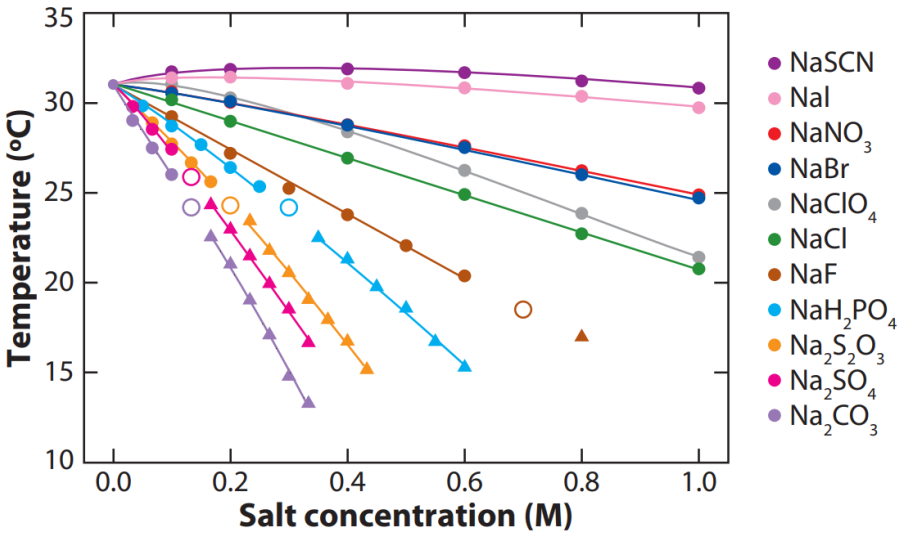

Figure 4.5. *Plot of the lower critical solution temperature values for PNIPAA as a function of salt concentration between 0.0 and 1.0 M for a series of 11 Hofmeister salts. Used with permission of Annual Reviews, Inc. from Chemistry of Hofmeister anions and osmolytes, Zhang, Yanjie; Cremer, Paul S., 61, 2010]; permission conveyed through Copyright Clearance Center, Inc.*

According to this series, low salt concentrations and more chaotropic ions help heighten the polymer LCST (*i.e.*, maintain it in the solubilized state). Among the listed salts, sodium nitrate is one of the most stabilizing for PNIPAA. Since we had used an eluent mixture containing this salt for the CND runs (0.1 M $NaNO_3$ pH 2.6/CH_3COOH on cationic columns), we checked if these conditions were suitable for copolymer 3 by carrying out some ζ-potential measurements (**Table 4.2**).

Table 4.2. *ζ-potential values of copolymer 3 in different aqueous solutions, listed from the less chaotropic salt to the more chaotropic one.*

Solvent	ζ-potential (mV)
0.1 M NaCl pH 2.6/HCl	-1.8 ± 1.1
0.1 M KCl pH 2.6/HCl	-2.2 ± 2.1
0.1 M LiBr pH 2.6/HCl	-2.6 ± 1.2
0.1 M $NaNO_3$ pH 2.6/CH_3COOH	-3.3 ± 1.5
0.1 M $NaNO_3$ pH 2.6/HNO_3	-4.6 ± 1.7
0.1 M $NaClO_4$ pH 2.6/HCl	-5.0 ± 0.5

These results showed ζ-potential values and chaotropic nature of the salt used followed and inverse trend. More stable was the polymer in solution (*i.e.*, more chaotropic was the salt, thus higher was the LCST of the polymer), less positive was the ζ-potential retrieved. Therefore, according to this data, it was not possible to analyze this polymer on cationic columns in the same conditions optimized for CNDs. This is because a neutral to negative superficial charge of the NIPAA-based polymer would inevitably lead to strong interaction with the column packing material during the chromatographic separation, which would not yield the desired results.

Assessed that, we thought of using a stationary phase made of neutral hydrophilic film bonded silica, optimized for hydrophobic samples, and sodium perchlorate ($NaClO_4$, *i.e.*, the most chaotropic of the analyzed species) as salt for the mobile phase. This was done to try to minimize the strong hydrophobic character of copolymer 3 expressed at room temperature (*i.e.*, LCST of 24 °C). The optimized aqueous conditions for GPC analysis are reported in **Table 4.3**.

Table 4.3. *GPC aqueous set-up for copolymer **3** analysis.*

Stationary phase	Zenix-C-SEC-300
Mobile phase	0.1 M $NaClO_4$ pH 4/HCl
Concentration (mg mL^{-1})	3
Injection Volume (µL)	50
Flow rate (mL min^{-1})	0.5
Autosampler Temperature (°C)	4
Column Oven Temperature (°C)	20
Detector Oven Temperature (°C)	20

With this set-up, we managed to analyze copolymer 3 also in aqueous conditions (**Figure 4.6**) with good quality chromatograms and derived data (see Experimental Section, 4.4.5 Multi-detector GPC analysis of PNIPAA-*co*-AEMA*Boc-*co*-RhB, **Figure S4.4**). They showed a monomodal distribution of copolymer 3, indicating the presence of a single polymer specie, and a very narrow molecular weight distribution as showed from the molecular weight curve (**Figure 4.6.b**) which has a constant trend over retention volume range of 8 to 10 mL.

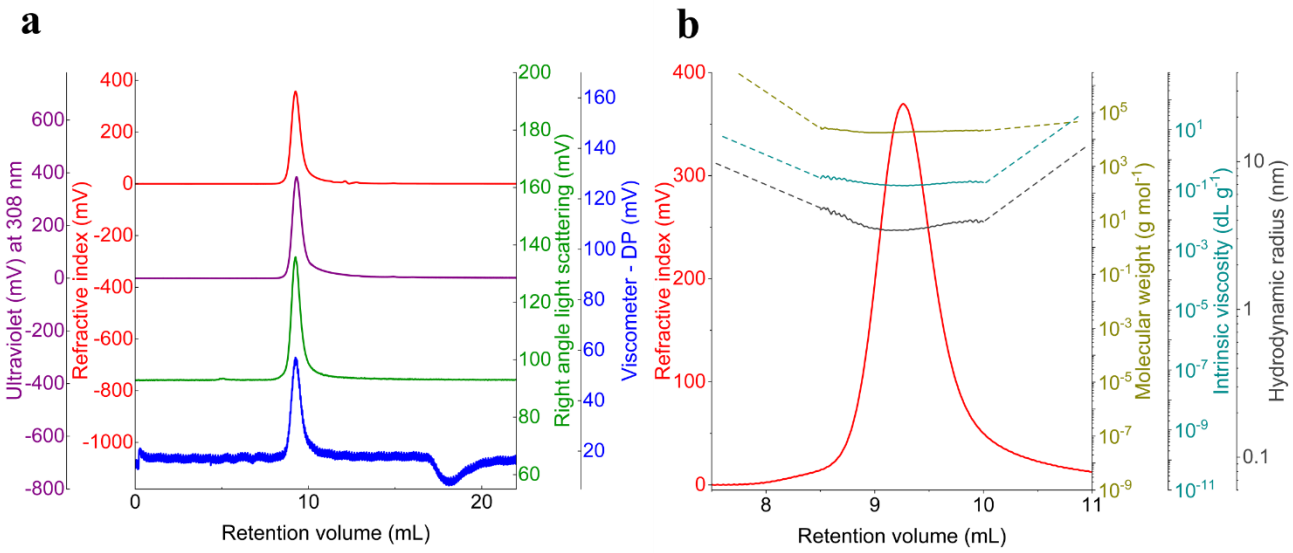

Figure 4.6. *GPC chromatograms of copolymer 3 (0.1 M $NaClO_4$ pH 4/HCl) on Zenix-C-SEC-300 silica column, from top to bottom, refractive index (RI) curve (red), ultraviolet (UV) curve (purple), right angle light scattering (RALS) curve (green), and viscometer curve (blue), respectively;* ***b)*** *Derived data of a copolymer 3 run, showing trends of molecular weight (dark yellow line), intrinsic viscosity (teal line), and hydrodynamic size (dark gray line) with respect to the polymer RI peak. The dashed lines reported for each trend are predicted values.*

To confirm our results, we could not rely on tubing tests in aqueous conditions for this polymer as previously done for the organic set-up. Therefore, we validated the dA/dC of copolymer 3 using UV-Vis data acquired previously (see Experimental Section, 4.4.5 Multi-detector GPC Analysis of PNIPAA-*co*-AEMA*Boc-*co*-RhB) and, once again, we determined the concentration underlying the RI chromatographic peak from the dA/dC of the polymer at 308 nm.

The obtained results were an average M_n of 20,106 ± 1,079 g mol^{-1}, an average M_w of 20,241 ± 1,055 g mol^{-1}, and a very low dispersity ($Đ$ = 1.007). These values were in good agreement with the ones obtained in organic conditions, considering the experimental error. Moreover, it was interesting to notice that the calculated refractive index increment of this polymer in aqueous conditions was 0.185, that is the same number used to determine the molecular weight distribution of proteins. This outcome matched with the chemistry of our system since the analyzed polymer is a polyamide, such as proteins which are biomolecules that comprises one or more chains of polypeptides.

4.2.3 Synthesis and Characterization of CND/polymer Nanoconjugates

After an in-depth characterization of copolymer 3, we moved on to the synthesis of its nanoconjugates with CNDs. The CNDs employed for this synthesis are described in detail in Chapter II and have been previously reported by the Prato group.[32]

CNDs were functionalized with copolymer 3 to yield CND/polymer nanoconjugates (see Experimental Section, 4.4.6 Synthesis of CND/polymer Nanoconjugates). They were obtained by an amidation reaction promoted by the mercaptothiazoline-activated terminal carbonyl in the polymer which reacted with the surface primary amine groups of CNDs (**Figure 4.7.a**).

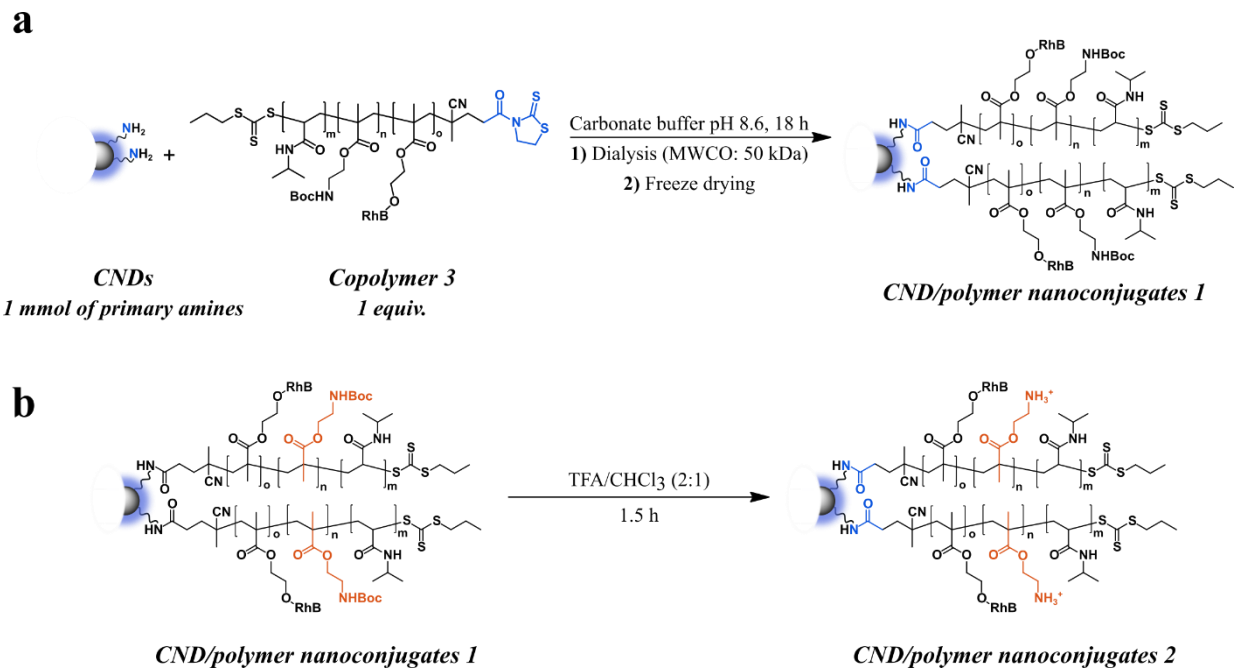

Figure 4.7. a) *Coupling reaction between CNDs and copolymer 3 in 0.1 M Na_2CO_3/$NaHCO_3$ carbonate buffer pH 8.6* via *amidation reaction between primary amines on CND surface and activated carbonyl of the polymer;* ***b)*** *Deprotection reaction in TFA/$CHCl_3$ mixture to eliminate the Boc protecting group from the primary amines on the polymer chains.*

The success of this conjugation step was confirmed by ^{1}H-NMR experiments (**Figure 4.8.a**) which displayed the absence of protons of the leaving group at 4.56 ppm (*i.e.*, methylene protons in α to nitrogen of the mercaptothiazoline), compared to the ^{1}H-NMR of the polymer (**Figure 4.8.a**). It was interesting to observe that the NMR profile of the CND/polymer nanoconjugates 1 closely matched the NMR spectrum of copolymer 3. This was because the ^{1}H NMR signals from CNDs are broad and low in intensity compared to those of copolymer 3, and thus did not appear in the nanoconjugate 1 spectrum (**Figure S4.5**).

After this coupling reaction, the Boc-protective groups on the CND/polymer nanoconjugates were cleaved with TFA in order to make the primary amines on the polymer available for further reactions (*i.e.*, crosslinking) (**Figure 4.7.b**).

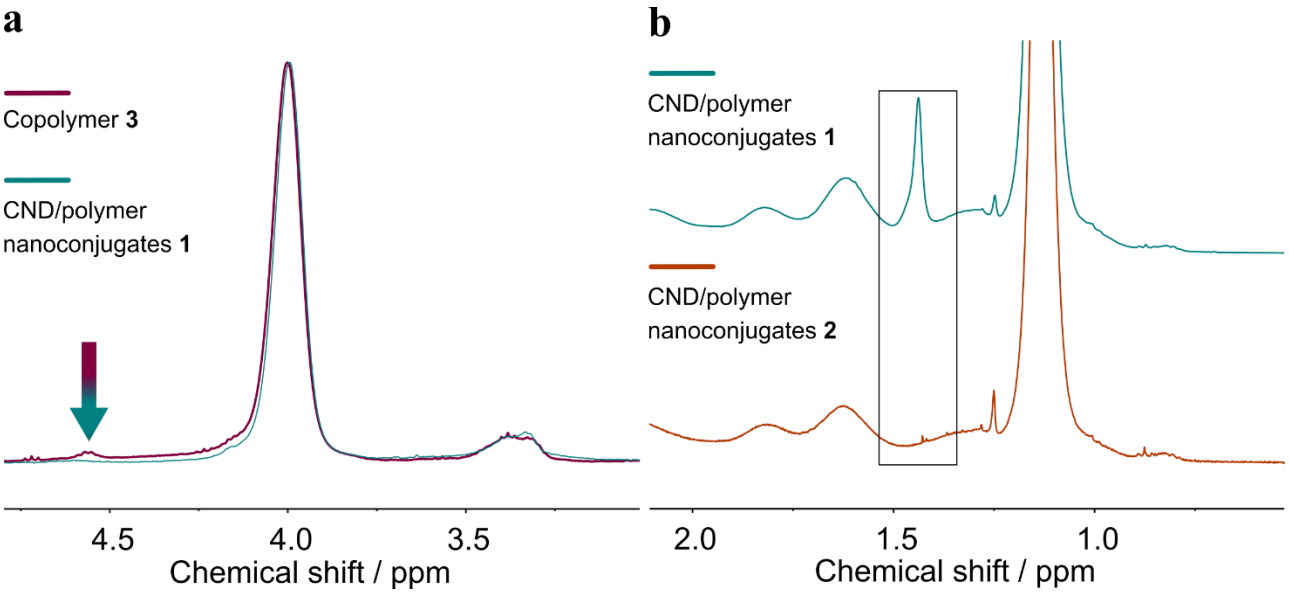

Figure 4.8. a) *^{1}H-NMR superimposed spectra overlay of copolymer 3 (dark purple profile) and CND/polymer nanoconjugates 1 (teal profile) in deuterated chloroform, referenced against solvent residual peak (δH: 7.26 ppm, 400 MHz, r.T);* ***b)*** *^{1}H-NMR stacked spectra overlay of CND/polymer nanoconjugates 1 (top, teal profile) and 2 (bottom, dark orange profile) in deuterated chloroform, referenced against solvent residual peak (δH: 7.26 ppm, 400 MHz, r.T).*

The deprotection was confirmed by comparing the ^{1}H-NMR spectra of CND/polymer nanoconjugates 1 and 2 (**Figure 4.8.b**). In particular, the signal at 1.44 ppm, associated with Boc protecting group, was not visible in the deprotected CND/polymer nanoconjugates spectrum. Moreover, the effective removal of TFA from the sample was proved by ^{19}F NMR spectroscopy, which did not show the -75 ppm signal of TFA (**Figure S4.6**).[33]

From now on, if not otherwise stated, the characterization data will refer to the CND/polymer nanoconjugates 2 (deprotected CND/polymer nanoconjugates), which is the final (active) form of the building blocks employed to build CND-based microcapsules.

To further demonstrate the successful synthesis of CND/polymer nanoconjugates, we ran DOSY experiments and compared the results with the ones obtained previously for the CNDs. The DOSY profile showed a homogeneous signal trace ascribed to the CND/polymer nanoconjugates, at different diffusion coefficients with respect to the solvent residual peak (**Figure 4.9**). The retrieved D_0 for CND/polymer nanoconjugates was an order of magnitude smaller than CND diffusion coefficient (4.47×10^{-11} m^2 s^{-1} and 2.75×10^{-10} m^2 s^{-1}, respectively). This finding meant that the

species in solution is larger than CNDs, therefore diffuses more slowly, further supporting the effective coupling between CNDs and copolymer 3.

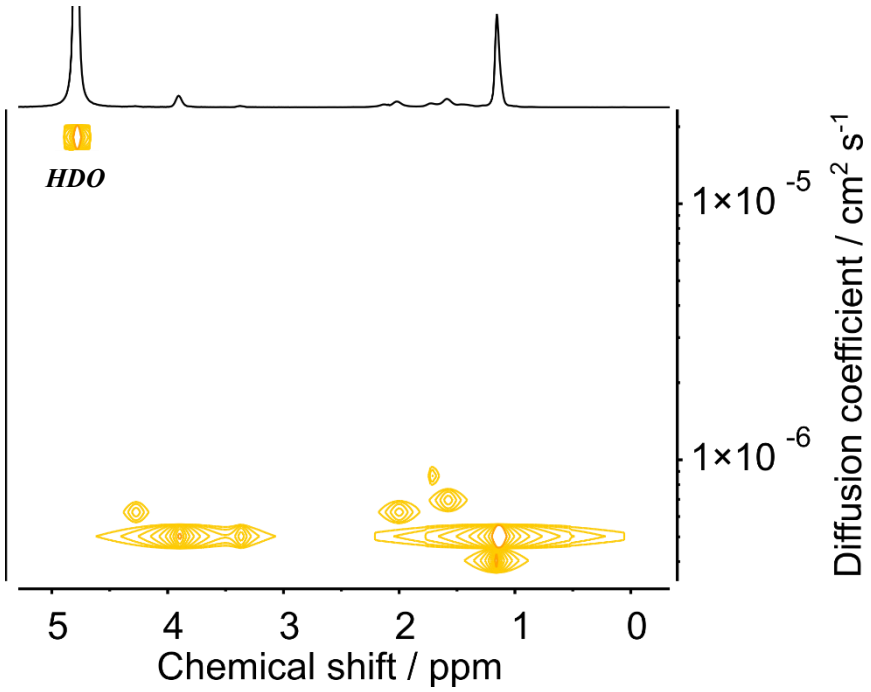

Figure 4.9. *DOSY trace of CND/polymer nanoconjugates in deuterium oxide, referenced against solvent residual peak (δH: 4.79 ppm, 500 MHz, r.T).*

ATR-FTIR spectroscopy (**Figure 4.10**), as for NMR spectroscopy, showed a profile for CND/polymer nanoconjugates 2 that corresponded almost completely to the spectrum of the copolymer 3. Specifically, the band at 3289 cm^{-1} (N-H stretching), the bands at 2971 and 2933 cm^{-1} (C-H stretching), and the peak at 1640 cm^{-1} (carbonyl of amides) derived from the polymer structure, whereas the peak at 1739 cm^{-1}, assigned to C=O stretching, might come from the CND structure.[32]

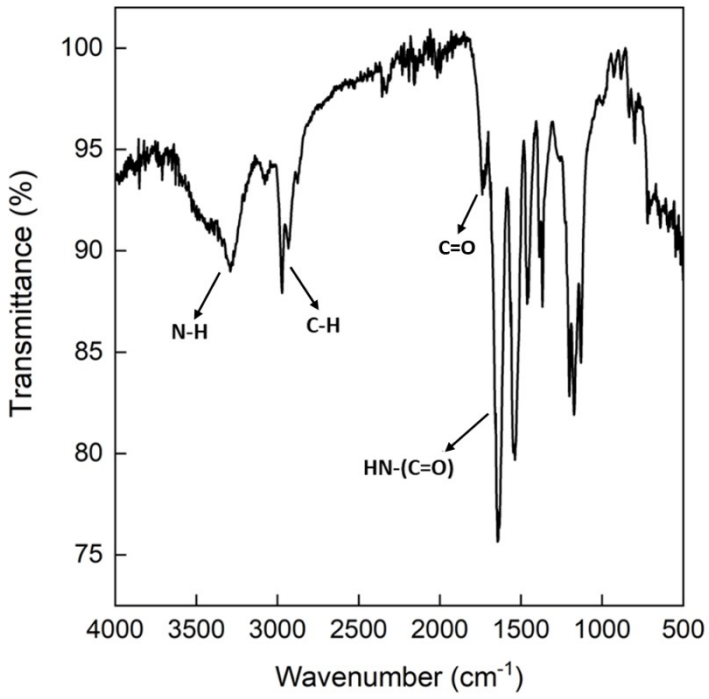

Figure 4.10. *ATR-FTIR of CND/polymer nanoconjugates* ***2****.*

AFM (**Figure 4.11**) micrographs, acquired in tapping mode on drop-casted samples from methanol, showed round shaped objects with an average size of 10 ± 3 nm. These results were in accordance with AFM measurements performed in the same conditions on CNDs and copolymer 3 (4 ± 1 nm and 5 ± 2 nm, respectively, **Figure S4.2**) supporting the evidence of the coupling between the two species.

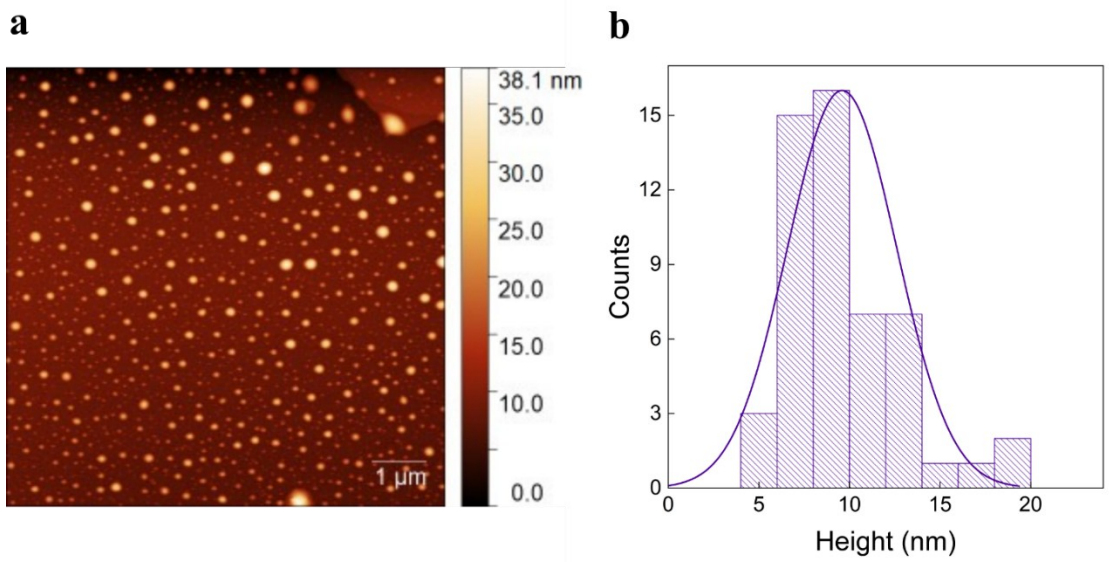

Figure 4.11. a) *Tapping mode AFM topography image of CND/polymer nanoconjugates* ***2*** *drop-casted on a mica substrate from a methanol solution (1 ng mL^{-1}) at room temperature. Color brightness indicates the relative height, from lowest (dark) to highest (bright);* ***b)*** *Size distribution of CND/polymer nanoconjugates.*

Then we moved to investigate whether CND/polymer nanoconjugates 2 retained the features of their individual building blocks. Specifically, these features include the photophysical properties of CNDs and the thermoresponsive properties of copolymer 3.

At first, we carried out photophysical characterization of the CND/polymer nanoconjugates 2 *via* UV-Vis and fluorescence spectroscopy. In **Figure 4.12.a** we reported the absorbance spectrum of CND/polymer nanoconjugates 2 (dark orange profile) compared to the pristine CND (blue profile) and copolymer 3 (dark purple profile). It was well-observable that, also in this case, the absorbance profile resembled more the polymer one except for the absence of the 280 nm band. This band is assigned to the mercaptothiazoline, as we could confirm by acquiring the absorption spectrum of compound 1 (RAFT agent) and its analogous without mercaptothiazoline (**Figure S4.7**). This head group in copolymer 3 is the leaving group of the first step of CND/polymer nanoconjugates synthesis. Consequently, this supported the functionalization of CNDs with copolymer **3**. **Figure 4.12.b** shows the normalized emission map of CND/polymer nanoconjugates 2, which expresses a wavelength-dependent emission behavior as CNDs in the 300 – 400 nm excitation wavelength range.[32] Instead, the spectral region centered at 558 nm is linked to the RhB emission in copolymer 3 and it did not present excitation wavelength dependency, since RhB is a molecular fluorophore and was not affected by the proximity to the CNDs.[34]

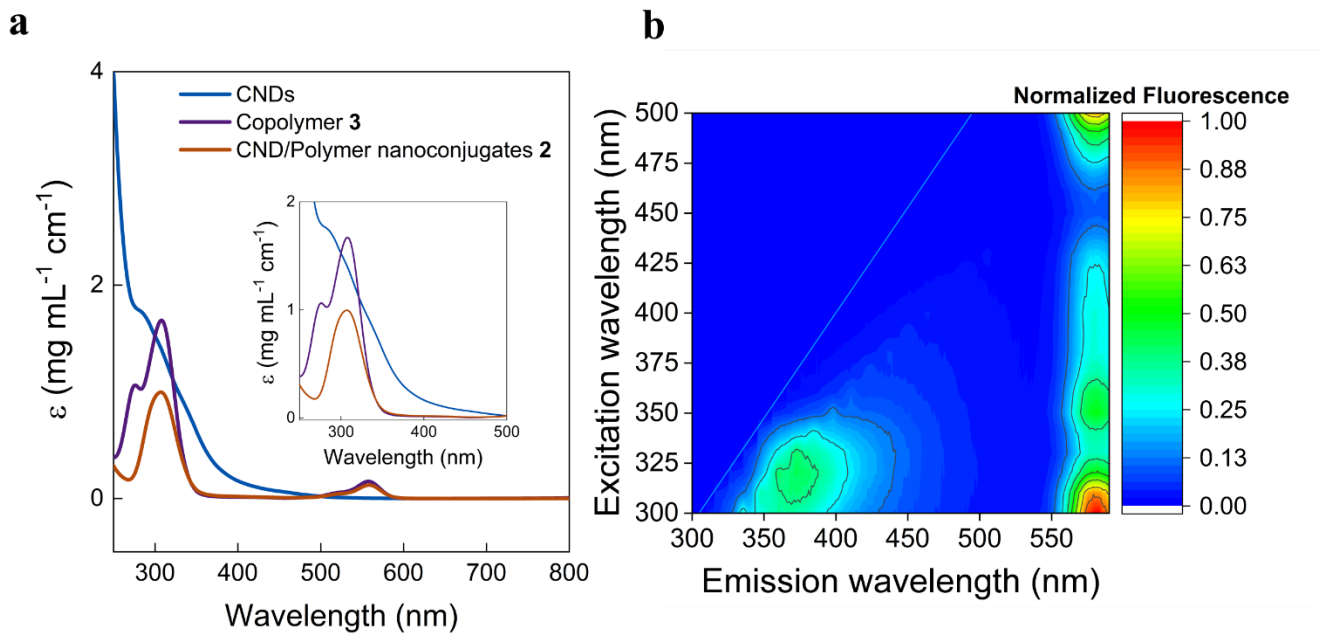

Figure 4.12. a) *UV-Vis spectra comparison in molar absorption coefficient of CNDs (blue curve), copolymer* ***3*** *(dark purple curve), and CND/polymer nanoconjugates* ***2*** *(dark orange curve) in MilliQ water;* ***b)*** *Normalized fluorescence emission map of CND/polymer nanoconjugates in MilliQ water. The light blue line shown limits the region of real values acquired during the experiments.*

We subsequently studied CND/polymer nanoconjugates 2 by turbidimetric analysis to assess whether they retained their thermoresponsive properties. In detail, the CND/polymer nanoconjugates showed a reversible solubility behavior depending on the solution temperature change and an average LCST value of 41.4 ± 0.5 °C (**Figure 4.13**). This higher value compared to the pristine polymer (24 ± 2 °C) could be explained considering the increasing hydrophilicity of the final composite. Both CNDs and the free primary amine moiety on the polymer chain (AEMA) contributed to render CND/polymer nanoconjugates 2 more hydrophilic, thus heightening their LCST.[35]

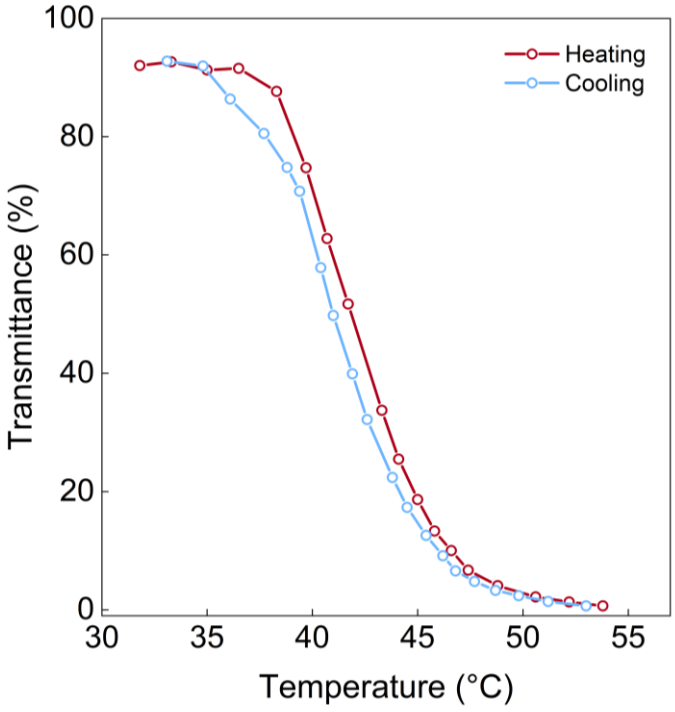

Figure 4.13. *Transmittance spectra of CND/polymer nanoconjugates (0.5 mg mL^{-1} solution in MilliQ water). Red curve is registered increasing the temperature, while blue curve is registered decreasing the temperature. LCST was determined by measuring the temperature at which transmitted light (400 nm) corresponds to 50%.*

4.2.3.1 Multi-detector and Compositional GPC Characterization of CND/polymer Nanoconjugates

In addition to the classical multi-detector GPC analysis shown so far, it was also possible to perform another type of characterization on CND/polymer nanoconjugates, known as compositional analysis.

The objective of compositional analysis is to determine the concentrations of two components, A and B, within a sample, regardless of their structural arrangement. Whether the two components are covalently bound in random or alternating sequences, linked as separate blocks, or exist as physical mixture of distinct molecules, compositional analysis focuses solely on quantifying each component's presence within the sample. In this analysis, the two unknown parameters are the concentrations of the two components.[36] **Equation 1** and **2** describe the signal outputs for a general sample composed of A and B from the RI and UV detectors, the two concentration-sensitive detectors used in this method.[37]

$$RIsig \propto C_A \times \left(\frac{dn}{dC}\right)_A + C_B \times \left(\frac{dn}{dC}\right)_B \quad \textbf{Equation 1}$$

$$UVsig \propto C_A \times \left(\frac{dA}{dC}\right)_A + C_B \times \left(\frac{dA}{dC}\right)_B \quad \textbf{Equation 2}$$

where C_A and C_B are the concentrations of component A and B, respectively, $(dn/dC)_A$ and $(dn/dC)_B$ are the refractive index increments of A and B, respectively, and $(dA/dC)_A$ and $(dA/dC)_B$ are the specific absorption coefficients of A and B, respectively.

Certain conditions must be met for effective compositional analysis. The dn/dC and dA/dC values of both components of the sample must be known for the specific mobile phase and wavelength employed. In addition to exploit both concentration-sensitive detectors, at least one component in the sample must be UV active. Ideally, only one component should be UV active to simplify calculation by removing the dA/dC of the other component or have a negligible absorption at the chosen wavelength. Lastly, a UV active narrow standard should be used to calibrate the method, allowing determination of the UV detector constant.[36]

This methodology, specifically on a Malvern Panalytical instrument, has previously been applied to viral and lipid-based vectors for vaccines.[38] Although some studies have utilized both concentration-sensitive detectors to analyze polymeric co-structure and blends,[37,39,40] to the best of our knowledge, this approach has not yet been applied to carbon nanomaterial composites.

We applied this characterization method exclusively to CND/polymer nanoconjugates 1 (protected CND/polymer nanoconjugates) in order to understand precisely their composition, precisely the polymer-to-CND ratio. This approach was chosen based on the principles discussed earlier regarding compositional analysis, as we had determined the dn/dC and dA/dC values for both the CNDs and copolymer 3. These values were not available for the deprotected form of the polymer, which is present in CND/polymer nanoconjugates 2. For CND/polymer nanoconjugates 2, we performed the standard multi-detector GPC analysis to determine their molecular weight, but not their composition.

As it was stated previously, in order to run compositional analysis, the knowledge of dn/dC and dA/dC of both constituents of the composite, namely CNDs and copolymer 3, was required. In order to simplify the calculations, we picked dA/dC values at a wavelength at which one of the two species would have a negligible absorption. The chosen wavelength was 355 nm, at which only CNDs showed a measurable absorption, while the copolymer 3 absorption was approximately

zero. Therefore, compositional analysis calculations relied on **Equation 3** and **4** for CND/polymer nanoconjugates 1 concentration.

$$RIsig \propto C_{CNDs} \times \left(\frac{dn}{dC}\right)_{CNDs} + C_{Polymer} \times \left(\frac{dn}{dC}\right)_{Polymer} \quad \textbf{Equation 3}$$

$$UVsig \propto C_{CNDs} \times \left(\frac{dA}{dC}\right)_{CNDs} \quad \textbf{Equation 4}$$

Where C_{CNDs} and $C_{Polymer}$ are the concentrations of CNDs and copolymer 3 giving the output signal, $(dn/dC)_{CNDs}$ and $(dn/dC)_{Polymer}$ are the refractive index increments of CNDs and copolymer 3, and $(dA/dC)_{CNDs}$ is the specific absorption coefficient of CNDs at 355 nm.

In **Table 4.4** are reported the corresponding parameters used for the calculation method, retrieved from CNDs elution in 0.1 M $NaNO_3$ pH 2.6 on cationic columns (see Chapter II) and copolymer 3 elution in 0.1 M $NaClO_4$ pH 4 on silica column.

Table 4.4. *dn/dC and dA/dC (at 355 nm) values of CNDs and copolymer 3 used for compositional analysis calculation.*

Sample	dn/dC (mL g^{-1})	dA/dC at 355 nm (mL g^{-1} cm^{-1})
CNDs	0.1939	0.5667
Copolymer 3	0.1850	0

Since we were analyzing CND/polymer nanoconjugates 1 (*i.e.*, AEMA*Boc on the polymer chains), we chose to run these samples in the same aqueous conditions used for the copolymer 3 (**Table 4.3**). The resulting chromatograms are showed in **Figure 4.14**. The plots show that there is a bimodal distribution indicating presence of at least two different species.

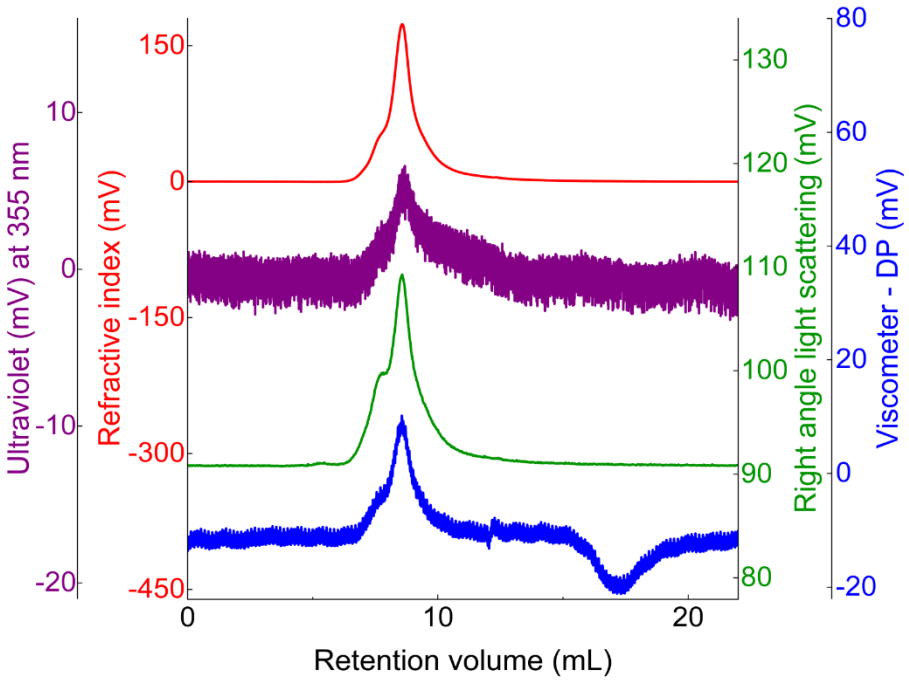

Figure 4.14. *Chromatograms of protected CND/polymer nanoconjugates 1 (0.1 M $NaClO_4$ pH 4/HCl) on Zenix-C-SEC-300 silica column, from top to bottom, refractive index (RI) curve (red), ultraviolet (UV) curve (purple), right angle light scattering (RALS) curve (green), and viscometer curve (blue), respectively.*

The graphs of compositional derived data are shown in **Figure 4.15.a**, specifically CNDs and copolymer 3 concentration curves underlying RI profile, and CND/polymer nanoconjugates 1 molecular weight trend, which decreased in value with increasing retention volumes, as expected. Moreover, by performing compositional analysis calculations (**Figure 4.15.b**), we discovered that underlying the profile of CND/polymer nanoconjugates 1 there were two families of nanoconjugates with the same weight fraction of CNDs and copolymer 3, but with different molecular weight.

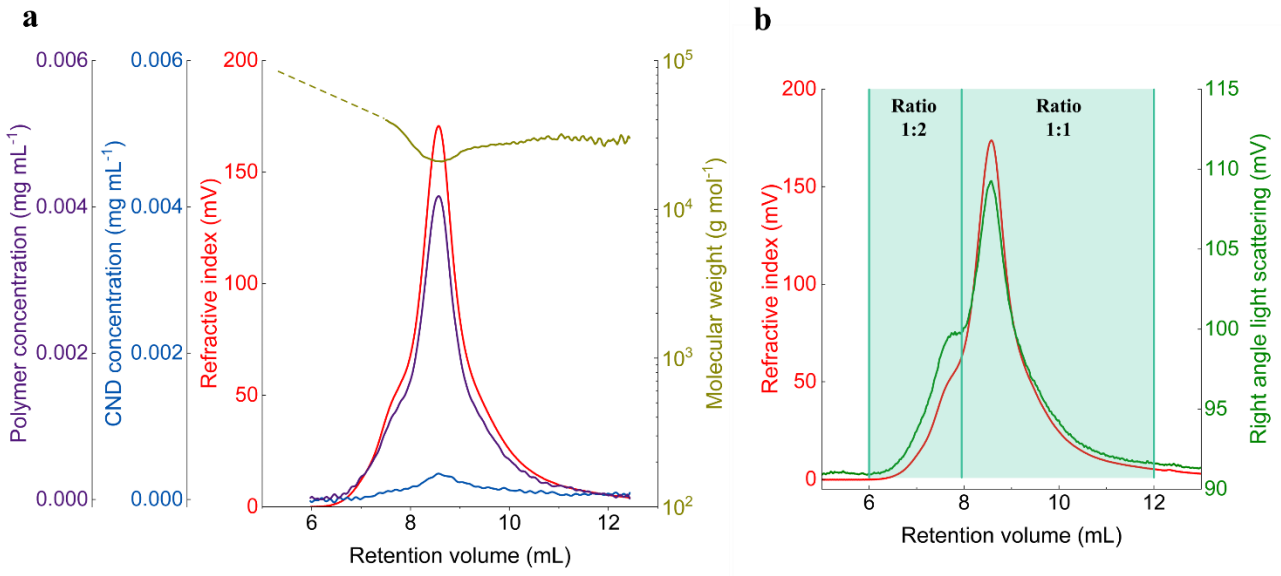

Figure 4.15. a) *Compositional analysis derived profile of CND/polymer nanoconjugates 1, showing concentration curves of CNDs (blue profile) and copolymer* ***3*** *(dark purple profile) underlying RI peak and molecular weight trend (dark yellow line). The dashed line reported corresponds to predicted values;* ***b)*** *RI and RALS chromatograms of CND/polymer nanoconjugates 1, highlighting the two peak regions that reflect varying CND-to-polymer ratios within the nanoconjugate structure.*

Particularly, the vast majority of the sample has a M_w of 24,000 g mol^{-1} and is composed of a CND coupled with one polymer chain, whereas there was a minor part of the sample with higher M_w composed of a CND coupled with two polymer chains (see Experimental Section, 4.4.7 Compositional GPC Analysis of CND/polymer nanoconjugates 1 in aqueous conditions for the table with complete results). In Chapter II, multi-detector GPC analysis on pristine CNDs yielded the number of primary aliphatic amines available for reaction at room temperature of two, on average. These moieties and reaction conditions are the ones exploited in the coupling with copolymer 3. Finding that in CND/polymer nanoconjugates 1 there were two distributions of composites with 1:1 and 1:2 CND-to-polymer ratio corroborated perfectly with the previously obtained outcomes on CNDs.

Furthermore, comparison with protein/polymer nanoconjugates synthesized using a similar NIPAA-based copolymer revealed a comparable degree of conjugation. Specifically, Huang *et al.* and Gobbo *et al.*, through mass spectrometry analysis, observed a protein-to-polymer ratio distribution ranging from 1 to 3 polymer chains per protein center.[19,41]

Interestingly, the calculated dn/dC for CND/polymer nanoconjugates 1 was 0.186 which almost identical to the one calculated for the copolymer 3 (dn/dC = 0.185). This meant that, even though

we were analyzing a composite material, its overall contribution to the refractive index change could be linked mainly to its polymeric part. In addition, we observed that the recovery was 71%, highlighting that CND/polymer nanoconjugates 1 might express partial aggregation and therefore being removed from solution, due to the post columns filters present in the system.

Even though it was not possible to perform compositional GPC characterization of CND/polymer nanoconjugates 2, we carried out the multi-detector analysis instead to characterize their molecular weight. This was due to the change into polymer chain structure after the deprotection step (*i.e.*, loss of Boc protecting group), therefore the dn/dC and the dA/dC of copolymer 3 were not representative anymore for the CND/polymer nanoconjugates 2.

Due to their higher hydrophilicity compared to their protected analogues, CND/polymer nanoconjugates 2 were analyzed in the same conditions of pristine CNDs (0.1 M $NaNO_3$ pH 2.6/CH_3COOH, see Experimental Section, 4.4.7 Multi-detector GPC analysis of CND/polymer nanoconjugates for Table with detailed GPC set-up conditions). In **Figure 4.16**, the RI chromatogram overlays of copolymer 3 and CND/polymer nanoconjugates 1 (**Figure 4.16.a**) and CNDs and CND/polymer nanoconjugates 2 (**Figure 4.16.b**) are reported, respectively. We observed that, in both cases, there was a shift of the CND/polymer nanoconjugate peak to smaller retention volumes compared to the corresponding single component. This meant that analyzed CND/polymer nanoconjugates had a larger hydrodynamic size, supporting again the successful conjugation of CNDs with copolymer 3.

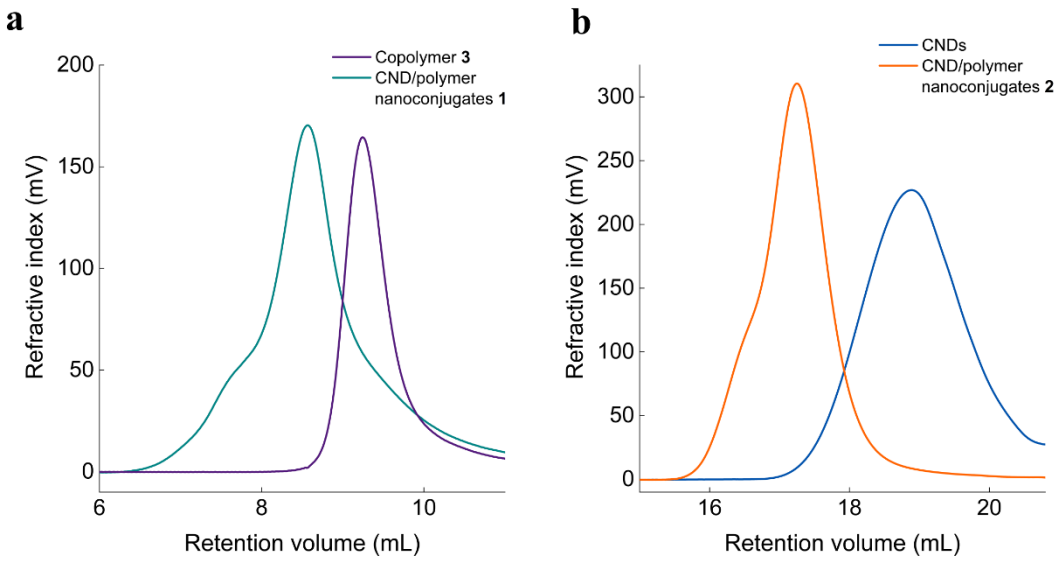

Figure 4.16. a) *RI chromatogram overlay of CND/Polymer nanoconjugates 1 (dark orange curve) and copolymer 3 (dark purple curve) (0.1 M $NaClO_4$ pH 4/HCl) on Zenix-C-SEC-300 silica column;* ***b)*** *RI chromatogram overlay of CND/Polymer nanoconjugates 2 (orange curve) and CNDs (blue curve) (0.1 M $NaNO_3$ pH 2.6/acetic acid) on cationic columns.*

Table 4.5 showed the retrieved molecular weights for CND/polymer nanoconjugates 2. The molecular weight moments are in full agreement with previously obtained results, however it was not possible to differentiate the contributions of the two individual components.

Table 4.5. *Summary of molecular weight moments, dispersity and refractive index increment of CND/polymer nanoconjugates 2 in aqueous conditions, and CND/polymer nanoconjugates 1 and 2 in organic conditions.*

CND/polymer nanoconjugates	**M_n (g mol^{-1})**	**M_w (g mol^{-1})**	**Đ (M_w/M_n)**	**Calc. dn/dC (mL g^{-1})**
2 in 0.1 M $NaNO_3$/pH 2.6	24,746 ± 94	27,587 ± 94	1.115 ± 0.001	0.146
1 in 1 w/V% TBAB in THF	25,139 ± 305	26,932 ± 396	1.071 ± 0.003	0.130
2 in 1 w/V% TBAB in THF	25,876 ± 209	27,135 ± 182	1.048 ± 0.002	0.130

Finally, we were interested in comparing CND/polymer nanoconjugates 1 and 2, both in aqueous and organic conditions, owing to their amphiphilic nature, to check whether there were some changes in polymer structure (*e.g.*, depolymerization, degradation) after the deprotection step. In **Figure 4.17** are shown the RI chromatograms overlay of the two CND/polymer nanoconjugates in aqueous (**Figure 4.17.a**) and in organic conditions (**Figure 4.17.b**), respectively, while in **Table 4.5** are reported the corresponding molecular weight moments and dispersity.

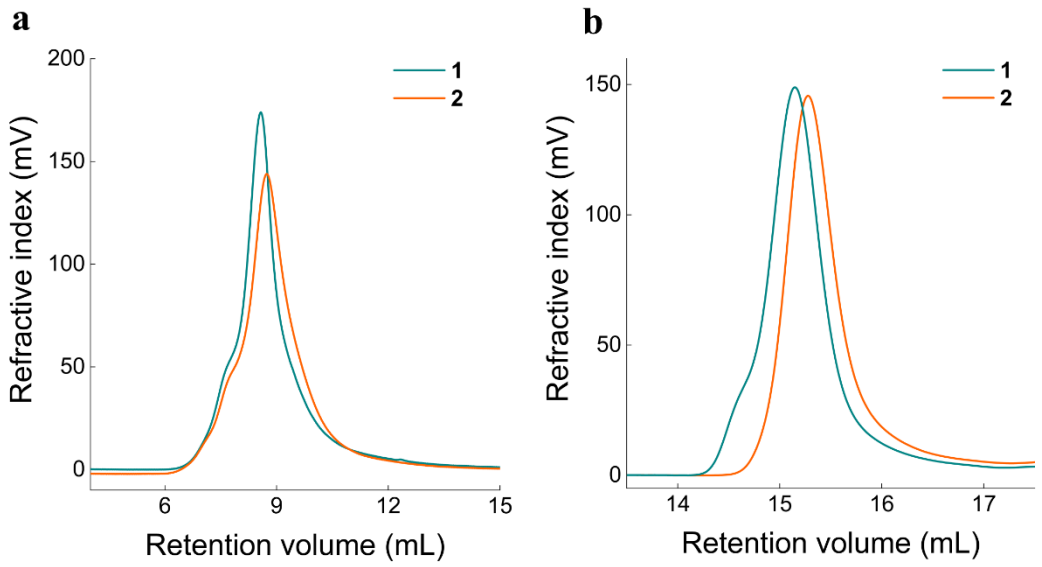

Figure 4.17. a) *RI chromatogram overlay of CND/Polymer nanoconjugates 1 (dark orange curve) and CND/Polymer nanoconjugates 2 (orange curve) in 0.1 M $NaClO_4$ pH 4/HCl on Zenix-C-SEC-300 silica column;* ***b)*** *RI chromatogram overlay of CND/Polymer nanoconjugates 1 (dark orange curve) and CND/Polymer nanoconjugates 2 (orange curve) in 1 w/V% TBAB in THF on T6000M + T2500 columns.*

These experiments revealed no significant differences between the two CND/polymer nanoconjugate species in terms of chromatogram shape or molecular weight distribution. A slight shift of the RI maximum for CND/polymer nanoconjugate 1 toward higher retention volumes was observed (**Figure 4.17**). This outcome is consistent with the structure of the protected form, as the presence of the Boc protecting group on the polymer chains may modestly increase the overall hydrodynamic size of the composite.

4.3 Conclusions

In summary, in this Chapter we first designed and synthesized a NIPAA-based copolymer, namely PNIPAA-*co*-AEMA*Boc-*co*-RhB, by RAFT polymerization. Afterwards, we carried out its in-depth characterization with different instrumental techniques, such as NMR spectroscopy, ATR-FTIR spectroscopy, turbidimetry, AFM, and multi-detector GPC. Notably, the thermoresponsive properties of the copolymer were determined by turbidimetry, revealing an average LCST of 24°C. Additionally, multi-detector GPC provided molecular weight moments and distribution for the copolymer in both organic and aqueous conditions. These values showed high consistency but with a slight overestimation compared to the molecular weight calculated from the ^{1}H NMR spectrum. Following this, we synthesized CND/polymer nanoconjugates in a two-step process, verifying the successful synthesis *via* NMR spectroscopy. Detailed analysis of these novel nanocomposites confirmed that they retained the key characteristics of the precursors – the NIPAA-based polymer thermoresponsive behavior and the inherent blue fluorescence of CNDs. To gain a deeper understanding of the structure of CND/polymer nanoconjugates, we finally performed compositional and multi-detector GPC characterization. It revealed a predominant 1:1 polymer-to-CND ratio across most of the sample, with a portion exhibiting a 2:1 ratio. These findings were consistent with the outcomes from GPC experiments on pristine CNDs (see Chapter II), which indicated an average availability of two reactive moieties on CND surface.

For future work, we plan to perform GPC analysis on the deprotected copolymer to enable the comprehensive compositional analysis of the deprotected CND/polymer nanoconjugates 2 (deprotected form). This approach will allow us to fully investigate the active form of these CND/polymer nanoconjugates, which is essential for fabricating CND-based protocells.

Overall, GPC has proven to be an invaluable tool for characterizing both simple polymers and more complex structures, providing detailed structural insights, such as single component concentration and molecular weight distribution within hybrid systems. Remarkably, GPC often yield this level of structural information within a single chromatographic run, making it a highly efficient and powerful technique for exploring composite systems.

However, it is important to emphasize that this analytical method may have limitations, particularly when additional modifications are introduced to the hybrid structure. For instance, introducing new functional groups or other chemical modifications alter both the stability and the molecular interactions within the hybrid material, potentially affecting interactions with the stationary phase. Consequently, a GPC characterization of the precise structures composing the hybrid is recommended a to support accurate interpretation of subsequent compositional analyses.

4.4 Experimental Section

4.4.1 Materials and Methods

4,4'-azobis(4-cyanovaleric acid) (≥98%), 2-Thiazoline-2-thiol, *N,N*-dicyclohexylcarbodiimide (99%), 4-(dimethylamino)pyridine (ReagentPlus®, ≥99%), sodium hydride (60% in oil), 1-propanethiol (99%), carbon disulphide (anhydrous, ≥99%), potassium ferricyanide (99%) NIPAA (97%), 2-Aminoethyl methacrylate hydrochloride (*ca.* 500 ppm phenothiazine as stabilizer, 90%), triethylamine (≥99.5%), Boc (ReagentPlus®, 99%), AIBN (≥98.0% (GC)), 1,4-dioxane (suitable for HPLC, ≥99.5%), methanol (≥99%), ethyl acetate (suitable for HPLC, ≥99.7%), chloroform (99.0-99.4% (GC)), CH_3CN (≥99.8% (GC)), DMF (suitable for HPLC, ≥99.9%), diethyl ether (≥99.8% (GC), ACS reagent), hexane (≥95%, suitable for HPLC), sodium perchlorate monohydrate (EMSURE®), HCl (ACS reagent, 37%), sodium nitrate (EMSURE® ACS), and acetic acid (ACS reagent, ≥99.8%) were purchased from Sigma-Aldrich. Methacryloxyethyl thiocarbamoyl rhodamine B was purchased from Polysciences Inc. All chemicals were used without further purification unless otherwise stated. MilliQ water was obtained from a Millipore Milli-Q Plus 185 apparatus and presented a resistivity of 18.2 MΩ cm. Dialysis tubes (SpectraPor® Biotech Cellulose Ester) with molecular weight cut-off of 12-14 and 50 kDa were bought from Repligen.

^{1}H and ^{13}C-NMR spectra were recorded on Varian 400 MHz spectrometer (^{1}H: 400 MHz). DOSY experiments were recorded on Varian Inova spectrometer (^{1}H: 500 MHz) equipped with Performa II-Z gradient coils with Absolute Value – gradient compensated stimulated Echo gHMBC. Chemical shifts were reported in ppm using the solvent residual signal as an internal reference (D_2O: δH = 4.79 ppm, $CDCl_3$: δH = 7.26 ppm). All spectra were recorded at 25 °C. All the spectra were analyzed with MestReNova v12.0.1-20560.

Attenuated Total Reflectance (ATR) Fourier-Transform Infrared spectroscopy was performed on a Shimadzu IRAffinity1S equipped with a QATR-10 with diamond crystal. Samples were analyzed as powders by placing them on the crystal and pressing them to record the spectrum.

AFM images were obtained with a Nanoscope IIIa (VEECO Instruments), using tapping mode with a HQ:NSC19/ALBS probe (80 kHz; 0.6 N/m) (MikroMasch). Samples were prepared by drop-casting methanol solutions (concentration = 1 ng mL^{-1}) on an exfoliated mica substrate. The obtained micrographs were analyzed with Gwyddion 2.63.

Turbidimetry experiments to monitor the thermoresponsive behavior of PNIPAA-*co*-AEMA*Boc-*co*-RhB and CND/polymer nanoconjugates were performed on a stirred 0.5 mg mL^{-1} solution in MilliQ water using an optical fiber (400 μm diameter) UV-Vis spectrophotometer Flame (Ocean

Optics) and a 10 mm path-length cuvette holder CUV (Ocean Optics, in-house modified to include a Peltier temperature control system – Thorlabs – in a 10 mm path-length quartz cuvette). The solution temperature was monitored with a K type thermocouple (RS Components) inside the cuvette and a temperature data logger (Lascar Electronics). LCST was determined by measuring the transmittance at 400 nm as the temperature at which transmitted light corresponds to 50%.

GPC measurements were performed on a OMNISEC RESOLVE/OMNISEC REVEAL system from Malvern Panalytical Ltd. The OMNISEC RESOLVE system comprises an isocratic pump with continuous back seal washing that can operate between 0.005 - 10 mL/min of flowrate and with an accuracy of ±1%, a degasser with > 90% degassing capacity, a thermostated autosampler (4 – 60 °C) with a 250 µL glass syringe and a 300 µL injection loop, a column oven containing two Malvern Panalytical styrene-divinyl benzene-based columns (T6000M + T2500) connected in series, or two Tosoh Bioscience TSKgel GMPW$_{XL}$-CP (G6000 + G3000PWXL-CP) cationic columns connected in series or a Zenix-C-SEC-300 silica column. The OMNISEC REVEAL comprises four detectors: *(1)* Refractive index deflection detector operating at 640 nm with a 12 µL reference cell; *(2)* Diode-array-based UV-Vis spectrophotometer working between 190 – 900 nm (accuracy < 1 nm) and equipped with 7.5 µL cell with a 10 mm path length; *(3)* Light scattering detector comprising a Right Angle Light Scattering detector (RALS) positioned at 90° to the sample flow, and a Low Angle Light Scattering detector (LALS) positioned at 7° to the sample flow, a 640 nm laser (50 mW) light source, cell volume 18 µL; *(4)* 4-capillary Wheatstone bridge viscometer with self-balancing mechanism, user-exchangeable capillaries and one delay column. For the organic set-up, column and detector ovens were kept at 35 °C, whereas the autosampler was kept at 20 °C. A typical run was performed using 1 w/v% TBAB in THF as mobile phase, which was pre-filtered through a glass filtering apparatus with a 0.22 µm PTFE filter (Merck). The copolymer 3 and CND/polymer nanoconjugates (1 and 2) samples were prepared at a concentration of *ca.* 1-3 mg mL^{-1}, dissolved in the eluent, and filtered through 0.45 µm PTFE syringe filters. For the aqueous set-up, column and detector ovens were kept at 20 °C, whereas the autosampler was kept at 4 °C. A typical run was performed using either 0.1 M $NaNO_3$ + 0.5 V/V% acetic acid (pH 2.6) or 0.1 M $NaClO_4$ pH 4/HCl as mobile phase, which was pre-filtered through a bottle vacuum filter funnel with a 0.22 µm PES membrane (Steritop®, Merck). The copolymer 3 and CND/polymer nanoconjugates (1 and 2) samples were prepared at a concentration of *ca.* 3-5 mg mL^{-1}, dissolved in the eluent, and filtered through 0.45 µm regenerated cellulose syringe filters.

ζ-Potential measurements were performed on a Zetasizer Ultra Red (Malvern Panalytical Ltd) using a ζ-Potential cuvette (Malvern Panalytical Ltd, model DTS1070). Copolymer 3 samples were prepared at a concentration of *ca.* 3 mg mL^{-1} in a pre-filtered salt solution. Before

measurement, sample solutions were also filtered through a 0.45 μm regenerated cellulose syringe filter.

Absorption spectra were collected with an Agilent Cary 5000 UV-Vis spectrophotometer. Spectra were acquired at a concentration of 1 mg mL^{-1} in MilliQ water at room temperature, using 10 mm path-length quartz cuvettes.

Fluorescence spectra were recorded on an Edinburgh instruments FS5 spectrofluorometer using a 150 W CW Ozone-free xenon arc lamp as source and a Photomultiplier R928P (spectral coverage: 200 nm – 900 nm) as detector. All spectra were registered with an absorbance equal to 0.1 in MilliQ water at room temperature using 10 mm path-length quartz cuvettes.

4.4.2 Synthesis of RAFT agent

The general scheme of RAFT agent synthesis is shown in **Figure 4.18**. The synthesis was adopted from a published procedure.[19]

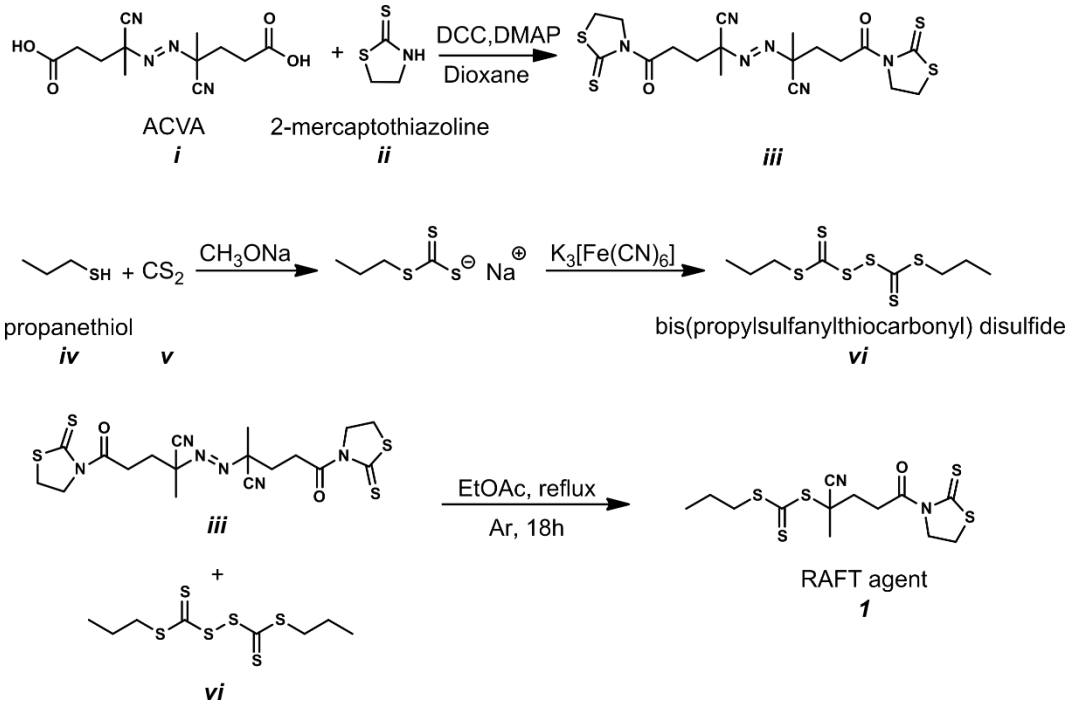

Figure 4.18. *Reaction scheme of RAFT agent synthesis.*

A solution of 4,4'-azobis(4-cyanovaleric acid) (ACVA, ***i***, 14.6 mmol) was dissolved in 1,4-dioxane (100 mL) and degassed with Ar for 15 minutes. 2-mercaptothiazoline (***ii***, 28.3 mmol), *N,N*-dicyclohexylcarbodiimide (DCC, 33.9 mmol) and 4-(dimethylamino)pyridine (DMAP, 1.64 mmol) were added to solution and it was purged with Ar for 10 minutes. Then the flask was sealed, and the reaction mixture was left reacting for 18 h. The reaction crude was filtered and

concentrated. The product ***iii*** was recrystallized from cold diethyl ether. After drying under vacuum, it was obtained as a yellow powder.

^{1}H NMR (400 MHz, $CDCl_3$): 4.60 ppm (t, 2H), 3.31 ppm (t, 2H), 3.12-3.66 ppm (m, 2H), 2.42-2.64 ppm (m, 2H), 1.76 ppm (s, 3H).

For the second step, methanol was introduced in a 250 mL round-bottom flask and purged with Ar for 10 minutes. Sodium hydride (83 mmol) was added to the solvent. Then, propanethiol (***iv***, 83 mmol) was added with a glass syringe and let to stir for 10 minutes. Finally, carbon disulfide (***v***, 99 mmol) was added at the mixture, and the solution was purged with Ar for 15 minutes and left to react for 18 h. The reaction crude, after eliminating the methanol under reduced pressure, was dissolved in a strongly acid aqueous solution and purified by liquid-liquid extraction with diethyl ether. Then, the collected product in organic phase was re-extracted with 0.5 M NaOH aqueous solution. Potassium ferricyanide ($K_3[Fe(CN)_6]$, 35 mmol) was added to the collected aqueous phase and the reaction was left to stir for 18 h under atmosphere pressure. The product was extracted with diethyl ether. Then, bis(propylsulfanylthiocarbonyl) disulfide ***vi*** was dried over sodium sulfate and left drying under vacuum.

^{1}H NMR (400 MHz, $CDCl_3$): 3.29 ppm (t, 4H), 1.75 ppm (sextet, 4H), 1.02 ppm (m, 6H).

In the last step, bis(propylsulfanylthiocarbonyl) disulfide (***vi***, 3.3 mmol) was dissolved in ethyl acetate (100 mL) in a two-neck round bottom flask, equipped with a condenser and a bubbler. The solution was purged with Ar for 15 minutes and then the diazo compound (***iii***, 3.3 mmol) was added. After 10 minutes of Ar purging, the reaction was heated to reflux and left stirring for 18 h. Following rotary evaporation of the solvent, the product **1** was isolated after column chromatography using silica gel as the stationary phase and 4:1 hexane/ethyl acetate and 1:1 hexane/ethyl acetate as the eluents.

^{1}H NMR (400 MHz, $CDCl_3$): 4.58 ppm (t, 2H), 3.57 ppm (m, 2H), 3.31 ppm (t, 4H), 2.55 ppm (m, 2H), 1.89 ppm (s, 3H), 1.73 ppm (sextet, 2H), 1.02 ppm (t, 3H).

^{13}C NMR (101 MHz, $CDCl_3$): 217.22 ppm (s), 201.81 ppm (s), 172.55 ppm (s), 119.30 ppm (s), 56.13 ppm (s), 46.48 ppm (s), 38.99 ppm (s), 34.54 ppm (s), 34.06 ppm (s), 28.60 ppm (s), 25.05 ppm (s), 21.43 ppm (s), 13.62 ppm (s).

^{1}H and ^{13}C NMR are shown in **Figures 4.19** and **4.20**.

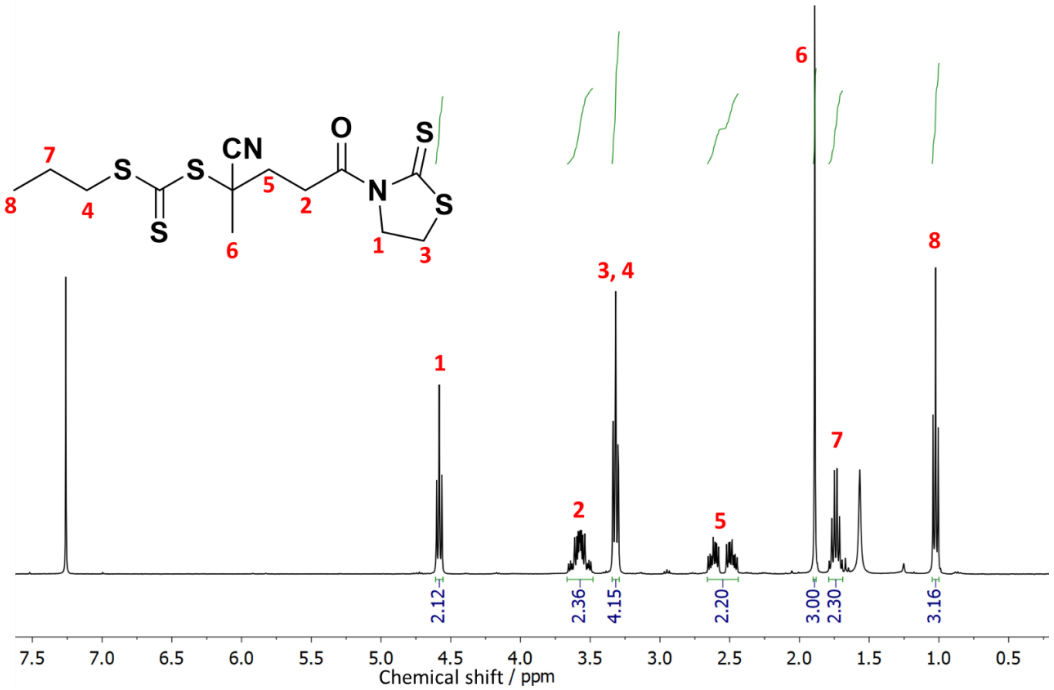

Figure 4.19. *^{1}H NMR spectrum in deuterated chloroform, referenced against solvent residual peak (δH: 7.26 ppm).*

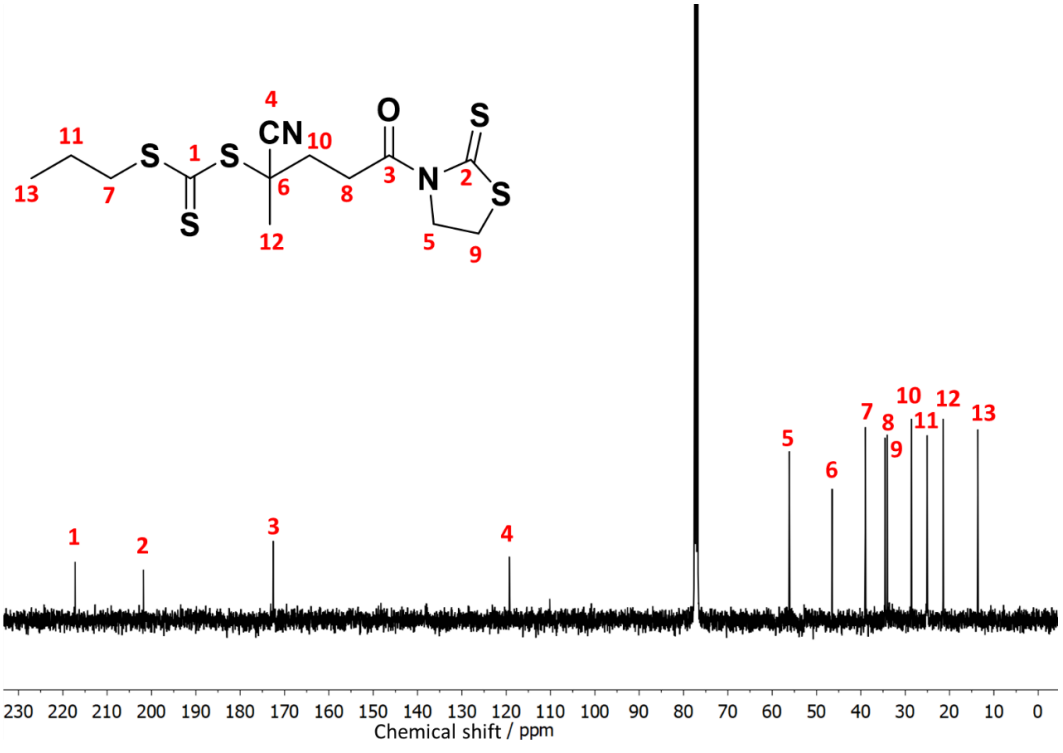

Figure 4.20. *^{13}C NMR spectrum in deuterated chloroform, referenced against solvent residual peak (δC: 77.16 ppm).*

4.4.3 Synthesis of AEMA*Boc

The protection of AEMA is described in **Figure 4.21**.

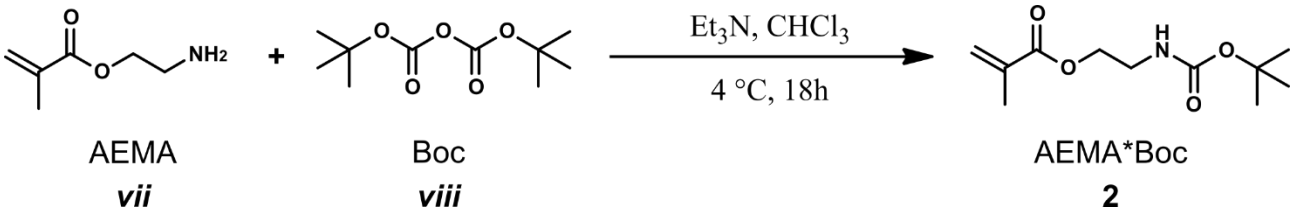

Figure 4.21. *Reaction scheme of AEMA*Boc synthesis.*

Briefly, 2-Aminoethyl methacrylate hydrochloride (***vii***, 3 mmol) was solubilized in $CHCl_3$ (10 mL) in a round bottom flask. Then triethylamine (6 mmol) was added, and the solution was cooled down to 4 °C. At last, Boc (***viii***, 3.3 mmol) was added in the reaction mixture and the solution was left to stir for 18 h. Upon addition of ethyl acetate and vacuum filtering the reaction crude, the product was separated after an ethyl acetate/MilliQ water liquid-liquid extraction on a separating funnel. The organic phase was dried with sodium sulfate and AEMA*Boc (2) was isolated after evaporation under reduced pressure.

^{1}H NMR (400 MHz, $CDCl_3$): 6.11 ppm (s, 1H), 5.57 ppm (s, 1H), 4.79 ppm (s, 1H), 4.19 ppm (t, 2H), 3.42 ppm (t br, 2H), 1.93 ppm (s, 3H), 1,43 ppm (s, 9H).

4.4.4 RAFT Polymerization of PNIPAA-*co*-AEMA*Boc-*co*-RhB

NIPAA and AIBN were freshly recrystallized three times each from hexane and methanol, respectively. NIPAA (8 mmol), AEMA*Boc (**2**, 0.41 mmol), RhB (1.44 µmol), DMF (8 mmol), AIBN (15 µmol) and RAFT agent (**1**, 70 µmol) were dissolved in 4 mL of acetonitrile in a 10 mL Schlenk glass tube equipped with a stirrer bar. The tube was sealed, and the solution underwent 4 freeze-pump-thaw cycles. Finally, the reaction mixture was purged with Ar. Polymerization was carried out at 65 °C for 13.5 h. The final polymer was isolated by precipitation from 1:1 hexane/diethyl ether as a bright-pink crystalline powder.

Figure 4.22 showed the ^{1}H NMR spectra of the reaction crude before the polymerization start (t_0) and at the end of the polymerization (t_f). By comparing the integral of the vinyl protons of NIPAA and the DMF (internal standard) ones of the two spectra, we could retrieve the conversion percentage of the reaction of 81% (100 of NIPAA at t_0 – 19 of NIPAA at t_f = 81 NIPAA converted).

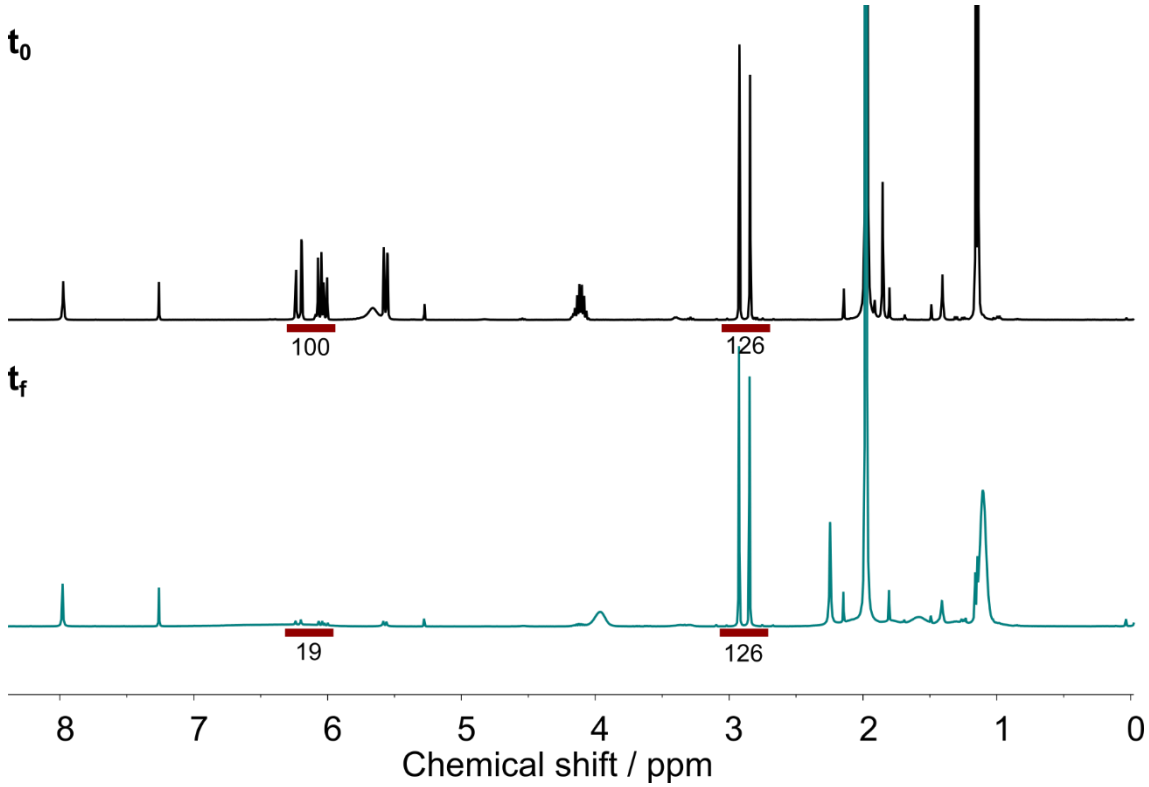

Figure 4.22. *^{1}H-NMR stacked spectra of starting mixture crude (t_0) and finale mixture crude (t_f, after 13. 5 h) of copolymer 3 synthesis in deuterated chloroform, referenced against solvent residual peak (δH: 7.26 ppm, 400 MHz, r.T). The two singlets at 2.78 and 2.94 ppm (integral = 126) are assigned to the internal standard (DMF), while the protons at 6.00-6.23 ppm are the vinyl protons of NIPAA monomer.*

4.4.5 Multi-detector GPC Analysis of PNIPAA-*co*-AEMA*Boc-*co*-RhB

All polymer analyses carried out with an organic set-up were performed by injecting – at the same concentration – 100 µL of sample and at a flowrate of 1 mL min^{-1}. In **Table S4.1** are reported the values retrievable from three consecutive injections during a multi-detector GPC.

Table S4.1. *Summary of molecular weight moments, dispersity and refractive index increment of PNIPAA-co-AEMA*Boc-co-RhB in organic conditions.*

	M_n (g mol^{-1})	M_w (g mol^{-1})	Đ (M_w/M_n)	Calc. dn/dC (mL g^{-1})
Injection 1	18,416	19,242	1.045	0.1594
Injection 2	18,340	19,183	1.046	0.1588
Injection 3	18,393	19,367	1.0543	0.1571
Mean value	18,383 ± 39	19,264 ± 94	1.048 ± 0.005	0.1584 ± 0.0012

As for CNDs (see Chapter II), we applied a calculation procedure to precisely obtain the concentration of the sample of the integrating area of the RI chromatogram. To fully understand it, we need to recall the simplified equations governing three of the four GPC detectors (**Equation 5 – 7**):

$$R\,Is\;\;i\;\;g\;\;t(mV) = K_{R\,I} \times \frac{d\;\;n}{d\;\;C} \times C \qquad \textbf{Equation 5}$$

$$U\,Vs\;\;i\;\;g\;\;t(mV) = K_{U\,V} \times \frac{d\;\;A}{d\;\;C} \times C \qquad \textbf{Equation 6}$$

$$L\;Ss\;\;i\;\;g\;\;t(mV) = K_{L\;S} \times M_w \times \left(\frac{d\;\;n}{d\;\;C}\right)^2 \times C \qquad \textbf{Equation 7}$$

where for **Equation 5** K_{RI} is the constant of the RI detector determined during the instrument calibration, dn/dC is the sample refractive index increment, and C is the concentration of the sample giving that output signal. For **Equation 6**, K_{UV} is the constant of the UV detector determined during the instrument calibration, dA/dC is the specific absorption coefficient of the sample, and C is the concentration of the sample giving that output signal. Lastly, for **Equation 7**, K_{LS} is the constant of the LS detector determined during the instrument calibration, M_w is the molecular weight of the sample, dn/dC is the sample refractive index increment, and C is the concentration of the sample giving that output signal.

Therefore, we exploited the second detector responding to the sample concentration – the UV detector – since it does not show any permeation peaks. We integrated the whole UV peak and used **Equation 6** to determine the dA/dC of CNDs, using the input concentration (*i.e.*, the known concentration at which the sample was prepared). After that, we solved **Equation 6** for the concentration and used the calculated dA/dC to integer the UV peak area corresponding to the RI peak, not considering the permeation peaks. This allowed us to quantify the actual concentration

beneath that RI peak area. Knowing the correct concentration, we could use **Equation 5** to calculate the dn/dC of CNDs and hence, exploiting **Equation 7**, molecular weight moments and dispersity (Đ).

To check that our initial hypothesis was correct (*i.e.*, determine the dA/dC from sample UV signal and its input concentration) and test whether could be an influence caused by an interaction with the stationary phase, we performed GPC runs of the samples without columns. These experiments are called tubing tests. They consisted of replacing columns with a long PTFE tube and running the sample in the same elution conditions used before. In this way, even though there was not an actual chromatographic separation, the sample chromatograms were still registered, analyzed, and then compared to the previously acquired ones. By doing so, we could confirm that the dA/dC estimation was accurate, validating the molecular weight distribution results obtained.

In **Table S4.2** are reported the dA/dC of copolymer 3 obtained from a normal chromatographic run and from a tubing test.

Table S4.2. *Comparison table between multi-detector GPC average results, namely dA/dC at 308 nm, of copolymer **3** obtained from a chtomatographic run and a tubing test.*

dA/dC (mL g^{-1} cm^{-1})	dA/dC tubing (mL g^{-1} cm^{-1})
0.923 ± 0.009	0.927 ± 0.003

All polymer analyses carried out with an aqueous set-up were performed by injecting – at the same concentration – 50 µL of sample and at a flowrate of 0.5 mL min^{-1}. In **Table S4.3** are reported the values retrievable from two consecutive injections during a multi-detector GPC.

Table S4.3. *Summary of molecular weight moments, dispersity and refractive index increment of copolymer 3 in aqueous conditions.*

	M_n (g mol^{-1})	M_w (g mol^{-1})	Đ (M_w/M_n)	Calc. dn/dC (mL g^{-1})
Injection 1	20,869	20,987	1.006	0.1851
Injection 2	19,343	19,495	1.008	0.1850
Mean value	20,106 ± 1,079	20,241 ± 1,055	1.007 ± 0.001	0.1851 ± 0.0001

To validate copolymer 3 results obtained in aqueous conditions following the same considerations described before, we confirmed its dA/dC from UV-Vis measurements done on a spectrophotometer. In **Figure 4.23.a** are shown the molar extinction coefficient trend in the 250-

800 nm wavelength range, and in **Figure 4.23.b** is reported the calibration curve for dA/dC at 308 nm.

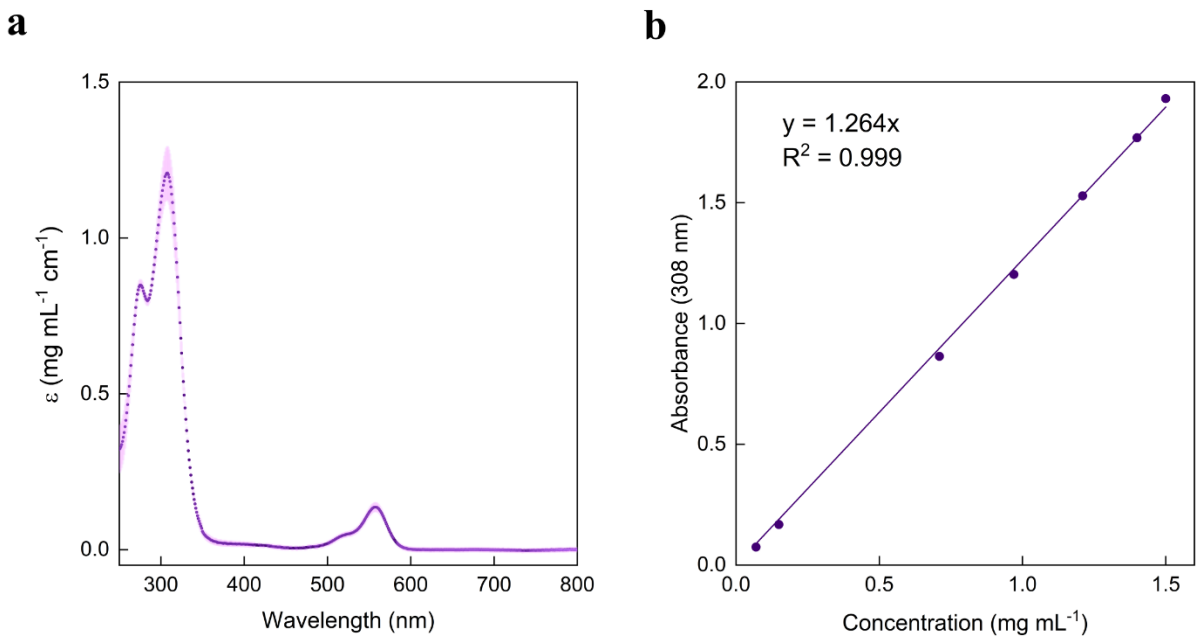

Figure 4.23. a) *Molar extinction coefficient (ε) of copolymer **3** in MilliQ water. Dotted profile are the average values, while the transparent green profile is the experimental error retrieved after three experiments;* ***b)*** *dA/dC calibration curve of copolymer **3** in MilliQ water at 308 nm.*

4.4.6 Synthesis of CND/polymer Nanoconjugates

For a CND/polymer nanoconjugates synthesis, 10 mg of CNDs (*L*-arginine and ethylenediamine-derived CNDs, see Chapter II for details on the synthesis) were dissolved in 5 mL of carbonate buffer solution (pH 8.5, 100 mM) in a 40 mL glass vial equipped with a stirrer bar. In a separate vial, 175 mg (1 equiv. with respect of CND Kaiser Test quantification of primary amines in moles) of copolymer 3 was dissolved in 5 mL of MilliQ water and cooled down to let the polymer dissolve completely. The polymer solution was added dropwise to a stirred solution of CNDs, and the conjugation reaction was carried out for 18 h at room temperature. CND/polymer nanoconjugates (1, protected nanoconjugates) were then isolated by dialysis (MWCO: 50 kDa) against MilliQ water for 24 h (three water changes during the day, every three hours). The recovered solution was lyophilized and stored as a solid in a desiccator (mass yield = 80%).

For the deprotection step, CND/polymer nanoconjugates were solubilized in chloroform in a 20 mL glass vial equipped with a stirrer bar (concentration = 20 mg mL^{-1}). The glass vial was sealed with a PTFE cap with a needle for gas exit. Then, TFA was added with a syringe and the reaction was left to stir for 1.5h at room temperature. CND/PNIPAA-*co*-AEMA-*co*-RhB nanoconjugates

(deprotected nanoconjugates) were isolated after a series of reduced pressure solvent evaporations to be sure that all TFA was efficiently removed. At first, the reaction mixture was dried with rotary evaporator, then it was solubilized in methanol (five times), chloroform (three times), and diethyl ether (twice), and evaporated each time under reduced pressure. The recovered solid was left under vacuum for 18 h and dialyzed (MWCO: 12-14 kDa) against MilliQ water for 24h (three water changes during the day, every three hours). The recovered solution was lyophilized and stored as a solid in a desiccator (mass yield = quantitative).

4.4.7 Compositional GPC Analysis of CND/polymer Nanoconjugates 1 in Aqueous Conditions

For compositional analysis, protected CND/polymer nanoconjugates 1 runs were carried out in an aqueous set-up by injecting 50 µL of sample and at a flowrate of 0.5 mL min^{-1}. In **Figure 4.24** are shown the two integration regions of the sample peak, and in **Table S4.4** are reported the values retrievable from two consecutive injections.

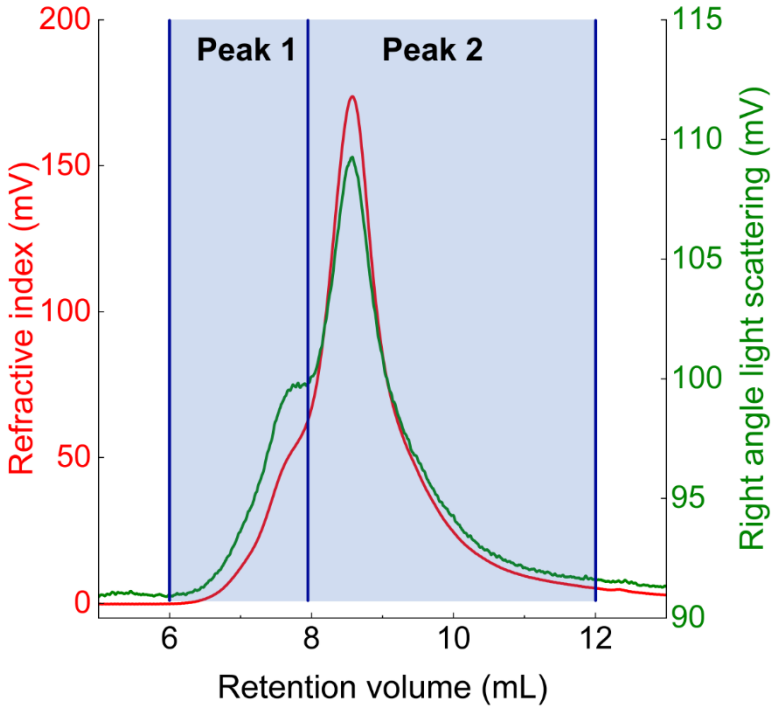

Figure 4.24. *RI and RALS chromatograms of protected CND/Polymer nanoconjugates 1 (0.1 M $NaClO_4$ pH 4/HCl on Zenix-C-SEC-300 silica column) showing the two integration areas for compositional analysis quantification.*

Table S4.4. *Summary table of compositional analysis parameters (molecular weight moments, CNDs and polymer weight fractions, CNDs and polymer molecular weights in the nanoconjugates, and dn/dC) of the of protected CND/polymer nanoconjugates.*

		M_n (g mol^{-1})	M_w (g mol^{-1})	CND weight fraction (%)	Polymer weight fraction (%)	CND M_w (g mol^{-1})	Polymer M_w (g mol^{-1})	dn/dC (mL g^{-1})
Injection 1	**Peak 1**	36,638	38,147	12	88	4,544	33,603	0.1861
	Peak 2	23,655	23,961	13	87	3,233	20,728	0.1862
Injection 2	**Peak 1**	31,996	33,642	11	89	3,465	30,177	0.1859
	Peak 2	21,298	21,510	14	86	3,141	18,369	0.1863

4.4.8 Supplementary Figures

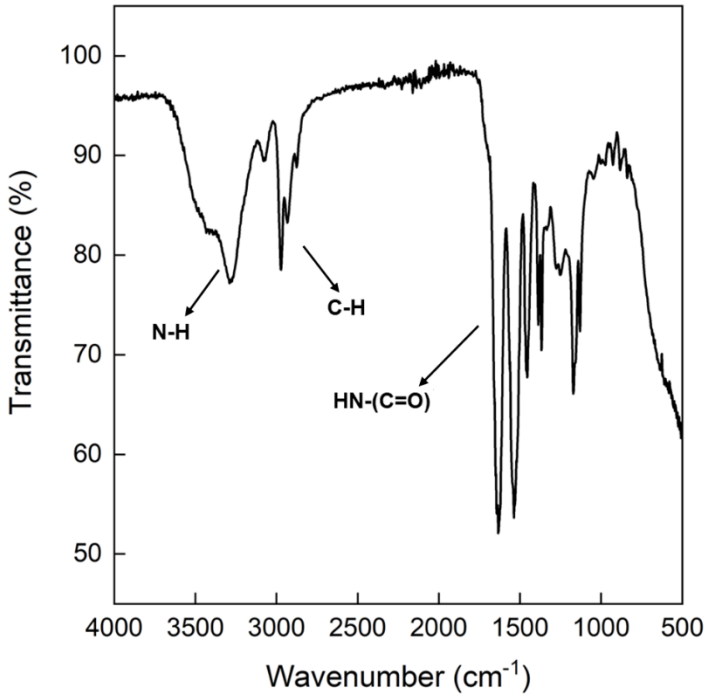

Figure S4.1. *ATR-FTIR spectrum of purified copolymer 3.*

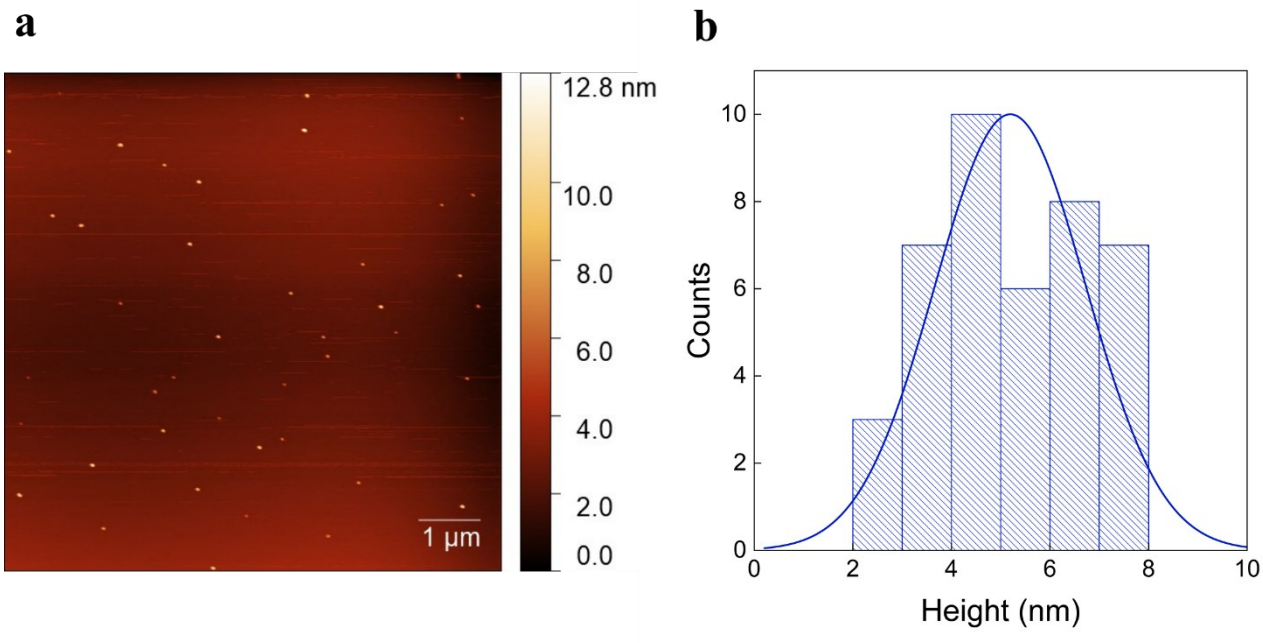

Figure S4.2. a) *Tapping mode AFM topography image of purified copolymer 3 drop-casted on a mica substrate from a methanol solution (1 ng mL^{-1} Color brightness indicates the relative height, from lowest (dark) to highest (bright); b) Size distribution of purified copolymer 3. The average size is 5 ± 2 nm.*

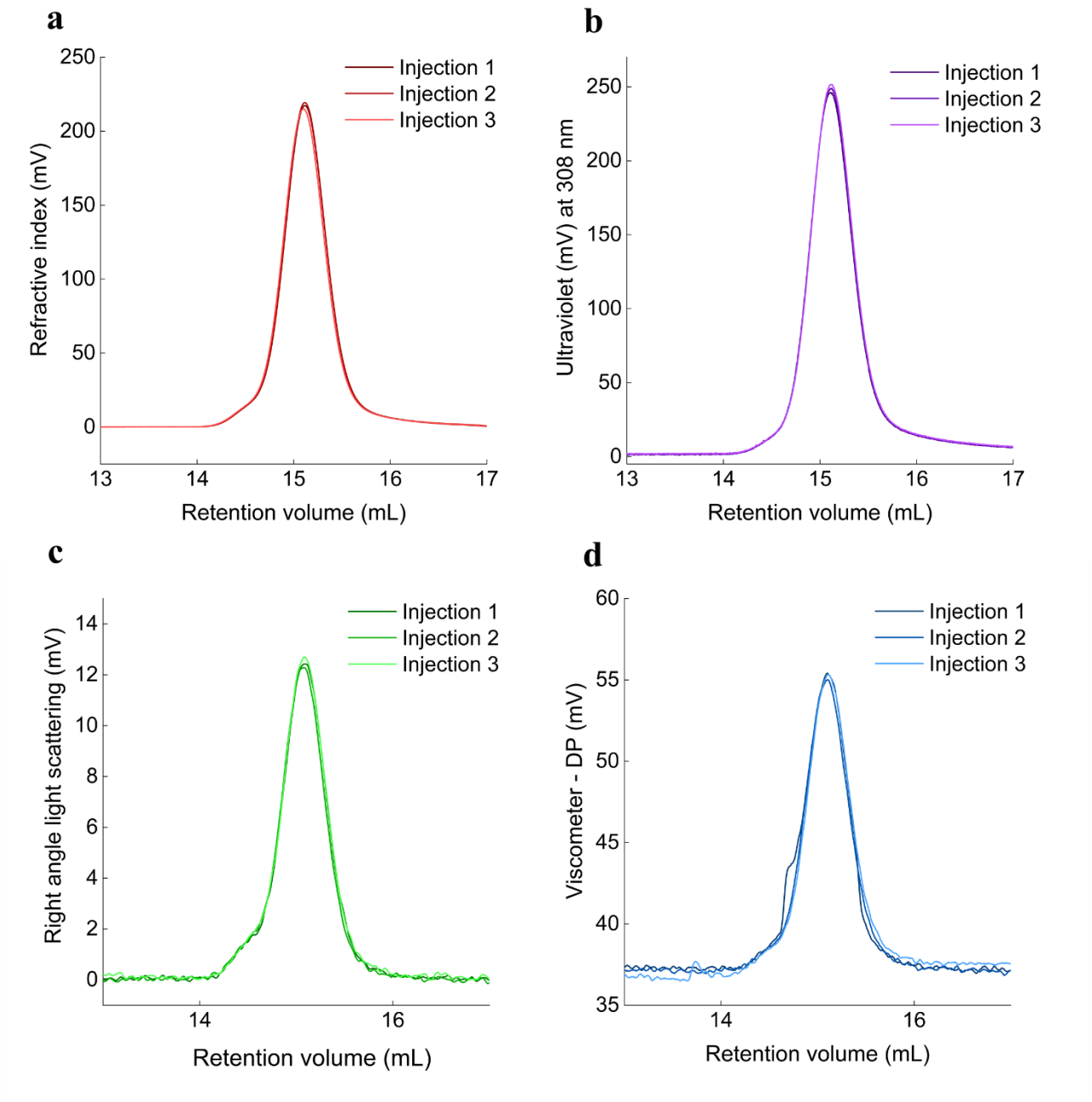

Figure S4.3. *GPC chromatogram overlays of copolymer 3 for three different injections (1 w/V% TBAB in THF on T6000M + T2500 columns):* ***a)*** *refractive index curves (red),* ***b)*** *UV curves (purple),* ***c)*** *light scattering curves (green),* ***d)*** *viscometer (DP) curves (blue).*

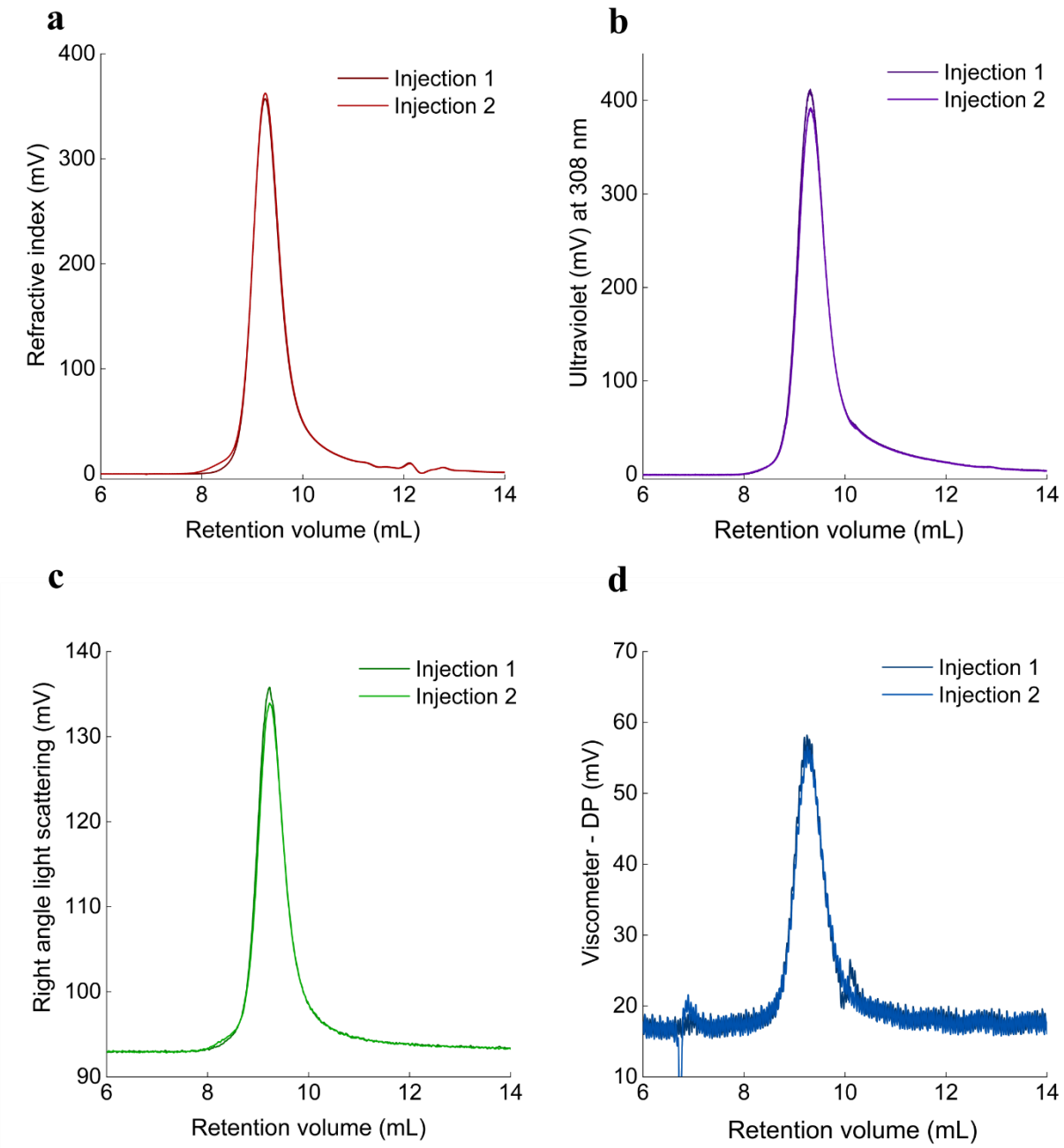

Figure S4.4. *GPC chromatogram overlays of copolymer 3 for two different injections (0.1 M $NaClO_4$ pH 4/HCl on Zenix-C-SEC-300 silica column):* ***a)*** *refractive index curves (red),* ***b)*** *UV curves (purple),* ***c)*** *light scattering curves (green),* ***d)*** *viscometer (DP) curves (blue).*

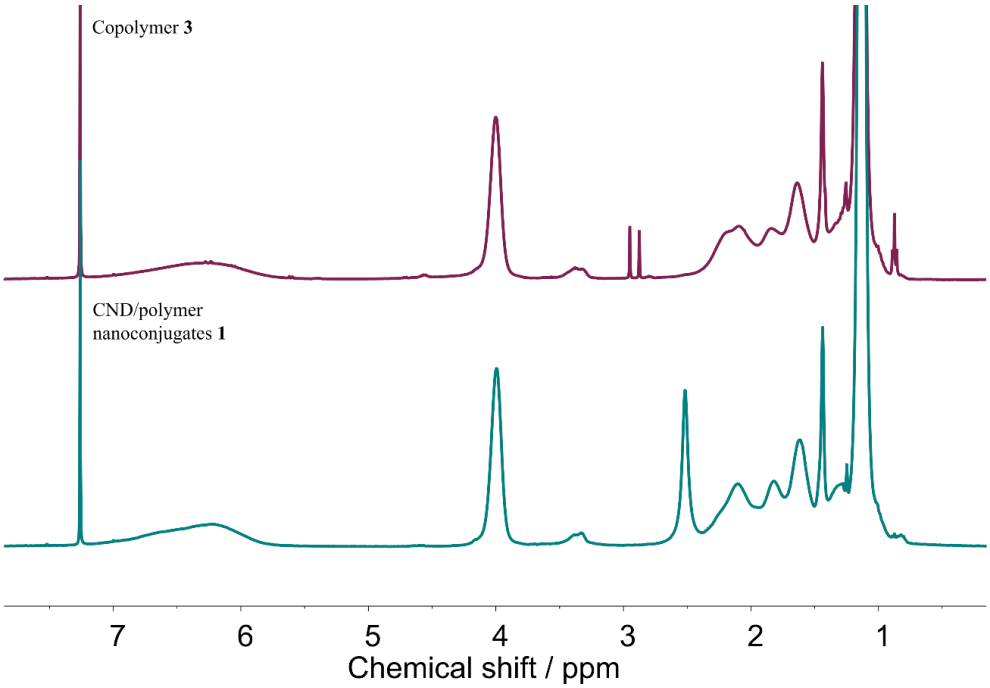

Figure S4.5. *^{1}H NMR stacked spectra of copolymer 3 and CND/polymer nanoconjugates 1 in deuterated chloroform, referenced against solvent residual peak (δH: 7.26 ppm, 400 MHz, r.T).*

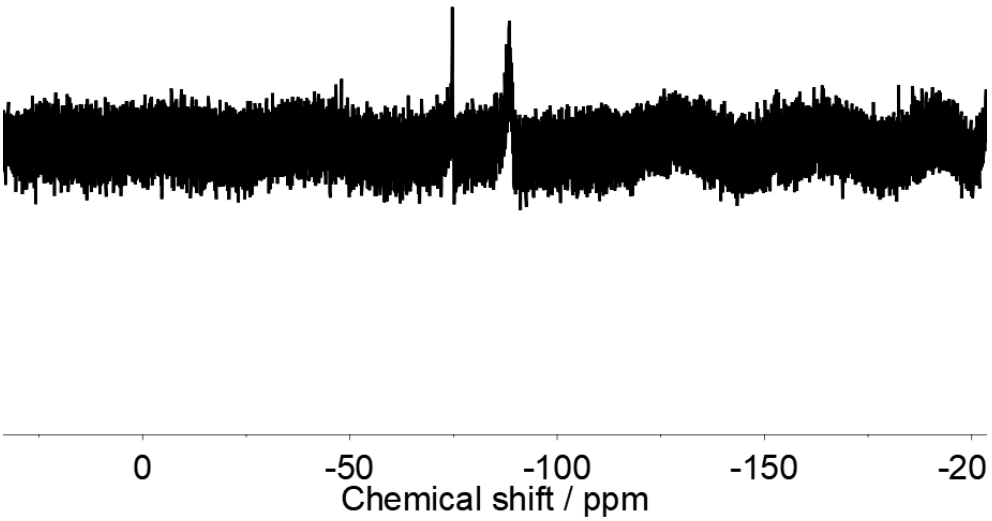

Figure S4.6. *^{19}F NMR spectrum of CND/polymer nanoconjugates 2 in deuterated chloroform (376 MHz, r.T). The spectrum does not show any fluorine signal.*

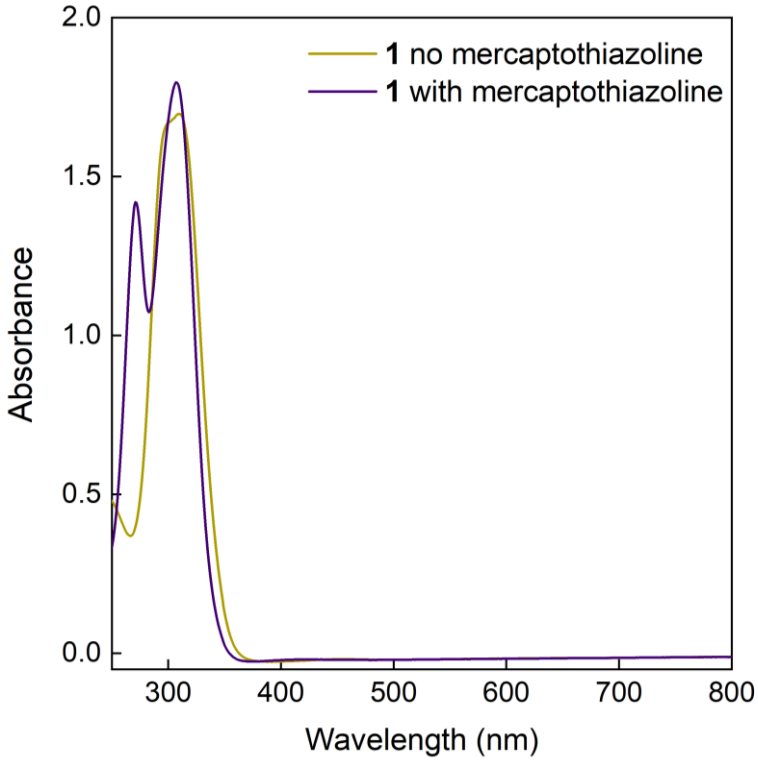

Figure S4.7. *Absorption spectra comparison of compound 1 (RAFT agent with mercaptothiazoline, purple curve) and compound 1 without mercaptothiazoline (olive yellow curve) at 50 μg mL^{-1} in chloroform.*

4.5 References

1. Kar, D. K., V, P., Si, S., Panigrahi, H. & Mishra, S. Carbon Dots and Their Polymeric Nanocomposites: Insight into Their Synthesis, Photoluminescence Mechanisms, and Recent Trends in Sensing Applications. *ACS Omega* **9**, 11050–11080 (2024).
2. Doberenz, F., Zeng, K., Willems, C., Zhang, K. & Groth, T. Thermoresponsive polymers and their biomedical application in tissue engineering – a review. *J. Mater. Chem. B* **8**, 607–628 (2020).
3. Clark, E. A. & Lipson, J. E. G. LCST and UCST behavior in polymer solutions and blends. *Polymer* **53**, 536–545 (2012).
4. Li, B. & Thompson, M. E. Phase transition in amphiphilic poly(*N*-isopropylacrylamide): controlled gelation. *Phys. Chem. Chem. Phys.* **20**, 13623–13631 (2018).
5. Zhang, Q., Weber, C., Schubert, U. S. & Hoogenboom, R. Thermoresponsive polymers with lower critical solution temperature: from fundamental aspects and measuring techniques to recommended turbidimetry conditions. *Mater. Horiz.* **4**, 109–116 (2017).
6. Frazar, E. M., Shah, R. A., Dziubla, T. D. & Hilt, J. Z. Multifunctional temperature-responsive polymers as advanced biomaterials and beyond. *J. Appl. Polym. Sci.* **137**, 48770 (2020).
7. Zhao, X., Zhu, S., Song, Y., Zhang, J. & Yang, B. Thermal responsive fluorescent nanocomposites based on carbon dots. *RSC Adv.* **5**, 15187–15193 (2015).
8. Sun, L. *et al.* Facile synthesis and performance of pH/temperature dual-response hydrogel containing lignin-based carbon dots. *Int. J. Biol. Macromol.* **175**, 516–525 (2021).
9. Zhao, D. *et al.* The Preparation of Green Fluorescence-Emissioned Carbon Dots/Poly(N-Isopropylacrylamide) Temperature-Sensitive Hydrogels and Research on Their Properties. *Polymers* **11**, 1171 (2019).
10. Zhao, C. *et al.* Programmed Stimuli-Responsive Carbon Dot-Nanogel Hybrids for Imaging-Guided Enhanced Tumor Phototherapy. *ACS Appl. Mater. Interfaces* **14**, 10142–10153 (2022).
11. Forte, G., Consiglio, G., Satriano, C., Maugeri, L. & Petralia, S. A nanosized photothermal responsive core-shell carbonized polymer dots based on poly(N-isopropylacrylamide) for light-triggered drug release. *Colloids Surf. B Biointerfaces* **217**, 112628 (2022).
12. Yang, S., Liao, B., Yi, S., Liang, E. & He, B. Tetraphenylethylene and N-isopropylacrylamide block polymer-grafted carbon dots with their application in cellular imaging. *Mater. Today Chem.* **23**, 100703 (2022).
13. Li, L., Zhang, T., Lü, J. & Lü, C. A facile construction of Au nanoparticles stabilized by thermo-responsive polymer-tethered carbon dots for enhanced catalytic performance. *Appl. Surf. Sci.* **454**, 181–191 (2018).

14. Algarni, F. *et al.* Thermo-Responsive Membranes from Blends of PVDF and PNIPAM- *b* - PVDF Block Copolymers with Linear and Star Architectures. *Macromolecules* **54**, 10235–10250 (2021).
15. Zeng, T., Yang, D., Li, H., Cheng, C. & Gao, Y. The fabrication of amphiphilic double dynamers for responsive Pickering emulsifiers. *Polym. Chem.* **9**, 627–636 (2018).
16. Wang, X. *et al.* Thermosensitive ZrP-PNIPAM Pickering Emulsifier and the Controlled-Release Behavior. *ACS Appl. Mater. Interfaces* **9**, 7852–7858 (2017).
17. Park, J. H. *et al.* Colloidosomes as a Protocell Model: Engineering Life-Like Behaviour through Organic Chemistry. *Eur. J. Org. Chem.* **2022**, e202200968 (2022).
18. Yi, D., Jeong, G., Seo, J.-H., Yoo, M. J. & Yang, H. Carbon Dots with Tailored Surface Wettability as Pickering Emulsifiers. *ACS Appl. Nano Mater.* **5**, 10258–10267 (2022).
19. Huang, X. *et al.* Interfacial assembly of protein–polymer nano-conjugates into stimulus-responsive biomimetic protocells. *Nat. Commun.* **4**, 2239 (2013).
20. Perrier, S. 50th Anniversary Perspective: RAFT Polymerization—A User Guide. *Macromolecules* **50**, 7433–7447 (2017).
21. Zhang, X.-F., Zhang, Y. & Liu, L. Fluorescence lifetimes and quantum yields of ten rhodamine derivatives: Structural effect on emission mechanism in different solvents. *J. Lumin.* **145**, 448–453 (2014).
22. Radiul, S. M., Chowdhury, J., Goswami, A. & Hazarika, S. Fluorescence spectroscopy based characterisation method for aggregation behaviour of rhodamine B (RhB) in water, ethanol, and propanol. *Laser Phys.* **32**, 075602 (2022).
23. Osváth, Z. & Iván, B. The Dependence of the Cloud Point, Clearing Point, and Hysteresis of Poly(N-isopropylacrylamide) on Experimental Conditions: The Need for Standardization of Thermoresponsive Transition Determinations. *Macromol. Chem. Phys.* **218**, 1600470 (2017).
24. Doberenz, F., Zeng, K., Willems, C., Zhang, K. & Groth, T. Thermoresponsive polymers and their biomedical application in tissue engineering – a review. *J. Mater. Chem. B* **8**, 607–628 (2020).
25. Stoica, F., F. Miller, A., Alexander, C. & Saiani, A. Thermo-Responsive PNIPAAm Copolymers with Hydrophobic Spacers. *Macromol. Symp.* **251**, 33–40 (2007).
26. Chen, S., Zhang, Y., Wang, K., Zhou, H. & Zhang, W. N-Ester-substituted polyacrylamides with a tunable lower critical solution temperature (LCST): the N-ester-substitute dependent thermoresponse. *Polym. Chem.* **7**, 3509–3519 (2016).
27. Dargaville, T. R. *et al.* Determination of molecular weight distributions of novolac resins by gel permeation chromatography. *J. Polym. Sci. Part Polym. Chem.* **35**, 1399–1407 (1997).

28. Hutchings, L. R. *et al.* HyperMacs to HyperBlocks: A Novel Class of Branched Thermoplastic Elastomer. *Macromolecules* **42**, 8675–8687 (2009).
29. Humphreys, B. A., Wanless, E. J. & Webber, G. B. Effect of ionic strength and salt identity on poly(N-isopropylacrylamide) brush modified colloidal silica particles. *J. Colloid Interface Sci.* **516**, 153–161 (2018).
30. Zhang, Y. & Cremer, P. S. Interactions between macromolecules and ions: the Hofmeister series. *Curr. Opin. Chem. Biol.* **10**, 658–663 (2006).
31. Zhang, Y. & Cremer, P. S. Chemistry of Hofmeister Anions and Osmolytes. *Annu. Rev. Phys. Chem.* **61**, 63–83 (2010).
32. Arcudi, F., Đorđević, L. & Prato, M. Synthesis, Separation, and Characterization of Small and Highly Fluorescent Nitrogen-Doped Carbon NanoDots.
33. Okaru, A. O. *et al.* Application of 19F NMR Spectroscopy for Content Determination of Fluorinated Pharmaceuticals. *J. Anal. Methods Chem.* **2017**, 9206297 (2017).
34. Ragazzon, G. *et al.* Optical processes in carbon nanocolloids. *Chem* **7**, 606–628 (2021).
35. Ohnsorg, M. L. *et al.* Tuning PNIPAm self-assembly and thermoresponse: roles of hydrophobic end-groups and hydrophilic comonomer. *Polym. Chem.* **10**, 3469–3479 (2019).
36. Malvern Panalytical. How to use GPC/SEC for compositional analysis. Available online: https://www.malvernpanalytical.com/en/learn/knowledge-center/application-notes/an170113compositionalcopolymer.
37. Huang, N.-J. & Sundberg, D. C. A gel permeation chromatography method to determine grafting efficiency during graft copolymerization. *Polymer* **35**, 5693–5698 (1994).
38. Markova, N. *et al.* Biophysical Characterization of Viral and Lipid-Based Vectors for Vaccines and Therapeutics with Light Scattering and Calorimetric Techniques. *Vaccines* **10**, 49 (2022).
39. Medrano, R., Laguna, M. T. R., Saiz, E. & Tarazona, M. P. Analysis of copolymers of styrene and methyl methacrylate using size exclusion chromatography with multiple detection. *Phys. Chem. Chem. Phys.* **5**, 151–157 (2003).
40. Rowland, S. M. & Striegel, A. M. Characterization of Copolymers and Blends by Quintuple-Detector Size-Exclusion Chromatography. *Anal. Chem.* **84**, 4812–4820 (2012).
41. Gobbo, P. *et al.* Programmed assembly of synthetic protocells into thermoresponsive prototissues. *Nat. Mater.* **17**, 1145–1153 (2018).

Chapter V – Self-assembly of Carbon NanoDot-based Protocells and their Cell-like Properties

Abstract

In this Chapter, the fabrication process of Carbon NanoDots (CND)-based protocells and a preliminary evaluation of their cell-like behavior is studied.

Initially, the self-assembly of microcapsules, namely colloidosomes (*i.e.*, microcapsules built from colloidal particles) *via* Pickering emulsion technique is described. As building blocks, nanocomposites made of CNDs and an amphiphilic *N*-isopropyl acrylamide (NIPAA)-based copolymer, namely CND/polymer nanoconjugates (see Chapter IV), are chosen as Pickering emulsifiers. The Pickering emulsions are characterized by brightfield and wide field fluorescence microscopy, evaluating their shape and dimensions.

Since microcapsules in Pickering emulsion are not stable themselves and any change in environment could lead to their disassembly, crosslinking agents are needed to lock the microstructures in their spheroidal shape. Hence, after assembling the colloidosomes *via* the Pickering emulsion technique, we study the effect of several crosslinking agents on the microcapsules' morphology. These investigations lead us to determine the best crosslinker to then transfer the CND-based microcapsules into aqueous media. At this stage, we characterize CND-based colloidosomes by brightfield, wide-field fluorescence microscopy, and confocal microscopy, evaluating their shape, dimensions, and proving the co-localization of their constituent fluorophores (*i.e.*, CNDs and RhB on the polymer chains).

Lastly, leveraging on the possibility that CND/polymer nanoconjugates might be expressing enzyme-like activity, or nanozymes, we engineer our system to mimic a two-enzyme cascade reaction (the glucose oxidase (GOx) – horseradish peroxidase (HRP) system).

In detail, we encapsulate GOx into CND-based colloidosomes, and we test whether the microcapsules themselves can act as the second enzyme (*i.e.*, HRP). We discover that our system expressed an enzyme-like nature, paving the way for promoting CND-based colloidosomes to protocells.

All the experimental activities described in this Chapter were carried out within the Gobbo group, under the supervision of Prof. Pierangelo Gobbo and Prof. Maurizio Prato.

5.1 Introduction

Colloidosomes received lot of attention as an emerging protocell model due to several advantages over other types of protocells, which include ease of membrane engineering, strong mechanical stability, and an extensive variety of constituent materials.[1]

As previously described in Chapter I, microcompartments, such as colloidosomes in this case, should mimic at least one characteristic of living cells (*e.g.*, communication based on diffusible chemical signals, enzymatic activity, adhesion capability)[2–6] to gain the classification of protocell.[7] Several examples of colloidosomes, as either single units or consortia, designed to have cell-like behaviors are reported in literature. Rodríguez-Arco *et al.* described a primitive form of artificial phagocytosis in binary community composed of silica colloidosomes and magnetic Pickering emulsion droplets.[8] Another interesting case is shown by *Bai et al.* in which, taking inspiration from chloroplasts processes, they construct a bioinspired compartmentalized photocatalytic system utilizing silica-based colloidosomes.[9] Lastly, the enzyme-mimicking properties of colloidosomes are also described and generally based on the encapsulation in the microcapsule lumen or absorption on its surface of a specific enzyme.[10,11]

To implement enzyme-like behavior in these confined systems, enzyme cascade reactions are the most common type of bio-derived machinery.[12] The most established system is the glucose oxidase (GOx) – horseradish peroxidase (HRP) cascade due to the high activity and stability of these two enzymes.[13–19] In the presence of dioxygen, GOx catalyzes the oxidation of glucose to *D*-glucono-1,5-lactone (which then hydrolyses to *D*-gluconic acid) and hydrogen peroxide. The latter is the substrate for HRP which then oxidizes usually a chosen non-colored and non-fluorescent molecule to a colored and fluorescent probe, whose production over time can be detected with a spectrophotometer or a fluorescence detector.[20] This enzyme cascade reaction has been successfully performed by integrating the enzymes within metal-organic frameworks,[21] in lattice-like DNA nanostructures,[22] and in protocellular systems as well. In detail, this was used to achieve communication based on diffusible signals between protocell populations and within tissue-like materials.[10,14–17]

In the field of enzyme mimicry, an emerging area is the one of nanozymes, *i.e.*, nanomaterials with enzyme-like activities.[23] These materials have been developed to overcome the intrinsic disadvantages of natural enzymes such as high-cost storage, structural instability, and chemical sensitivity.[24] Several examples have been reported in the last decade. Some examples of metal-based nanozymes have been described either mimicking peroxidase or carbonic anhydrase activity.[25–27] On the other hand, both Yin *et al.* and Fu *et al.* reported metal-free nanozymes based on polymeric structure and zeolitic framework, respectively, being active as peroxidase and

hydrolase.[28,29] Moreover, also carbon-based nanozymatic systems have been described relying either on carbon nanospheres, single-walled carbon nanotubes or carbon nitrides, all expressing peroxidase-like activity.[30–32]

Among carbon-based nanozymes, especially Carbon Dots (CDs) have generated strong interest due to their biocompatibility, high catalytic activity, and ease in surface functionalization. Among their possible enzyme-like activity, the peroxidase-like is one of the most described, since peroxidases are ubiquitous in nature, greatly versatile, and used in fields such as chemical and food industry, biotechnology and environmental science.[33] Recently, on this note, it was shown how CDs can enhance the peroxidase-like catalytic performances of other nanozymes.[34,35]

In this Chapter the spontaneous self-assembly of Carbon NanoDots (CND)-based microcapsules exploiting the Pickering emulsion technique is firstly illustrated.[36] Then, the influence of the addition of a crosslinker on the morphology of microcapsules is shown, and the optimized formulation to prepare stable CND-based colloidosomes is described. Each step of the fabrication process (*e.g.*, Pickering emulsion formation, crosslinking, transfer into water medium) is characterized by brightfield and fluorescence microscopy. Finally, a preliminary evaluation of peroxidase-like activity of CND-based colloidosomes will be shown to demonstrate the enzyme-mimicking abilities of these novel protocells.

5.2 Results and Discussion

5.2.1 Self-assembly of Microcapsules *via* Pickering Emulsions Technique

As discussed in Chapter IV, we designed, synthetized and characterized CND/polymer nanoconjugates to employ them as amphiphilic building blocks to fabricate CND-based colloidosome, which to the best of our knowledge, is the first example of protocells with this new class of carbon nanomaterials.

In particular, the amphiphilic nature of these nanocomposites was imparted to CND from the NIPAA-based polymer grafted onto their surface.

At first, they were tested as amphiphiles for water-in-oil Pickering emulsion fabrication. In detail, we examined if CND/polymer nanoconjugates were effective as Pickering emulsion stabilizers. A schematic representation of our Pickering emulsion composition is reported in **Figure 5.1.a**. Briefly, CND/polymer nanoconjugates are dissolved in the aqueous phase, and then an organic oil phase, precisely 2-ethyl-1-hexanol, is added on top (aqueous/oil volume fraction of 0.06). By shaking manually for 15 s, we obtained Pickering emulsions as cloudy suspensions shown in **Figure 5.1.b** (see Experimental section, 5.4.2 Preparation of CND-based colloidosomes *via* the Pickering emulsion technique). As negative control experiment, we also used pristine CNDs as Pickering emulsifiers in the same fashion, confirming that they did not stabilize any emulsions which led to a phase separation (**Figure 5.1.b**).

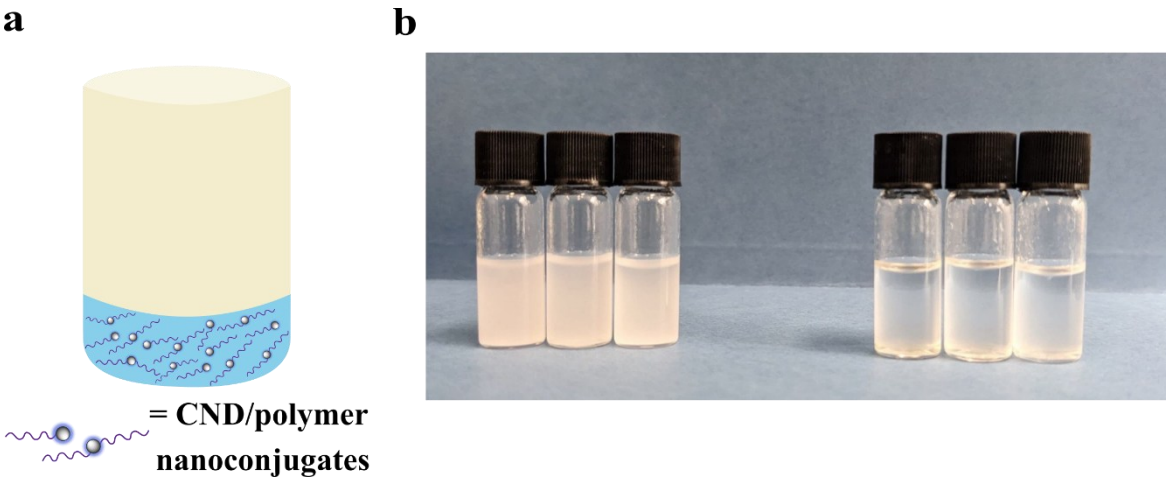

Figure 5.1 a) *Schematic representation of a water-in-oil Pickering emulsion composition. Lower aqueous phase (light blue region) with dissolved CND/polymer nanoconjugates, upper oil phase (yellow region, 2-ethyl-1-hexanol);* ***b)*** *Emulsion tests at three different concentrations (2, 4, 8 mg* mL^{-1}*) of CND/polymer nanoconjugates (on the left, cloudy suspensions) and of pristine CNDs (on the right, biphasic systems).*

Having established that the CND/polymer nanoconjugates can stabilize Pickering emulsions, we investigated the effect of emulsifier concentration on the final size and morphology of the microcapsules. As shown in **Figure 5.2**, using brightfield microscopy, we investigated the impact of changing the concentration of CND/polymer nanoconjugates on the Pickering emulsions. This was done by preparing five different aqueous solutions using different concentrations of CND/polymer nanoconjugates (0.5, 1, 2, 4, 8 mg mL^{-1}).

At low concentrations of CND/polymer nanoconjugate, 0.5 and 1 mg mL^{-1}, the Pickering emulsions were not stabilized efficiently by the CND/polymer nanoconjugates. As can be seen from brightfield microscopy images (**Figure 5.2.a** and **c**), microcapsules are formed. However, they are surrounded by large water droplets, which will eventually coalesce (phase separation). In both cases, the formed microdroplets are polydisperse and had an average size of 14 ± 5 μm (relative standard deviation (RSD) of 30%) (**Figure 5.2.b** and **d**).

Moving to CND/polymer nanoconjugates concentration of 2 mg mL^{-1}, the morphology of the droplets is improved since there was no phase separation (large water droplets), and the microcapsules resulted more spherical (**Figure 5.2.e**).

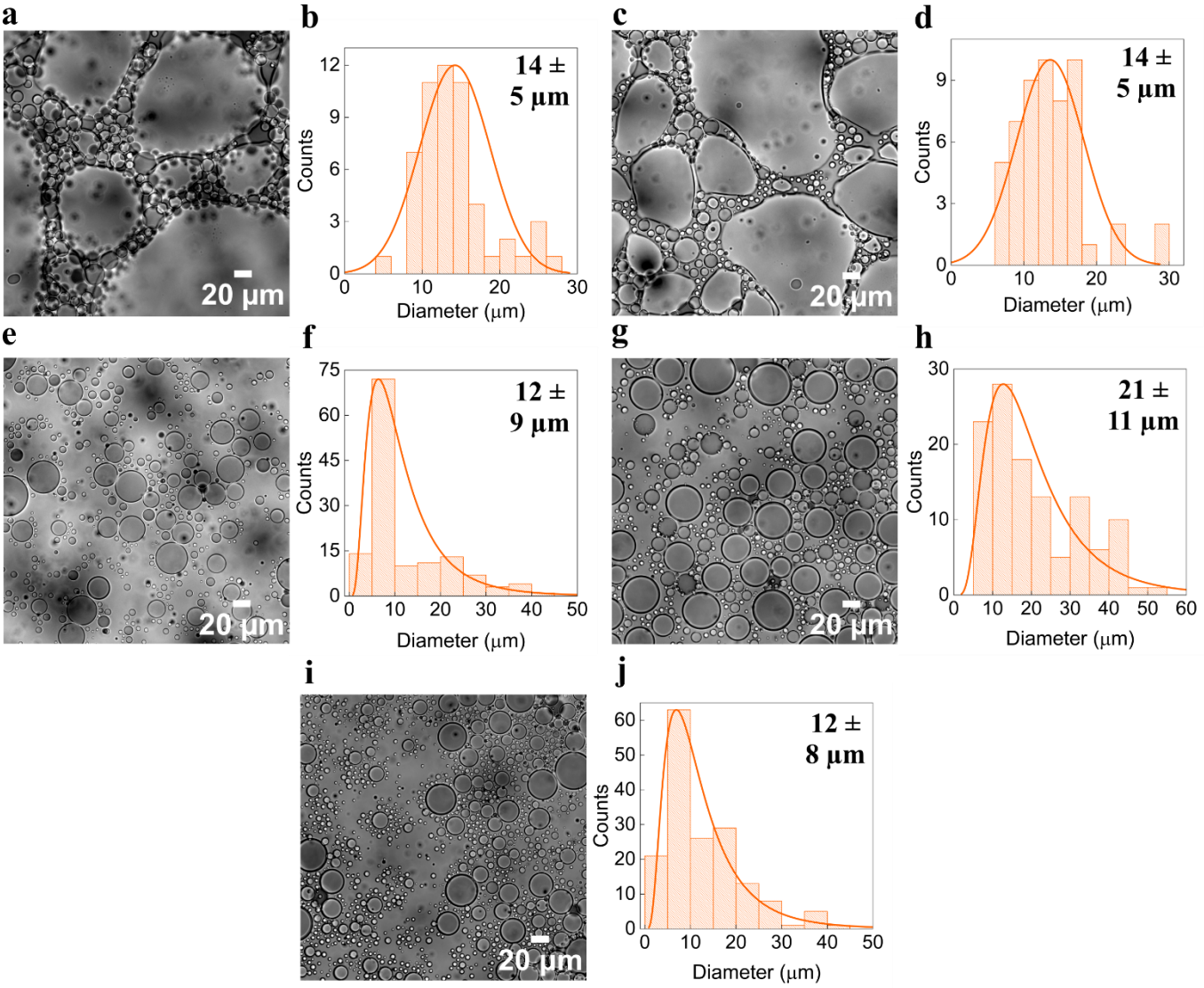

Figure 5.2 a, c, e, g, i) *Brightfield microscopy images of Pickering emulsions stabilized by CND/polymer nanoconjugates at concentration of 0.5, 1, 2, 4 and 8 mg mL^{-1}, respectively;* ***b, d, f, h, j)*** *Size distribution graphs of Pickering emulsion microcapsules at a CND/polymer nanoconjugates concentration of 0.5, 1, 2, 4 and 8 mg mL^{-1}, respectively.*

Therefore, we concluded that this was the lower CND/polymer nanoconjugates threshold to form good quality and stable Pickering emulsions. However, the number of produced microcapsules was low, similarly to their average size (12 ± 9 µm). The RSD of their size distribution (73%) was high, thus the sample resulted quite polydisperse (**Figure 5.2.f**).

The Pickering emulsion yielded with 4 mg mL^{-1} of CND/polymer nanoconjugates concentration is shown in **Figure 5.2.g**, which gave the best results in terms of microcapsules dimensions and quantity, even though their size distribution RSD is still high (56%) (**Figure 5.2.h**). Interestingly, their average size was comparable to the one reported for similar protocells.[10]

Lastly, the highest CND/polymer nanoconjugates concentration (8 mg mL^{-1}) delivered Pickering emulsions with microcapsules with decreasing diameter and higher RSD (67%), compared to the 4 mg mL^{-1} ones (**Figure 5.2.i** and **h**).

It is worth highlighting that the high RSD values for all the size distributions may be ascribed to the preparation of the Pickering emulsions by manual shaking. Implementing a homogenizer or a microfluidic device for the emulsification of the biphasic systems would improve these values.

In conclusion, with these screening experiments, we determined that the best concentration of CND/polymer nanoconjugates is 4 mg mL^{-1}, which yield Pickering emulsions with a diameter of 21 ± 11 µm.

5.2.2 Evaluation of Crosslinker Influence on Microcapsules Morphology

Moving forward into the fabrication of stable colloidosomes, it was essential to block the formed microcapsules in their spheroidal shape. To achieve that, we exploited the chemical crosslinking of these microdroplets *via* amide-bond formation chemistry. In particular, the reaction occurred between the primary amines on the polymer chains of the nanoconjugates and the activated carbonyl group of a crosslinker, namely *N*-hydroxysuccinimide (NHS) activated (**Figure 5.3**).

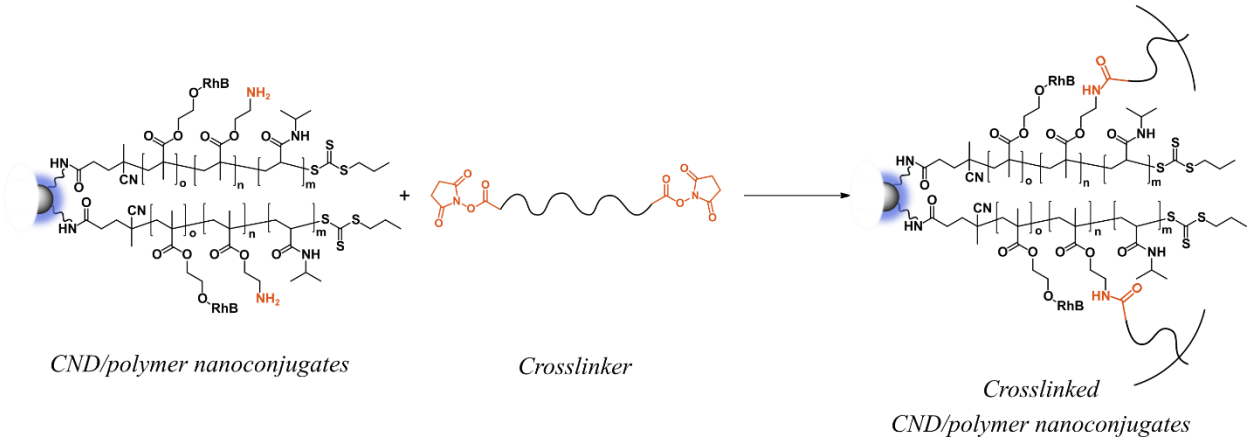

CND/polymer nanoconjugates *Crosslinker* *Crosslinked CND/polymer nanoconjugates*

Figure 5.3. *Reaction scheme between CND/polymer nanoconjugates and a general crosslinker with NHS activated carbonyl groups, yielding crosslinker CND/polymer nanoconjugates in Pickering emulsion (crosslinking reaction = 48 h).*

Specifically, the crosslinker was added, either to water or oil phase, before shaking the biphasic system, to then deliver the Pickering emulsions. Efficiently crosslinking CND/polymer nanoconjugates at the interface of the Pickering emulsion would allow us to isolate the microcapsules into the desired aqueous medium.

Several crosslinkers – either commercially available or synthetized (see Experimental section, 5.4.3 Synthesis of crosslinkers) – were tested and are listed in **Table 5.1**, with the tested amount used per Pickering emulsion and their success rate in crosslinking CND-based microdroplets.
To assess if the crosslinking was effective or not, we solubilized, after 48 hours, part of the Pickering emulsion in 70 V/V% ethanolic aqueous solution, to partially remove the oil and observe whether the microcapsules remained intact. We also investigated whether solubilizing these (macro)molecules either in the water or oil phase of the Pickering emulsion could influence their crosslinking efficacy (see Experimental section, 5.4.2 Preparation of CND-based colloidosomes *via* Pickering emulsion technique).

Table 5.1. *List of tested crosslinkers, organized from the most polar (top) to the least polar (bottom), showing the quantity per emulsion used and their efficacy in crosslinking CND-based microcapsules.*

Crosslinker	Quantity per emulsion (mg)	Emulsion phase	Effective crosslinking
PEG-diNHS	2, 4	Water	X
		Oil	V
TEG-diNHS	2	Water	X
		Oil	-
PDEGMA-*co*-NHS	2	Water	X
		Oil	-
POEGMA-*co*-NHS	2	Water	X
		Oil	-
PNIPAA-*co*-NHS	0.2, 1, 2	Water	V
		Oil	V
Suberic acid-diNHS	0.2, 1, 2	Water	-
		Oil	V

V crosslinked, X not crosslinked, - test not done. PEG-diNHS: O,O'-Bis[2-(*N*-Succinimidyl-succinylamino)ethyl]polyethylene glycol, TEG-diNHS: Tetraethylene glycol-bis(succinic acid *N*-hydroxysuccinimide ester), PDEGMA-*co*-NHS: Polydi(ethylene glycol) dimethacrylate-*co*-acrylic acid *N*-hydroxysuccinimide ester, POEGMA-co-NHS: Polyoligo(ethylene glycol) dimethacrylate-*co*-acrylic acid *N*-hydroxysuccinimide ester, PNIPAA-*co*-NHS: Poly *N*-Isopropylacrylamide-*co*-acrylic acid N-hydroxysuccinimide ester, Suberic acid-diNHS: Suberic acid bis(N-hydroxysuccinimide ester).

After the synthesis of the crosslinkers, all the quantities reported in **Table 5.1** were tested.

Firstly, it is important to highlight that the tested crosslinkers had different chemical natures. Particularly, PEG-diNHS and TEG-diNHS were the most polar crosslinkers, whereas PDEGMA-*co*-NHS, POEGMA-*co*-NHS, and PNIPAA-*co*-NHS had an amphiphilic nature, and lastly suberic acid-diNHS was soluble just in the oil phase, being the least polar. These differences reflected in the morphology of the Pickering emulsions and in the achieved crosslinking (**Figures 5.4** and **5.5**). In **Figure 5.4** are reported the resulting Pickering emulsions obtained with the linear ethylene glycol-based and amphiphilic crosslinkers. Concerning the more polar crosslinkers, PEG-diNHS and TEG-diNHS (**Figure 5.4.a** and **b**, respectively), we observed a difference in the size distribution of two microcapsule families. In particular, the microcapsules crosslinked with PEG-diNHS (2 mg) were shrunken with respect to the ones fabricated without a crosslinker. Instead, the Pickering emulsion crosslinked with the TEG-diNHS (2 mg) more closely resembled the one obtained without a crosslinker. Regardless, in both cases, no successful transfer of the microcapsules was achieved once they were solubilized in 70 V/V% ethanolic aqueous solution (**Figure 5.5.b**).

Interestingly, the amphiphilic crosslinkers, PDEGMA-*co*-NHS, POEGMA-*co*-NHS, and PNIPAA-*co*-NHS, delivered multiple Pickering emulsions (**Figure 5.4.c-e**). This evidence of multi-compartmentalized emulsions was attributed to the amphiphilicity of the crosslinker, as also supported by recent reports.[37,38]

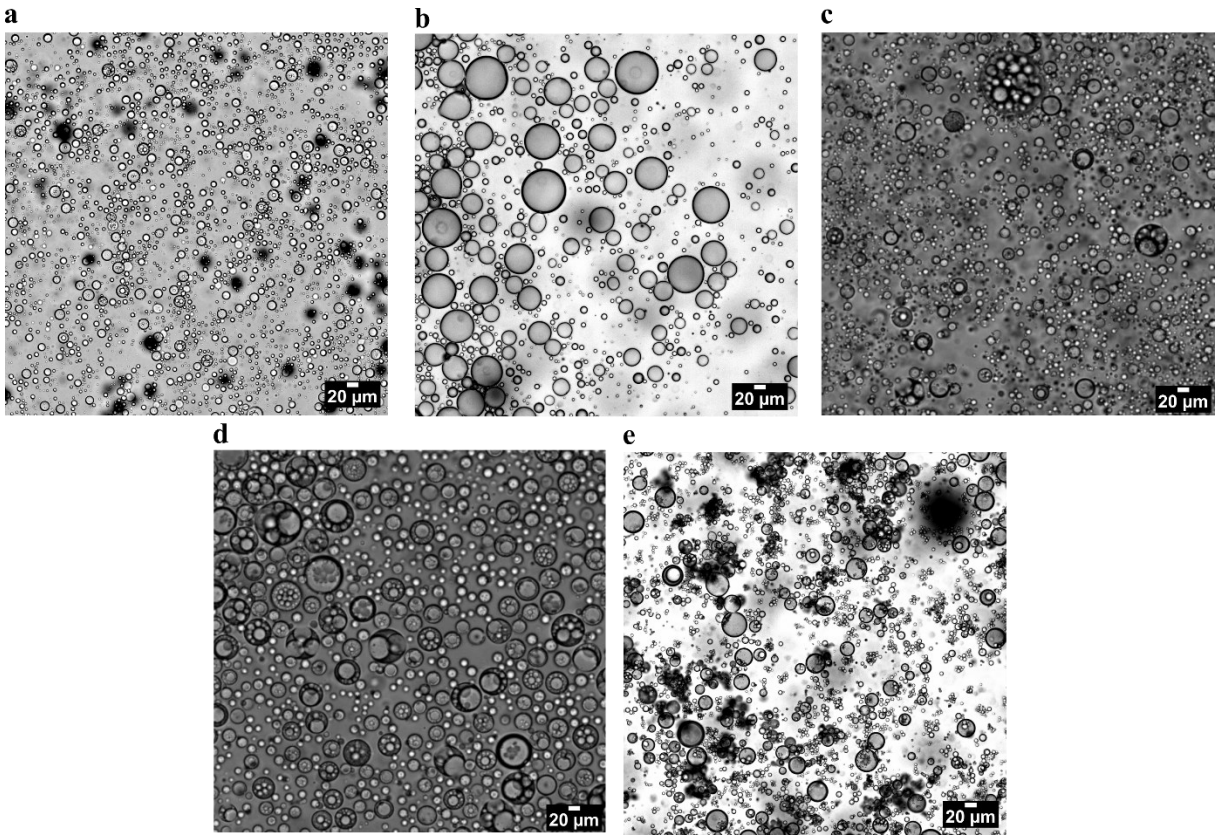

Figure 5.4. a, b, c, d, e) *Brightfield microscopy images of Pickering emulsions stabilized by CND/polymer nanoconjugates at concentration of 4 mg mL^{-1} and crosslinked from aqueous phase with PEG-diNHS (2 mg), TEG-diNHS (2 mg), PDEGMA*-co-*NHS (2 mg), POEGMA*-co-*NHS (2 mg), and PNIPAA*-co-*NHS (0.2 mg), respectively.*

The Pickering emulsion crosslinked with the amphiphilic PNIPAA-*co*-NHS was the only successful result among the water-crosslinked microcapsules, and to minimize the effect of the multi-compartmentalization of the emulsions we chose to lower the amount of crosslinker (0.2 mg). To further confirm the effective crosslinking, we reported the fluorescence image of the corresponding transfer in 70 V/V% ethanolic aqueous solution, in which it could be noticed some aggregation due to the highly reactive crosslinker (**Figure 5.5.d**). We chose to show particularly the microscopy image of the RhB-tagged polymer emission because it has a higher quantum yield than CNDs in ethanolic aqueous solution. **Figure 5.5.b** showed a representative example of a failed transferring test, valid for all the other crosslinkers tested so far.

Finally, it was possible to transfer these PNIPAA-*co*-NHS-crosslinked colloidosomes in water, observing that they retained they multi-compartmentalized morphology (**Figure S5.1**).

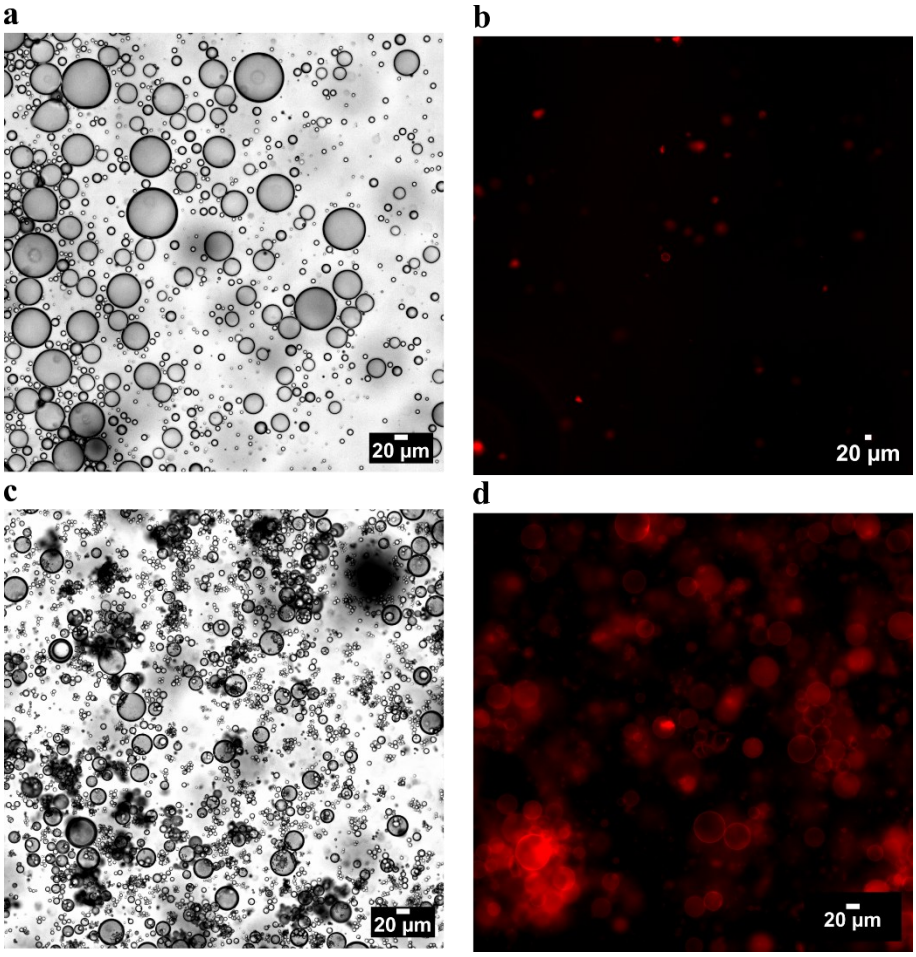

Figure 5.5. a, c) *Brightfield microscopy images of Pickering emulsions stabilized by CND/polymer nanoconjugates at concentration of 4 mg* mL^{-1} *and crosslinked from aqueous phase with TEG-diNHS (2 mg) and PNIPAA*-co-*NHS (0.2 mg), respectively;* ***b)*** *Fluorescence microscopy image of failed test of transferring in 70 V/V% ethanolic aqueous solution Pickering emulsion* ***a*** *(*λ_{exc} *= 564 nm, RhB-tagged polymer fluorescence).* ***d)*** *Fluorescence microscopy image of corresponding colloidosomes of Pickering emulsions* ***c*** *transferred in 70 V/V% ethanolic aqueous solution (*λ_{exc} *= 564 nm, RhB-tagged polymer fluorescence).*

From these results, we concluded that the primary amines in the polymer chains of the CND/polymer nanoconjugates were not available for interfacial chemistry at the water phase interface, except for the PNIPAA-*co*-NHS crosslinker case.

This outcome was surprising since all the amphiphilic crosslinkers (PDEGMA-*co*-NHS, POEGMA-*co*-NHS, and PNIPAA-*co*-NHS) were synthetized using the same molar percentage amount of reactive crosslinking group (5 mol% of NHS, see Experimental Section, 5.4.3 Synthesis of crosslinkers). However, this difference could be influenced by other factors such as the type of polymer (NIPAA-based *vs* ethylene glycol-based), polymer molecular weight and dispersity.[39] Especially on the last two parameters we did not have any precise control since we synthetized

those crosslinkers *via* free radical polymerization. Moreover, recent findings also showed that ethylene glycol-based homopolymers might have, in some cases, the number of hydrophilic groups on the side chains sufficient to overcome the hydrophobicity of the polymer backbone, canceling their thermoresponsive behavior, strictly linked to their amphiphilicity.[40] Finally, taking into account all these factors, we hypothesized that PNIPAA-*co*-NHS had a predominant hydrophobic character, therefore reaching the primary amines on CND/polymer nanoconjugates more available from the oil phase of the Pickering emulsion.

To further prove out hypothesis that CND/polymer nanoconjugates active moieties were more prone to react in the oil phase, we used oil-soluble crosslinkers to study the crosslinking efficacy of the Pickering emulsions. As shown in **Table 5.1** and **Figure 5.6**, this had a much higher success rate.

Alongside the brightfield images of the Pickering emulsions, shown in **Figure 5.6.a**, **c**, and **e**, are displayed fluorescence images of the corresponding microcapsules transferred in 70 V/V% ethanolic aqueous solution (**Figure 5.6.b**, **d**, **f**). Even in this case, the fluorescence images reported showed the microscopy image of the RhB-tagged polymer emission only, since it has a higher quantum yield than CNDs in ethanolic aqueous solution.

We observed that crosslinking with suberic acid-diNHS delivered the most monodispersed microcapsules (19 ± 5 μm, RSD 24%). We chose to study the lowest amount of crosslinker (0.2 mg) since higher amounts delivered too concentrated solution, thus not stable Pickering emulsions. Surprisingly PNIPAA-*co*-NHS did not yield multiple emulsions once it was added from the oil phase. This new yet interesting behavior was not further investigated since it was beyond the scope of this thesis.

At that stage, all three systems were promising candidates to yield robust CND-based colloidosomes.

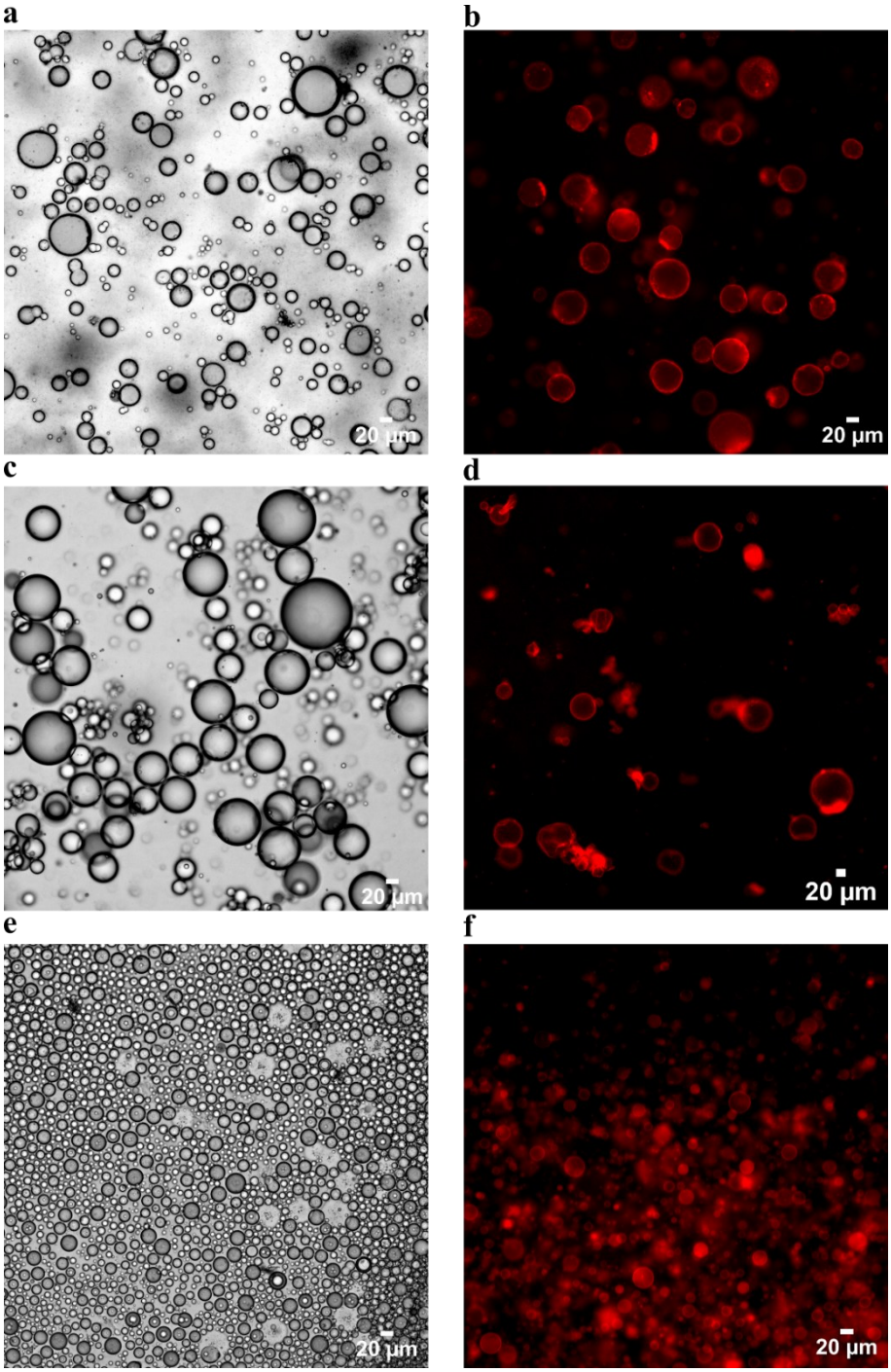

Figure 5.6. a, c, e) *Brightfield microscopy images of Pickering emulsions stabilized by CND/polymer nanoconjugates at concentration of 4 mg* mL^{-1} *and crosslinked from oil phase with PEG-diNHS (2 mg), PNIPAA-co-NHS (0.2 mg), and suberic acid-diNHS (0.2 mg), respectively;* ***b, d, f)*** *Fluorescence microscopy images of corresponding microcapsules of Pickering emulsion* ***a, c, e*** *transferred in 70 V/V% ethanolic aqueous solution (*λ_{exc}*= 564 nm, RhB-tagged polymer fluorescence).*

5.2.3 Isolation and Characterization of Colloidosomes into Aqueous Phase

A schematic representation of our methodology to fabricate CND-based colloidosomes is described in **Figure 5.7**, starting from the Pickering emulsion and ending to the microcapsules isolated in water.

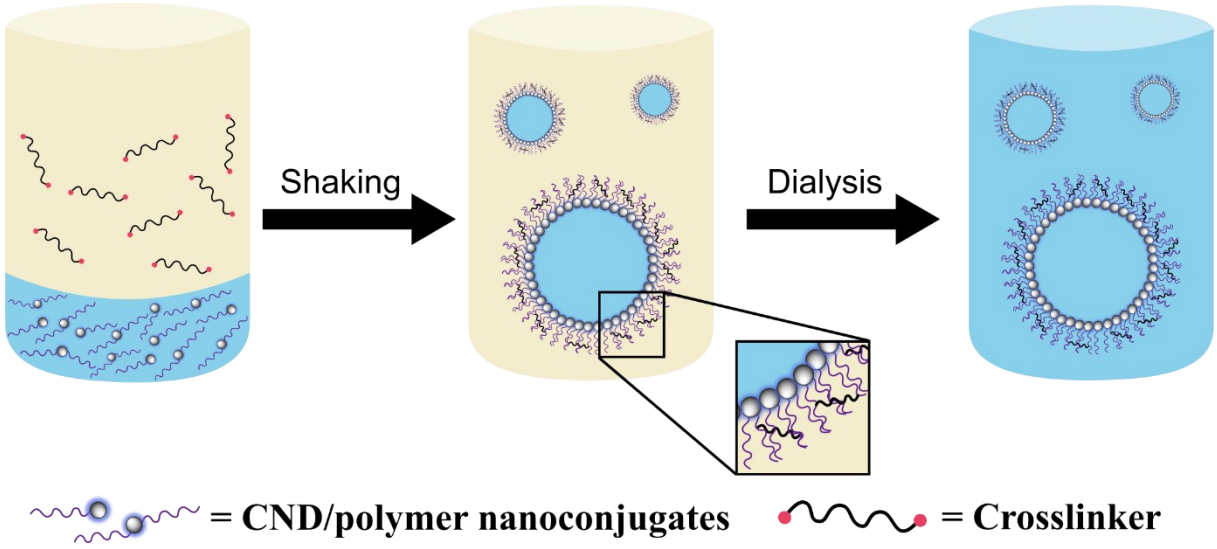

Figure 5.7. *Schematic representation of CND-based colloidosomes fabrication. The first step is a water-in-oil Pickering emulsion in which CND/polymer nanoconjugates are dissolved in the aqueous phase (light blue region) and the crosslinker is dissolved in the oil phase (yellow region). After shaking for 30s time, microcapsules are formed and left to crosslink for 48 h. The fully stabilized microcapsules, now colloidosomes, can be transferred to water.*

In short, CND/polymer nanoconjugates were dissolved in the aqueous phase. Then, the crosslinker is solubilized in the oil phase, and the mixture is added on top of the aqueous layer (aqueous/oil volume fraction of 0.06). By shaking manually for 15 s, we delivered Pickering emulsions which were left to crosslink for 48 hours. Subsequently, the crosslinked Pickering emulsions were dialyzed against ethanolic aqueous solutions at increasing polarity to just MilliQ water. Finally, the colloidosome solutions were left to sediment, and the supernatant was removed, thereby concentrating them, and characterized by fluorescence microscopy (see Experimental section, 5.4.2 Preparation of CND-based colloidosomes *via* the Pickering emulsion technique).

Pickering emulsions crosslinked with PNIPAA-*co*-NHS (**Figure 5.8.a** and **b**) yield stable microcapsules. However, we observed that the colloidosomes tended to aggregate overtime once transferred in water. This behavior was ascribed to the higher reactivity of the crosslinker used.

On the other hand, the microcapsules crosslinked with suberic acid-diNHS were not transferable to water due to a sudden shrinkage when changing the dialysis solvent polarity (**Figure S5.2**). This

outcome was linked to the water insolubility of suberic acid-diNHS compared to the other crosslinkers, probably leading to an excessively high hydrophobic character of the whole system. From these experiments, the most promising colloidosomes were yielded by Pickering emulsions crosslinked with PEG-diNHS (2 mg). These were more reproducible (*i.e.*, similar capsule morphology between different batches), robust (i.e., colloidosome not disrupted after several transfers to aqueous environments) and did not show a tendency to aggregation.

Therefore, the optimized formulation for our CND-based colloidosomes was 4 mg mL^{-1} of CND/polymer nanoconjugates and 2 mg of PEG-diNHS as crosslinker from the oil phase.

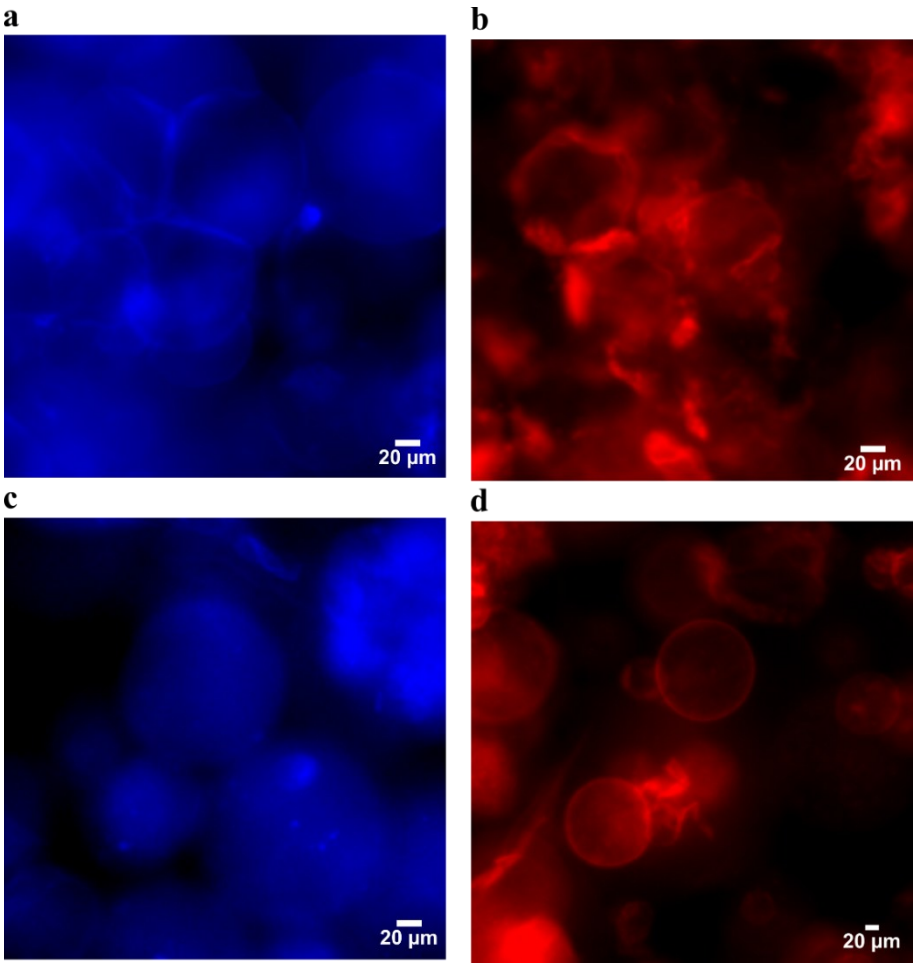

Figure 5.8. *CND-colloidosomes (CND/polymer nanoconjugates concentration = 4 mg mL^{-1}, PNIPAA-co-NHS from oil phase (0.2 mg,* ***a****,* ***b****) or PEG-diNHS from oil phase (2 mg,* ***c****,* ***d****) characterized by wide-field fluorescence microscopy:* ***a, c)*** *Fluorescence microscopy image of CNDs (λ_{exc}= 405 nm, blue fluorescence);* ***b, d)*** *Fluorescence microscopy images of RhB-tagged polymer (λ_{exc}= 564 nm, red fluorescence).*

We went further with CND-based colloidosomes characterization by observing them with the confocal microscope. **Figure 5.9** showed the Pickering emulsion (prepared as previously

described), imaged both in brightfield (**Figure 5.9.a**) and in fluorescence mode (**Figure 5.9.b-d**). It should be highlighted that to overcome the issue of some aggregate of unreacted CND/polymer nanoconjugates, we increased the amount of crosslinker used to prepare the emulsion from 2 to 4 mg. Moreover, it is observable that the lumen of the colloidosomes transferred in MilliQ water exhibits some fluorescence, which it might be associated with some free unreacted CND/polymer nanoconjugates.

As it was evident from the fluorescence channel overlay (**Figure 5.9.b**), we proved the colocalization of the nanoconjugate constituents – and fluorophores – namely CNDs (blue fluorescence) and RhB-tagged polymer (red fluorescence) at the interface of the biphasic system. This exact colocalization could also be observed in the CND-colloidosomes transferred to MilliQ water (**Figure 5.9.e** and **f**). By analyzing the size distributions of the Pickering emulsion and of CND-based colloidosomes in aqueous medium, we determined that the corresponding diameters were in good agreement (22 ± 5 μm and 26 ± 4 μm, respectively), considering the experimental error.

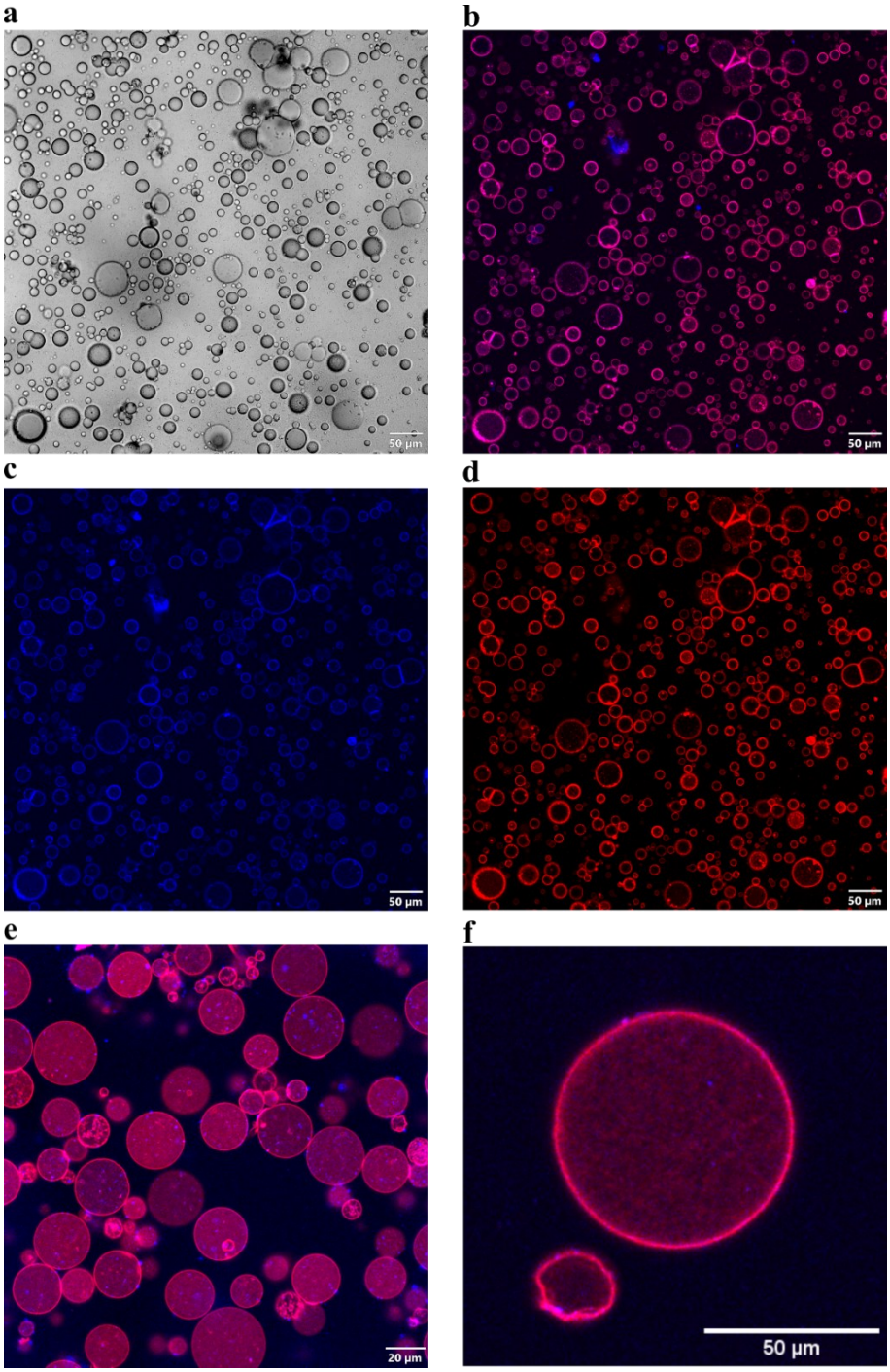

Figure 5.9. *CND-colloidosomes (CND/polymer nanoconjugates concentration = 4 mg mL^{-1}, PEG-diNHS from oil phase = 4 mg) characterized by brightfield and fluorescence confocal microscopy:* ***a)*** *Brightfield microscopy image of the Pickering emulsion;* ***b-d)*** *Overlayed and single confocal fluorescence microscopy image (CNDs (λ_{exc}= 405 nm, blue fluorescence), RhB-tagged polymer (λ_{exc}= 564 nm, red fluorescence)) of the Pickering emulsion;* ***e, f)*** *Overlayed confocal fluorescence microscopy image (CNDs (λ_{exc}= 405 nm, blue fluorescence), RhB-tagged polymer (λ_{exc}= 564 nm, red fluorescence)) of isolated colloidosomes in water.*

5.2.4 Preliminary Assessment of CND-based Colloidosomes Enzyme-like Behavior

Lastly, we investigated the possibility of turning these CND-based colloidosomes into protocells, by mimicking cell communication *via* diffusive chemical signals. As previously discussed, a significant number of reports described CDs acting as nanozymes (nanomaterials with enzyme-like activity).[33] Therefore, we chose to test whether our system could express the same nanozymatic activity. In particular, due to the oxygenated moieties available on our CND surface (*e.g.*, hydroxyl and carboxylic groups), they could manifest peroxidase-like activity. Specifically, HRP was chosen, being capable of oxidizing various organic substrates by reducing hydrogen peroxide to water.

The first qualitative assessment was performed on the CND/polymer nanoconjugates in bulk aqueous solution upon the addition of hydrogen peroxide, using the *o*-phenylene diamine (*o*-PD) as the oxidable substrate. The oxidation of *o*-PD was qualitatively observed by the solution color change, from pink to orange (**Figure S5.3**).[41]

Knowing that CND/polymer nanoconjugates could oxidize *o*-PD, the next step was to test our system using an enzyme cascade reaction. For this reason, we designed our system to couple the HRP-mimicking with another enzyme, namely GOx, which oxidizes glucose to hydrogen peroxide and *D*-glucono-δ-lactone in the presence of oxygen.[20]

To do so, first, we encapsulated GOx in the lumen of CND-based colloidosomes by adding the enzyme in the aqueous phase of the Pickering emulsion and following the same procedure previously described. Then, we isolated these loaded microcapsules in an aqueous environment (see Experimental section, 5.4.2 Preparation of CND-based colloidosomes *via* the Pickering emulsion technique). A schematic representation of our enzyme-nanozyme cascade reaction is shown in **Figure 5.10.a**.

To study the reaction, we used as substrates glucose and *o*-PD, which will oxidize into 2,3-diaminophenazine (2,3-DAP), used as fluorescent probe (λ_{exc} = 488 nm).

Briefly, a concentrated solution of colloidosomes in MilliQ water were added to 10 mM PBS buffer pH 6.8 (1:3 V/V) in a 96 multi-well plate. The reaction was initiated by addition of the substates, and it was followed using a widefield fluorescence microscope, by measuring the fluorescent 2,3-DAP formation in solution over time (see Experimental Section, 5.4.4 Enzyme cascade reaction assessment in CND-based colloidosomes).

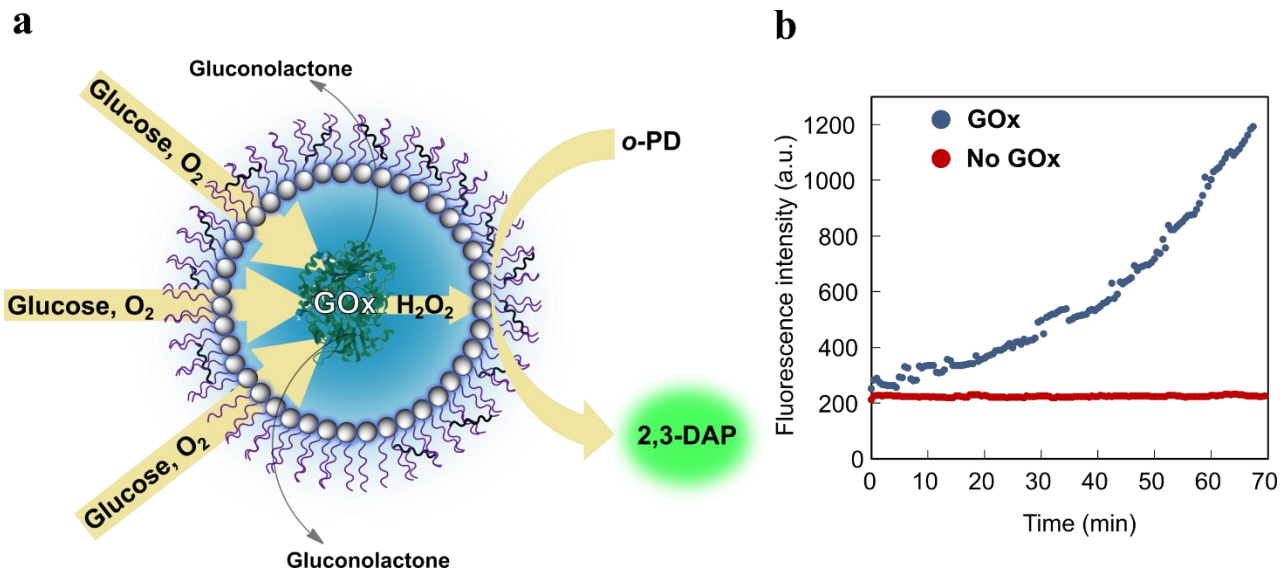

Figure 5.10. a) *Schematic representation of enzyme-nanozyme cascade reactions occurring in our CND-based colloidosomes;* ***b)*** *Graph of fluorescence intensity over time (λ_{exc}= 488 nm, 2,3-DAP fluorescence) of the described cascade reaction with (blue curve) and without (red curve) the presence of GOx acquired (0.5 mM o-PD, 1 mM glucose, 10 mM PBS buffer pH 6.8).*

As shown in **Figure 5.10.b**, the initial stage of the cascade reaction was successfully monitored using widefield fluorescence microscopy. Moreover, when the colloidosomes were prepared without encapsulated GOx, no fluorescence formation was registered under the same experimental conditions. This meant that the whole enzyme-nanozyme system is necessary to make the cascade reaction to occur.

These were the first steps to demonstrate that our CND-based nano- (nanoconjugates) and micro-systems (colloidosomes) have an enzyme-like activity that can act in tandem with other enzymes, paving the way to define these entities as protocells.

5.3 Conclusions

In summary, this Chapter first outlined the self-assembly of colloidosomes *via* the Pickering emulsions technique, where we optimized the concentration of CND/polymer nanoconjugates at the water-in-oil interface by brightfield microscopy. Then, we examined the impact of different crosslinkers (from more polar to less polar) on microcapsule morphology and crosslinking effectiveness. In detail, we tested two strategies: adding the crosslinkers either in the aqueous or oil phase of the emulsion, with the latter proving the most effective. This mmethodology enabled us to successfully transfer CND-based colloidosomes into an aqueous environment. Widefield and confocal fluorescence microscopy allowed us to characterize the microcapsules, evaluating their morphology and proving the co-localization of CNDs and RhB-tagged polymer at the microcapsule membrane. Eventually, we design and fabricate our protocellular system to mimic an enzyme cascade reaction, with preliminary tests indicating its successful functionality.

As future work, we plan to further validate the reproducibility of the enzyme-like behavior of our system, by examining the kinetics of the enzyme cascade reaction as well. Moreover, investigating the specific contributions of each component – the CNDs and the NIPAA-based copolymer – to the overall reactivity of the CND/polymer nanoconjugates and colloidosomes will be insightful.

To the best of our knowledge, this work represents the first example of CND-based protocells, paving the way to the design and fabrication of organic colloidosomes with features beyond those previously achieved.[1,36] For instance, CNDs enable the synthesis of intrinsically fluorescent membranes and can serve as enzyme-mimicking platforms, endowing the protocell membrane with catalytic properties without complex derivatization or costly enzymes to achieve cell-like functionality. This approach simplifies the synthesis of colloidal amphiphilic species used in Pickering emulsions, expanding the potential applications and versatility of protocell systems.

5.4 Experimental Section

5.4.1 Materials and Methods

PEG (2,000 Da, BioUltra), succinic anhydride (≥99% (GC)), 4-(Dimethylamino)pyridine (ReagentPlus®, ≥99%), DMF (≥99.8%, anhydrous), NHS (Novabiochem®), N,N′-Dicyclohexylcarbodiimide (99%), DCM (contains 40-150 ppm amylene as stabilizer, 99.8%, anhydrous), TEG (for synthesis), ethyl acetate (suitable for HPLC, ≥99.7%), DEGMA (95%), 2,2′-Azobis(2-methylpropionitrile) (≥98.0%, (GC)), acetonitrile (≥99.8% (GC)), OEGMA (average Mn 500, 100 ppm MEHQ and 200 ppm BHT as inhibitors), N-Isopropylacrylamide (97%), and suberic acid bis(N-hydroxysuccinimide ester) (≥95%) were purchased from Sigma-Aldrich. *N*-acryloxysuccinimide was purchased from Acros Organics. All chemicals were used without further purification unless otherwise stated. MilliQ water was obtained from a Millipore Milli-Q Plus 185 apparatus and presented a resistivity of 18.2 MΩ cm.

^{1}H-NMR spectra were recorded on Varian 400 MHz spectrometer (^{1}H = 400 MHz). Chemical shifts were reported in ppm using the solvent residual signal as an internal reference (D_2O: δH = 4.79 ppm). All spectra were recorded at 25 °C. All the spectra were analyzed with MestReNova v12.0.1-20560.

Pickering emulsions and CND-based colloidosomes were characterized by brightfield microscopy using a fluorescence microscope Axio Observer 7 (Zeiss) equipped with a CMOS Orca Flash 4.0 V3 camera (Hamamatsu). The instrument includes a motorized XYZ sample holder stage for tiled imaging acquiring mode. Brightfield pictures were obtained using a LED transmitted light source. Moreover, they were characterized by confocal fluorescence microscopy imaging using a FV3000 confocal laser scanning microscope (Evident). The system is equipped with 5 excitation laser lines: 375, 405, 488, 561 and 640 nm (Coherent), a galvanometric scanning head and 4 spectral detectors allowing simultaneous imaging of up to 4 fluorescence channels. Brightfield images were acquired using a scanning laser line and a transmitted light detector. The IX 83 inverted microscope body (Olympus) includes a motorized sample stage (Prior Scientific) for multi-area mosaic image acquisition. Analysis of colloidosomes number and size distribution was performed using ImageJ v1.54k.

5.4.2 Preparation of CND-based colloidosomes *via* the Pickering emulsion technique

CND-based colloidosomes were prepared by mixing an aqueous CND/polymer nanoconjugates solution (see Chapter IV for the detailed synthesis of CND/polymer nanoconjugates) with 2-ethyl-1-hexanol followed by shaking the mixture by hand for 15 s. The samples were prepared at a constant aqueous/oil volume fraction of 0.06. Typically, 60 µL of aqueous CND/polymer nanoconjugates (4 mg mL^{-1}, 100 mM $NaHCO_3/Na_2CO_3$ sodium carbonate buffer, pH 8.5) were mixed with 1 mL of the oil. The colloidosomes were then crosslinked in the continuous oil phase by addition of PEG-diNHS (4 mg), previously dissolved in chloroform. The crosslinker reacted with free primary amine groups of the polymer. Transfer of the crosslinked CND-based colloidosomes into water was achieved as follows. After 3 h sedimentation, the upper clear oil layer was discarded, and 1 mL of 70 V/V% ethanolic aqueous solution was added and the emulsion gently shaken. The dispersion was then dialyzed against 70 V/V% ethanolic aqueous solution for 5 h, 30 V/V% ethanolic aqueous solution for 3 h, and MilliQ water for 18 h to complete the phase transfer process. CND-based colloidosomes comprising encapsulated GOx (0.5 mg) were prepared following the above procedures except that the enzyme was added to the aqueous CND/polymer nanoconjugates solution before mixing with the oil phase.

5.4.3 Synthesis of Crosslinkers

The ethylene glycol-based crosslinkers were synthesized using similar reaction steps. First, the alcohol was converted to a carboxylic acid by reaction with the succinic anhydride, and then this was activated with NHS. The two reaction steps are illustrated in **Figure 5.10**.

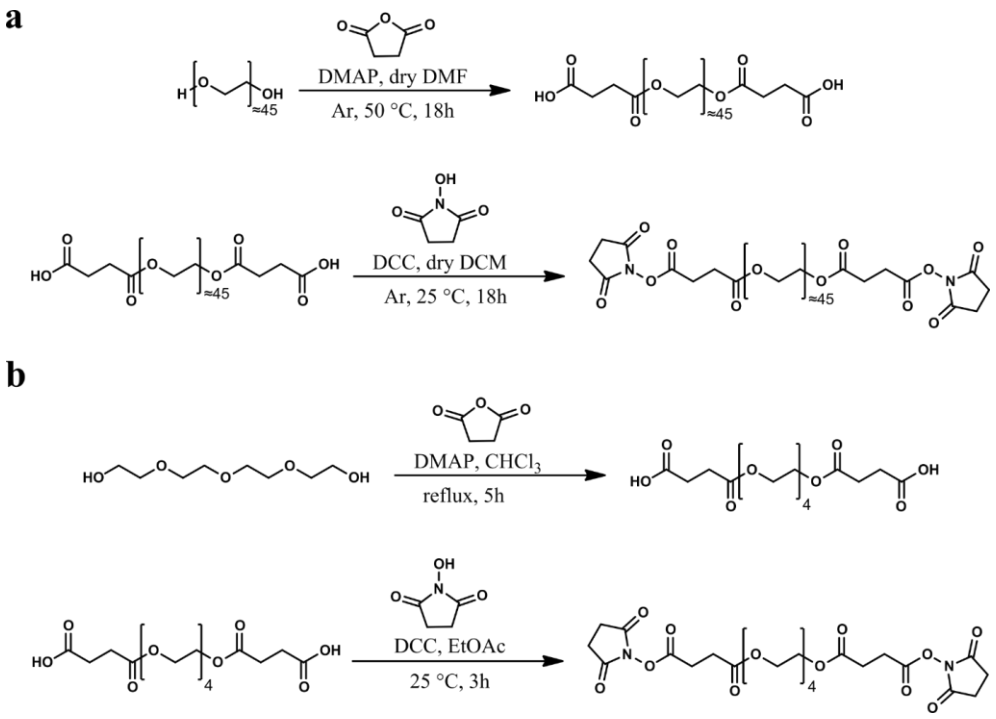

Figure 5.10. a) *Reaction scheme of PEG-diNHS synthesis;* ***b)*** *Reaction scheme of TEG-diNHS synthesis.*

Synthesis of PEG-diNHS

STEP 1. In detail, previously dried PEG 2000 (7.5 mmol) was added in a 250 mL Schlenk tube equipped with a magnetic stirrer bar under Ar atmosphere. Subsequently, succinic anhydride (21.2 mmol) and *N,N*-Dimethylpyridine-4-amine (DMAP, 2.8 mmol) were added. Using a syringe, 110 mL of anhydrous DMF was added. The solution was left reacting under inert atmosphere at 50°C for 18 hours. Then, the mixture was filtered and precipitated in 1 L of cold diethyl ether. The supernatant was removed, and the obtained white precipitate was dissolved in DCM and precipitated in cold diethyl ether again. The PEG diacid was isolated as white solid after evaporation under reduce pressure (MW ≈ 2234.16 g mol^{-1}, 15.03 g, yield 89%).

^{1}H NMR ($CDCl_3$, 400 MHz): 4.25 ppm (m, 4H), 3.64 ppm (m, 175H), 2.64 ppm (m, 8H).

STEP 2. The PEG diacid (2.2 mmol) in a 250 mL Schlenk tube equipped with a magnetic stirrer bar under Ar atmosphere. Then, N-hydroxysuccinimide (NHS, 6.1 mmol) and *N,N'*-dicyclohexylcarbodiimide (DCC, 6.0 mmol) were added. 135 mL of dry DCM was added with the aid of a syringe. The solution was left reacting under inert atmosphere at 25°C for 18 hours. Subsequently, the mixture was filtered and precipitated in 1 L of cold diethyl ether. The supernatant was removed, and the obtained white precipitate was dissolved in DCM and precipitated in cold diethyl ether again. PEG-diNHS was obtained as white solid after evaporation under reduce pressure (MW ≈ 2398.32 g mol^{-1}, 3.27 g, yield 60%).

^{1}H NMR ($CDCl_3$, 400 MHz); 4.27 ppm (t, 4H), 3.63 ppm (m, 180H), 2.95 ppm (t, 4H), 2.83 ppm (m, 8H), 2.77 ppm (t, 4H).

Synthesis of TEG-diNHS

STEP 1. The TEG (2.5 mmol) was added in a 150 mL round bottom flask equipped with a magnetic stirrer bar. Subsequently, 30 mL of $CHCl_3$ was added to solubilize the solid. Succinic anhydride (12.5 mmol) and DMAP (12.8 mmol) were added. The solution was heated to reflux and left reacting for 5 hours. A hydrogen carbonate solution (10 mL, 5 V/V%) was added to the crude product, that then was acidified to pH 1 with 6 N HCl. The TEG diacid was extracted with $CHCl_3$ and isolated after drying over sodium sulfate and evaporation under reduced pressure. (MW = 394.37 g mol^{-1}, yield 30%).
^{1}H NMR ($CDCl_3$, 400 MHz): 4.23 ppm (t, 4H), 3.68-3.64 ppm (m, 12H), 2.64-2.59 ppm (m, 8H).
STEP 2. The TEG diacid (1.0 mmol) and NHS (3.0 mmol) were solubilized in 10 mL of ethyl acetate (EtOAc) in a 50 mL round bottom flask equipped with a magnetic stirrer bar. Then, the reaction was cooled down to 4°C and DCC (3.0 mmol) was added. The solution was left reacting at room temperature for 3 hours. Subsequently, the mixture was cooled down, filtered and precipitated in 200 mL of cold diethyl ether. The supernatant was removed, and the obtained white precipitate was dissolved in DCM and precipitated in cold diethyl ether again. TEG-diNHS was obtained as white solid after evaporation under reduce pressure (MW = 556.52 g mol^{-1}, yield 80%).
^{1}H NMR ($CDCl_3$, 400 MHz); 4.27 ppm (t, 4H), 3.68-3.64 ppm (m, 12H), 2.95-2.73 ppm (m, 16H).

Synthesis of amphiphilic crosslinkers

The amphiphilic crosslinkers PDEGMA-*co*-NHS, POEGMA-*co*-NHS, and PNIPAA-*co*-NHS were all synthetized *via* free radical polymerization and the reaction scheme is reported in **Figure 5.11**.

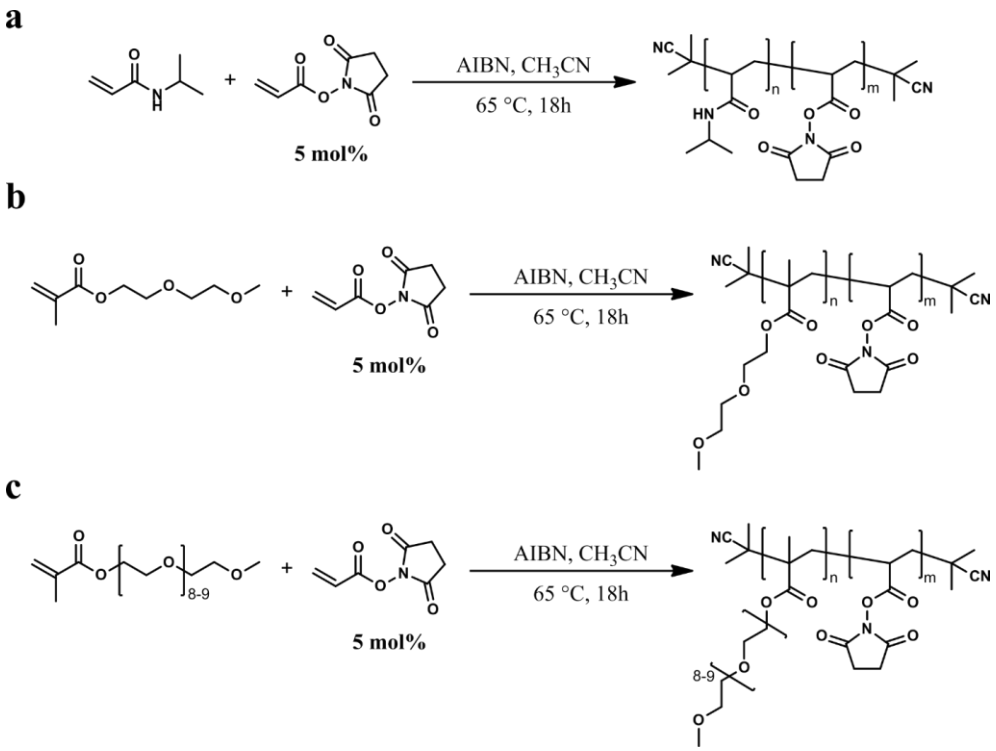

Figure 5.11. a) *Reaction scheme of PNIPAA*-co-*NHS synthesis;* ***b)*** *Reaction scheme of PDEGMA*-co-*NHS synthesis;* ***c)*** *Reaction scheme of POEGMA*-co-*NHS synthesis.*

A general procedure is carried out as follows. The principal monomer (NIPAA (7.9 mmol), DEGMA (4.8 mmol), OEGMA (1.6 mmol) was dissolved in CH_3CN (3 mL), in which *N*-acryloxysuccinimide (5 mol% of the principal monomer) was already solubilized, in a 7 mL glass vial equipped with a magnetic stirrer bar. At last, AIBN (5 mol%) was added to the mixture. The reaction was sealed and heated to 65 °C. After 18 hours, the crude was precipitated in 1:1 hexane/diethyl ether. PNIPAA-*co*-NHS was isolated as a white powder, whereas PDEGMA-*co*-NHS and POEGMA-*co*-NHS were isolated as viscous colorless fluids. In **Figure 5.12-14** are reported the corresponding ^{1}H NMR spectra.

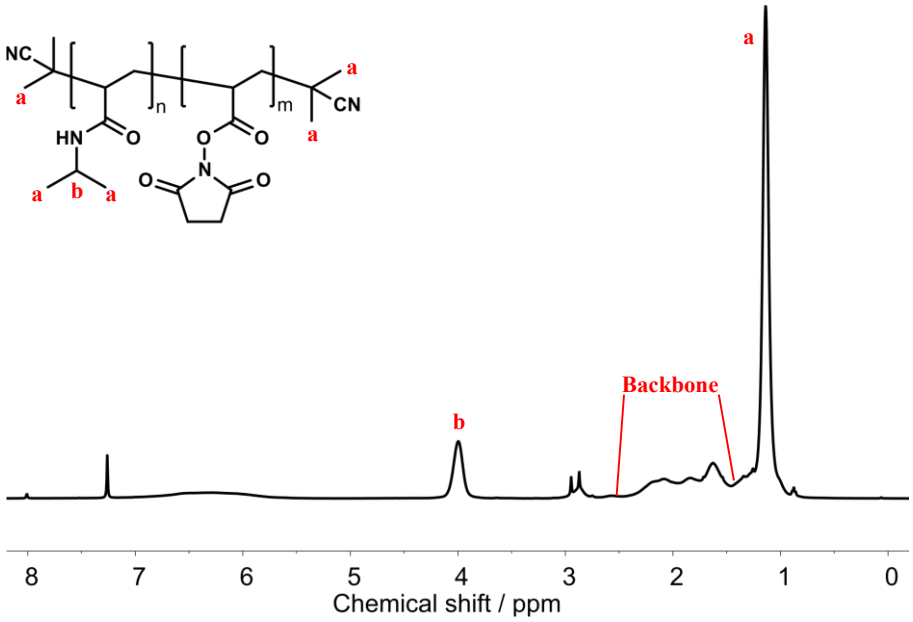

Figure 5.12. *^{1}H NMR spectrum of PNIPAA-co-NHS in deuterated chloroform, referenced against solvent residual peak (δH = 7.26 ppm).*

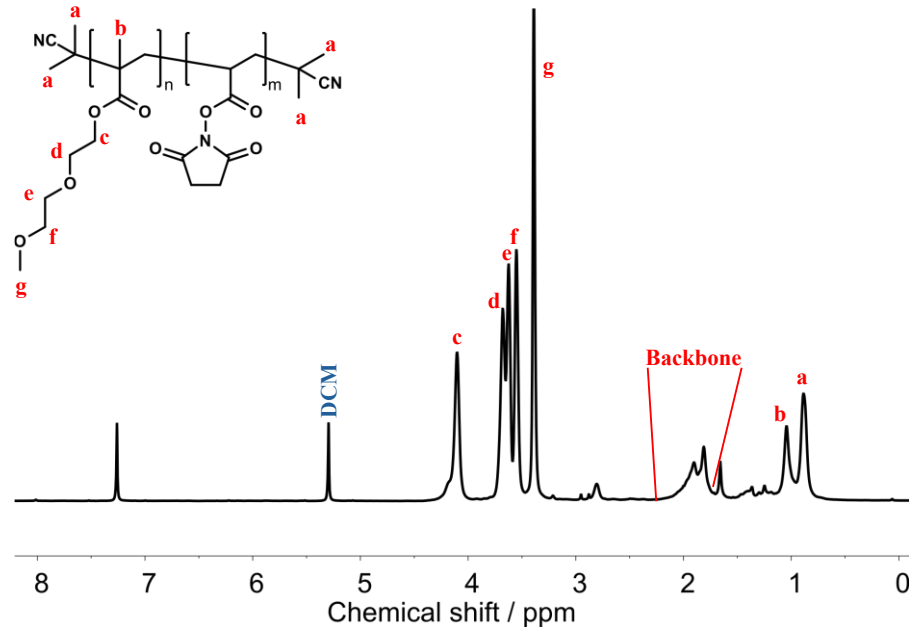

Figure 5.13. *^{1}H NMR spectrum of PDEGMA-co-NHS in deuterated chloroform, referenced against solvent residual peak (δH = 7.26 ppm).*

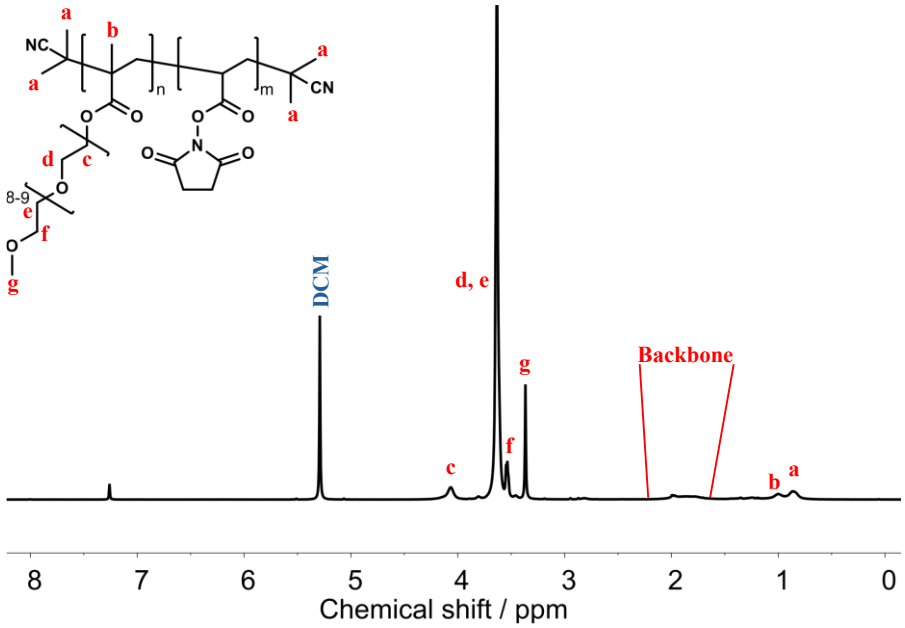

Figure 5.14. *^{1}H NMR spectrum of POEGMA-co-NHS in deuterated chloroform, referenced against solvent residual peak (δH = 7.26 ppm).*

5.4.4 Enzyme Cascade Reaction Assessment in CND-based Colloidosomes

Pickering emulsions of crosslinked GOx-containing CND-based colloidosomes were prepared using the procedure outlined above (see Experimental Section, 5.4.2 Preparation of CND-based colloidosomes *via* Pickering emulsion technique) with the exception that an aqueous solution of GOx (10 µL, 50 mg mL^{-1}) was mixed with a solution of the CND/polymer nanoconjugates. The GOx/HRP-like enzyme cascade reaction in the colloidosomes was monitored on a 96 multi-well plate mounted on the microscope sample holder. In a well, 100 µL of concentrated colloidosomes in MilliQ water were added to 300 µL of 10 mM PBS buffer (pH 6.8). The reaction was initiated by addition of the substates (10 µL of 0.5 mM *o*-PD solution and 10 µL of 1 mM glucose solution, respectively). The reaction (*i.e.*, 2,3-DAP fluorescence forming) was monitored for 70 minutes using wide-field fluorescence microscopy (λ_{exc} = 488 nm).

5.4.5 Supplementary Figures

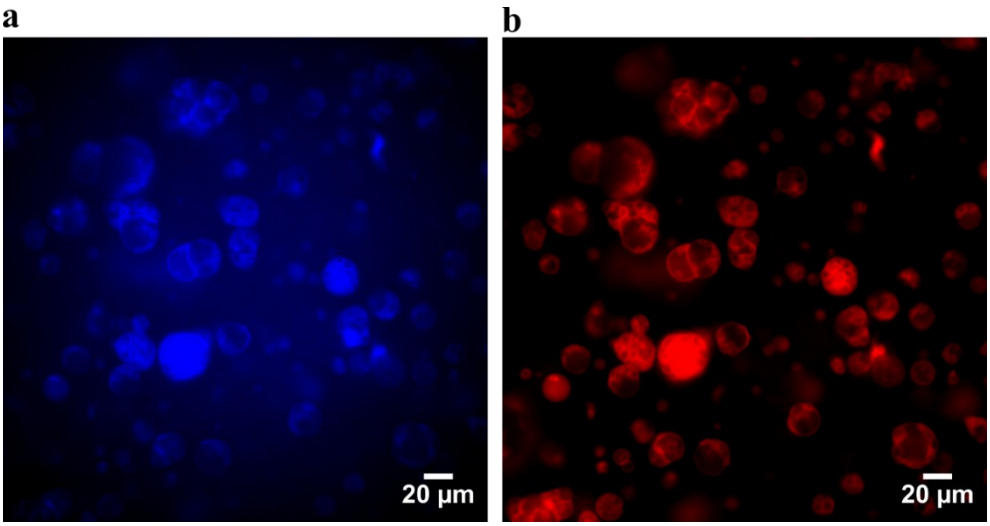

Figure S5.1. *Widefield fluorescence microscopy image of CND/polymer nanoconjugate-based colloidosomes (CND/polymer nanoconjugates at concentration = 4 mg mL^{-1}, PNIPAA-co-NHS quantity = 0.2 mg) in MilliQ water:* ***a)*** *CNDs (λ_{exc} = 405 nm, blue fluorescence);* ***b)*** *RhB-tagged polymer (λ_{exc} = 564 nm, red fluorescence).*

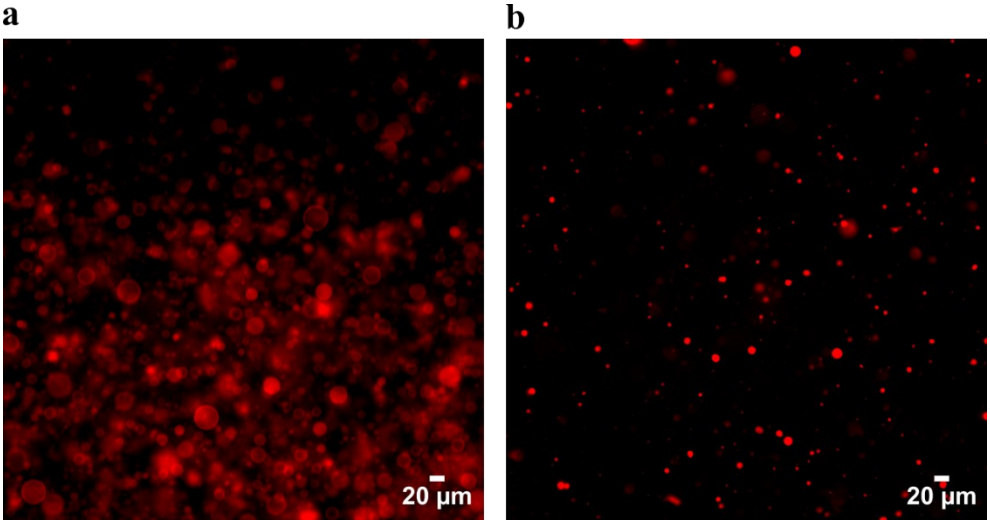

Figure S5.2. a) *microscopy image of CND/polymer nanoconjugate-based colloidosomes (CND/polymer nanoconjugates at concentration = 4 mg mL^{-1}, suberic acid-diNHS quantity = 0.2 mg) in 70 V/V% ethanolic aqueous solution (RhB-tagged polymer red fluorescence, λ_{exc} = 564 nm);* ***b)*** *Widefield fluorescence microscopy image of CND/polymer nanoconjugate-based colloidosomes (CND/polymer nanoconjugates at concentration = 4 mg mL^{-1}, PNIPAA-co-NHS quantity = 0.2 mg) in MilliQ water (RhB-tagged polymer red fluorescence, λ_{exc} = 564 nm) .*

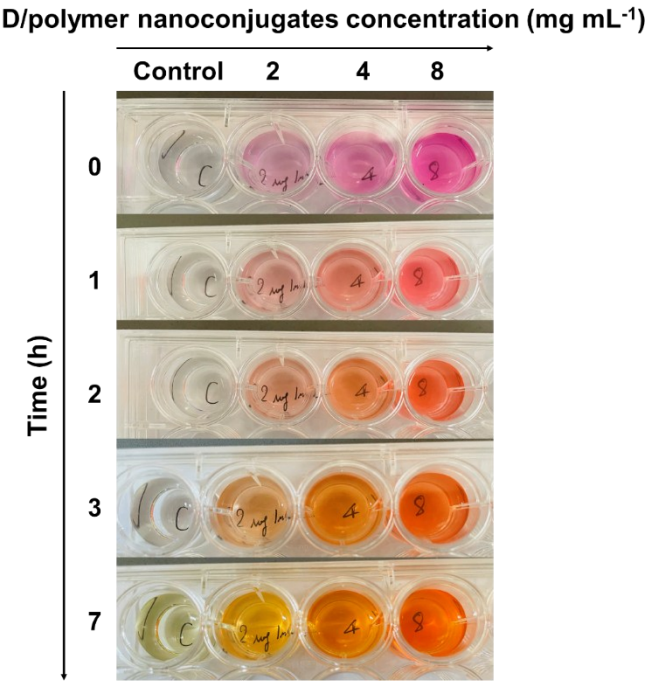

Figure S5.3. *Qualitative test in bulk of HRP-mimicking activity of CND/polymer nanoconjugates in 24 multi-well plate monitored over 7 hours. From left to right: control (MilliQ water), 2, 4, and 8 mg* mL^{-1} *of CND/polymer nanoconjugates, respectively (0.5 mM o-PD, 1 mM hydrogen peroxide).*

5.5 References

1. Wei, M., Lin, Y. & Qiao, Y. Engineered colloidosomes as biomimetic cellular models. *Giant* **13**, 100143 (2023).
2. Taylor, H., Gao, N. & Mann, S. Chemical Communication and Protocell-Matrix Dynamics in Segregated Colloidosome Micro-Colonies. *Angew. Chem.* **135**, e202300932 (2023).
3. Akkarachaneeyakorn, K., Li, M., Davis, S. A. & Mann, S. Secretion and Reversible Assembly of Extracellular-like Matrix by Enzyme-Active Colloidosome-Based Protocells. *Langmuir* **32**, 2912–2919 (2016).
4. Wu, H., Du, X., Meng, X., Qiu, D. & Qiao, Y. A three-tiered colloidosomal microreactor for continuous flow catalysis. *Nat. Commun.* **12**, 6113 (2021).
5. Thompson, K. L. *et al.* Direct Observation of Giant Pickering Emulsion and Colloidosome Droplet Interaction and Stability. *Langmuir* **28**, 16501–16511 (2012).
6. Jia, J. *et al.* High-gravity-assisted Fabrication of Self-assembled Colloidosomes. *Ind. Eng. Chem. Res.* **61**, 6934–6944 (2022).
7. Jiang, W. *et al.* Artificial Cells: Past, Present and Future. *ACS Nano* **16**, 15705–15733 (2022).
8. Rodríguez-Arco, L., Li, M. & Mann, S. Phagocytosis-inspired behaviour in synthetic protocell communities of compartmentalized colloidal objects. *Nat. Mater.* **16**, 857–863 (2017).
9. Bai, C. *et al.* Bioinspired electron carrier mediated transmembrane photocatalytic hydrogen evolution in silica colloidosomes. *Inorg. Chem. Front.* (2024).
10. Huang, X. *et al.* Interfacial assembly of protein–polymer nano-conjugates into stimulus-responsive biomimetic protocells. *Nat. Commun.* **4**, 2239 (2013).
11. Liu, Z. *et al.* Bioinspired Dual-Enzyme Colloidosome Reactors for High-Performance Biphasic Catalysis. *ACS Appl. Mater. Interfaces* **10**, 41504–41511 (2018).
12. van Oers, M., Rutjes, F. & van Hest, J. Cascade reactions in nanoreactors. *Curr. Opin. Biotechnol.* **28**, 10–16 (2014).
13. Huang, X., Li, M. & Mann, S. Membrane-mediated cascade reactions by enzyme–polymer proteinosomes. *Chem. Commun.* **50**, 6278–6280 (2014).
14. Mason, A. F., Buddingh', B. C., Williams, D. S. & van Hest, J. C. M. Hierarchical Self-Assembly of a Copolymer-Stabilized Coacervate Protocell. *J. Am. Chem. Soc.* **139**, 17309–17312 (2017).
15. Gobbo, P. *et al.* Programmed assembly of synthetic protocells into thermoresponsive prototissues. *Nat. Mater.* **17**, 1145–1153 (2018).
16. Li, Q., Li, S., Zhang, X., Xu, W. & Han, X. Programmed magnetic manipulation of vesicles into spatially coded prototissue architectures arrays. *Nat. Commun.* **11**, 232 (2020).

17. Ramsay, K., Levy, J., Gobbo, P. & S. Elvira, K. Programmed assembly of bespoke prototissues on a microfluidic platform. *Lab. Chip* **21**, 4574–4585 (2021).
18. Tian, L. *et al.* Nonequilibrium Spatiotemporal Sensing within Acoustically Patterned Two-Dimensional Protocell Arrays. *ACS Cent. Sci.* **4**, 1551–1558 (2018).
19. Galanti, A. *et al.* A Floating Mold Technique for the Programmed Assembly of Protocells into Protocellular Materials Capable of Non-Equilibrium Biochemical Sensing. *Adv. Mater.* **33**, 2100340 (2021).
20. Rebasa-Vallverdu, A. *et al.* Protocell Communication through the Eyes of Synthetic Organic Chemists. *Eur. J. Org. Chem.* **26**, e202300529 (2023).
21. Bai, J., Peng, C., Guo, L. & Zhou, M. Metal–Organic Framework-Integrated Enzymes as Bioreactor for Enhanced Therapy against Solid Tumor via a Cascade Catalytic Reaction. *ACS Biomater. Sci. Eng.* **5**, 6207–6215 (2019).
22. Wang, D., Chai, Y., Yuan, Y. & Yuan, R. Lattice-Like DNA Tetrahedron Nanostructure as Scaffold to Locate GOx and HRP Enzymes for Highly Efficient Enzyme Cascade Reaction. *ACS Appl. Mater. Interfaces* **12**, 2871–2877 (2020).
23. Wei, H. & Wang, E. Nanomaterials with enzyme-like characteristics (nanozymes): next-generation artificial enzymes. *Chem. Soc. Rev.* **42**, 6060–6093 (2013).
24. Zhang, R., Yan, X. & Fan, K. Nanozymes Inspired by Natural Enzymes. *Acc. Mater. Res.* **2**, 534–547 (2021).
25. Fan, K. *et al.* Optimization of Fe3O4 nanozyme activity via single amino acid modification mimicking an enzyme active site. *Chem. Commun.* **53**, 424–427 (2016).
26. Ji, S. *et al.* Matching the kinetics of natural enzymes with a single-atom iron nanozyme. *Nat. Catal.* **4**, 407–417 (2021).
27. Liang, S., Wu, X.-L., Zong, M.-H. & Lou, W.-Y. Zn-triazole coordination polymers: Bioinspired carbonic anhydrase mimics for hydration and sequestration of CO2. *Chem. Eng. J.* **398**, 125530 (2020).
28. Yin, M. *et al.* A visualized colorimetric detection strategy for heparin in serum using a metal-free polymer nanozyme. *Microchem. J.* **145**, 864–871 (2019).
29. Fu, T. *et al.* Zeolitic Imidazolate Framework-90 Nanoparticles as Nanozymes to Mimic Organophosphorus Hydrolase. *ACS Appl. Nano Mater.* **4**, 3345–3350 (2021).
30. Fan, K. *et al.* In vivo guiding nitrogen-doped carbon nanozyme for tumor catalytic therapy. *Nat. Commun.* **9**, 1440 (2018).
31. Wu, W. *et al.* Biomimetic design for enhancing the peroxidase mimicking activity of hemin. *Nanoscale* **11**, 12603–12609 (2019).

32. Zhang, P. *et al.* Modified carbon nitride nanozyme as bifunctional glucose oxidase-peroxidase for metal-free bioinspired cascade photocatalysis. *Nat. Commun.* **10**, 940 (2019).
33. Lopez-Cantu, D. O. *et al.* Enzyme-mimicking capacities of carbon-dots nanozymes: Properties, catalytic mechanism, and applications – A review. *Int. J. Biol. Macromol.* **194**, 676–687 (2022).
34. Yang, Z. *et al.* One-pot synthesis of CeO2-carbon dots with enhanced peroxidase-like activity and carbon dots for ratiometric fluorescence detection of H2O2 and cholesterol. *J. Alloys Compd.* **862**, 158323 (2021).
35. Liu, C. *et al.* Carbon dot enhanced peroxidase-like activity of platinum nanozymes. *Nanoscale* **16**, 4637–4646 (2024).
36. Park, J. H. *et al.* Colloidosomes as a Protocell Model: Engineering Life-Like Behaviour through Organic Chemistry. *Eur. J. Org. Chem.* **2022**, e202200968 (2022).
37. Whitby, C. P. & Parthipan, R. Influence of particle concentration on multiple droplet formation in Pickering emulsions. *J. Colloid Interface Sci.* **554**, 315–323 (2019).
38. Zhao, H. *et al.* A review of multiple Pickering emulsions: Solid stabilization, preparation, particle effect, and application. *Chem. Eng. Sci.* **248**, 117085 (2022).
39. Terashima, T. Controlled Self-Assembly of Amphiphilic Random Copolymers into Folded Micelles and Nanostructure Materials. *J. Oleo Sci.* **69**, 529–538 (2020).
40. Christopoulou, A., Kazamiakis, C., Iatridi, Z. & Bokias, G. Controlled Amphiphilicity and Thermo-Responsiveness of Functional Copolymers Based on Oligo(Ethylene Glycol) Methyl Ether Methacrylates. *Polymers* **16**, 1456 (2024).
41. Ye, Q. *et al.* Fluorescent and Colorimetric Sensors Based on the Oxidation of o-Phenylenediamine. *ACS Omega* **5**, 20698–20706 (2020).

Chapter VI – General Conclusions

The primary aim of this Thesis was to engineer microcompartments that mimic life-like behaviors, namely protocells, using Carbon NanoDots (CNDs) as versatile building blocks. By leveraging the unique physicochemical properties of CNDs, such as high (photo)stability, intrinsic fluorescence, and ease of functionalization, this research establishes a robust methodology for creating stable, cost-effective, and functional carbon-based microcompartments, specifically organic colloidosomes. Each chapter addresses a key stage in microstructure fabrication, from CND characterization and functionalization to their assembly into protocells, yielding insights into CND surface reactivity, molecular weight distribution, and precise covalent coupling with probe molecules, polymers, and other CNDs.

Through a comprehensive characterization and analysis, this work provides structural and compositional details on both CNDs and their conjugated nanocomposites, either with CNDs or polymers. This was possible by relying on technique such as multi-detector gel permeation chromatography (GPC), NMR and IR spectroscopies, UV-Vis, fluorescence spectroscopy, and more advanced optical spectroscopies and microscopies. These findings confirm GPC efficacy in characterizing complex nanoscale particles and assemblies, offering unprecedent level of detail for a chromatographic technique. Establishing the molecular weight of CNDs lays a foundation for their rational application in advanced scientific fields, such as bio-photocatalysis.

The successful fabrication of CND-based colloidosomes demonstrates the potential of CNDs as multivalent platforms that can form synthetic cell membranes. These self-assembled microcapsules exhibit intrinsic fluorescence and enzyme-like functionality, marking a significant step forward in designing protocells that combines simplicity with multifunctionality. Notably, this achievement overcomes present limitations seen in other organic colloidosomes, such as proteinosomes, which, being protein-based, suffer from high production costs and limited stability.

While this research provides valuable insights, it is currently limited to a single type of CNDs – specifically, blue-emitting *L*-arginine and ethylenimine-derived CNDs. This choice, however, has provided a robust benchmark for both detailed carbon dot characterization and protocell fabrication.

As the first study to produce CND-based protocells, this work opens new avenues for synthetic biology and nanotechnology, laying a foundation for developing programmable microsystems with applications in catalysis and biosensing.

Future studies will focus on refining the kinetics of enzyme-mimicking reactions within these colloidosomes, aiming to better understand CNDs contribution as nanozymes. This approach could lead to the fabrication of colloidosomes with specific enzyme-like behaviors, tailored by the CNDs in their membranes.

Ultimately, this Thesis establishes a basis for further advancements in carbon dot research field and CND-based microcompartment fabrication, promoting CNDs as sustainable, tunable, and biocompatible tools for the next-generation bottom-up synthetic biology constructs.